ISSN: 0439-5689

HORMIGÓN y ACERO

REVISTA CUATRIMESTRAL DE ACHE ASOCIACIÓN ESPAÑOLA DE INGENIERÍA ESTRUCTURAL

Mayo - Agosto 2025 I Volumen 76 - Número 306

www.hormigonyacero.com

NUEVA VERSIÓN DE SOFiSTiK DISPONIBLE

- Novedoso visor para una actualizada experiencia visual durante el post-proceso.
- Mejoras en el diseño de vigas para el flujo de trabajo en modelos 3D.
- Nuevas secciones estándar en T por un solo lado para el contorno.
- Implementación del ciclo vital y la huella de carbono del modelo estructural.
- Comprobaciones elásticas en límite último de servicio para puentes mixtos.
- Nuevo interfaz gráfico para el análisis dinámico de puentes ferroviarios.
- Análisis del espectro de respuesta en sismos para edificación.

y más novedades en los procesos de modelado y de delineación.

INFORMACIÓN DETALLADA AQUÍ

SOFiSTiK 2025

SOFiSTiK

SOFiSTiK 2025 BiM TOOLS LIBRARY

FOTO DE PORTADA: Desmontaje del tramo tipo sobre la rampa de acceso de la M-607, en Madrid.

HORMIGÓN y ACERO

Mayo - agosto 2025 I Volumen 76 - Número 306

REVISTA CUATRIMESTRAL DE LA ASOCIACIÓN ESPAÑOLA DE INGENIERÍA ESTRUCTURAL

El Consejo Editorial de la revista tiene como misión la definición de la política editorial (estilo de la revista, redacción, normas de presentación de originales, diseño, creación y orientación de las distintas secciones). **El Comité de Redacción** se constituye como un comité permanente del Consejo Editorial y se encarga de dirigir y supervisar la gestión diaria de la revista, controlar la selección de contribuciones y tomar las decisiones sobre los contenidos que han de conformar cada número de la revista. La función del **Consejo Asesor Científico** es la de velar por el prestigio científico y técnico de la revista, promoviendo e impulsando su difusión internacional.

Una descripción más amplia puede consultarse en *www.hormigonyacero.com*

ÍNDICES Y SERVICIOS DE INFORMACIÓN: *Hormigon y Acero esta indexada en las bases de datos siguientes: Emerging Sources Citation Index/Web of Science Core Collection (ESCI/WoS) - Journal Citation Reports (JCR) – Scopus - Pascal – InDICEs-CSIC – Dialnet-Sumaris – Catalogo Latindex 2.0 – ScienceDirect.*

ISSN 0439-5689
Publicación cuatrimestral (3 números al año)
www.hormigonyacero.com
https://doi.org/10.33586/hya.2025.GRANADA

Protección de datos: CINTER DIVULGACIÓN TÉCNICA, S.L. declara cumplir lo dispuesto por la Ley orgánica 15/1999, de 13 de diciembre, de Protección de Datos de Carácter Personal.

Suscripciones y atención al cliente

CINTER DIVULGACIÓN TÉCNICA

CINTER DIVULGACIÓN TÉCNICA, S.L.
C/Doctor Santero, 7 , 28039 Madrid (España)
Teléfono: 913191200
Correo electrónico: cinter@cinter.es

Impresa en España por Gráficas Muriel
Diseño gráfico y maquetación: Antonella Genovese / Mgráfico
Depósito legal: M-853-1958

HORMIGÓN y ACERO

Disponible en **www.hormigonyacero.com**

SUMARIO | CONTENTS

MAYO - AGOSTO 2025 I Volumen 76 - Número 306

May - August 2025 I Volume 76 - Issue 306

Publicado por Cinter Divulgación Técnica S.L.
E.T.S.I. de Caminos, Canales y Puertos. Laboratorio de Estructuras. Avda. del Profesor Aranguren, s/n. 28040 Madrid
Tel.: (+34) 91 067 41 64 - www.e-ache.com

ACHE

CINTER

MIEMBROS PATROCINADORES DE LA ASOCIACIÓN ESPAÑOLA DE INGENIERÍA ESTRUCTURAL (ACHE)

Según los Estatutos de la Asociación existen dos tipos de miembros, uno para personas jurídicas y otro para personas físicas. De entre los primeros, y por la importancia que tienen para la Asociación por su contribución económica, destacan los miembros Patrocinadores y los Protectores. Hasta la fecha de cierre del presente número de la Revista, figuran inscritos como **Miembros Patrocinadores** los que a continuación se indican, citados por orden alfabético:

ACCIONA INFRAESTRUCTURAS
Avda. de Europa, 18
28108 ALCOBENDAS (MADRID)

ALLPLAN Systems

ARENAS & ASOCIADOS, INGENIERÍA DE DISEÑO, S.L.P.
C/ Marqués de la Ensenada, 11 - 3º
39009 SANTANDER

C/ Jordi Girona 31 - 2º, Edifici Til·lers
08034 - BARCELONA

AZUL CONSTRUCCIÓN REPAIR, S.A.
Pq. Comercial San Jerónimo, Calle A,
Nave 11. 41015 SEVILLA

CALIDAD SIDERÚRGICA
C/ Orense, 58 - 10º
28006 MADRID

CARLOS FERNANDEZ CASADO, S.L.
OFICINA DE PROYECTOS
C/ Orense, 10
28020 MADRID

CEDEX (Laboratorio Central)
C/ Alfonso XII, 3
28014 MADRID

CONSEJO GENERAL COLEGIOS ARQUITECTOS TÉCNICOS
Paseo de la Castellana, 155 - 1º
28046 MADRID

CYPE INGENIEROS, S.A.
Avda. Eusebio Sempere, 5 - Bajo
03003 ALICANTE

DRAGADOS, S.A.
Avda. Camino de Santiago, 50
28050 MADRID

EDARTEC CONSULTORES
C/ Manufactura, 4 - Planta 2 - Mod. 3
41297 MAIRENA DE ALJARAFE (SEVILLA)

E.T.S. INGENIEROS DE CAMINOS - DPTO. MECÁNICA
Ciudad Universitaria, s/n
28040 MADRID

FCC CONSTRUCCIÓN, S.A.
Avda. Camino de Santiago 40
28050 MADRID

FHECOR ingenieros consultores S.A.
C/Barquillo, 23. 1º izq.
28004 MADRID

FLORENTINO REGALADO INGENIERÍA & ARQUITECTURA S.L.P.
C/ Granja de Rocamora, 18
03015 ALICANTE

GRUPO MECÁNICA ESTRUCTURAL S.L
C/ Amílcar González Díaz, 18
38550 ARAFO (SANTA CRUZ DE TENERIFE)

HILTI ESPAÑOLA, S.A.
Avda. Fuente de la Mora, 2 - Edificio I
28050 MADRID

INSTITUTO EDUARDO TORROJA
C/ Serrano Galvache, 4
28033 MADRID

IECA
C/ José Abascal, 53 - 2º
28003 MADRID

MAMMOET
P.I. Los Frailes. Ctra Alcalá de Henares a Daganzo,
km 9. P 101-106, 28814 DAGANZO (MADRID)

MEKANO4 INNOVATIVE SOLUTIONS
P.I. Can Nadal, Carrer Can Nadal, s/n, Nave 1-A, 08185
Lliçà de Vall, Barcelona

OVE ARUP & PARTNERS, S.A.
C/ Alfonso XI, 12
28014 Madrid

PUENTES Y CALZADAS, GRUPO DE EMPRESAS, S.A.
Ctra. de la Estación, s/n
15888 SIGÜEIRO-OROSO (A CORUÑA)

SORIGUÉ ACSA
Calle de la Pirotecnia. 28052.
Madrid

MEMBER OF BASQUE RESEARCH
& TECHNOLOGY ALLIANCE

MIEMBROS PROTECTORES DE LA ASOCIACIÓN ESPAÑOLA DE INGENIERÍA ESTRUCTURAL (ACHE)

Según los Estatutos de la Asociación existen dos tipos de miembros, uno para personas jurídicas y otro para personas físicas. De entre los primeros, y por la importancia que tienen para la Asociación por su contribución económica, destacan los miembros Patrocinadores y los Protectores. Hasta la fecha de cierre del presente número de la Revista, figuran inscritos como **Miembros Protectores** los que a continuación se indican, citados por orden alfabético:

ANEFHOP
APF ingeniería
ArcelorMittal
ARPO
ar2v: ingeniería
ayesa
calter ingeniería de estructuras
COL·LEGI D'APARELLADORS I ARQUITECTES TÈCNICS DE GIRONA
COMSA
DEGREE OF FREEDOM
DYWIDAG
ESTEYCO
ferrovial agroman
FH INGENIEROS
FERNANDEZ Y HERNANDEZ INGENIEROS, S.L.L.
FREYSSINET
SUSTAINABLE TECHNOLOGY
GRACE
HEMPEL
Trust is earned
imesAPI
Servicios · Movilidad
ines
ingenieros consultores
IDOM
itc GRUPO ATISAE
INSTITUTO TECNICO DE LA CONSTRUCCION S.A.
INTEMAC
METIRE UT SCIAS
JULIÁN ARUMÍ, S.L.
PREFABRICADOS DE HORMIGÓN
MAURER
MeKano MK4
MAPEI
MOTT MACDONALD
OHL
ORRAMOS
INGENIERÍA S.L.
PACADAR
PRECON
PROES
Pujol
Prefabricados de Hormigón
RETiNEO
SOCOTEC
SOLUCIONES STEEL URBAN
SOLURBAN
sitt
CONSOLIS
TECNYCONTA
tecpresa
Tierra Armada
TORROJA
INGENIERÍA
Grupo
TYPSA
ULMA
VSL
WELL LINK

HORMIGÓN y ACERO

CARTA DEL DIRECTOR

A propuesta del anterior director de la revista Gonzalo Ruiz, el Consejo de la Asociación de Ingeniería Estructural ACHE me nombró nuevo director de *Hormigón y Acero* en su reunión de finales del mes de abril del 2025.

Asumo este reto con ilusión para continuar el excelente trabajo llevado a cabo por el Consejo Editorial bajo la dirección de los dos últimos directores, Luis Ortega Basagoiti y Gonzalo Ruiz.

La revista *Hormigón y Acero* de ACHE publicará artículos en inglés o español sobre estructuras, incluyendo investigaciones, estudios y proyectos realizados en edificación y obra civil. Los temas abarcarán el proyecto, la construcción, el mantenimiento, la reparación, el refuerzo y la demolición de estructuras. La publicación combinará números ordinarios con números monográficos.

En los próximos meses, está prevista la publicación de un número monográfico sobre la renovación del estadio Santiago Bernabéu del club de futbol Real Madrid y la de otro en honor a los profesores Hugo Corres y Toni Marí. También se trabaja en la preparación de un monográfico sobre las acciones explosivas en estructuras y de otro dedicado a Jörg Schlaich.

Asimismo, se fomentará la publicación de artículos derivados de las numerosas y relevantes ponencias presentadas en el congreso ACHE, celebrado en Granada a finales de junio. Los resúmenes de dichas ponencias han sido publicados por *Hormigón y Acero* en junio de 2025.

Para todo este trabajo, cuento con el apoyo del Comité de Redacción para el trabajo del día a día que colaborará con el Editor jefe. Asimismo, cuento con el Consejo Editorial que tras el verano será renovado y que abordará temas estratégicos para la revista como el logro de artículos de calidad a publicar, la difusión e internacionalización de la revista y la mejora de sus factores de impacto, entre otros. Más adelante, se analizará también y se potenciará la función del Consejo Asesor Científico de la revista.

Este número ordinario nº 306 de la revista, correspondiente al periodo mayo-agosto 2025, incluye nueve artículos, cinco en inglés y cuatro en español. En primer lugar, se incluye un artículo sobre la demolición del tablero dañado de un puente y su sustitución por uno nuevo en un nudo de comunicaciones de alta densidad de tráfico próximo a la ciudad de Madrid. Seguidamente, se incluyen ocho artículos sobre estudios de puentes y estructuras.

Finalmente, invito a los autores de artículos sobre estructuras que consideren Hormigón y Acero como una revista de interés para su publicación. Además, en la web www.hormigonyacero.com pueden descargarse todos los artículos publicados hasta la fecha de forma gratuita.

Jesús Rodríguez
DIRECTOR DE *HORMIGÓN Y ACERO*

LETTER FROM THE DIRECTOR

At the proposal of the previous director of the journal Gonzalo Ruiz, the Council of the Association of Structural Engineering ACHE appointed me as new director of *Hormigón y Acero* journal at its meeting at the end of April 2025.

I take on this challenge with enthusiasm to continue the excellent work carried out by the Editorial Board chaired by the last two directors, Luis Ortega Basagoiti and Gonzalo Ruiz.

ACHE's *Hormigón y Acero* journal will publish articles in English or Spanish on structures, including research, studies and projects on building and civil works. Topics will cover the design, construction, maintenance, repair, strengthening and demolition of structures. The publication will combine ordinary issues with monographic ones.

In the coming months, a monographic issue on the renovation of the Santiago Bernabéu stadium of the Real Madrid football club and another in honour of professors Hugo Corres and Toni Marí are expected to be published. Work is also being done on the preparation of a monographic issue on explosive actions in structures and another one dedicated to Jörg Schlaich.

Likewise, the publication of articles derived from the numerous and relevant papers presented at the ACHE congress, held in Granada at the end of June, will be encouraged. The abstracts of these presentations have been published by *Hormigón y Acero* in June 2025.

For all this work, I will have the support of the Editorial Committee for the day-to-day work that will collaborate with the Editor-in-Chief. I also have the support of the Editorial Board that will be renewed after the summer and that will address strategic subjects for the journal such as the achievement of quality articles to be published, the dissemination and internationalization of the journal and the improvement of its impact factors, among others. Later, the role of the journal's Scientific Advisory Board will also be analysed and strengthened.

This ordinary issue No. 306 of the journal, corresponding to the period May-August 2025, includes nine articles, five in English and four in Spanish. The first one is dealing with the demolition of the damaged deck of a bridge and its replacement with a new one in a high-density traffic road junction near the city of Madrid. The other eight articles cover studies on bridges and structures.

Finally, I am inviting authors of future articles on structures to consider *Hormigón y Acero* journal as an appropriate one for their publications, either in English or in Spanish, being the web www.hormigonyacero.com where all published articles till now can be downloaded for free.

Jesús Rodríguez
DIRECTOR OF *HORMIGÓN Y ACERO*

Disponible en **www.hormigonyacero.com**
https://doi.org/10.33586/hya.2024.3090

Replacement of the Deck and Rehabilitation of the Viaduct at the Link Between M-40 and M-607 in Madrid (Spain)

Sustitución del tablero y rehabilitación del viaducto del enlace entre la M-40 y la M-607 en Madrid (España)

Juan Rodado [a], Fátima Otero [b]

[a] *Dr. Ingeniero de Caminos, Canales y Puertos. Director Técnico de Ingeniería. Grupo Puentes*
[b] *Ingeniero de Caminos, Canales y Puertos. Directora General Técnica. Grupo Puentes*

Recibido el 14 de julio de 2022; revisado el 23 de mayo de 2023, aceptado el 20 de mayo de 2024

ABSTRACT

The existing concrete viaduct 560 m long at the link between M-40 ring road and M-607 expressway in Madrid (Spain) was subjected to a very comprehensive process of evaluation and testing after high deck deflections and surface cracking were detected. As conclusion of these studies very severe damages and a process of concrete degradations were confirmed which led to the decision of dismounting the existing deck structure and constructing a new one supported on the existing substructure which had to be repaired and reinforced. Grupo Puentes has carried out both the process of deck disassembly and the construction of the new deck in a record time of approximately nine months. The viaduct is in a very traffic congested link to approach Madrid and crosses over not only the main roads, M-40 ring road and M-607 expressway, but also two approach ramps and two railway lines, one of them high-speed line.

KEYWORDS: viaduct, rehabilitation, precast, concrete, disassembly.

RESUMEN

El viaducto de hormigón existente en el enlace entre la carretera de circunvalación M-40 y la vía rápida M-607 en Madrid (España), con 560 m de longitud, fue sometido a un proceso de evaluación y ensayos muy completo tras ser detectadas grandes deformaciones del tablero y fisuración superficial. Como conclusión de estos estudios se confirmaron daños severos y un proceso de degradación del hormigón que dieron lugar a la decisión de desmontar el tablero existente y construir uno nuevo aprovechando la subestructura, que tuvo que ser reparada y reforzada. Grupo Puentes ha llevado a cabo tanto el proceso de desmontaje del tablero como la construcción del nuevo en un tiempo récord de nueve meses. El viaducto se sitúa en un enlace muy congestionado de tráfico para el acceso a Madrid y cruza no solo sobre las carreteras principales, vía de circunvalación M-40 y vía rápida M-607, sino también sobre dos ramales de acceso y dos líneas ferroviarias, una de ellas de alta velocidad.

PALABRAS CLAVE: viaducto, rehabilitación, prefabricado, hormigón, desmontaje.

* Persona de contacto / *Corresponding author*:
Correo-e / *e-mail*: j.rodado@grupopuentes.com (Juan Rodado)

Cómo citar este artículo: Rodado, J., & Otero, F. (2025). Replacement of the Deck and Rehabilitation of the Viaduct at the Link Between M-40 and M-607 in Madrid (Spain). *Hormigón y Acero*. 76(306):7-16. https://doi.org/10.33586/hya.2024.3090

1. EXISTING VIADUCT

1.1. General description

The original viaduct located at the link between M-40 ring road and M-607 in Madrid was built in the nineties and allowed the connection of the south-ward carriageway of this last road with the north-ward carriageway of M-40 (Figure 1).

The viaduct consisted of 17 spans with span lengths of 20 + 32 + 35 + 37 + 55 + 32 + 36 + 38 + 29 + 28.5 + 36 +

Figure 1. Viaduct general location plan.

2×29 + 2×32.5 + 30 + 20 m, and a total length of 551.5 m, all dimensions referred to the curved alignment axis according to the existing definitive design (Figure 2).

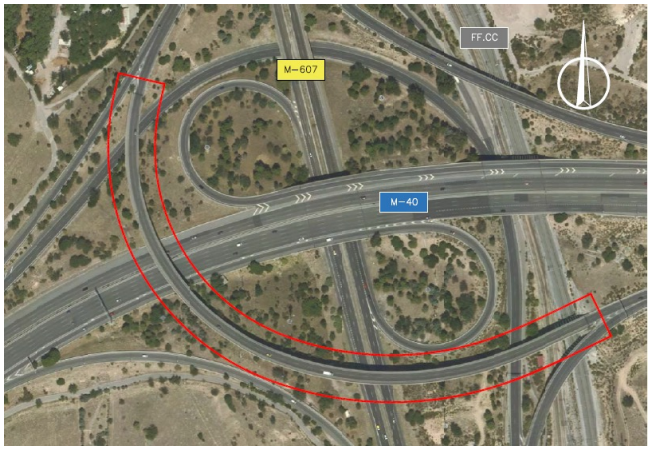

Figure 2. Existing viaduct general aerial view.

The deck cross section was a post-tensioned concrete slab with longitudinally constant depth, except at both piers adjacent to 55 m long span, and cylindrical longitudinal voids of different diameter formed by expanded polystyrene. The soffit of the section was curve with maximum depth of 1.4 m at central axis (Figure 3).

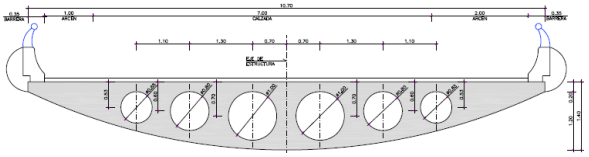

Figure 3. Existing viaduct deck typical cross section.

The piers consisted of simple shafts with ellipsoidal constant section, and they were founded by means of footings.

1.2. Detected damages and actions to carry out

Due to the high vertical deflections observed in some of the longest spans of the viaduct, it was subjected to a special inspection at the end of 2018. As conclusion of the studies and tests carried out during this inspection very severe damages were detected, with clear affection to the strength and de-formability of the concrete of the deck and its capacity to withstand the required loads [2][3].

Since no repair procedure was found economically feasible and possible to reinforce the deck, the road authority final decision was the dismantling of the deck and its replacement by a new one. The sub-structure, piers, abutments, and foundations would be kept with the necessary reinforcement actions.

2. DISASSEMBLY PROCESS

2.1. General considerations

All the process of dismantling the existing viaduct deck has been developed following some requirements to guarantee the safety and accuracy of all operations [4]. The following lines have guided this process:

- All deck cuts were made by means of diamond wire; in this way no demolition of aerial structures was carried out at deck position. The deck pieces were moved afterwards to the in-site demolition area.
- A detailed design was prepared, by Pondio Ingenieros, to define all operations and the exact position of each deck cut, taken into account the prestressing design, the deck sections (voided or not) and the weight of the resulting pieces [5].
- All pieces of deck were fully supported, or hanged as explained below, before beginning of cutting operations.
- The removal of deck sections was carried out by cranes of appropriate capacity.
- The removal of those deck sections located over service roads was made in the night hours.
- The traffic was kept along the different roads existing in the link and it was stopped only some hours at night when removal operations must be developed.
- Wind velocity was measured continuously to guarantee the safety conditions for cranes operations. There were some alert values to stop operations depending on each machine.

Figure 4. Temporary steel towers to support existing deck sections.

2.2. Typical spans

The process of disassembly of the typical spans of the old deck has been performed by means of cutting completely the

sections with diamond wire, which has advantages from the point of view of safety and control of the structural behaviour of the bridge. The concrete barriers on both sides of the deck were cut together with the deck sections. In this way, the deck was divided in sections with variable length which, after being supported by temporary steel towers (Figure 4), were taken away by means of cranes to the demolition area (Figure 5). In this way, no demolition itself is made at the elevated deck position, not even that for concrete barriers. All products resulting from demolition, concrete and steel, was fully recycled by specialized companies.

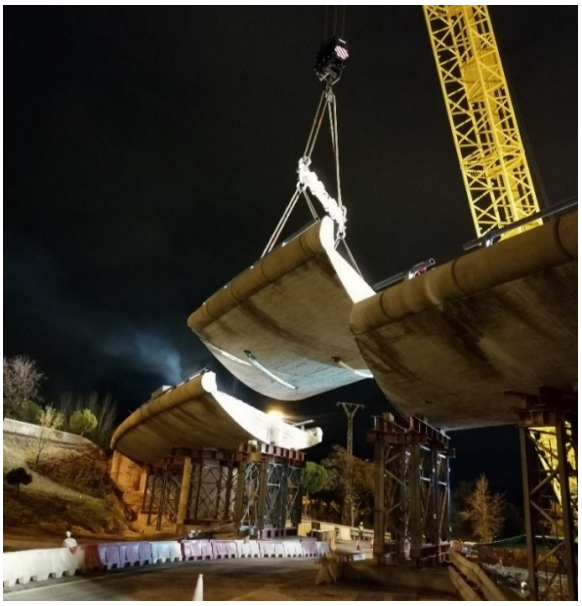

Figure 5. Disassembly of typical span section over M-607 approach ramp.

The cutting order and the corresponding procedures have been carefully studied to ensure the stability and integrity of the structure and to avoid in all time the complete traffic cutting of the roads under the bridge.

Figure 6. Cross section view of a disassembled segment of typical span.

The typical length of the deck sections to be re-moved was 12 m with a weight of 2708 kN for voided sections (Figure 6). Nevertheless, the maximum weight of the heaviest section was 3090 kN for the section placed on pier P7 which was 12,67 m long. In turn, the longest sections with a length of 13 m had a weight of 2943 kN, corresponding to voided deck sections.

Figures 7 to 24 show the disassembly phases span by span. The green numbers over the different sections represent the order of sections removal once the cuttings have been done:

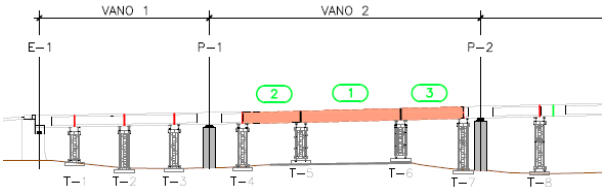

Figure 7. Phase 1: Disassembly of span 2.

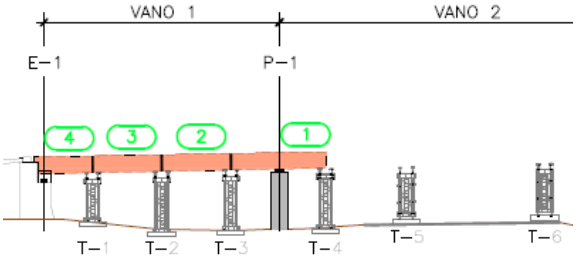

Figure 8. Phase 2: Disassembly of span 1.

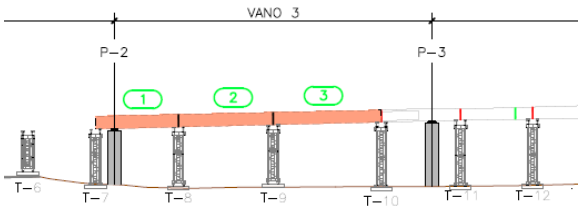

Figure 9. Phase 3: Disassembly of span 3.

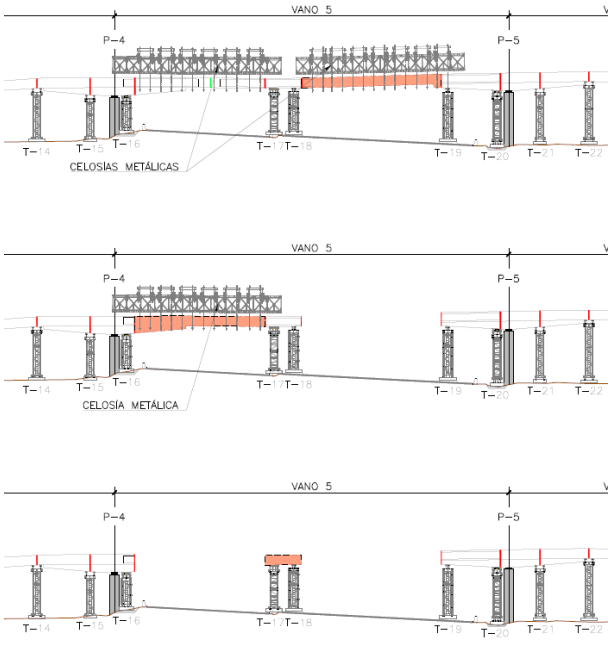

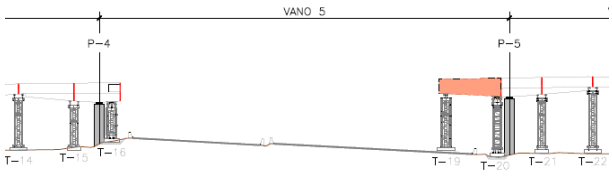

Figure 10. Phase 4: Disassembly of span 5 over M-40.

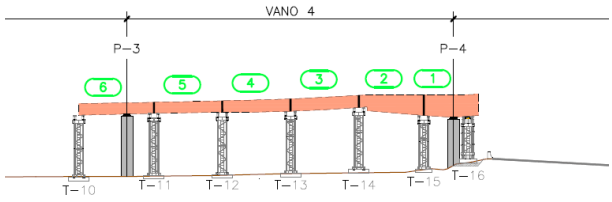

Figure 11. Phase 5: Disassembly of span 4.

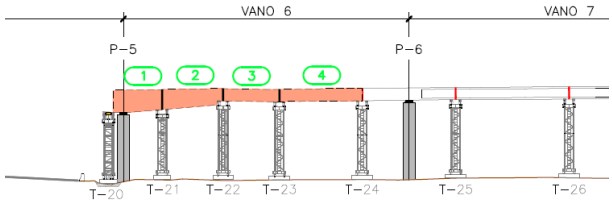

Figure 12. Phase 6: Disassembly of span 6.

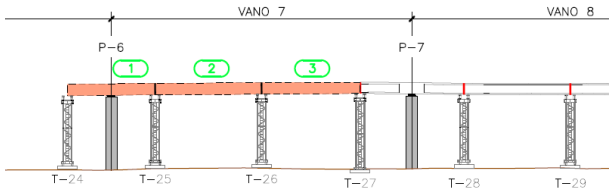

Figure 13. Phase 7: Disassembly of span 7.

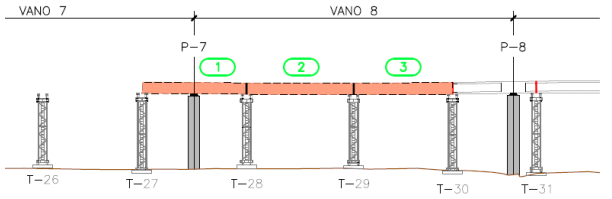

Figure 14. Phase 8: Disassembly of span 8.

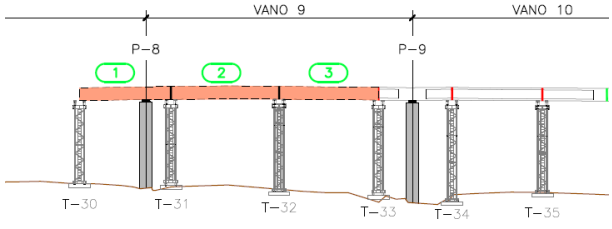

Figure 15. Phase 9: Disassembly of span 9.

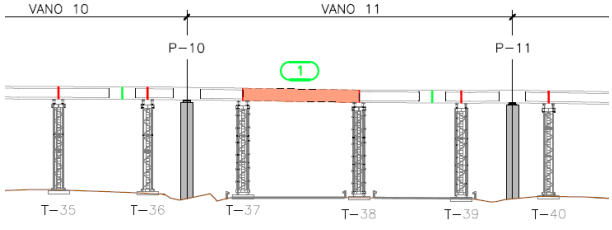

Figure 16. Phase 10: Disassembly of span 11 midspan segment over M-607.

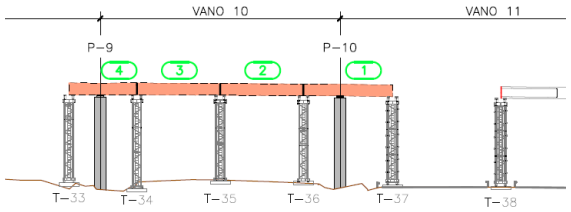

Figure 17. Phase 11: Disassembly of span 10.

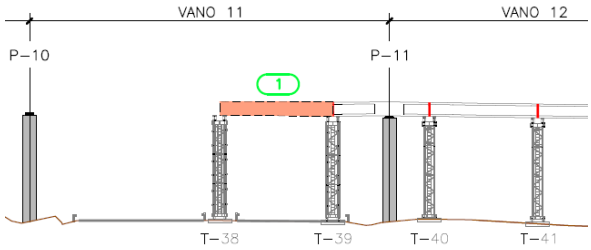

Figure 18. Phase 12: Disassembly of rest of span 11 over M-607.

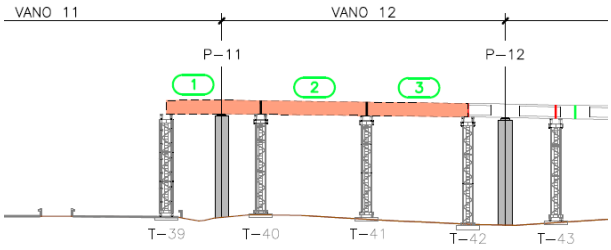

Figure 19. Phase 13: Disassembly of span 12.

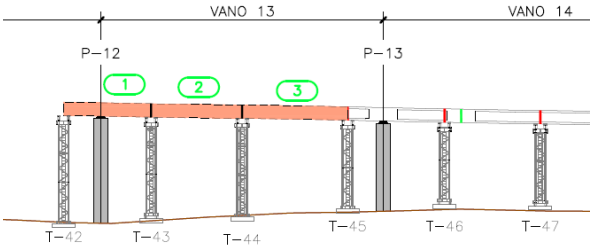

Figure 20. Phase 14: Disassembly of span 13.

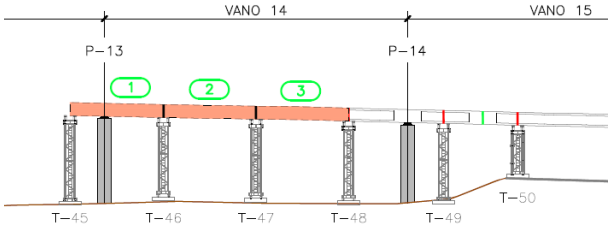

Figure 21. Phase 15: Disassembly of span 14.

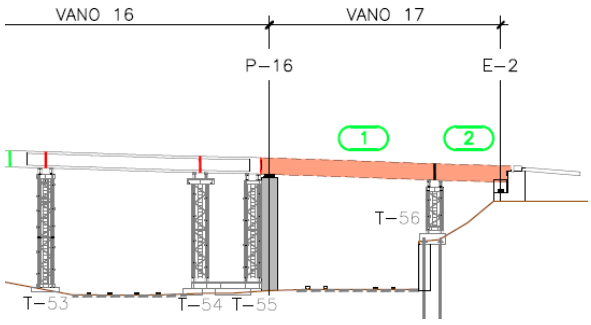

Figure 22. Phase 16: Disassembly of span 17 over railway line.

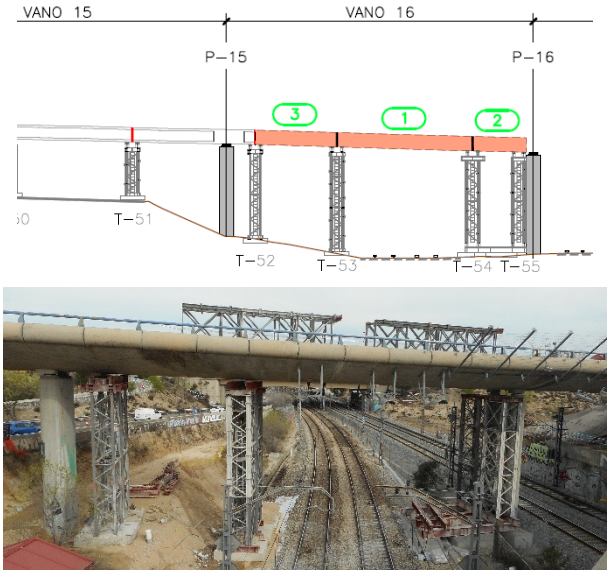

Figure 23. Phase 17: Disassembly of span 16 over railway line.

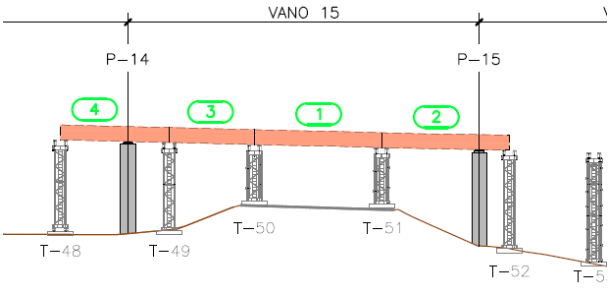

Figure 24. Phase 18: Disassembly of span 15.

At the spans over the railway lines between piers P15 and P16 and between P16 and abutment E2 (Figures 22 and 23), respectively, longest sections were needed, up to 14 m and 3414 kN, due to the presence of the railway lines, which required wider horizontal clearances between towers. For those sections additional cuts had to be performed to divide the sections into lighter parts by removing the ends of the section in first phase and then the central core in second phase (Figure 25). The three parts were tied together by means of a steel cross beam over the deck and prestressed bars (Figure 26). The sections on this area were cut and removed in close coordination with the railway administration to provide gaps without traffic of trains for these operations, always in night hours.

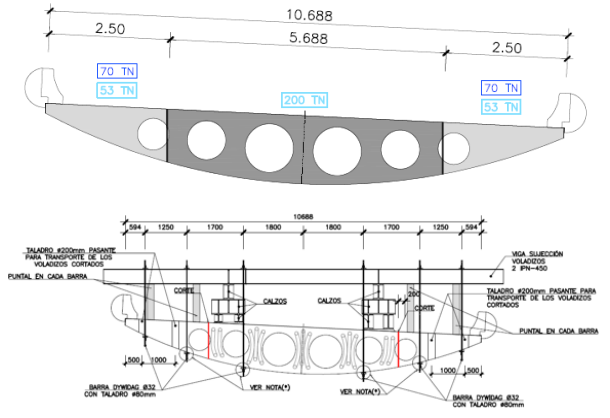

Figure 25. Deck cross section divided into three parts at spans 16 and 17 over railway lines.

Figure 26. Auxiliary steel structure to tie deck cross section over railway lines.

2.3. *Span over M-40 main road*

The phase of disassembly of the span over the M-40 ring road, between piers P4 and P5, was particularly difficult and hazardous due to the span length, the longest one (56.227 m), and the presence of traffic at least in one carriageway of M-40 ring road. For this spans the towers could only be placed in the road berms and in the central reserve of M-40 and, therefore, it was necessary to find out an unique way of supporting the deck sections to be cut.

This alternative method had to ensure the safety during all operations with the traffic under the deck during certain phases. It was decided to place steel trusses over the deck spanning each carriageway of the M-40 ring road (Figure 27). These trusses were supported on the deck over the existing substructure and on temporary towers placed on the berms and on the central reserve (Figure 28). The procedure consisted of dividing the span into shorter deck segments to be hanged from the trusses before been cut and allowing the removal of the different segments.

In fact, this span was divided into 14 sections (Figure 27). The central one, 5.3 m long and 1187 kN heavy, was directly supported on two steel towers placed at the central reserve of the M-40. The rest of the deck segments had different lengths ranging from 2 to 3.5 m and weights up to 961 kN. Each one of these segments were hanged from the steel trusses before cutting them, by means of four 32 mm or 36 mm diameter prestressing bars stressed to forces ranging from 147 to 245 kN; diameter chosen according to the weight of the segment. The cuts were conducted, in the same way as the rest of them, by means of diamond wire including the concrete barrier.

Once all the segments were cut and fully hanged from the trusses, they were taken by the cranes to be lowered in the vertical of their position. In this position each segment was left on a truck cage to be transported to the demolition area (Figure 30). The whole operation was conducted during the night, cutting only the traffic on one of the carriageways of the M-40 each time. In this way, to dismantle the complete span two nights were required. All the operations were finished with success, without any incident, as they had been planned.

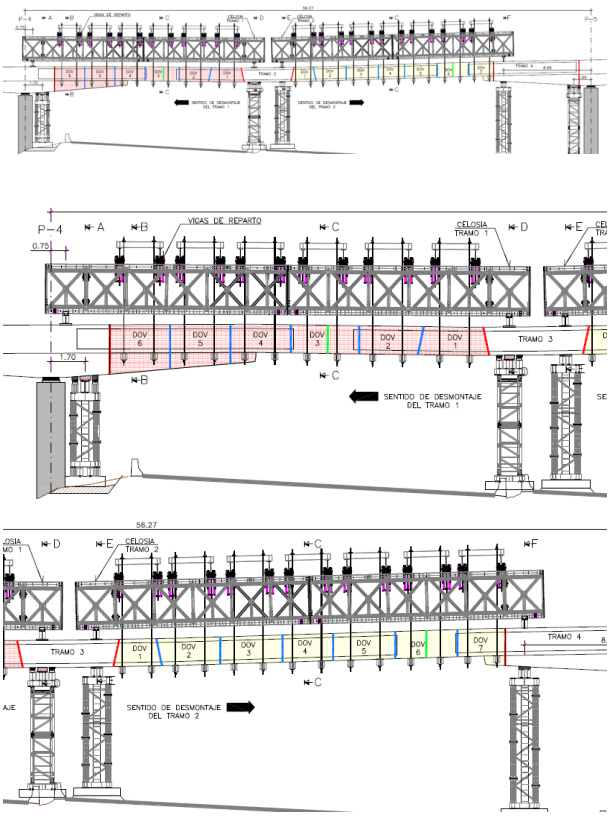

Figure 27. Deck sections distribution and cuts at span 5 over M-40.

Figure 28. Truss girders for auxiliary structure to dismantle main span over M-40.

The process of disassembly of this span may be summarized in the following phases:

- Installation of temporary towers.
- Loading of the towers by means of jacks supporting the deck.
- Drilling of deck holes for hanging bars.
- Installation of truss girders and rest of steel structure.
- Installation of bars and supporting beams under the deck and stressing of the bars.
- Cutting of segments in one half span.
- Removal of cut segments, lowering them on trucks by means of a crane.
- Cutting and removal of segments in the other half span.
- Disassembly of truss girder structure.

2.4. Auxiliary means

To conduct the disassembly of segments in the typical spans, a 5886 kN crawler crane was used (Figure 29), whose position was carefully studied to minimize the translation operations according to the working distances. A working performance of one segment per day was achieved in general in the disassembly process, including cutting and removing of segments.

Figure 29. High-capacity crawler crane during disassembly operations.

As explained above, specific auxiliary construction equipment was designed and used to disassembly the main span over M-40 ring road between piers P4 and P5. This auxiliary structure consisted of four groups of truss girders placed on the deck.

Figure 30. Disassembly of the span over M-40 carriageways.

Figure 31. Detail view of truss girders for auxiliary structure.

Each of these groups, 24 m long and 1344 kN in weight, was composed by four truss girders 2.45 m high properly assembled covering each half span over M-40 (Figure 31). The truss girders were supported at their ends on transverse bottom beams at 22 m longitudinal distance, supported, in their turn, on the existing deck over piers P4 and P5 and over the central reserve where steel temporary towers were provided.

The structure of each group of girders was completed by pairs of transverse top IPE-550 beams 3 m spaced where additional secondary longitudinal beams were supported to anchor the vertical prestressing bars which the deck was hanged from.

3. THE NEW DECK

3.1. *General description*

The main constraint for the new viaduct deck was to keep the same alignment and span lengths as the old one, since the original piers and foundations are also kept with only some rehabilitation works. Therefore, to comply with all these conditions the viaduct has been designed, by Pondio Ingenieros, as a continuous deck with 17 spans, a total length of 560.4 m and variable span lengths, with a maximum value of 56.227 m, over the M-40 ring road [6][7]. The accurate span length distribution is: 20.484 + 32.627 + 35.196 + 38.243 + 56.227 + 32.727 + 36.674 + 38.669 + 29.466 + 28.869 + 36.507 + 29.437 + 29.431 + 32.914 + 32.924 + 30.045 + 19.972 m.

Figure 32. Precast beam before installation.

The deck section consists of a U precast post-tensioned beam curved in plan and a top concrete slab cast in place over thin precast slabs. The total deck is composed by 22 U beams fully connected along the deck by means of prestressing bars and tendons in such a way to achieve a continuous deck along all the length of the viaduct. The deck is 10.7 m wide to carry two 4.65 m wide lanes, hard shoulders included, and steel protection barriers placed on 0.7 m wide concrete kerbs.

All the precast concrete U beams were fabricated at Grupo Puentes factories of Prethor in Lugo (Spain) (Figure 32). The depth of the precast beams is, in general, constant of 1.70 m for most of the spans but it is in-creased linearly up to 2.55 m at the piers located close to the longest spans (piers P4, P5, P7, P10 and P11) (Figure 33). The length and weight of the beams is variable depending on their position along the deck and their depth. It is interesting to outline the following data:

- Longest U beam: Beam V-6 at midspan over M-40 (span length = 56.227 m) between piers P4 and P5. 36.187 m long and 1874 kN in weight with constant depth.
- Heaviest U beam: Beam V-3 at span between piers P2 and P3. 35.156 m long and 1923 kN in weight with constant depth.
- Shorter and lighter U beam: Beam V-11 at midspan over M-607 (span length = 36.507 m) be-tween piers P10 and P11. 16.467 m long and 961 kN in weight with constant depth.
- Variable depth U beams: at piers P4, P5, P7, P10 and P11. 12 m long and 1668 kN weight each one.

The properties of the materials used for this new deck are as follows:

- Precast beams concrete grade: C60/75-XC4.
- In place slab over piers P4, P5, P7, P10 and P11 concrete grade: C45/55-XC4/XF4.
- In place slab general: C35/45-XC4/XF4.
- Reinforcement steel: B-500B
- Prestressing steel: Y-1860C.

In general, the continuity of the beams over piers was achieved by means of prestressing bars joining the end diaphragm of both beams. For the connections between variable depth beams and constant depth ones also prestressing tendons were provided through the joints. All the joints between beams with 4 cm gaps were grouted before prestressing.

3.2. *Construction process*

Due to the specificity of this kind of modular bridge and the necessity of minimizing the traffic cutting on the roads crossing under the viaduct, the erection process for the beams has been very carefully studied and executed, with full control of all the movements which has allowed to place the beams at their positions with very reduced tolerances to provide continuity to the deck.

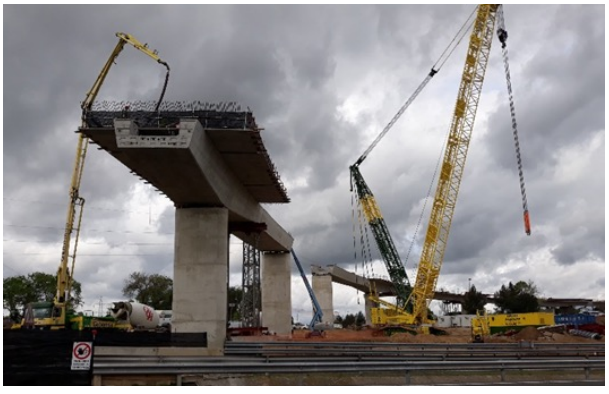

Figure 33. Construction of new deck over M-607 carriageways.

During this erection process auxiliary structures together with temporary bearings have been used to support some of the beams previously to the connections between them. Other beams have been temporary supported on the adjacent ones without temporary cantilever steel supporting structures. All the beams were placed in their definitive position by means of the same 5886 kN crawler crane used for the disassembly of deck segments (Figure 34).

Figure 34. Crawler crane during beams placement.

The erection process of this deck can be summarized in the following phases:

- ***Phase 1:*** (Figure 35)
- Placement of beams between abutment E1 and pier P2 and between piers P3 and P4, using one temporary tower at span P3-P4 to support the joint between variable depth and constant depth beams, connecting them by means of prestressing bars and tendons.
- Placement of beam between piers P2 and P3 and connections to the adjacent ones.
- Reinforcing and cast of the top slab 6.75 m wide central section over pier P4, 18.5 m long, by means of thin precast slabs supported on the beams (Figure 36).

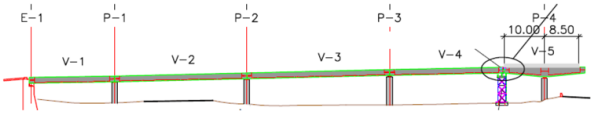

Figure 35. Construction of new deck: phase 1

Figure 36. Construction of top slab by means of thin precast slabs over precast U beam.

- ***Phase 2:*** (Figure 37)
- Placement of beams between piers P5 and P7 and between piers P9 and P10, using temporary towers at the three spans to support the joint be-tween variable depth and constant depth beams (Figure 11), connecting them by means of prestressing bars and tendons. Counterweights were used in some cases to balance the variable depth beams.
- Reinforcing and cast of the top slab 6.75 m wide central section over piers P5, P7, and P10, 18,5 m long, by means of thin precast slabs supported on the beams (Figure 38).

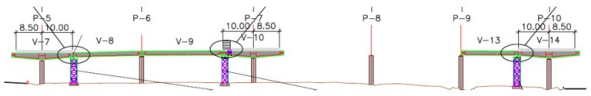

Figure 37. Construction of new deck: phase 2.

Figure 38. Top slab during reinforcing installation.

- ***Phase 3:*** (Figure 40)
- Placement of the beam between piers P4 and P5, over M-40 carriageways (Figure 39), supporting it on the cantilevers from the adjacent beams by means of temporary steel pieces, connection of them by means of prestressing bars and tendons.

Figure 39. Erection of precast beam over M-40 main carriageways.

- Placement of beams between piers P7 and P9 and connections to the adjacent ones by prestressing bars.

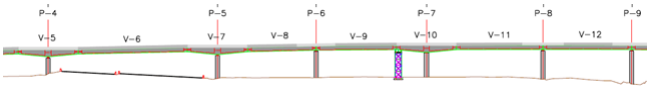

Figure 40. Construction of new deck: phase 3.

- Cast of the rest of the transverse section of the slab over piers P4, P5 and P7.
- Reinforcing and cast of the top slab 6.75 m wide central section over piers P1, P2, P3, P6, P8 and P9, ranging from 13 to 15 m long, by means of thin precast slabs sup-ported on the beams.

- Reinforcing and cast of the top slab 6.75 m wide central section at the rest of spans provided the slab over the two adjacent piers is already cast.

- ***Phase 4:*** (Figure 41)
- Placement of beams between piers P11 and P12, using one temporary tower to support the joint between variable depth and constant depth beams, connecting them by means of prestressing bars and tendons.
- Reinforcing and cast of the top slab 6.75 m wide central section over pier P11, 18.5 m long, by means of thin precast slabs sup-ported on the beams.
- Placement of the beam between piers P12 and P13 and connection to the pre-ceding beam.

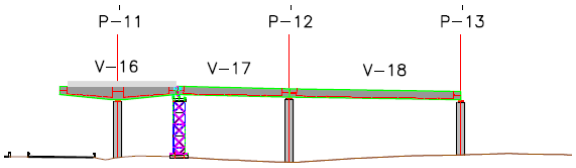

Figure 41. Construction of new deck: phase 4.

- ***Phase 5:*** (Figure 43)
- Placement of the beam between piers P10 and P11, over M-607 carriageways (Figure 42), supporting it on the cantilevers from the adjacent beams by means of temporary steel pieces, connection of them by means of prestressing bars and tendons.

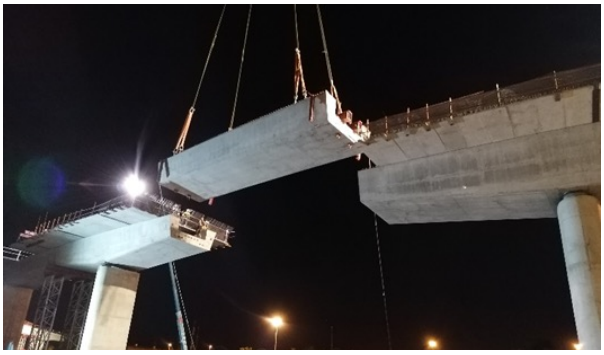

Figure 42. Erection of precast beam over M-607 main carriageways.

- Placement of the beam between piers P13 and P14 and connections to the adjacent ones by prestressing bars.

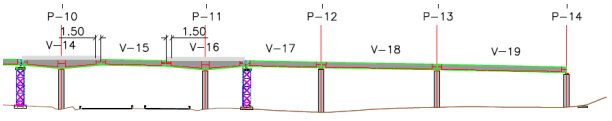

Figure 43. Construction of new deck: phase 5.

- Cast of the rest of the transverse section of the slab over piers P10 and P11.
- Reinforcing and cast of the top slab 6.75 m wide central section between piers P8 and P10.

- ***Phase 6:*** Placement of beams between piers P14 and P16 and connection between them and to the preceding beams (Figure 44).

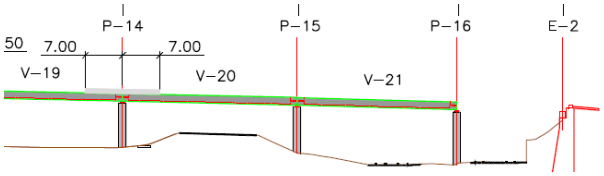

Figure 44. Construction of new deck: phase 6.

- ***Phase 7:*** (Figure 45)
- Placement of the beam between pier P16 and abutment E2, connecting it to the preceding beam by means of prestressing bars. It must be remarked that the beams over the railway lines were placed in position during two consecutive nights, only three hours per night, without railway traffic disruption).

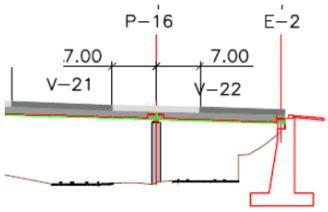

Figure 45. Construction of new deck: phase 7.

- Reinforcing and cast of the top slab 6.75 m wide central section over piers P12, P13, P14, P15 and P16, ranging from 13 to 14 m long, by means of thin precast slabs supported on the beams.
- Reinforcing and cast of the top slab 6.75 m wide central section at the rest of spans provided the slab over the two adjacent piers is already cast.
- Cast of the rest of the top slab transverse section.

Figure 46. Bottom view of the new deck during construction.

The object of this complex construction process is to guarantee that during its execution the forces induced at the beams sections and slabs are always under the values of resistance of those elements, which is governed by the service loads and conditions, together with the stability of all the precast elements during the construction process (Figure 46).

3.3. *Existing facilities*

Concerning the existing facilities in the zone, special attention was paid to the underground water sewage facilities. In the site area three main water pipes were detected with diameters ranging from 1 to 2 m at variable ground depths of 0,65 to 2 m from surface level. No cranes installation was allowed over

the pipe alignments and only truck traffic was permitted to run on this area. Specific analyses were carried out to check the pressures transmitted to the soil, not greater than 55 kN/m², and to guarantee the safety of the existing facilities.

4. OTHER REPARATION ACTIONS

The analysis of the existing substructure, piers and foundations, lead to the conclusion that no deterioration process had taken place in those elements and that they had enough capacity to withstand the loads transferred by the new deck. Because of that and to ensure an increased durability, only reparation of the external surface was found necessary. Nevertheless, to increase the service life of the piers a reinforced concrete cover 15 cm thick was provided along the whole height of the external surface of all the piers (Figure 47). Additionally new bearings and joints were installed since the old ones have arrived the end of their service life. The reparation of the piers and the concrete cover were conducted before installation of beams for the new deck. The definitive bearings were in-stalled during deck construction according to the construction process.

Figure 47. Rehabilitation of piers before deck construction.

5. CONCLUSIONS

Several conclusions may be got from this construction experience, from both, the point of view of conservation and that of construction itself. The process of concrete degradation in bridges takes place in some cases quicker than expected due to the effect of environmental conditions combined with specific material properties. The advance in material behaviour knowledge, the difficulties to recover the lost mate-rial properties and the cost of the options for rehabilitations may drive to the decision of replacement of structure instead of its rehabilitation, which is what happened with the deck of the viaduct object of this paper. In this paper it has been shown that it is possible to carry out such operations keeping in service for the traffic the rest of the link, only with partial traffic diversions and cuttings.

The result is a bridge with a new deck fully consistent with the current standards increasing the service life of the bridge more than a hundred of years (Figure 48). Of course, one of the problems is to keep, as much as possible, the service conditions of the road link, in this case, allowing traffic flow during all the construction process, which has as consequence the optimization of methods to increase productivity and to reduce the total construction period.

Figure 48. View of the bridge after completion.

The expertise in bridge construction and a close coordination between construction itself and concrete precast fabrication are one of the keys to guarantee the quality, efficiency, and success of all the processes up to the completion of the bridge.

Special mention shall be made to the importance of a proper geometric and setting-out control during beams fabrication and during beams assemblage. Since only 4 cm wide gaps were provided between precast beam, any mistake could have had fatal consequences. For this reason, it is necessary a technical office support team to check all the construction da-ta and a full coordination of this team with the in-place construction team. The accurate fabrication process and the installation control by means of cranes should be developed under closed supervision.

The bridge with the new deck was opened to traffic in August 2020 after a record time of nine months of works, including disassembly of the old deck, reparation and reinforcement of the substructure and fabrication and erection of the new deck. The main conclusion to be extracted from this experience is that when bridge structural properties are proved to be poor enough to provide appropriate service conditions, the option of construction of a new deck should be considered feasible even in traffic congested areas as the reference link.

References

[1] Dirección General de Carreteras (2012) Guía de Inspecciones Principales de Obras de Paso – Red de Carreteras del Estado – Serie Normativas – Ministerio de Fomento.

[2] ISO 13822 (2010) Basis of design of structures – Assessment of existing structures, International Organization for Standardization, ISO, Geneve.

[3] CEN/TS 17440 (2020) Technical Specification – Assessment and retrofitting of existing structures, European Committee for Standardization, CEN.

[4] Dirección General de Carreteras, Pliego de Prescripciones Técnicas Generales para Obras de Carreteras y Puentes (PG-3), Ministerio de Fomento.

[5] Comisión Permanente del Hormigón (2008) Instrucción de Hormigón Estructural EHE-2008, Ministerio de Fomento.

[6] Dirección General de Carreteras (2011) Instrucción de Acciones en Puentes de Carretera IAP-11, Ministerio de Fomento.

[7] UNE-EN-1992-2: 2013. Eurocódigo 2: Proyecto de estructuras de hormigón. Parte 2: Puentes. Cálculo y disposiciones constructivas. AENOR.

Disponible en **www.hormigonyacero.com**
https://doi.org/10.33586/hya.2025.4125

Critical Discussion on the Performance of Underslung Movable Scaffolding Systems Strengthened With an Active Prestressing System

Discusión crítica sobre el desempeño de cimbras autolanzables inferiores reforzadas con un sistema de pretensado activo

Marck Anthony Mora Quispe [a,*] y Leonardo Todisco[a]

[a] *Department of Continuum Mechanics and Structures, ETS de Ingenieros de Caminos, Canales y Puertos, Universidad Politécnica de Madrid*

Recibido el 15 de abril de 2025; revisado el 22 de mayo de 2025, aceptado el 11 de julio de 2025

ABSTRACT

Movable Scaffolding Systems (MSSs) are widely used for the in-situ construction of prestressed concrete bridge decks, particularly in span-by-span methods. Underslung MSSs are typically applied to spans up to 60 meters; however, recent developments incorporating active prestressing systems have extended their applicability to longer spans. This paper presents a critical assessment of the performance of underslung MSSs with and without active prestressing, focusing on structural optimization and practical limitations across all construction stages. A case study based on the modular C-60 system is analysed for different span lengths (50 m, 60 m, and 70 m), evaluating both Ultimate and Serviceability Limit States. Finite element modelling and staged loading simulations are employed to assess performance under pouring and launching conditions. Results show that while active systems reduce main girder stresses (yielding up to 19% weight savings in localized modules) their influence is constrained by the construction sequence and inapplicability during launching. Furthermore, the modest overall weight reduction (~10%) may not justify the additional cost and complexity of implementing active control. The study concludes by discussing contexts where such systems may be advantageous and recommends directions for future development, including integrated economic evaluations and systems capable of multi-phase actuation.

KEYWORDS: movable scaffolding systems, external post-tensioning, active prestressing, span-by-span construction, launched structures, steel structures.

RESUMEN

Las cimbras autolanzables (MSS, por sus siglas en inglés) son un método ampliamente utilizado para la construcción in situ de tableros de puentes de hormigón pretensado, especialmente mediante procesos tramo a tramo. En particular, las cimbras de tipo inferior (underslung) son comúnmente utilizadas en vanos de hasta 60 m; sin embargo, la incorporación reciente de sistemas de pretensado exterior activo ha permitido extender su aplicación a vanos de mayores luces. Este artículo presenta una evaluación crítica del desempeño estructural de MSS inferiores, con y sin sistemas de pretensado activo, abordando su optimización estructural y las limitaciones prácticas en todas las etapas constructivas. Se analiza un caso de estudio basado en el sistema modular para vanos de 50 m, 60 m y 70 m. Mediante modelado por elementos finitos y simulaciones de carga por etapas, se determina el comportamiento estructural durante las fases de hormigonado y lanzamiento. Los resultados muestran que, si bien los sistemas activos reducen los esfuerzos en las vigas principales (logrando ahorros de hasta un 19% en módulos localizados) su eficacia está limitada por la secuencia constructiva y su inoperancia durante el lanzamiento. Además, la reducción total de peso (~10%) podría no justificar los costos adicionales asociados. El estudio concluye identificando los contextos en los que estos sistemas resultan más ventajosos, así como los escenarios donde su aplicación podría no ser justificable.

PALABRAS CLAVE: cimbras autolanzables, pretensado exterior, pretensado activo, construcción de vano a vano, estructuras empujadas, estructuras metálicas.

* Persona de contacto / *Corresponding author*:
Correo-e / *e-mail*: marck.mora.quispe@alumnos.upm.es (Marck Anthony Mora Quispe)

Cómo citar este artículo: Mora, M.A., & Todisco, L. (2025). Critical Discussion on the Performance of Underslung Movable Scaffolding Systems Strengthened With an Active Prestressing System. *Hormigón y Acero*. 76(306):17-32. https://doi.org/10.33586/hya.2025.4125

Figure 1. Construction of a bridge with an underslung MSS.

1. INTRODUCTION

Movable Scaffolding Systems (MSSs) are an in-situ full-span-by-span construction method used for concrete bridge decks. This technique was first implemented in 1961 on the Krahnenberg Bridge in Germany, designed by Hans Wittfoht [1]. The construction process involves external formworks supported by the MSS, whose assembly depends on the structural configuration - typically defined by the main supporting girders or a bowstring scheme with a similar concept [2]. After a span is poured and it obtains the minimum allowable resistance, the MSS removes the formwork from the deck, changes its supports, and then it is launched to build the next span. This process occurs repeatedly until the last span is cast. Therefore, it must be observed that MSSs work under different structural situations. For example, the supporting devices when pouring the deck are not usually the same during the launch process. Furthermore, this latter manoeuvre results in different structure arrangements with specific support situations. More detailed information is included in Section 2. According to different authors [2–6], MSSs are often the preferred choice compared to other bridge construction equipment (BCE) for multi-span bridge construction due to the following advantages:

- Regarding bridge design, there is a reduction in post-tensioning steel minimizing material consumption.
- Regarding bridge construction, the geometry control becomes simpler and improves safety during construction, as it requires less manpower and facilities, resulting also in cost-effective production.
- Regarding the emplacement of the bridge, it is suitable for areas with strict architectural requirements and/or difficult topography.

Although these advantages are significant, it is important to account for the costs associated with shipping, assembly, dismantling, technological demands, and potential modifications to the original bridge design.

MSSs are commonly classified based on their relative position to the deck [7]:

- Overhead MSSs: Positioned on the deck. See example in [5].
- Underslung MSSs: Positioned under the deck. See the example in Figure 1.

In particular, underslung MSSs have been widely and successfully employed in spans ranging from 25 to 60 m. However, spans up to 70 m were reached using active external prestressing systems [8,9]. The latter is named active as the load in the prestressing tendons, or unbonded cables, varies in real-time according to a specific objective. In the case of MSSs, this objective is typically set to limit the deflection on the main span during the pouring stage. As a direct consequence, the structural demand for the MSS structure is also reduced, as more detailed in Section 3.

Although active external prestressing devices directly impact on a reduction of the steel of structural elements, this material save can be significantly constrained by other factors, such as the MSS launching procedure or the construction sequence of the bridge deck. In addition, the optimization with active systems usually considers an MSS that is not initially optimized [10]. Therefore, in this paper, the structural optimization through the use of active prestressing systems is presented and analysed, discussing its limitations. To illustrate this, a case study of an existing MSS is examined and optimized using this strategy alongside a conventional design approach.

2. CONVENTIONAL DESIGN OF MSSs

2.1. Stationary stage

As mentioned in Section 1, one of the main MSS conditions is the stationary stage. In this situation, the MSS is positioned to pour the concrete of the deck that is about to be built. In multi-span bridge construction, it is common practice to build on every sequence a full span length according to a

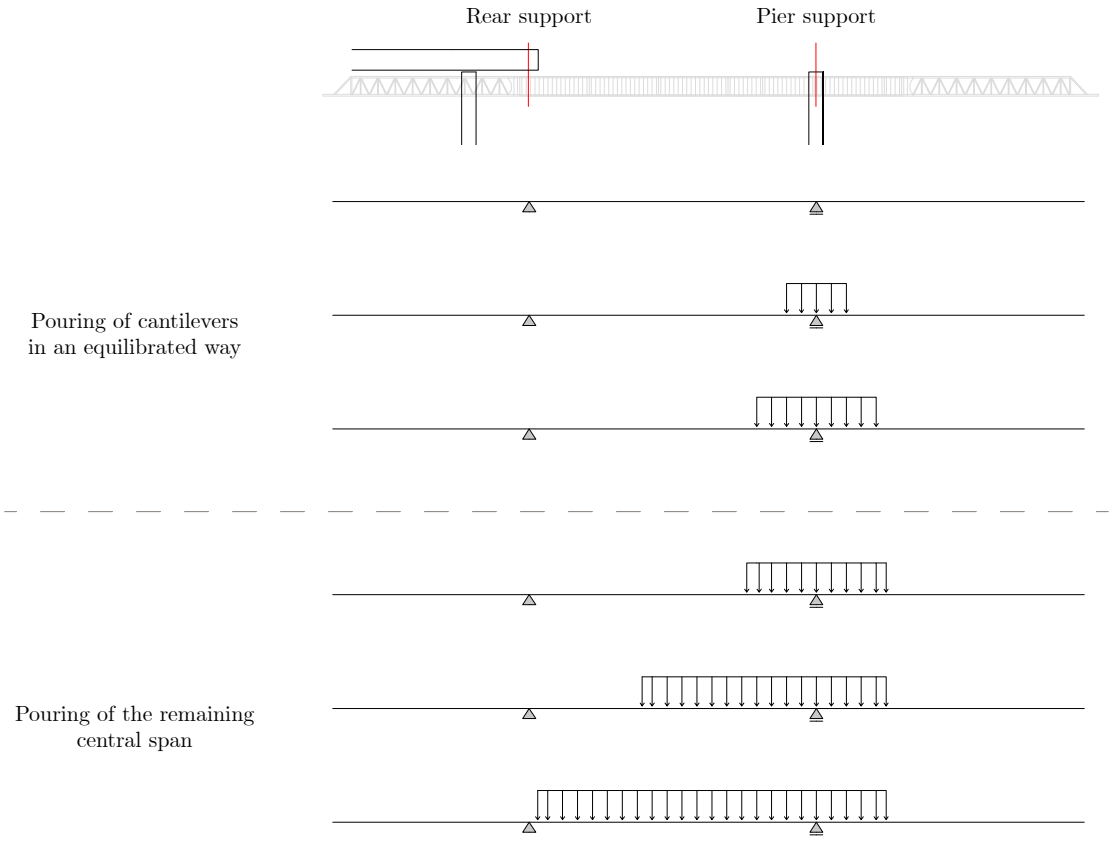

Figure 2. Typical pouring sequence in bridge deck construction with MSSs.

part of the zone between the piers and a cantilever [11,12]. Therefore, if L is the span length and *Lcant* is the cantilever length, it is built the remaining length (*L-Lcant*) between piers and *Lcant* after the last pier location obtaining the whole span length. The cantilever length usually ranges from $L/5$ to $L/4$ as this is the approximate location of zero or minimum bending moments due to self-weight.

Ideally, the MSS would be in the stationary stage for only the concrete pouring. However, it remains here in all the situations before and after pouring that do not include the launch phase (see Section 2.2). The latter requires meeting specific requirements related mostly to weather conditions to proceed safely. Consequently, during the stationary phase, the MSS may also be subjected to different challenging conditions such as out-of-service wind scenarios, and unexpected snowfall, among others. The pouring stage is detailed in Section 2.1.1, while Section 2.1.2 briefly addresses the additional scenarios.

2.1.1. Pouring stage

The underslung MSSs are usually supported by a rear support on the deck and a pier support. Therefore, the structure is simply supported with two remaining cantilevers at the extremes, (refer to the top row of Figure 2). To properly quantify the structural demand that comes from the weight of the deck, it is important to consider its construction sequence.

Two principal procedures are employed for deck pouring. The most widely adopted sequence, illustrated in Figure 2, begins with a compensated cantilever pour, followed by casting the remaining centre span. In the alternative sequence, the cantilever is also poured first; however, the main span is then cast progressing from the pier toward the rear support location [13].

As it can be seen, the load is first incremented on the cantilevers, and then on the main span. This construction process produces that, first, the bending moments in the cantilevers are increased without modifying the bending moments in the main span, to finally increase them on the central span. An example of this behaviour is illustrated in Figure 3, where the dashed lines represent the bending moments without the influence of fresh concrete (initial condition), and the two situations addressed previously in Figure 2: the balanced pouring of cantilevers (orange line) and the fully cast deck (green line). Additionally, the envelope is shown in grey.

This specific construction process allows better control when pouring the diaphragm at the pier, which is why it marks the beginning of the building sequence in all common scenarios. Additionally, the construction sequence plays a crucial role in evaluating the efficiency of active systems, a topic that will be further discussed in Section 4.2.

2.1.2. Other load situations

Other stages in which the MSS also remains in the same stationary configuration can be the following:

- Out-of-service wind: Both the pouring stage and the launching stage are limited to specific weather conditions to ensure safety in each of these processes. Among them, the most important is the wind speed. Therefore, it is

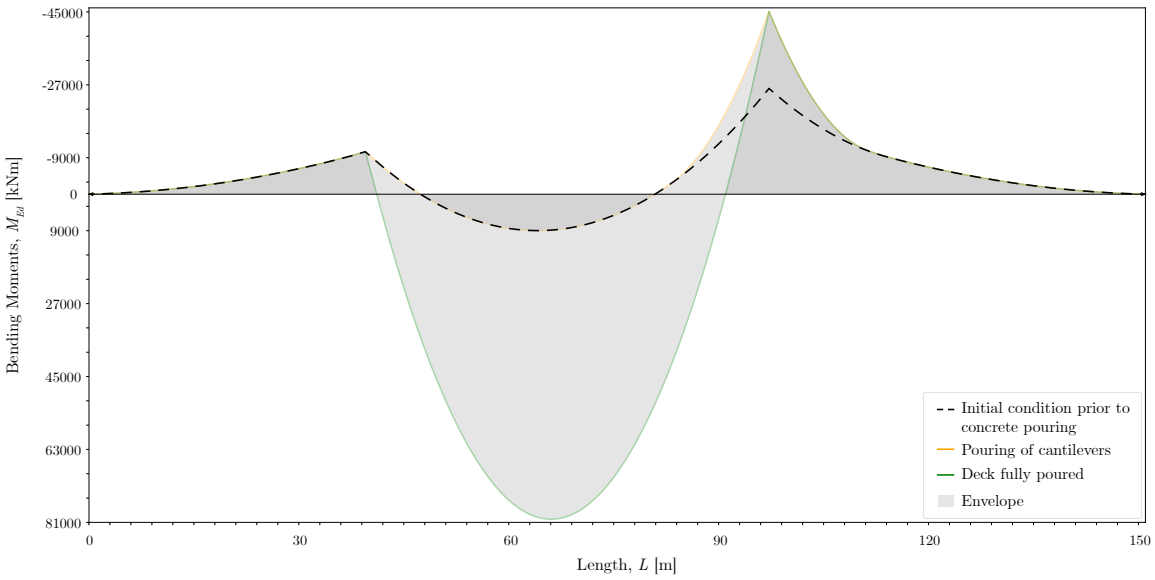

Figure 3. Bending moments during the pouring sequence.

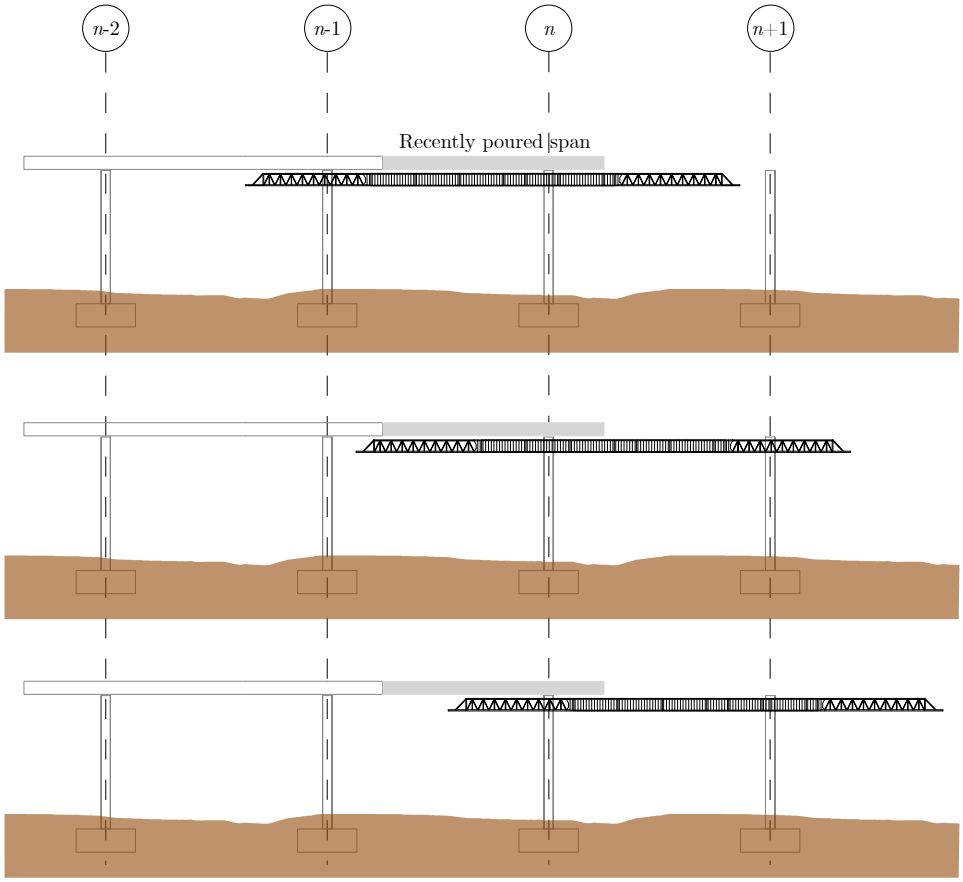

Figure 4. Typical launching sequence of an MSS.

common practice to have an anemometer on site and to continuously review the forecast to plan each of these procedures. The out-of-service wind scenario refers to conditions in which the support configuration remains identical to that of the pouring stage. In this situation, the structure receives primarily the permanent load and the full wind action corresponding to higher wind speeds.

- Earthquake loads: Since they are difficult to predict, seismic actions are usually considered in all situations of the MSS, but with a low return period of occurrence [2]. Nonetheless, when knowing the high probability of occurrence of them is known, there are specific manoeuvres which most of them consist of fixing the MSS on the deck [11].
- Other loads: The MSS might also be exposed to scenarios

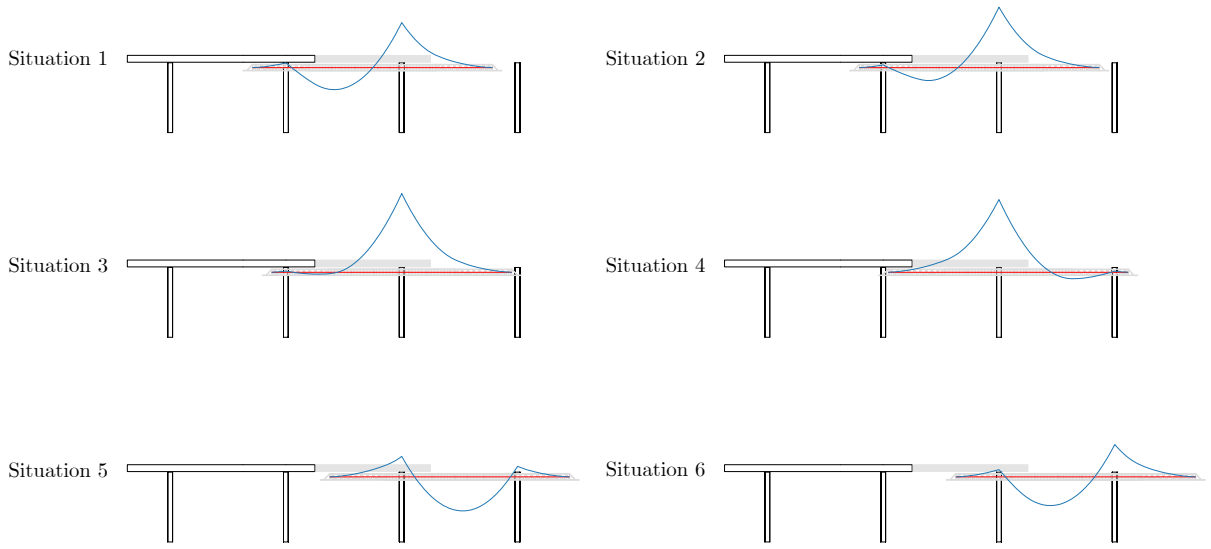

Figure 5. Bending moments during the launching phase.

such as snow occurrence and accidental loads. However, any of these situations can occur in both the stationary and launching stages [2,11,12,14].

2.2. Launching stage

This stage includes all configurations of the MSS from the end of one stationary phase to the beginning of the next. Provided that all necessary conditions for launching are satisfied, the following sequence occurs (see Figure 4).

First, once the recently poured span has obtained the minimum required strength, the formwork is removed from the deck. Subsequently, the rear support, located between axes *n*-1 and *n*, is detached from the structure. Concurrently, a pier support is prepared at axis n-1 to receive the MSS. Another pier support is also installed at the upcoming pier on axis *n*+1, anticipating the forward movement of the MSS. The launching process then begins with the MSS initially supported at axes *n*-1 and *n*. As it advances, it transitions through an intermediate configuration where it is temporarily supported on three axes (n-1, n, and *n*+1) before finally being fully supported between axes *n* and *n*+1. Throughout this process, the MSS undergoes several structural configurations. Once it reaches the designated position for the next span, the pier support at axis *n* is reconfigured into the new rear support, marking the beginning of the subsequent stationary phase.

For example, Figure 5 presents the main representative situations that occur during the launching stage, also illustrating qualitatively the permanent loads' bending moments (in blue) for each specific case:

- Situations 1 and 6: Initial and last situation of the launching process (identical, but with a different MSS location).
- Situation 2: Example of first stages with increasing front leading cantilever.
- Situation 3: Maximum front cantilever.
- Situation 4: Maximum back cantilever.
- Situation 5: Maximum positive bending moment during launch.

As seen, the launching process involves several situations that the MSS goes through, in which the span length of the bridge works as both maximum cantilevers and the main span of the MSS. Therefore, each situation should be considered in the design of such elements. Herein, it is common practice to plot the envelopes of the whole launch for all the structural configurations to analyse specific scenarios. An example of this envelope is shown in Section 4.2.

3. ACTIVE PRESTRESSING SYSTEMS

3.1. Concept and applications

Active structures are systems where part of them can adapt their configuration in response to specific performance criteria. To achieve this, it is necessary to install sensors, actuators, and a control system [15]. The usual functioning of this scheme is as follows. First, given an external stimulation, the sensors perceive the response of the structure. Subsequently, the control scheme receives the information from the sensors and processes it to then send an instruction to the actuators. Finally, the motion is defined to meet the control objective. Here, there are many particularities, since active systems can be used for different purposes and with different types of control units. For instance, it is common practice to use active control for Vibration Serviceability Limit States (VSLS) using Tuned Mass Dampers (TMDs) [16]. Therefore, a convenient way to divide them would be to control static responses such as deflection or to fulfil vibration serviceability responses, v.g., accelerations. The first type is the focus of this study.

A simple application is presented in Figure 6 to consistently understand the advantages of active systems. This example presents an active system that is set to limit the deflection to zero at midspan in a simply supported beam with one strut in the centre of the span and external prestressing tendons. When an

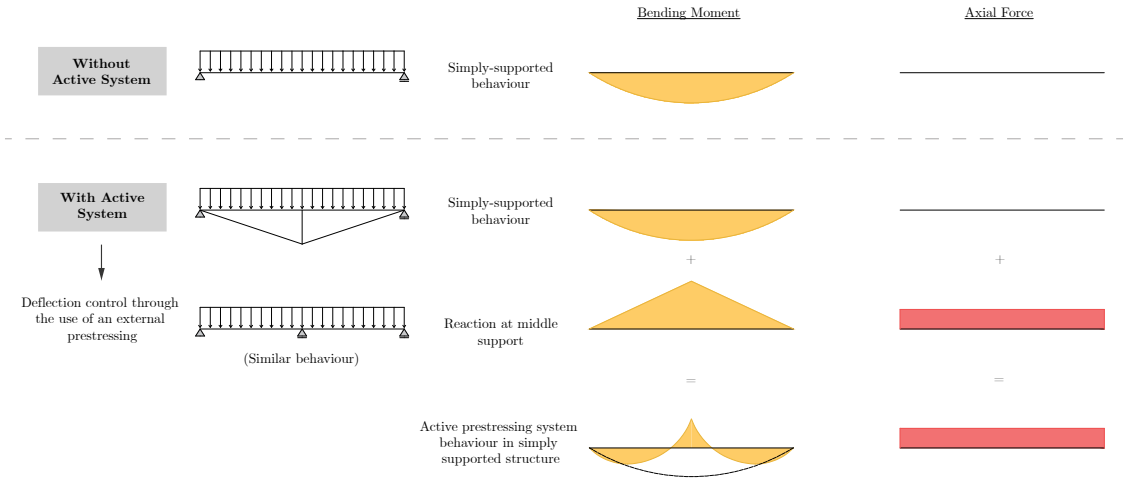

Figure 6. Concept of a responsive prestressing system for deflection control.

external load acts on the beam, the midspan point behaves as another support, since the vertical displacements are 'restricted', making a new system of a beam supported in three points. However, this can also be observed as follows. Since the instruction is to limit the deflection to zero, to accomplish this, the prestressing load increases, and this force is then transmitted to the strut as a compression. This element transmits this force to the beam, resulting in an uplift force and thus a negative bending moment. At the same time, the cables introduce an axial force at the edges. Therefore, the result is the sum of both bending moments, the simply supported one and the negative coming from the vertical force, and the axial force on the beam.

It can be observed for this example that there is a considerable improvement in the positive bending moments plus new, but small, negative ones. Herein, the axial load must not be disregarded, as it could play a restricting role depending on the type of cross-section and the material that is being assessed. For instance, the use of thin-walled steel cross sections could be prone to plate buckling sooner under pure compression stresses than under exclusively bending compression stresses. Further information and examples of active systems can be consulted in [16–18].

In the case of underslung MSSs, the active system is typically incorporated to control the deflection of the main span by using external prestressing tendons or unbounded cables. Herein, the prestressing load is changed by an actuator. As far as the authors know, there is only one full-scale realization for underslung MSSs in [8,9]. Nonetheless, there are other studies on the feasibility of using them in MSSs [10,19]. In Section 3.2, the implementation of active prestressing systems in MSSs is explained further.

3.2. Application on MSSs

3.2.1. Stationary stage

As mentioned in Section 3.1, active prestressing systems in MSSs consist of varying the load on external tendons or cables to control the deflection on the main span. During the stationary stage, it is during the pouring stage that the active system can be more efficient, as it can control the deflection when the fresh concrete is placed over the formwork. Given that in the stationary stage, there is no space over the MSS, the external system only can be either inside the cross section or below the structure. From both, the most efficient is to use an external prestressing under the main girders, resulting in an under-deck cable-stayed structural typology [20,21].

For the whole scheme, there are two possible solutions in terms of actuator location (see Figure 7). Option A varies the load in the prestressing by modifying the length of the strut which is also the actuator. Consequently, the deformation and load on the cable change proportionally to the actuators' opening. When having more than one strut, the actuator could be in one or more of them. Option B modifies the load on the cables by directly jacking the tendons. For that reason, the actuator needs to be in one of the anchorages.

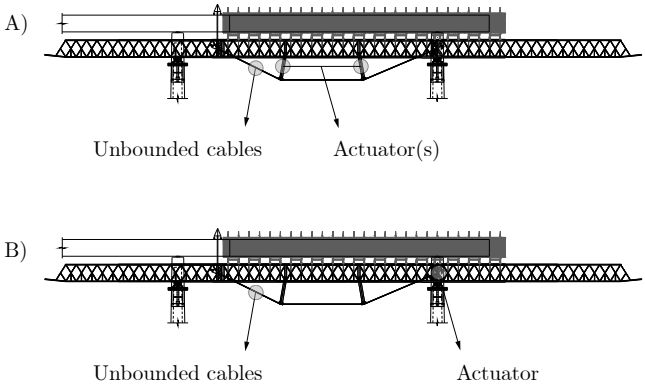

Figure 7. Actuator locations in MSSs with active systems.

There are many possibilities in terms of structural configuration. For instance, in Figure 8, some possible solutions are presented which correspond to the following:

- Option I: One strut with anchorages in the supports.
- Option II: One strut with anchorages in the rear support and at the end of the cantilever.
- Option III: Two struts with anchorages in the rear support and at the end of the cantilever.

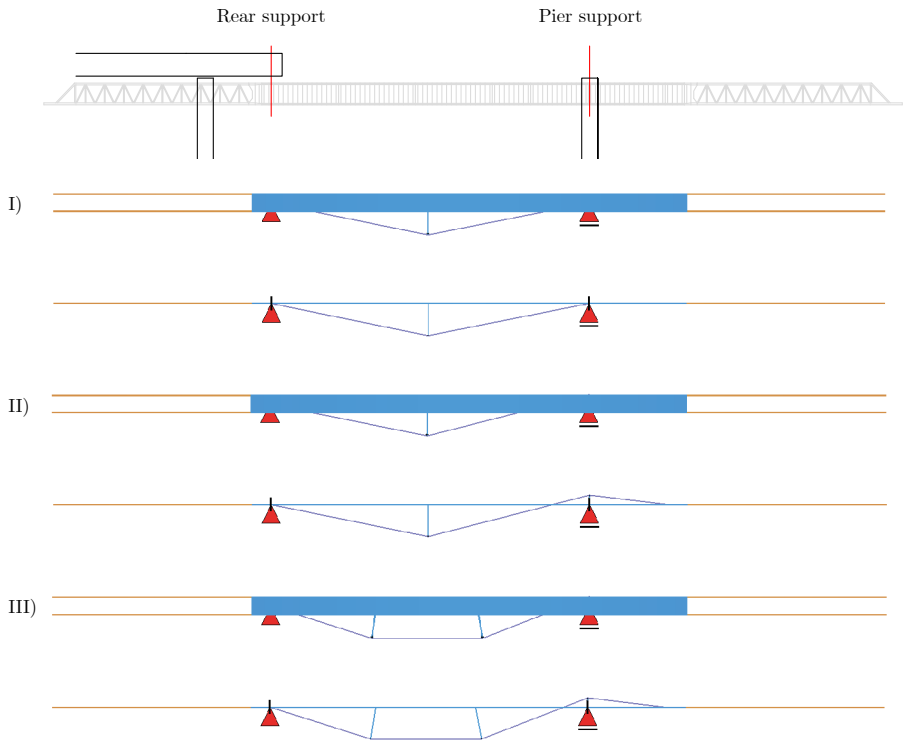

Figure 8. MSSs design solutions with external prestressing.

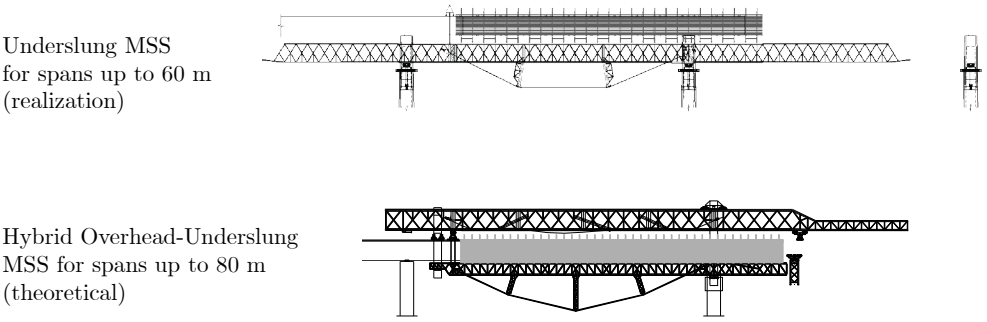

Figure 9. MSS configurations with active systems [19].

The difference between these alternative systems is that option I introduces an exclusively negative bending moment law, while options II and III also introduce a positive bending moment law on the cantilever. Also, the last two differ on the number of struts on the main span, in which option III accommodates better the bending moment introduced by the concrete pouring and requires a lower load on the cables to achieve the control objective.

It was previously pointed out that due to the lack of space, it is not usually possible to add new elements over the main girders of the underslung MSS. Therefore, the efficiency of the prestressing system on the cantilever zone is here conditioned by the space inside the cross-section, which is the height of the element.

Some examples of MSSs with active systems are presented in Figure 9 extracted from [19]. As seen, some of these solutions resemble the conceptual design presented previously.

As the main drawback of this technology, in other situations that differ from the pouring stage in the stationary position, the active system does not improve considerably the behaviour of the MSS since the prestressing system primarily affects the vertical response, and the rest of the situations are mostly affected by transversal actions, e.g., the out-of-service wind. Therefore, their effect in these situations is negligible.

3.2.2. Launching stage

For underslung MSSs, the typical launch procedure is the one presented in Section 2.2. As observed, it is necessary to have free space below the main girders, as they are from which the whole structure is launched. The active system for these situations must be either retired or retracted so it does not represent an obstacle when launching. Therefore, during this stage, the active prestressing system does not work, making the MSS work as a conventional MSS plus the load of the struts and cables, which might or may not be neglectable.

3.2.3. *Active prestressing and permanent loads*

In the design of stay-cable systems, e.g. cable-stayed and extradosed bridges, there are no specific criteria on how to apply favourable or unfavourable coefficients, but it is mentioned to decide according to the situation of each structure [22]. In this sub-section, this matter is discussed focusing on the European context, and using the concepts of 'active load' and 'passive load' on cables as the following [23]:

- Passive load (*Ppas*): The load increment on the cables due to their deformation caused by an external load on the deck. For instance, in a cable-stayed bridge with a composite concrete-steel cross section, during the placement of concrete of the top slab, the cables deform and, at the same time, the load on the cables rises.
- Active load (*Pact*): The one coming from jacking one of the anchorages, in any construction phase, to compensate part of the permanent load of the bridge. This is usually done during construction or after the installation of dead load. For example, in the case of a ballasted deck for railway traffic, this would be after the installation of the ballast and rails. In the context of MSSs -as further discussed at the end of this subsection- this load category most accurately represents the increase in active cable force in response to the pouring of fresh concrete.

In the European guidelines, prestressing loads and tension elements are treated differently. Eurocodes 2 and 3 [24–26] in the case of stay-cable systems recommend using EN-1993-1-11 [27] which indicates to use favourable and unfavourable coefficients for both permanent loads (G) and load on tension elements (P, being the total load, i.e., $P = Pact + Ppas$). Notably, this approach does not differentiate between active and passive components. This treatment is primarily based on the behaviour of cable-stayed bridges with highly flexible decks, where deformations directly influence cable forces. However, this assumption does not consistently hold for extradosed bridges or other stay-cable configurations, where the relationship between deck deformation and cable force can be significantly different [28,29]. On the other hand, for prestressing loads, Eurocode 2 [24] considers the action P to be fully independent of permanent loads using specific safety factors.

Virlogeux [30], Menn [31], Ruiz Terán [23], Mermigas [29], and Carrillo [32] agree on a different treatment of forces distinguishing them in an active and passive part. Specifically, they recommend treating the passive part together with the permanent loads as a group, and the active part differently with other safety factors. Then, Ploch [28] supported this procedure by studying the definition of security in external prestressing inside and outside the cross-section and demonstrated that the treatment of permanent actions and prestress together as a group does not lead to safe designs. Therefore, the latter also proposes the independent use of this force, indicating specific safety factors for each case.

For active systems applied to MSSs, the load increases proportionally with the fresh concrete load on the main span, closely resembling a purely active prestressing load (*Pact*). Therefore, it is recommended to use specific partial safety factors for this load. On the safe side, it is suggested to use the characteristics value of them and set some disequilibrium between the active load and the part of the permanent load that it compensates. For instance, Pacheco [33] considers the active system independent of permanent loads and applies the same safety factors as in the case of prestressed structures [26].

4. DESIGN OF A LARGE-SPAN MSS WITH AND WITHOUT AN ACTIVE PRESTRESSING SYSTEM

4.1. *Definition of case study*

To accurately evaluate the effectiveness of active systems, the same MSS is optimized in two configurations: with and without an active prestressing system. In both cases, the structural steel weight of the main girders is reduced by using lighter sections per module. The selected case study and its characteristics are described in the following sub-sections as well as the design basis and modeling.

4.1.1. *Geometry*

The C-60 model from Mecanotubo, previously employed in the literature [10], is selected as the reference MSS. The system is composed of different modules of different lengths, ranging from 3 to 12 m, and different cross sections, divided mainly into truss modules and box modules. The first ones are 3D-spatial trusses, and the second ones are steel plate box cross-section girders (see bottom of Figure 10). optimize the load-bearing capacity of the deck prior to self-resistance, box modules are employed in the central region. Then, at the extremes, lightweight truss configurations are employed to minimize weight. These truss ends function as launching noses during span transitions and as cantilevers during the stationary phase.

The C-60 system was initially conceived to build spans of up to 60 m. Its modular nature allows flexible assembly configurations to accommodate different span lengths. Consequently, it is also possible to use this structure with the rear support located at both $L/4$ and $L/5$. Cantilever lengths between these values are also possible. These two main assemblies are shown in Figure 10 for span lengths of 60 m.

In these configurations, the box cross sections are identical except to the ones located at supports during the stationary stage. These modules are distinguished due to the type of connection they have to their corresponding support. Thereby, their name starts with a C and A, respectively, for the cases of the rear support and pier support. In terms of stiffness of the cross-section, the only one stiffer than the rest is the one located in the pier support, which weighs 6% more than the rest of the modules.

For other lengths of pouring span, it is maintained the ratio of the total length of the MSS to the bridge span length, and the length proportions of each typology of modules to the total length of the MSS. Here, it is important to establish an appropriate length for the box modules since they must be at least in the span length to be poured, as they are the most resistant sections compared to the truss ones.

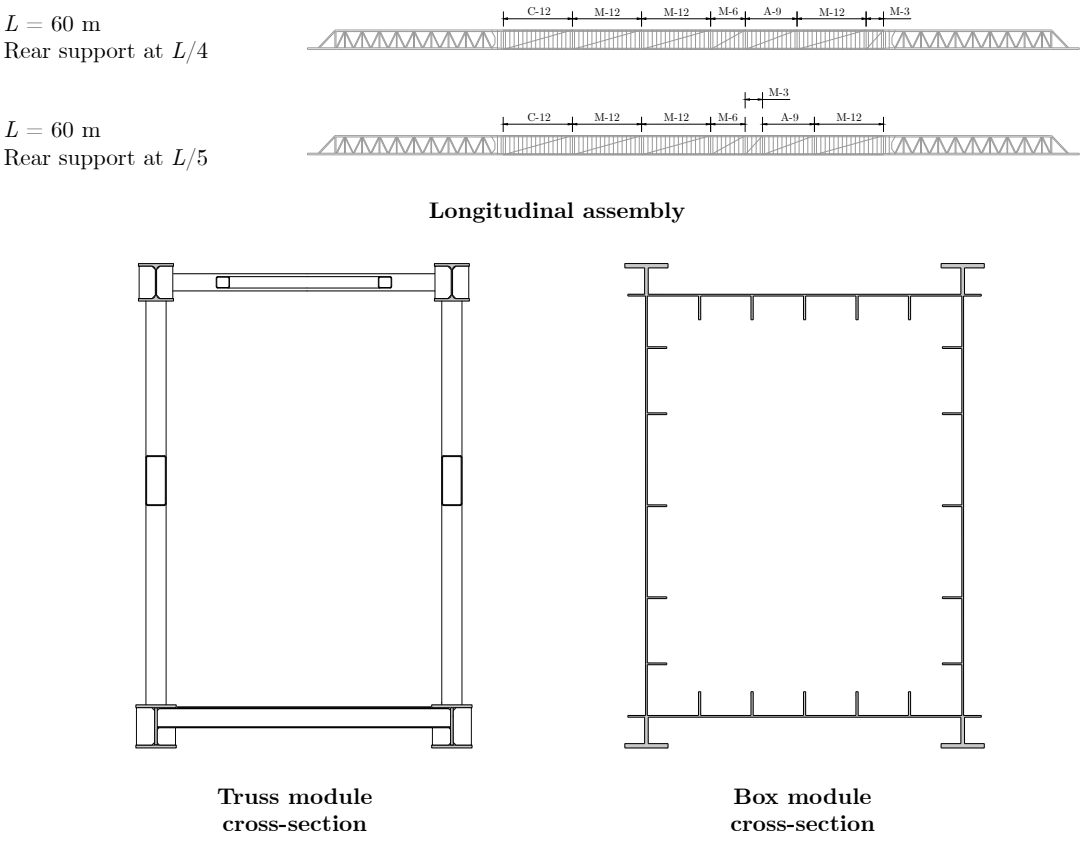

Figure 10. C-60 system by Mecanotubo as reference MSS.

4.1.2. Design basis

The design basis follows the methodology outlined in [2], which agrees with both American and European code provisions for Ultimate Limit States (ULS) and Serviceability Limit States (SLS) in terms of actions and load combinations. Nonetheless, the safety factors are according to Eurocode 0 [22] and Eurocode 3 for steel structures [34,35].

Regarding the treatment of active system loads, these are considered independent from permanent loads and are assigned favourable and unfavourable partial factors of 1.00. Additionally, a load imbalance of ±5% between the prestressing force and the compensated portion of the permanent load is verified, as recommended by the Spanish National Annex to Eurocode 1990 [22] and the Spanish National Guidelines [36,37].

For the calculation of fresh concrete weight, existing full-scale bridges are used as a reference. Specifically, the Asteasu Bridge (Figure 11) and the Molvizar Bridge (Figure 12) are used, respectively, to represent railway and highway bridges. The first one is a viaduct part of the Basque Country railway line located in the Hernialde – Zizurkil Section. Also, this bridge has a maximum span length of 51.86 m resulting in a height-to-span length ratio of 1/19. The second one is part of the Mediterranean Highway, specifically in the Amuñecar (Taramay) – Salobreña (Lobres) Section. Furthermore, this structure has a height-to-span ratio of 1/16. Thus, these bridges represent typical applications of MSSs for the construction of multi-span bridges for different traffic services ranging in deck heights from $L/15$ to $L/20$, with L being the maximum span length between piers.

4.1.3. Optimization goal and modeling

In terms of the loading condition problem for optimization of the MSS, the decks of Figures 11 and 12 are used and adjusted by extending the web to obtain the appropriate height for pouring spans of 50 m, 60 m, and 70 m. Here, it was decided to use $L/15$ and $L/20$ deck heights to span-length ratios for railway and highway bridges, respectively. Therefore, the goal is to obtain efficient modules for each span-length application. By that, it is considered that some modules are optimizable and that some reinforcements in specific points are also needed depending on the optimization strategy.

Verifications on the structure consider global resistance, stability, as well as local checks such as joints and patch loading for launching stages. As mentioned previously in Section 3.2.2, the MSS operates under identical conditions during launching, regardless of the presence of an active prestressing system. Therefore, the optimization results for both MSS configurations must satisfy the same performance criteria during launching manoeuvres.

The FE modelling has been performed in SOFiSTiK [38] using beam elements for the whole MSS. Two different model approaches were adopted for different verifications. For the box-section modules, one single beam element was

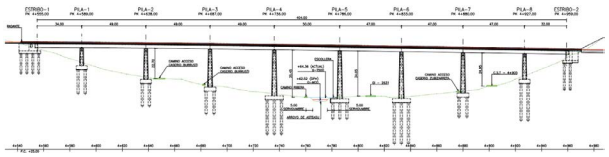

Layout

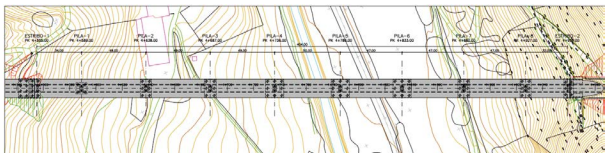

Plan view

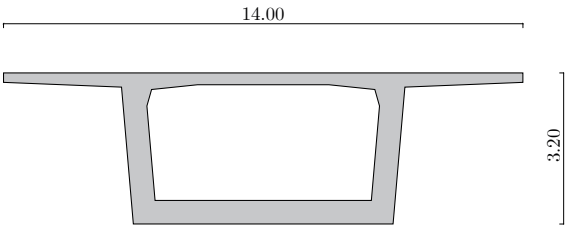

Cross section

Asteasu Viaduct

Figure 11. Deck case study for a railway bridge.

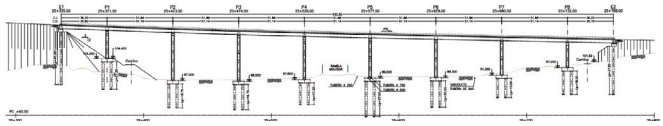

Layout

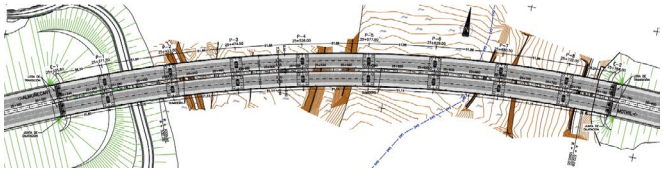

Plan view

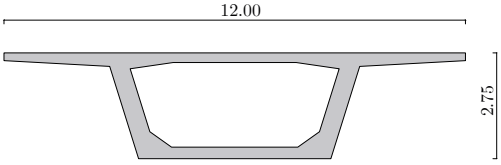

Cross section

Molvizar Viaduct

Figure 12. Deck case study for a highway bridge.

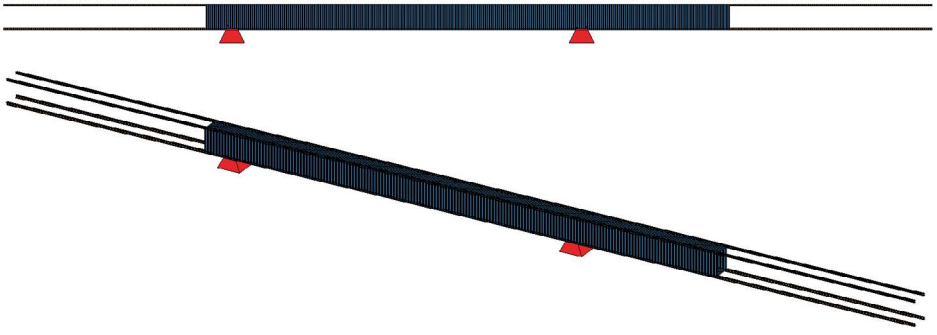

Figure 13. Modeling approach 1: Longitudinal beam elements representing the cross-section of each module.

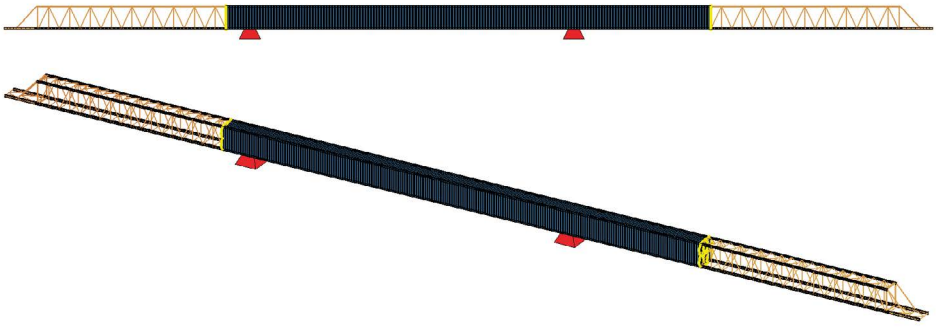

Figure 14. Modeling approach 2: Beam elements for the cross-section of each box module and truss components.

used to represent the cross-section of each module. For the truss-type modules, two approaches were applied: the first employed only longitudinal beam elements with equivalent cross-sectional stiffness to represent the truss behaviour (Figure 13), while the second modelled all the individual truss components (Figure 14). Both models were cross-compared to ensure that the simplified longitudinal-only model accurately captured the overall stiffness of the truss. The simplified one is used for most global analyses, whereas the more detailed one is applied for local analysis. Additionally, in specific launching cases, it was also modelled the behaviour of the launch devices in contact with the bottom chord.

4.2. MSS design optimization with an active prestressing system.

For the design optimization of MSSs with an active prestressing system, the cases previously presented in Figure 8 were studied. For these, the strut height was selected as the tenth of the main span length to not interfere with the vertical clearances that can be present below the bridge. It must be pointed out that the MSS is already of important dimensions below the deck which sometimes can be conditioning. Also, it is particularly used the options with the anchorage on the cantilever zone after the pier support.

The ULS and SLS verifications studied herein are the following.

- ULS: Interaction of normal stresses (bending moments and axial force) considering global buckling and plate buckling reductions, shear resistance and its interaction with normal stresses, patch loading (pure and interaction with concomitant bending moments), and connections.
- SLS: Displacement of the MSS to allow the correct pouring shape of the bridge deck, and connections.

The influence of the number of struts and the effectiveness of the active system during the pouring stage can be seen in Figure 15. Herein, it represents the envelope of the pouring stage of each case, varying the number of struts. Additionally, it is included in grey the envelope area of the case without using active prestressing. From this plot, the following can be observed:

- The effectiveness of having the cable system in the cantilever zone is almost negligible (see the zoom of the plot in the upper right of Figure 15). This is exclusively due to the construction process. In the initial stages when there is a balanced pouring of the cantilever zone (see Figure 2), there is no increase in bending moments in the central zone and, therefore no additional deformation in the main span; consequently, the active system does not work. In this situation, the maximum negative moment is reached without the contribution of the active system. The differences observed in the plot are due to the cables working as a passive element with a minor contribution.
- The grey area highlights the degree of minimization of the positive bending moments when the control system is working. This reduction is at least 85% for this specific case. Nevertheless, it must not be disregarded the axial force contribution which is not evident in this plot. To see the contribution of the axial load and the acting transverse forces, the maximum normal stresses in the box cross sections are presented in Figure 16. This plot includes the launching stage envelope (in yellow) apart from the cases of the active system during the stationary stage of Figure 15.
- Having one or two struts impacts the degree of compensation of the bending moments and their shape since with two struts it is possible to reproduce a better fit of the positive bending moments distribution. Also, when having two struts, a lower force is needed to reduce the deflection on the main span compared to the solution with one. This directly impacts the number of prestressing tendons.

As seen in Figure 16, the axial force component plays an important role that cannot be seen by observing only the bending moments. While there is a significant reduction according to Figure 15, when considering the rest of the concomitant acting forces, it results in a less impactful reduction. Then, the launching stage also introduces specific peaks on this plot that correspond to maximum cantilevers, back and front. The stress level of these zones shows that the launching procedure is more restricting than the pouring case in the central zone, while in the rest of the zones, it is the stationary stage. In the extreme zones where the active system is not as efficient, the stationary stage becomes the restricting situation.

To simultaneously observe the launching and stationary stages in a single plot, Figure 17 illustrates the envelope of this manoeuvre plus the pouring stage of the two studied options of Figures 15 and 16. The plot indicates that the configurations incorporating active systems during the pouring stage generally remain within the loading envelope of the launching stage, with the exception of the pier support zone.

However, when evaluated in terms of stress distribution (see Figure 16), their demand is comparable, with the stationary stage remaining critical in the extreme regions of the structure. Based on the observed behaviour of the active system during fresh concrete pouring, the configuration employing two struts is selected for structural optimization, as it offers the most effective reduction of stress in the main girders.

The optimization procedure for this case follows a systematic approach. First, the case of a pouring span length of 70 m with an adjusted configuration of the MSS for this scenario is studied. Then, after all the conditioning situations are identified, a search for more optimized modules for all these scenarios is performed. If a studied configuration allows for further optimization, the selected modules are reduced and reassessed one more time. This iterative process continues until a fully optimized MSS meeting both ULS and SLS criteria is achieved.

Table 1 presents the assessment of the initial configuration of the C-60 MSS (without any cross-sectional modifications) for a 70 m span using an active prestressing system. When ULS or SLS requirements are not satisfied, the table specifies the maximum required percentage of additional

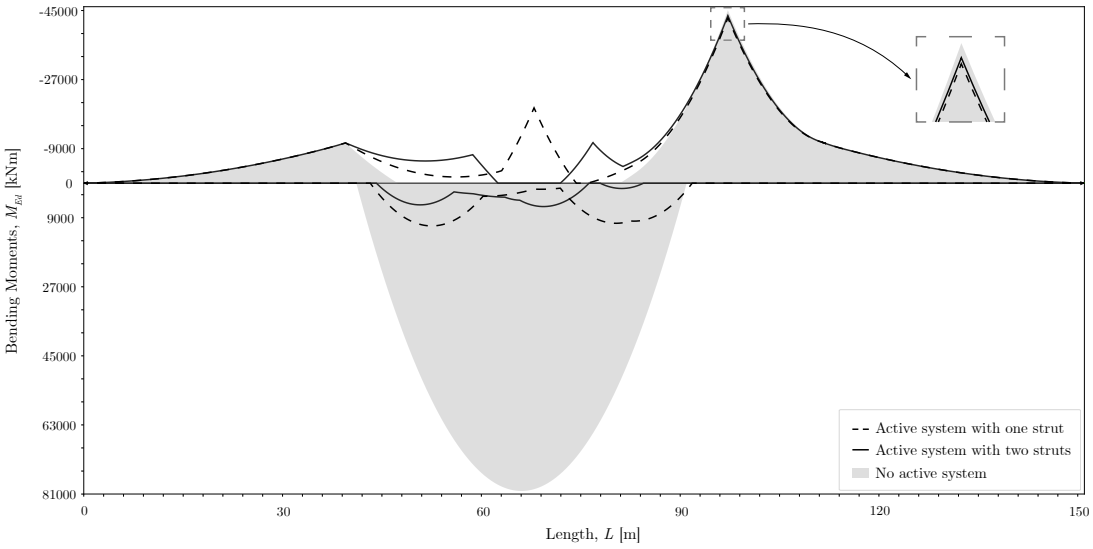

Figure 15. Influence of the struts number on active prestressing during stationary stage for a span length of 70 m.

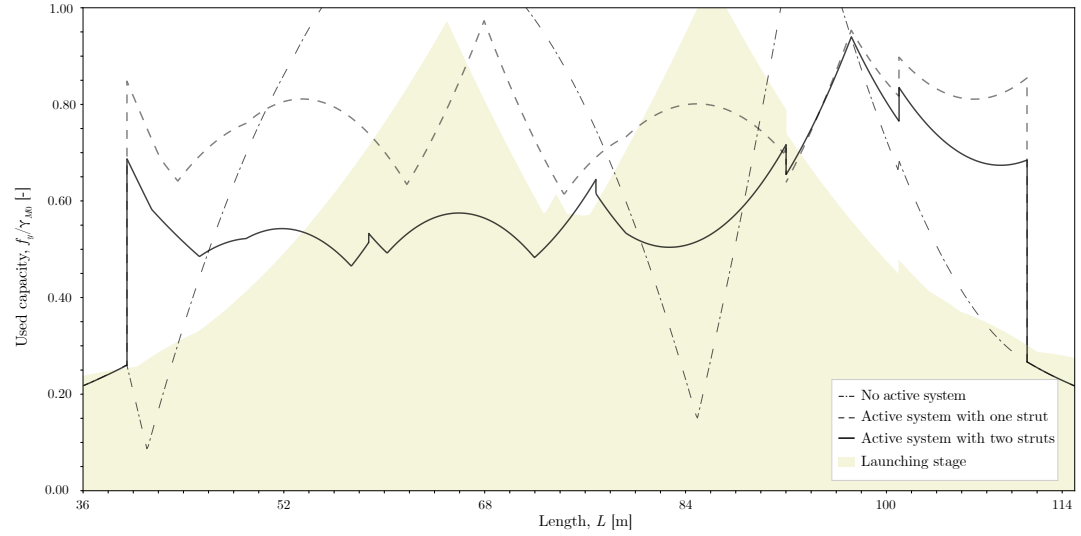

Figure 16. Maximum normal stresses for MSSs during stationary and launching stage for a span length of 70 m.

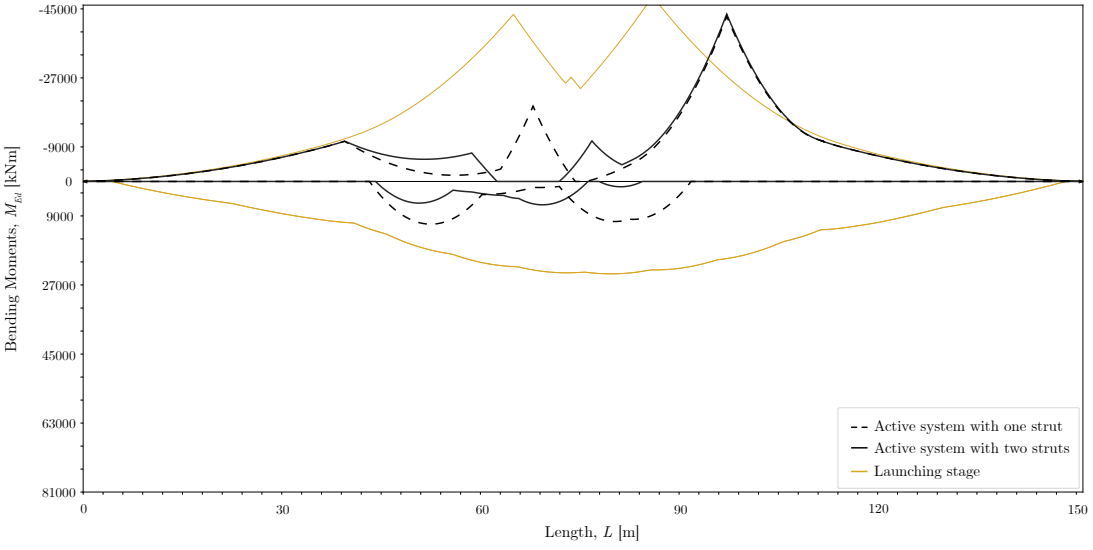

Figure 17. Launching and stationary stages for a span length of 70 m.

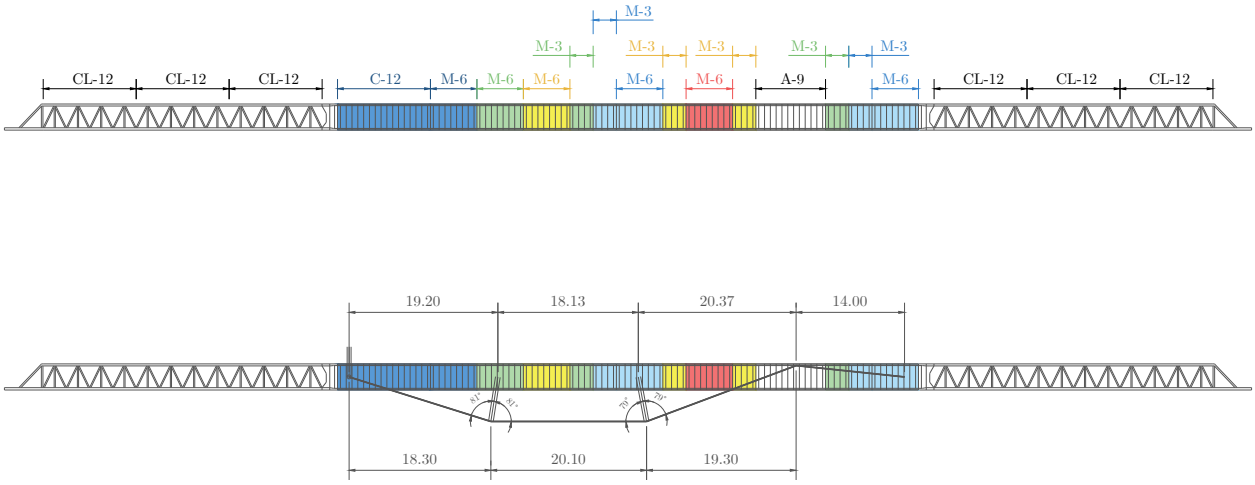

Figure 18. Optimized solution for a pouring span of 70 m using an external active system.

reinforcement. In this case, the governing constraint was the bending capacity, primarily limited by the plate buckling resistance under normal and tangent stresses during the launching stage. As shown previously in Figure 16, the modules satisfy ULS requirements during the stationary stage, with a similar response in SLS. Therefore, the optimization process is initiated from this baseline configuration. It is important to note that in MSSs incorporating active prestressing, the SLS criteria are inherently satisfied due to the prestressing effect, which reduces the margin for further optimization.

TABLE 1.
Limit States (SLS and ULS) the fulfilment for initial condition of MSS with an active system

Length [m]	Traffic service	ULS				SLS
		Stationary stage	%	Launching stage	%	
50	Highway	✓		✓		✓
	Railway	✓				✓
60	Highway	✓		✓		✓
	Railway	✓		✓		✓
70	Highway	✓		X	106%	✓
	Railway	✓		X		✓

Once obtained the optimized module configuration for the 70 m span, the case of the next smaller span length is studied using the same type of modules with a configuration that minimizes the MSS weight. Then, this process is repeated for the subsequent case. The final optimized configuration for a span length of 70 m is presented in Figure 18.

The modules shown in this figure correspond to the ones listed in Table 2. The number and percentage represent the reduction in terms of weight of each module. For instance, module 55%T means a weight reduction of 45% of the initial starting box section module.

TABLE 2.
Optimized modules for MSSs with an active prestressing system

Module	Length
55%T	12m 6m
75%T	6m 3m
85%T	6m 3m
100%T	6m 3m
106%T	6m

To ensure the best optimization for each case, the cantilever length is restricted to L/5 when using active systems, where L represents the pouring span length. This approach maximizes the benefits of the active prestressing by minimizing the cantilever and, consequently, reducing the maximum negative bending moment. This optimized solution can be now compared to a conventional one, which is defined in the next section.

4.3. MSS design optimization without an active prestressing system

For the design optimization of a conventional MSS (without any active prestressing system), a cantilever of $L/4$ is used, L being the pouring span length. This choice is primarily due to the magnitude of the maximum positive bending moment, which is strongly influenced by the main span length during the stationary stage. In contrast, the negative bending moment is directly related to the cantilever length, which does not increase as significantly. In the first scenario, the bending moments grow quadratically with the span length, while in the second case, they increase linearly with the cantilever length.

The ULS and SLS verifications are the same ones mentioned in Section 4.2. The main difference is that in these

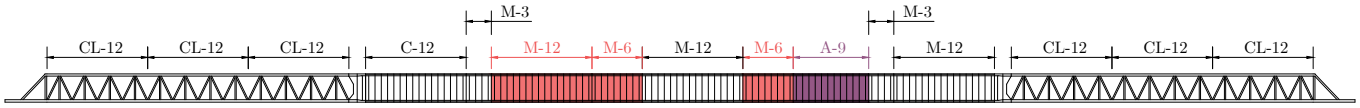

Figure 19. Optimized solution for a pouring span of 70 m without an external active system.

cases there is no axial compression, therefore there is no global buckling.

The optimization procedure is similar when having an active system. First, it is obtained a configuration for a span length of 70 m. Then, by detecting the zones with the need for reinforcement, new modules are introduced that can satisfy all conditions. Next, after a specific optimized configuration of modules is obtained, it is adjusted for a smaller span length and subsequently to the next one. In these cases, there is special attention to minimizing the weight of the MSS.

The fulfilment of the initial condition of the MSS C-60 –without any cross-sectional modification– for a 70 m span without an active system is presented in Table 3. When ULS or SLS requirements are not satisfied, the table specifies the maximum required percentage of additional reinforcement. In this case, the governing constraint was the bending capacity, primarily limited by the plate buckling resistance under normal and tangent stresses during both stationary and launching stages. Particularly, although the structure does not comply with ULS criteria during the stationary stage, SLS requirements are met, confirming that the ultimate strength governs the design.

TABLE 3.
Limit States (SLS and ULS) fulfilment for the initial condition of MSS without an active system

Length [m]	Traffic service	ULS				SLS
		Stationary stage	%	Launching stage	%	
50	Highway	✓		✓		✓
	Railway	✓				✓
60	Highway	✓		✓		✓
	Railway	✓		✓		✓
70	Highway	X	106%	X	106%	✓
	Railway	X	121%	X		X

The final optimized configuration for a span length of 70 m is presented in Figure 19.

For this specific case, since the modules were conceived for span lengths up to 60 m, an almost optimized solution was obtained for a span length of 70 m with the need for reinforcement in specific points. Therefore, the introduction of new modules for this present case is less impactful than the one in the previous sub-section. Specifically, it used the same 106%T module presented in Table 2 and introduced a new module named 121%A that corresponds to the original A box cross-section module with a 21% increase in weight.

4.4. Results and discussion

The results of all the optimization problems in terms of weight are presented in Tables 4 and 5. These solutions correspond to the final configurations after optimization approaches for bridge span lengths of 50 m, 60 m, and 70 m. Since the start of the optimization problem is 70 m, the results are given in reverse order. For the calculation of the steel weight, it was used a density of 78.50 kN/m^3 [39].

Table 4 presents the steel weight, in tonnes, of one MSS launching girder and quantifies the weight reduction achieved when using an active prestressing system compared to the optimized solution without it. The same comparison is made in terms of only the total weight of the box cross-section modules. For example, for a span of 70 m, the reduction of total weight in one girder is 8% when using an active prestressing system than when not using it, comparing both optimized MSSs.

In Table 5, the total weight of the MSS considering the two launching girders and other elements such as formworks, walkways, and other permanent loads is shown also following the same two approaches. Additionally, the lowest weight is contrasted with underslung MSSs found in the literature for both existing and theoretical proposals. Specifically, they are the ones found in [10,13,40–42].

TABLE 4.
Steel weight reduction when using an active system for one launching girder

Span length, *L* [m]	Steel weight on one launching girder [t]		% reduction of total weight	% reduction of box cross-section modules weight
	Without an active system	With an active system		
70	215	198	-8	-12
60	182	163	-10	-14
50	162	144	-11	-19

TABLE 5.
Total weight reduction of the MSS considering all permanent loads

Span length, *L* [m]	Total weight of MSS [t]		% difference compared to other studies	% difference to other existing MSSs
	Without an active system	With an active system		
70	795	761	-10	-1
60	679	641	-22	0
50	589	553	-	-3

From these results, the following conclusions are derived:

- The optimization results demonstrate a clear reduction in self-weight when active systems are integrated, compared to configurations without them. Its impact is more pronounced in the central zone of the main span than in other areas due to the construction process of the bridge deck.
- The effectiveness of the active system in the stationary stage is limited due to the typical pouring sequences of bridge decks, which start on the cantilever zones. Specifically, in the first stages, there is no increment of deflection on the main span which does not activate the control scheme.
- When optimizing the sections using active systems, in the beginning, there is a clear reduction in the sections for the centre of the span, but these same zones are then restricted to the launching stage structural demand. Therefore, it represents a lower bound of optimization.
- A hybrid active-passive system might improve the condition of the first point. For instance, the active system can initially present a higher value of prestressing on the cables, introducing a positive bending moment on the cantilever zone. Nonetheless, this produces on the bridge deck a negative deflection (upward) which is not usually desirable.
- The maximum reduction in terms of weight of an optimized MSS with and without an active prestressing system is a maximum of 11% comparing the total weight and 19% comparing only the weight of the main girders. However, these two values can be reduced to 8% and 12%, respectively, for a longer span.
- Despite there can be optimization reductions of up to 45% of the initial weight on some modules (see Section 4.2), this lands on a maximum reduction of 19% of the weight of the main girders. Also, this reduction is indirectly proportional to the span length, v. g., for span lengths of 70 m, the maximum reduction is 12%, while for 50 m, it is 19%.
- The results of MSSs using an active system land on similar weights of existing MSSs with these assemblies, which validates the optimization results for span lengths of 50 m, 60 m, and 70 m.

5. CONCLUSIONS

This paper presented a comprehensive analysis of the design and optimization strategies for underslung Movable Scaffolding Systems (MSSs), with and without the incorporation of active prestressing systems. The study considered various span lengths and covered all relevant construction stages. Based on the findings, the following conclusions can be drawn:

- The use of active prestressing systems clearly contributes to weight reduction in MSSs, particularly in the central modules during the stationary stage. However, two key limitations constrain the overall optimization potential:
  - Active systems are effective only during the stationary phase, specifically during the deck pouring process. As a result, the launching stage governs the design, imposing stricter structural requirements.
  - Their effectiveness during the pouring stage is limited on the cantilevers due to the construction process in which there is no increase in the deflection when pouring the cantilevers.
- The reduction in the total weight of MSSs with active systems of around 10% might not be sufficient to compensate for the cost of cables, struts, and anchorages, as well as the installation of an active control system, the sensors, and the actuators, among other elements. Therefore, from a cost-effectiveness perspective, the implementation of active prestressing may not always be justified.
- There are other advantages of the active systems that are not mentioned in this paper, such as the continuous monitoring of the MSS during the stationary stage. More information can be found in [43]. This has a direct impact on the safety of the MSSs during these manoeuvres and is of interest in some specific bridge projects.
- Future research on the implementation of active systems on MSSs could focus on the following directions.
  - A more comprehensive and integrated economic assessment should be investigated, incorporating not only the direct costs but also the potential benefits of emerging technologies.
  - The development of active systems capable of operating during both the stationary and launching stages should be explored. Extending their functionality to all construction phases may significantly enhance the overall optimization of MSSs.

References

[1] F. Leonhardt, Brücken, Deutsche Verlags-Anstalt GmbH, Munich, 1984.

[2] M.A. Mora Quispe, L. Todisco, H. Corres Peiretti, Design basis of movable scaffolding systems following american and european code provisions and recommendations, Baltic Journal of Road and Bridge Engineering 16 (2021) 151–177. https://doi.org/10.7250/bjrbe.2021-16.528.

[3] M. Däbritz, Movable scaffolding systems, Structural Engineering International: Journal of the International Association for Bridge and Structural Engineering (IABSE) 21 (2011) 413–418. https://doi.org/10.2749/101686611X13131377725442.

[4] J.R. Díaz de Terán, V.G. Haach, J. Turmo, J.J. Jorquera-Lucerga, Improved Construction of Concrete Viaducts with Movable Scaffolding Systems in Spain, Journal of Bridge Engineering 21 (2016) 04016050. https://doi.org/10.1061/(ASCE)BE.1943-5592.0000831.

[5] P. Pacheco, H. Coelho, P. Borges, A. Resende, D. Carvalho, New Frontiers in Multi-span Prestressed Concrete Deck Construction: A Case Study, Structural Engineering International (2020) 1–12. https://doi.org/10.1080/10168664.2020.1738906.

[6] M. Rosignoli, Bridge Construction Equipment, ICE Publishing, London, 2013. https://doi.org/10.1680/bce.58088.

[7] Members of IABSE WG 6, Bridge Deck Erection Equipment, ICE Publishing, London, 2018. https://doi.org/10.1680/bdee.61934.

[8] P. Pacheco, A. Guerra, P. Borges, H. Coelho, A Scaffolding System strengthened with Organic Prestressing – the first of a new Generation of Structures, Structural Engineering International 17 (2007) 314–321. https://doi.org/10.2749/101686607782359092.

[9] P. Pacheco, Gantry with auto-adjusting prestressing, US 7,366,634 B2, 2008.

[10] M.C. Ros, Estudio de la viabilidad del uso de atirantamiento en cimbras de avance para puentes, Ms Thesis, Universitat Politècnica de Catalunya, 2011.

[11] Confederación Nacional de la Construcción, Manual de Cimbras Autolanzables, Madrid, 2015.

[12] Asociación Española de Ingeniería Estructural, Diseño y Utilización de Cimbras, ACHE, Madrid, 2005.

[13] D. Gonçalves Bezerra, Studo da interacção cimbre / tabuleiro durante a betonagem em pontes construídas tramo a tramo, Ms Thesis, Universidade do Porto, 2008.

[14] P. Jacquet, J. Davy, J.E. Herrero, A. van der Horst, F. Imberty, P. Schmitt, M. Contreras, S. Curtis, J. Gonzalez, A. Neagoe, B. Normand, D. Tassin, G. Webster, fib Bulletin 48. Formwork and falsework for heavy construction, fib. The International Federation for Structural Concrete, 2009. https://doi.org/10.35789/fib.BULL.0048.

[15] M. del M. Corral, L. Todisco, J.M. Soria, Design, construction and testing of a smart under-deck cable-stayed footbridge prototype, Eng Struct 291 (2023). https://doi.org/10.1016/j.engstruct.2023.116387.

[16] I.M. Díaz, C.A. Gallegos, J. Ramírez Senent, C.M.C. Renedo, Interaction Phenomena to Be Accounted for Human-Induced Vibration Control of Lightweight Structures, Front Built Environ 7 (2021). https://doi.org/10.3389/fbuil.2021.658529.

[17] M.d.M. Corral, Smart under-deck cable-stayed footbridges: from conceptual design to experimental validation, PhD thesis, Universidad Politécnica de Madrid, 2023.

[18] I. Ajona Jover, Responsiveness and adaptability for structural purposes: State-of-the-art and application to a case study, Ms thesis, Universidad Politécnica de Madrid, 2020.

[19] P. Pacheco, H. Coelho, La evolución de las autocimbras - nuevas necesidades y nuevas soluciones, in: IV Congreso de La Asociación Científico - Técnica Del Hormigón Estructural - Congreso Internacional de Estructuras, 2008.

[20] A.M. Ruiz-Teran, A.C. Aparicio, Structural behavior and design criteria of under-deck cable-stayed bridges and combined cable-stayed bridges. Part 1: Single-span bridges, Canadian Journal of Civil Engineering 35 (2008) 938–950. https://doi.org/10.1139/L08-033.

[21] M. del M. Corral, L. Todisco, Structural design of a smart under-deck cable-stayed prestressed concrete viaduct: Theoretical basis and application to the Osormort viaduct, Structural Concrete 25 (2024) 1528–1545. https://doi.org/10.1002/suco.202300373.

[22] European Committee for Standardization (CEN), EN 1990:2010 Eurocode. Basis of structural design, 2010.

[23] A.M. Ruiz Terán, Puentes atirantados no convencionales. Comportamiento estructural y criterios de diseño., PhD thesis, Universidad Politécnica de Cataluña, 2005.

[24] European Committee for Standardization (CEN), EN 1992-1-1:2023 Design of concrete structures. Part 1-1: General rules and rules for building, bridges and civil engineering structures, 2023.

[25] European Committee for Standardization (CEN), EN 1993-2:2006 Eurocode 3: Design of steel structures. Part 2: Steel bridges, 2006.

[26] European Committee for Standardization (CEN), EN 1992-2:2013 Eurocode 2: Design of concrete structures. Part 2: Concrete bridges. Design and detailing rules., 2013.

[27] European Committee for Standardization (CEN), EN 1993-1-11:2006 Eurocode 3: Design of steel structures - Part 1-11: Design of structures with tension components, 2006.

[28] J. Ploch, Jan zur Definition und zum Sicherheitskonzept der Vorspannung, PhD thesis, Universität Stuttgart, 2004.

[29] K.K. Mermigas, Behavior and design of extradosed bridges, Ms thesis, University of Toronto, 2008.

[30] M. Virlogeux, J.-F. Fontaine, Second Order Analysis of Concrete Cable-stayed Bridges- The Example of the Evripos Bridge, in: Seminar on Cable-Stayed Bridges, Indian National Group of the International Association of Bridge and Structural Engineering, Greece, 1988.

[31] C. Menn, Prestressed Concrete Bridges, Birkhäuser Basel, Basel, 1990. https://doi.org/10.1007/978-3-0348-9131-8.

[32] L. Carrillo Alonso, Análisis teórico de la variación aleatoria de los esfuerzos de montaje de los cables en puentes atirantados, PhD thesis, Universidad Politécnica de Madrid, 2015.

[33] A. Guerra, A. André, P. Pacheco, A. Adão da Fonseca, PRÉ-ESFORÇO ORGÂNICO-APLICAÇÃO EM CIMBRES AUTOLANÇÁVEIS-BASES DO PROJECTO PILOTO, 2004. https://www.researchgate.net/publication/267830658.

[34] European Committee for Standardization (CEN), EN 1993-1-5:2024 Eurocode 3: Design of steel structures - Part 1-5: Plated structural elements, 2024.

[35] European Committee for Standardization (CEN), EN 1993-1-1:2022 Eurocode 3: Design of steel structures - Part 1-1: General rules and rules for buildings, 2022.

[36] Ministerio de Fomento, Instrucción relativa a las acciones a considerar en el proyecto de puentes de carretera (IAP-11), 2011.

[37] Ministerio de Fomento, Instrucción relativa a las acciones a considerar en puentes de ferrocarril (IAPF-10), 2010.

[38] A.G. SOFiSTiK, SOFiSTiK, (2022).

[39] European Committee for Standardization (CEN), EN 1991-1-1:2019 Eurocode 1: Actions on structures - Part 1-1: General actions - Densities, self-weight, imposed loads for buildings. Amendment 1: National annex., 2019.

[40] P. Pacheco, H. Coelho, P. Borges, A. Guerra, Technical Challenges of Large Movable Scaffolding Systems, Structural Engineering International 21 (2011) 450–455. https://doi.org/10.2749/101686611X13131377725640.

[41] P. Pacheco, Organic Prestressing Impact in Multi-Span Large Deck Construction, 2016.

[42] J.R. Gabaldón Bejarano, Estudio comparativo entre cimbras autolanzables con estructura portante por debajo del tablero o estructuctura portante por encima del tablero, (2016).

[43] A. Resende, S. Pereira, F. Magalhães, P. Pacheco, Continuous monitoring of a large movable scaffolding under operation, Autom Constr 156 (2023). https://doi.org/10.1016/j.autcon.2023.105084.

Disponible en **www.hormigonyacero.com**
https://doi.org/10.33586/hya.2025.4092

Influence of deep foundations in a deck slab high-speed railway bridge: A theoretical study

Influencia de las cimentaciones profundas en la losa de tablero de un puente ferroviario de alta velocidad: un estudio teórico

A. M. de la Concha[a], D. Suescum-Morales[b], M. Martínez Sánchez[a] y H. Cifuentes[a,*]

[a] *1School of Engineering, Department of Continuum Mechanics and Structural Analysis, University of Seville.*
bSchool of Civil Engineering, Construction Engineering Area, University of Cordoba.
**Corresponding author: School of Engineering, Department of Continuum Mechanics and Structural Analysis, University of Seville.*

Recibido el 14 de febrero de 2025; revisado el 22 de mayo de 2025, aceptado el 3 de junio de 2025

ABSTRACT

In this research, the importance of properly modeling the infrastructure of high-speed railway bridges with deep foundations when using the finite element method (FEM) is discussed. To do so, an isolated deck and several complete models with different characteristics were compared. Parameters such as the length of the piles, the stiffness of the supporting layers and the type of dynamic load (10 different trains) were explored. This study started with the analysis of various parameters that determine the behavior of deep foundations with piles in simplified models. Based on these findings, a complete model was built. This research shows the importance of including not only the surrounding terrain but also the main substructure (i.e., piers and abutments) in the model. Recommendations on the amount of soil to include, its mechanical properties and the length of the piles needed are also provided to ensure the reliability of results when considering the soil-structure dynamic interaction. With this research, a contribution to current knowledge is intended through a series of guidelines and tools to help structural engineers in dynamic simulations through a theoretical case study.

KEYWORDS: Dynamic analysis, high-speed trains, railway bridges, soil-structure interaction, pile foundation, infrastructure, numerical simulations.

RESUMEN

En esta investigación se discute la importancia de modelizar adecuadamente la infraestructura de los puentes ferroviarios de alta velocidad con cimentaciones profundas cuando se utiliza el método de elementos finitos (FEM). Para ello, comparamos la respuesta de un tablero aislado y varios modelos de puentes completos con modelos de terrenos de diferentes características. Se exploran parámetros como la longitud de los pilotes, la rigidez de las capas de soporte y el tipo de carga dinámica (10 trenes diferentes). Este estudio comienza con el análisis de varios parámetros que determinan el comportamiento de las cimentaciones profundas con pilotes en modelos simplificados. Basándonos en estos hallazgos, se construyen los modelos completos. Esta investigación muestra la importancia de incluir no solo el terreno circundante, sino también la subestructura principal (es decir, pilares y estribos) en el modelo. También se proporcionan recomendaciones sobre la cantidad de suelo a incluir, sus propiedades mecánicas y la longitud de los pilotes necesarios para garantizar la fiabilidad de los resultados al considerar la interacción dinámica suelo-estructura. Con esta investigación, pretendemos contribuir al conocimiento actual con una serie de directrices y herramientas para ayudar a los ingenieros estructurales en simulaciones dinámicas a través de un estudio de caso teórico.

PALABRAS CLAVE: Análisis dinámico, trenes de alta velocidad, puentes de ferrocarril, interacción suelo-estructura, cimentaciones profundas, infraestructura, simulaciones numéricas.

* Persona de contacto / *Corresponding author*:
Correo-e / *e-mail*: delaconcha@us.es (Antonio Martínez de la Concha)

Cómo citar este artículo: De la Concha, A.M., Suescum-Morales, D. Martínez, M., & Cifuentes, H. (2025). Influence of deep foundations in a deck slab high-speed railway bridge: A theoretical study. *Hormigón y Acero*. 76(306):33-46. https://doi.org/10.33586/hya.2025.4092

1. INTRODUCTION

High-speed railways have requirements for bridges due to the dynamic loads associated to train traffic. Considering this, the study of the dynamic behavior of railway bridges has become a key factor in the design of such structures [1–5]. The stresses and strains observed in a railway bridge due to train traffic can exceed the design limits (i.e., targets), particularly if the frequency of the applied loads matches the natural frequency of the structure as a result of undesired resonance. This is why the natural frequency of the structure should be tuned away from the frequency of the loads, as explained by Shen-Haw (2003) [6]. This phenomenon can lead to the inoperability of the structure and, in extreme cases, to its collapse.

The growth of the construction of high-speed railways has increased the concern and awareness of traffic-induced vibrations among engineers and scientists [7,8]. This has led to impose limits on maximum accelerations and deflections using different codes and to prescribe an impact factor that is used to scale up the static loads in an effort to capture the dynamic effects [9,10]. Dynamic simulations that are often conducted with time-consuming finite element methods (FEM) have become essential for avoiding such problems. Therefore, guidelines and tools to assist structural engineers in the process are needed [11].

Hence, capturing the behavior of the structure in a realistic manner is very important. In this regard, the development of computational methods has resulted in great progress in terms of knowledge and accuracy of analysis [12–14]. Some models take into account not only the motion of the loads on the bridge, but also changes in their magnitudes due to the dynamic interaction between the structure and the train suspension [15–17].

The dynamic loads used in this paper follow those proposed by the European design code [9], which are based on the High-Speed Load Model (HSLM) and comprise a series of fictitious trains proposed by ERRI D214 [8]. The loads are constant in magnitude for a given axle and move along the structure following the train motion. These load recommendations can also be found in other codes such as IAPF-07 [10]. It is not possible to conduct an analysis including multibody behavior because each train is composed of the car body, bogie, wheelset, primary and secondary suspension, axle box, yaw damper, lateral damper, antirolling torsion bar, rotating arm, lateral stop and traction rod [18,19]. This study focused on the envelope behavior of the potential traffic over the bridge, as is usual in codes.

As discussed in Martínez De la Concha et al. [20], most models only include the structure and disregard the supporting terrain by applying displacement boundary conditions directly on the structure. The simple linear elastic beams or frame structure are often used to simulate the vehicle-bridge dynamic response [21]. This simplification reduces the computational cost but assumes that the soil has infinite stiffness, as pointed out by Zangeneh et al. (2018) [22].

Limited material has been published regarding the influence of the soil-structure interaction (SSI) on the behavior of high-speed railway bridges. There are even fewer studies that also cover deep foundation models (i.e., with piles). An example is the study by Takemiya (2007) [23], which explored the behavior of high-speed railway structures and the surrounding terrain in Japan through the23 FEM. It concluded that including the soil-structure interaction was crucial to properly capture the behavior of the structure. Mahir Ülker-Kaustell had similar findings in his simplified analysis of a portal frame railway bridge [24]. Not including the supporting soil in the model can decrease the damping of the model, increasing the magnitude of displacements during resonance [25,26]. The boundary element method (BEM) has a great application in the study of the soil-structure interaction [27,28], allowing for more accurate analysis. It also eliminates the need to define an external contour in the model and has been used for longer than the FEM in this field [29]. Nevertheless, the FEM was chosen because it is widely used in the study of these structures. The BEM is less common in practical applications.

No references to previous studies that explored the SSI as well as the influence of the following parameters were found: (i) different soil stiffness; (ii) different soil depth (i.e., different depths of piles); (iii) a speed sweep from 20 km/h to 420 km/h; and (iv) using 10 trains with different wheelbases and loads per axle. Following the formulation used in a recent study [20], two analyses methods were used: direct integration analysis of the complete model using the Newmark method in Abaqus (Abaqus/standard, version 6.14), and modal superposition analysis using SAP2000. For the direct integration analysis of the complete model, an amplitude decay factor of $\gamma = 0.005$ was used. Abaqus 6.14 and SAP2000 v14 software were used, as they are among the most commonly used tools for this type of study. [30–33].

The main novelty from the previous research by Martínez-De la Concha et al. [20], was the study of deep foundations. Regarding this particular issue, all the parameters to build the model including the infrastructure were new. The aim of this theoretical study with the FEM was to compare the results of the dynamic impact coefficient from a model that does not include the infrastructure (e.g., surrounding soil, piers, abutment and pile foundation) to a model that includes it. Parameters such as the length of the piles, the stiffness of the supporting layers, and the type of dynamic load (i.e., 10 different trains) were explored.

This study began with the analysis of various parameters that control the behavior of deep foundations with piles in simplified models. Based on these findings, a complete model was built. A contribution to current knowledge is intended through a series of guidelines and tools to assist structural engineers in dynamic simulations, using a theoretical case study.

2. MODEL DESCRIPTION

2.1. Simplified foundation model

The objective of these analyses was to identify and tune the parameters that control the behavior of a deep foundation

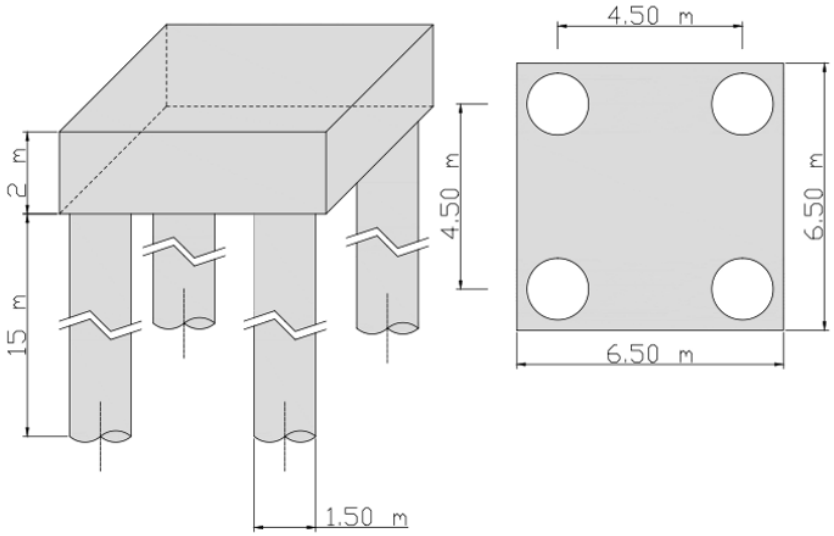

Figure 1. Model of pile cap for the simplified foundation model.

model (i.e., piles and pile cap) to ensure reliable converged results. Parameters such as finite element size and type, pulse duration, and the amount of soil to be included were considered. For this study, several simplified models were developed in which the influence of these parameters on the response was analyzed. Based on the results, a complete model was subsequently built. In the first simplified model, the response of a square pile cap (6.5 × 6.5 × 2.0 meters) was analyzed. The pile cap was supported on 4 circular piles with a length of 15 m and a diameter of 1.5 m (Figure 1).

The model included a portion of soil around the piles whose dimensions and characteristics were parameters to be studied. The piles and pile cap had the following mechanical characteristics: elastic modulus E=30 GPa, Poisson coefficient γ= 0.2 and a specific concrete weight of γ_c = 25 kN/m³. Two soil layers were considered: a 7 m meter deep superficial layer with softer properties (E = 3 MPa, ν = 0.35 and a specific soil weight of γ_s = 20 kN / m³); and a stiffer material layer underneath (E = 30 MPa, = 0.35 and a specific soil weight of γ_s = 20 kN / m³). A relatively low stiffness material was still used, since the behavior of the system was intended to be analyzed on a deformable elastic bed [34]. Five percent of the critical damping was used in the soil material definition [34,35].

In the five faces defined by the soil boundary included, (every face unless top face) normal displacements were constrained. There was no relative movement in the concrete-soil interface. Instead, both meshes moved together like a continuous mesh. For this foundation model, three sensitivity studies were carried out:

(1) finite element size;
(2) pulse duration; and
(3) volume of soil included in the model.

All model components were discretized using C3D4-type elements from the Abaqus library, that is, first-order tetrahedral elements. The models were run using direct integration in Abaqus/Explicit with the default values for numerical damping (i.e., a linear bulk viscosity of 0.06 and a quadratic bulk viscosity of 1.2). Since the same level of accuracy was not required in the entire modeled domain, local mesh refinements were applied where higher accuracy was needed. It is important to consider the effects on wave propagation when meshing the different models.

To identify the requirements for element size, the smallest model (Model 1 on Table 1) was meshed with three different element sizes – 30, 40 and 50 cm –, resulting in models with 43,469, 21,535 and 12,772 degrees of freedom respectively. A uniform pressure load was applied on the pile cap upper face. Its magnitude was time-dependent following triangular amplitude. The response was analyzed against two different loads: a short pulse of 1 MPa maximum pressure and a duration of 10 ms; and a long pulse of 20 kPa of peak pressure and a duration of 500 ms. In both cases, the magnitude of the pulse was the same. The first one aimed to highlight the behavior during higher frequency dynamic events while the second one assessed loads that better represent the typical dynamic loads produced by train traffic. This statement follows Frýba (1996) [36].

To identify the amount of soil to include in the FEM model, it was necessary to explore it to maintain result accuracy while keeping the computation cost down. Simpler theoretical models, which can be solved analytically assuming isotropic and homogeneous linear elastic properties, consider the soil as a homogeneous half-space. Such is the case of studies conducted with the boundary element method (BEM) [37]. Hence, our models had the same conditions.

Pile cap width (6.5 m) was adopted as the characteristic length in the model. Five models with different amounts of soil were analyzed. The size of the models was the result of adding 6.5 m of soil around the pile cap and also 6.5 m of soil under the pile toe line. Subsequent models were built by adding 6.5 m of soil in each direction to the previous model. Additionally, a model with a very large portion of soil (i.e., the Limit model) was analyzed to verify that the reflection

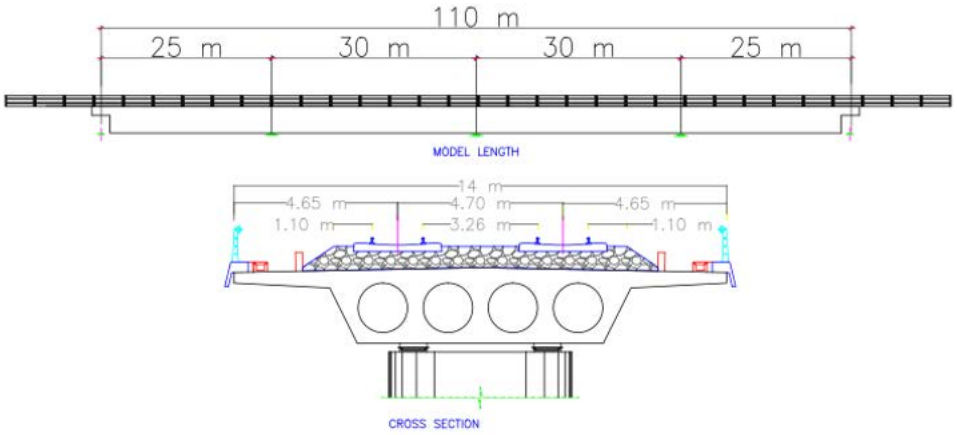

Figure. 2. Geometric description of the isolated deck model.

of waves in the boundary did not interfere with the simulation results meaningfully. To this end, the soil contours were moved out far enough so that the P waves had no time to reflect and return in the simulated time interval [22]. Table 1 presents the dimensions of the models described above.

TABLE 1.
Simplified foundation model dimensions

Model name	Dimensions (m)			Soil under the end pile
	X	Y	Z	
Model 1	19.5	19.5	23.5	6.5
Model 2	32.5	32.5	30	13
Model 3	45.5	45.5	36.5	19.5
Model 4	58.5	58.5	43	26
Limit model	162.5	162.5	95	78

2.2. Bridge models

To analyze the bridge structure, two models were built: one including infrastructure and one excluding it. Those models were studied using a specific bridge software package: SAP2000 v14. Both models were explored using both modal superposition and direct integration. Sometimes the model includes elements such as the abutments and/or piles, but it rarely includes the soil-structure interaction [38]. Bridges are typically analyzed with models that only consider their deck [36]. The aim of our models was to assess the impact of the previous simplification. This required assessing the behavior of a simply supported isolated deck so that it could be compared with a complete one, which included the infrastructure.

2.2.1. Isolated deck model

The deck of the bridge studied in this paper was identical to the one analyzed by the authors in previous research [20]. Its main characteristics are described below. In this model, we assumed displacement boundary conditions assuming infinitely stiff piers and abutments [14]. Shell elements with both membrane and plate degrees of freedoms were used. Flexural (i.e., plate) behavior considers rotational stiffness along the two axes in the element plane as well the displacement in the normal direction (i.e., Kirchoff's formulation) [32]. For the membrane behavior, we used an isoparametric formulation that included the translational degrees of freedom in the element plane as well as the rotation within it. Displacements in the element plane were considered using quadratic shape functions, and out-of-plane displacements were considered with cubic functions.

The modeled bridge had 4 spans so that the model included the interaction between spans accurately enough with an affordable computational cost. The bridge had two 30-m-long spans in the middle and one 25-m-long span at either end. The deck cross section was a 2.00-m-thick lightened slab with four 1.4-m-diameter circular lightening holes (Figure. 2). The slab was 14.00 m wide, which is standard for a double track line in Spain [39].

The location of the nodes in the cross section is shown in Figure 3. The thickness of the elements was adjusted to obtain a section with the same area (i.e., same mass) as the real deck. A 1 m element size was used in the cross section and matched the element size along the bridge, resulting in approximately square elements as shown in Figure 3.

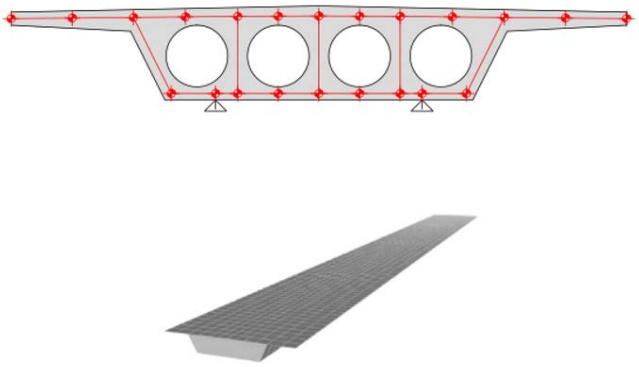

Figure. 3. Schematic view of the model cross section and mesh discretization of the isolated deck.

Elements in the deck cross section were added on top of the abutments and piles to model the diaphragms. To visualize this, the elements modeling the webs and the bottom slab were concealed in Figure 4.

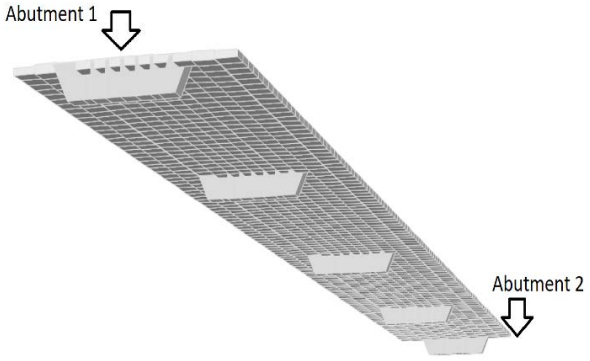

Figure. 4. Diaphragm modeling detailed view.

The masses corresponding to the permanent loads were distributed over the upper slab. The permanent loads attributed to each element were as follows (kN/m): 94.84 (ballast); 6.70 (sleepers); 1.18 (rails); 5 (small wall); 3.78 (troughs); 9.59 (barrier rail) and 1.02 (railings).

The vertical displacement in all support points (Figure 3) was constrained. The lateral motion was constrained in one support location per pier/abutment. Finally, the longitudinal displacement was constrained in both support nodes only at one end of the bridge (Abutment 1). The mechanical properties of the deck were as follows: elastic modulus (E) 30 GPa; Poisson coefficient v = 0.2 specific weight ρ = 25 kN/m³; and damping ξ 3%.

Universal dynamic A train loads, also known as High-Speed Load Model (HSLM) loads, were applied. They consist of 10 trains with different wheelbases and loads per axle in various configurations [8]. These are the dynamic loads recommended by the main regulations for the design of new railway lines [9,10]. Following the standards [10], a 350 km/h design speed was considered and, consequently, a speed sweep was analyzed from 20 km/h to 420 km/h (i.e., 1.2 times the design speed) with a 10 km/h step.

The traffic load was distributed among the nodes under the railway in the cross section. The applied force on each node was proportional to the surface of the sleeper over it (Figure 5). It was assumed that the load propagates uniformly with a 1/4 slope through the ballast and the sleeper distributes the load uniformly. This load application procedure is described in the Spanish code for this type of structures [10].

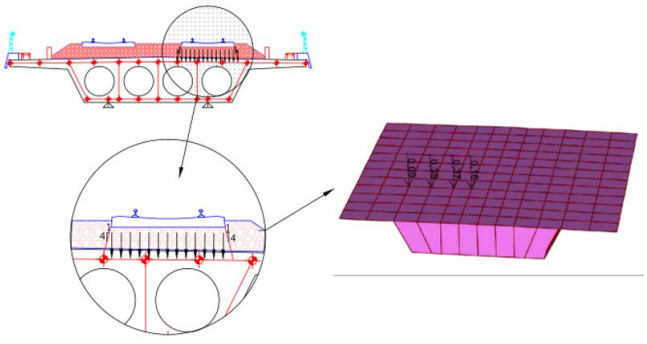

Figure 5. Load modeling in the cross section for the isolated deck model and complete model.

In the longitudinal direction, the load was distributed in a linear fashion among two consecutive sections based on the distance between the load and the section at that particular time. This resulted in a series of triangular history loads as the different axles of the train traveled over a specific cross section of the bridge (Figure 6).

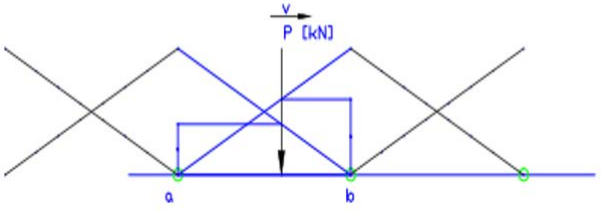

Figure 6. Longitudinal load distribution.

The study focused on the central section of the bridge, specifically on the node of the upper slab that is centered with the track where the time-history loads are applied. This node captures the displacements of the track supports and ultimately of the trains that travel on top of them. The maximum vertical displacement observed in this node during the entire simulation was compared.

Dynamic amplification is captured by the impact factor (Φ), a commonly used parameter [8,10] that normalizes the maximum deflection observed among all trains and across all speeds with that of the UIC-71 train [9] statically. For this paper and following the results of previous research [20], a different definition of the impact factor was used. Instead of using the UIC-71 train, each train dynamic response was normalized with its own static deflection.

2.2.2. Complete model of the railway bridge

In this section, the soil-structure interaction was introduced into models with deep foundations. The model used in this section consisted of a deck that was identical to that described in Section 2.2, both geometrically and regarding loads. That deck was supported by 10-m-high abutments and 3 piers. The outboard piers were 20 m high while the pier at the center of the bridge measured 25 m. The abutments were of the closed type and consisted of a 1.00-m-thick and 10-m-high front wall with two lateral walls (i.e., wing walls) that were also 1.00 m thick. The abutment foundations were pile caps (14.00 x 6.00 x 2.00 m) with 6 piles 1.50 m in diameter. The pile caps were flush with the wing walls and protruded 2.00 m beyond the front walls. The pier foundations were 6.00 x 6.00 x 2.00 m pile caps with 4 piles 1.50 m in diameter. Figure 7 represents the structure described above.

The piers were modeled with 1.00 x 1.00 m shell elements similar to those used on the deck. The pier cap was modeled with the same type of element and its mesh was adjusted so that the nodes would coincide with the deck above. The foundations of the piers were modeled with 1 m 8-node solid hexahedral elements based on the standard isoparametric formulation. For the pier-footing connection, the two bottom layers of nodes in the piers were rigidly coupled with three rows of nodes on the surface of the footing. This implied that they all moved as a rigid body, which modeled the embedding of

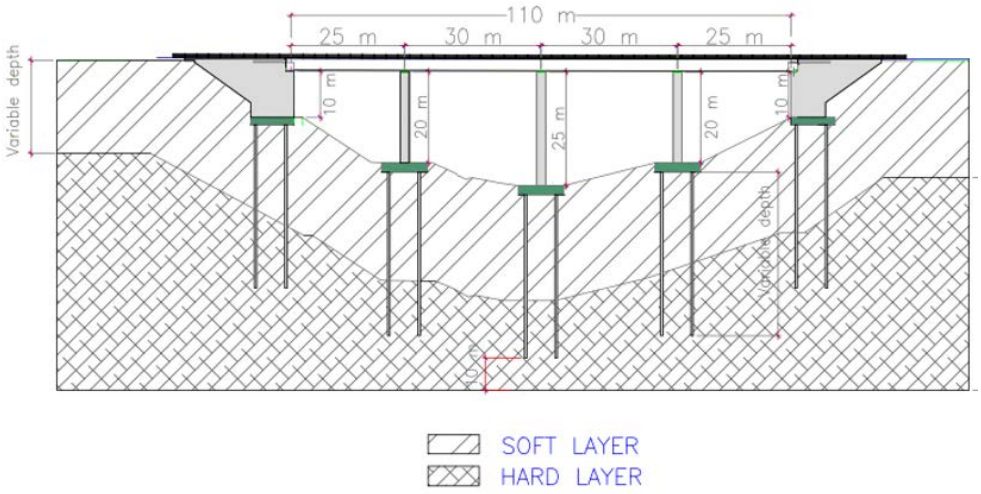

Figure. 7. Longitudinal section of the complete model.

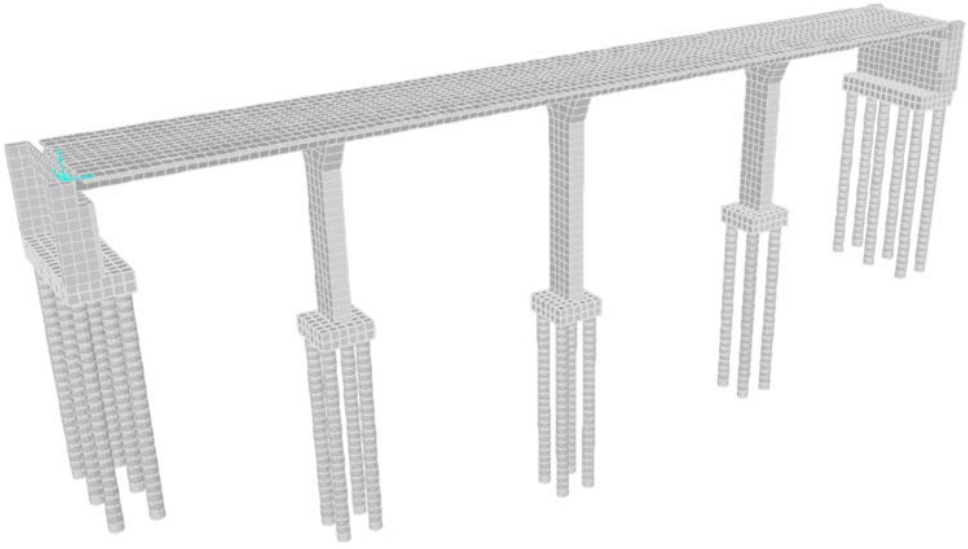

Figure. 8. Complete model discretization without soil.

the pier in the footing while allowing strains in the surrounding area. The abutments were also discretized in a similar way, with shell elements in the walls and solid elements in the foundations. Everything described above is shown in Figure 8.

A peculiarity of the abutments was that the soil inside them, specifically that contained between the wing walls and the back face of the front one, was included in the model as a solid element and matched the abutment element size. Thus, the overall stiffness and inertia of the system was better captured since it included the interaction with the backfill soil. The complete model also included the soil around the abutment and around the pile caps and piles. The model was extended with an additional 14 m of discretized soil around the foundation for a global model width of 34 m since the pile caps were 6 m wide (6 + 2 x 14). The soil depth of the soil included was 10 m greater than the deepest pile (i.e., middle pier foundation). The volume of soil included in these models was chosen in accordance with the results presented in Section 3.1.2.

Regarding soil stiffness, two different layers were considered: a soft layer, whose thickness and stiffness were variables to be explored, and a hard layer underneath, which extended 10 m below the deepest pile. The piles were always embedded 10 m within the stiffer material, whose mechanical properties were constant through the study. The pile caps are also embedded in the top layer and were 2 m high. Normal displacements were constrained on the soil boundary faces. A summary of the models analyzed is presented in Table 2 using Figure 9 to illustrate one of them.

TABLE 2.
Complete model dimensions

Soft layer depth (m)	Hard layer depth (m)	Pile foundation (m)	Modeled soil Depth (m)
4	20	12	24
6	20	14	26
8	20	16	28
10	20	18	30
12	20	20	32
14	20	22	34
16	20	24	36

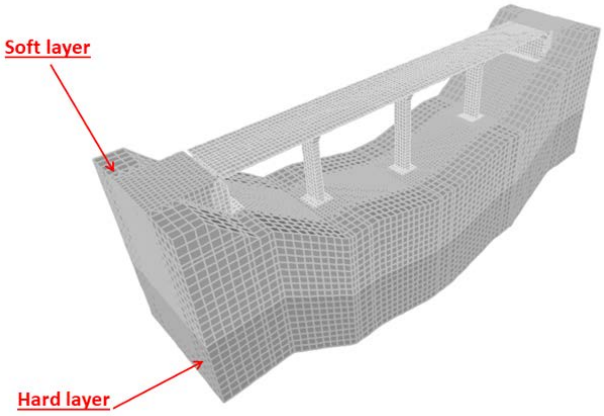

Figure. 9. Complete model discretization.

Multiple analyses using different soil stiffness were performed to verify the importance of including the soil substructure while modeling deep foundation structures when considering their dynamic behavior. These stiffnesses were related to the wave propagation velocity (C_s, C_p, C_r) through the equations that govern the behavior of homogeneous isotropic materials, whose derivation can be found in Yang & Hung (2209) [40]. To estimate the stiffness of the terrain, the shear wave velocity (C_s) was used following the values and criteria proposed by seismic regulations.

For the hard layer material (i.e., the bottom one), a shear wave velocity of 800 m/s was used, corresponding to a material with a Young's modulus of 3,500 MPa, which remained unchanged throughout the studies. This corresponds to Type I ground (compact rock) according to the NSCP-07 [41], Type A ground (rock or other rock-like geological formation) in the Eurocode 8 [42] and Type B ground (i.e., rock) in the ASCE-7 [43]. For the soft layer material, three different stiffness levels were analyzed for all the depths listed in Table 2 (4, 6, 8, 10, 12, 14 and 16 m). Table 3 shows the mechanical properties of the selected soft layer material options next to their description or classification according to the different codes.

TABLE 3.
Soft layer material properties and classifications

C_s (m/s)	E (MPa)	NCSP-07	EC-8	ASCE 7
100	55	IV Soft cohesive soil	D Loose to medium cohesionless soil	E Soft Clay soil
300	500	III Average compactness	C Dense sand	D Stiff soil
575	1800	II Fracture rock	B Very dense sand	C Very dense soil

3. RESULTS AND DISCUSSIONS

3.1. Simplified foundation model

The dynamic behavior of the simplified foundation models, as influenced by various parameters, was analyzed. Subsequently, complete models were constructed based on these findings.

3.1.1. Finite element size

Before considering the influence of element size, the effect of the meshing technique (i.e., pattern) on the results was analyzed. To this end, the displacement response at the center of the bottom face of the pile cap—when subjected to a short pulse (10 ms and 10 MPa)—was compared in the smallest foundation model variant (19.5 × 19.5 × 23.5) using two different mesh configurations. The first one – uniform mesh – had elements of similar dimensions throughout the domain (50 cm); the second one – locally refined mesh – had elements that increased in size in the soil when moving away from the foundation, from 50 cm at the interface with the foundation to 250 cm in the model outer contour. Figure 10 shows a comparison of these two meshing alternatives.

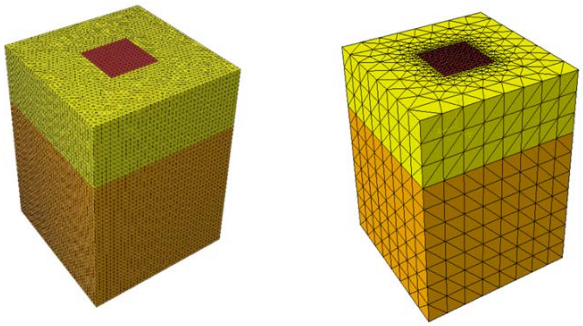

a) Uniform mesh b) Locally refined mesh

Figure 10. Meshing technique comparison: uniform mesh (a) and locally refined mesh (b).

As shown in Figure 11, both meshing techniques yielded similar results. Therefore, the foundation dynamic behavior appeared to be insensitive to the meshing technique for this particular application. The mesh sizes and seeding techniques explored did not have a meaningful impact on the response of interest. The results obtained were effectively the same both for the uniform mesh model (Figure 10 a) and the locally refined mesh (Figure 10 b). Therefore, the locally refined mesh was chosen to minimize computational cost.

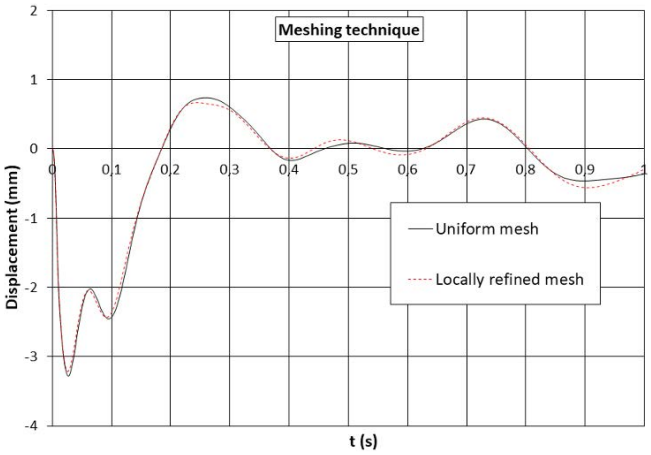

Figure. 11. Results of the comparison of different mesh techniques in the simplified foundation model.

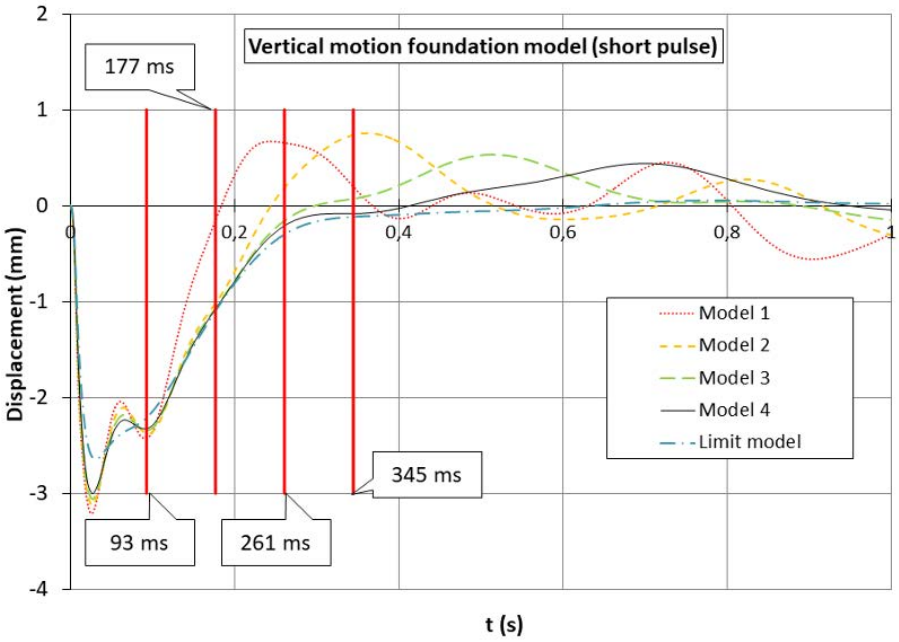

Figure 12. Terrain size response comparison under a 10 ms pulse (short pulse).

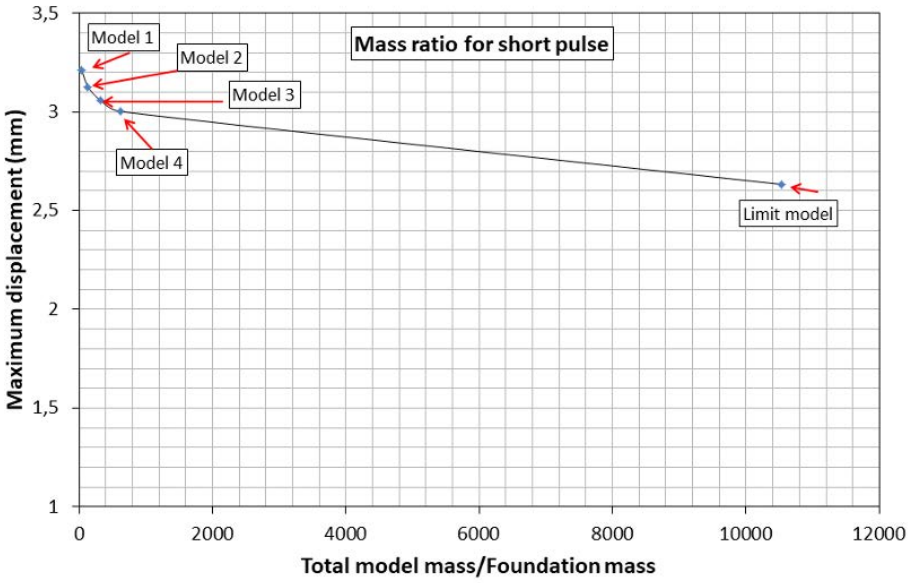

Figure 13. Maximum vertical displacements in the footing center for different total mass to footing mass ratios (short pulse).

Using the locally refined mesh technique, three element sizes were tested in the foundation, pile cap and piles: 30 cm, 40 cm and 50 cm, obtaining the following maximum displacement results (Table 4). The seeding on the soil outer boundary was kept at 250 cm across all models.

TABLE 4.
Maximum displacement for different element sizes

Element size (cm)	Maximum displacement (mm)
30	3.226
40	3.203
50	3.180

Similarly, for the locally refined models, the mesh refinement in the foundation, which ranged between 30 and 50 cm, did not affect the measured response either (Table 4). Consequently, a refined mesh of 50 cm in the interface was selected for the following studies with simplified foundations.

3.1.2. Influence of pulse duration and the amount of soil included

The response to a pulse of 10 ms (i.e., short pulse) was studied in the four models where the pile cap was surrounded by one, two, three or four times its dimension in soil (Table 1). In addition, a much larger model (162.5 x 162.5 x 95) was studied (Limit model). The vertical motion at the center of the bottom face of the pile cap is represented in Figure 12.

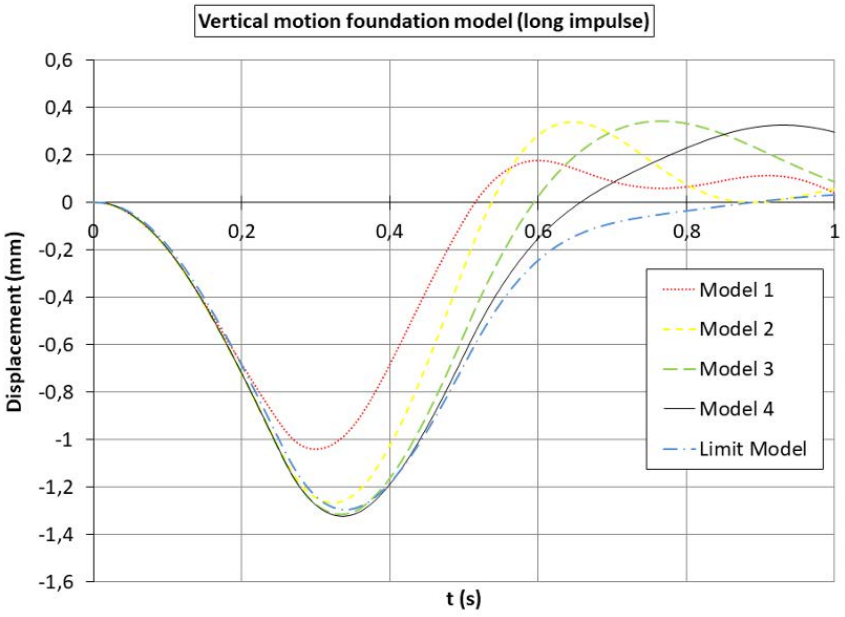

Figure. 14. Terrain size response comparison under a 500 ms pulse (long pulse).

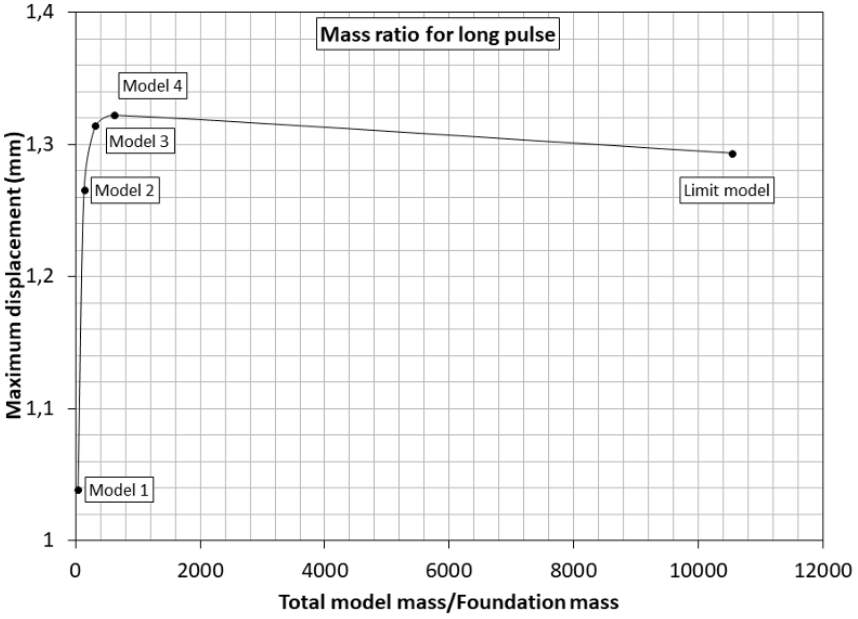

Figure 15. Maximum vertical displacements in the footing center for different total mass to footing mass ratios (long pulse).

¡A sudden settlement in the pile cap was observed immediately after the pulse, with a peak value that was very similar across models and that occurred approximately at 30 ms. After this first settlement, there was a high frequency oscillation that could not be due to the reflection of waves in the boundary since it occurred at the same time in all models. If it were due to the boundary wave reflection, the oscillation would be delayed by the increasing distance to the boundary.

In addition, the curves in Figure 12 diverged from the Limit model solution when the wave front, which had reached the boundary and bounced back, returned to the pile cap (93 ms, 177 ms, 261 ms, 345 ms). This high frequency oscillation that occurred at around 60 ms was indeed associated with the longitudinal vibration that occurs in the piles themselves. This can be proven by increasing the mass of the piles making the phenomenon disappear (not shown in this research).

Figure 13 shows the maximum vertical displacement in the center of the footing against the ratio between the total model mass and the foundation mass. The solution converged with mass ratios over 600. This result was higher than the previous data obtained in shallow foundation models [20], where good results were obtained with a mass ratio in the order of 100. This showed a relevant difference between shallow foundations and deep foundations for a short pulse.

It is important to highlight that the excitation trains actually produce on the foundations of structures has a lower frequency content than the one analyzed so far. For this reason, the previous analysis was reproduced with a longer duration

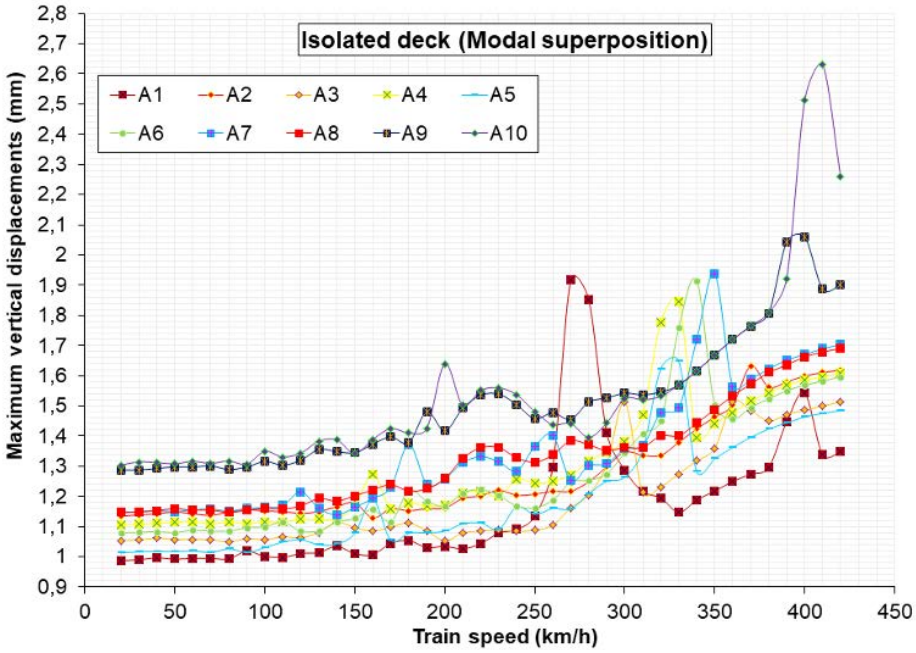

Figure. 16. Maximum vertical displacements in the isolated deck model (100 modes).

pulse – 500 ms – and a lower pressure – 20 KPa. Figure 14 shows the results under this new loading condition where more coincidences were observed.

Figure 15 shows the peak response against the ratio of the masses included in the model for long pulse analysis. It was observed that the mass required to be included in the model was significantly smaller than that required for short pulse analysis. In fact, the difference in results between Model 2 (32.5 x 32.5 x 30 m) and Model 4 (162.5 x 162.5 x 95 m) was only 2.17%, with the second model mass being only 130 times the mass of the foundation. Nevertheless, based on the aforementioned analysis, it was still necessary to include more soil in the deep foundation models than it was in the shallow foundation models, which only required a 20 total mass to foundation mass ratio under lower frequency excitation [20]. For longer pulses, (i.e., those that characterize the loading on high-speed railway bridge foundations), results were less sensitive to the amount of soil included, requiring as little as 100 times the mass of the foundation (Figure 15).

3.2. Bridge model

3.2.1. Isolated deck

The objective of this analysis was to evaluate the impact factor with traditional boundary conditions. These results were used as a benchmark to be compared against results of models where the soil substructure was included in order to understand its influence on the impact factor. Importantly, the impact factor definition used in this paper does not follow that specified in some standards such as the IAPF [10]. In those standards, the normalizing static load produces higher deformations and consequently lower impact factors. Figure 16 represents the recorded maximum displacement of the depicted node in Section 2.2.1 in 10 km/h speed increments for every HSLM train history load.

Modal superposition was used to obtain these results. The first 100 modes were used and captured 90.24% of the mass participation ratio associated to the vertical degrees of freedom. Results did not show any appreciable response amplification until 270 km/h were reached in the A1 train. This matched the bridge first resonance speed for A1 trains: 272.23 km/h. The resonance speed was obtained by multiplying the mode frequency by the distance between bogies of a particular train [44]. This same behavior also occurred with the other trains at higher speeds. In particular, the A10 train doubled its static response at 410 km/h. Proença et al. (2011) explored the effect of the type of track on the dynamic behavior of a high-speed railway bridge with 4 spans, also obtaining the maximum displacement for the A10 train.

Additionally, it was also shown previously [20] that these types of structures are well represented using the first few modes with the superposition method. More specifically, only a 0.228% difference was measured when comparing the superposition solution to that of a fully integrated model with the Newmark method (Impact factor - modal superposition = 2.011 vs. Impact factor - direct integration = 2.016).

3.2.2. Complete model of the railway bridge

Modal superposition should be used when considering the computational cost associated with performing an analysis in a model that includes piers, abutments, soil, and deep foundations using direct integration methods is unreasonable due to the number of analyses that need to be performed (i.e., multiple trains at multiple speeds).

3.2.2.1. Analysis with the number of modes included in the modal superposition

A sensitivity analysis of the number of modes included in the modal superposition was performed considering 100, 200, 300, 400 and 500 modes. As the number of modes increased,

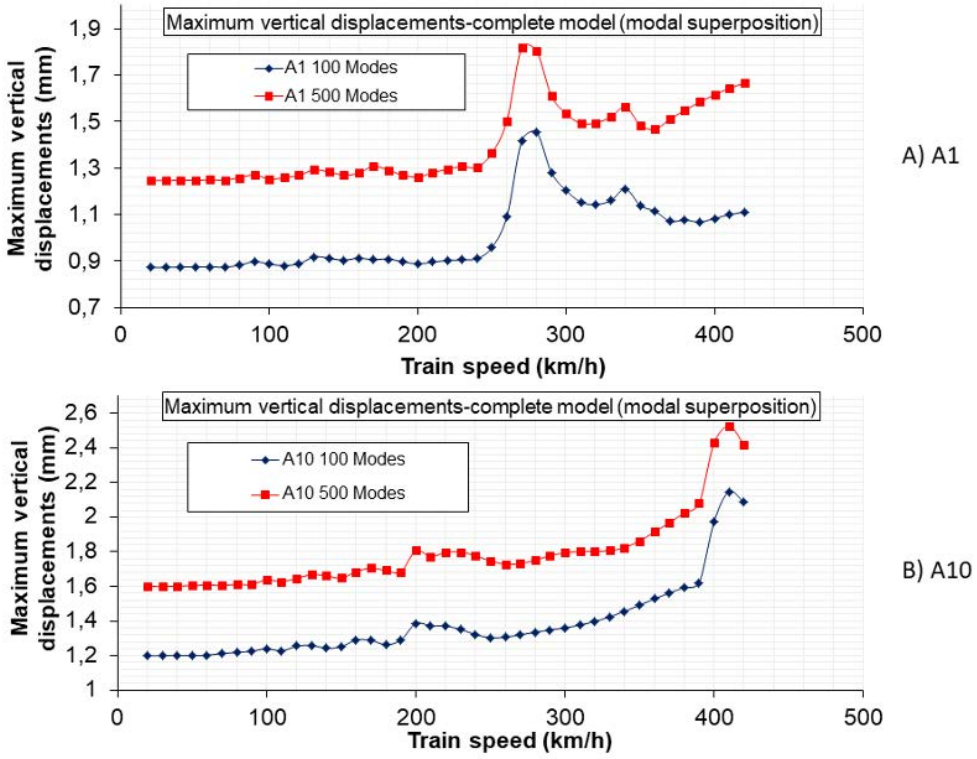

Figure 17. Maximum vertical displacements in the complete model (100-mode and 50-mode solutions for A1 and A10 trains).

the recorded maximum deflections also rose. Nevertheless, all the responses grew approximately proportionally across trains and speeds.

Figure 17 shows maximum displacement results obtained in models in which a 10 m soft layer of soil (C_s = 100 m/s) rests over a harder terrain (C_s = 750 m/s) for the A1 and A10 trains in the HSLM [9,10]. Maximum displacements for all the trains covered in the HSLM were computed but only A1 and A10 are represented for better readability of the results. As shown in Figure 17, the worst train-speed combination (A10 at 410 km/h) appeared to be independent of the number of modes included in the superposition analysis. The A10 train always exhibited a resonance at 410 km/h with a peak value that exceeded the maximum displacement for the A1 train and any other train in the HSLM at any speed, regardless of the number of modes included.

The maximum displacement increased with the number of modes included in the modal superposition solution without any sign of convergence, as observed in Figure 17. Consequently, the worst train-speed combination was rerun using direct integration to obtain accurate results. Given the results presented, it was decided to run the analysis sweeps in speeds and trains using modal superposition with 500 modes followed by a direct integration analysis of the worst-case model: the one with the train-speed combination that produced the highest displacements.

3.2.2.2. Soil stiffness sensitivity analysis

Figure 18 summarizes, for the train-speed combinations that produced the greatest displacements, the maximum vertical displacement for different soft layer material properties and depths. The maximum displacement for the isolated deck is also included for comparison. Please note that these are results obtained using direct integration in the worst cases identified through modal superposition.

When considering the effects of the soft layer material stiffness and depth (Figure 18) on the maximum displacement results, the response appeared to be insensitive to the depth of this superficial softer material layer but not to its stiffness. For the range of depths of soft material analyzed – 4 to 16 m – there was not a meaningful variation in the maximum displacement for a given layer stiffness, with all the results within 4% for each stiffness. However, the stiffness of this superficial layer played an important role in the final results, with higher maximum deflections when higher stiffness properties were used. This was the opposite of the effect on the static solution.

The train-speed combinations that produced the greatest displacements were 380, 390 and 410 km/h for A10 and A2 trains according to the HSLM classification used (Figure 18) [8]. The lack of trend in the speeds and type of train that produced the worst responses highlights the importance of exploring all types of trains used in the research and a wide range of speeds. Figure 19 shows, for the train-speed combinations that produced the greatest displacements, the maximum impact factor (Φ) for different soft layer material properties and depths. The impact factor for the isolated deck is also included for comparison.

When the results were analyzed in terms of the impact factor (Figure 19), which assesses dynamic amplification, the following was observed: response amplification depended very little on the soft layer depth but increased with its stiffness. This helps to understand why maximum displacement

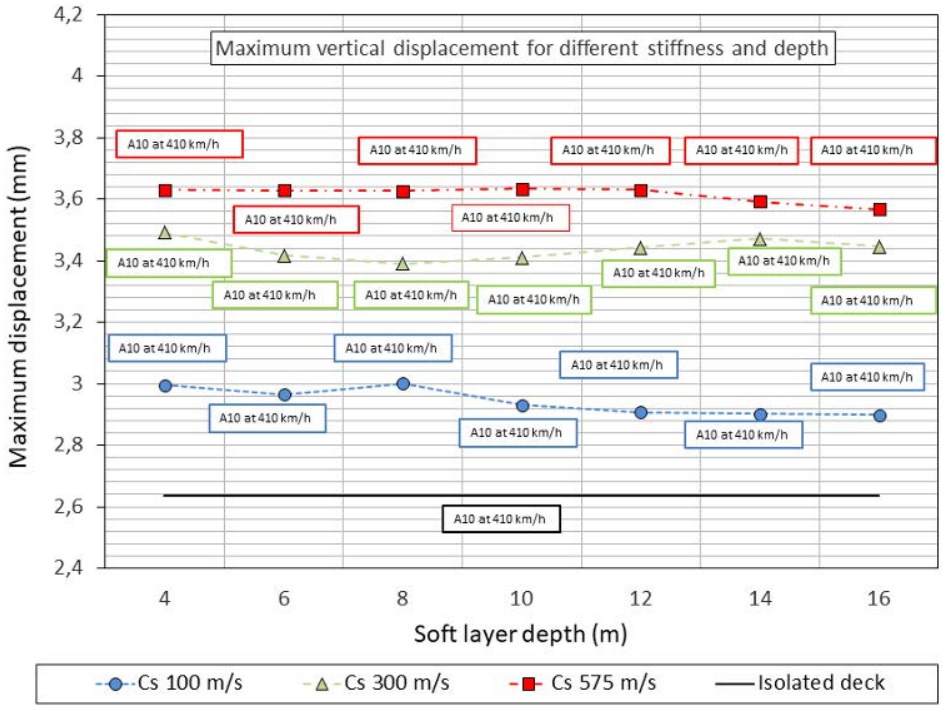

Figure 18. Maximum vertical displacements for different soft layer material stiffness and depth.

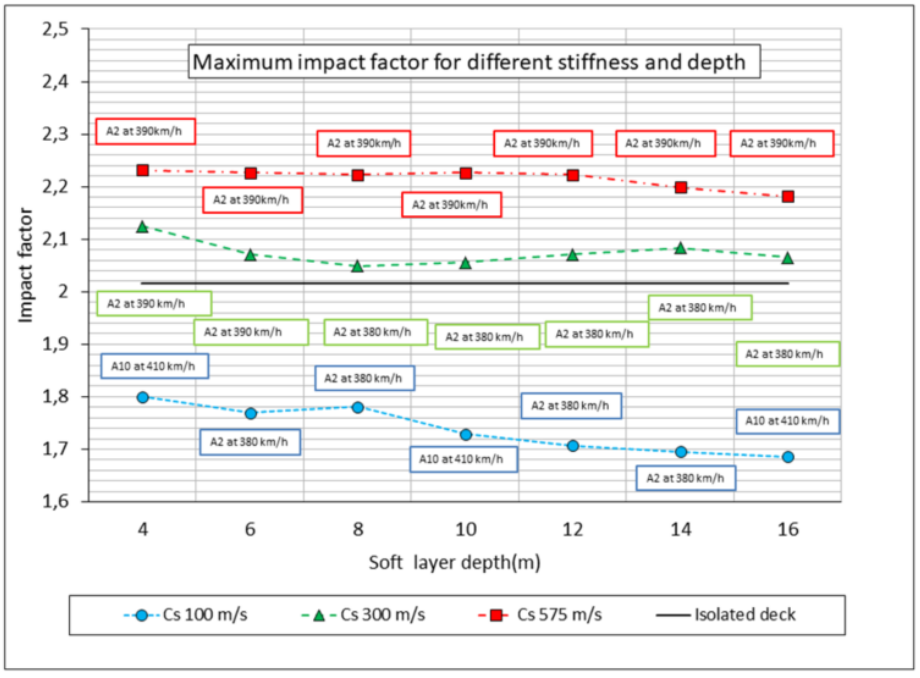

Figure 19. Maximum impact factor for different soft layer material stiffness and depth.

grows with soil stiffness. Even though a stiffer superficial layer slightly decreased the static deflection, the effect of stiffness on the impact factor coefficient was so important that it dominated the resulting dynamic maximum deflections.

When comparing these results with the benchmark – results of the isolated deck model – the maximum displacements of the isolated deck were even lower than the softer soft layer models. The impact factor coefficient lies somewhere between the different stiffness levels used for the soft layer. In other words, the isolated deck did not follow the trend defined by the stiffness of the soft layer material. To understand this, please note that, for an infinitely stiff soft layer material, the model analyzed would still include deformable piers and abutments. This conclusion could also be reached using stiffer soil models, but those models would not be realistic because they would not require deep foundations. This highlights the importance of including not only the surrounding terrain but also the main infrastructure (i.e., piers and abutments) in the model.

4. CONCLUSIONS

The aim of the manuscript was to compare the results of the dynamic impact coefficient of a model without any infrastructure (i.e., isolated deck) with those of a model that included infrastructure (i.e., complete model). The research was conducted using the finite element method. First, the effect of model parameters (i.e., element size, pulse duration and volume of soil included in the model) was studied in a simplified foundation model.

Based on the results, some complete models were built with different variables: soil stiffness and depth, depth of the piles and a speed sweep from 20 km/h to 420 km/h, using 10 trains with different wheelbases and loads per axle. The following conclusions can be drawn from the simplified foundation models:

1. In this study, mesh sizes and seeding techniques did not have a meaningful impact on the response. Results showed convergence with a finite element size of 50 cm, regardless of the type of mesh used.
2. For a short pulse, associated to higher frequency events, significant differences were observed in the maximum displacements with the amount of soil included. In this case, a mass ratio of about 600 is recommended between total model mass and foundation mass.
3. For longer pulses, such as those that characterize the loading on high-speed railway bridge foundations, results were less sensitive to the amount of soil included. A total mass/foundation mass ratio of 100 was enough.
4. We found a relevant difference between shallow foundations and deep foundations.

In addition, the following conclusions can be drawn from the bridge models:

1. There were no differences (regarding the impact factor) between using modal superposition or direct integration for an isolated deck (Impact factor – modal superposition = 2.011 vs. Impact factor – direct integration = 2.016)
2. The sensitivity analysis to the number of modes included in the modal superposition for the complete model indicated that, as the number of modes increased, the recorded maximum deflections also rose.
3. To be more efficient (i.e., reduce computational cost), it is recommended to run the analysis sweeps in speeds and trains using modal superposition with 500 modes followed by a direct integration analysis of the worst case model (which produces the highest displacements).
4. The maximum displacement results were insensitive to the depth of the superficial softer material considered in the complete model.
5. The changes in the maximum displacement with the stiffness of the superficial layer played an important role in the final results. With the highest stiffness for this superficial layer (E=1800 MPa), the maximum displacement was 27.28% higher than in the isolated deck.
6. The dynamic response amplification (i.e., impact factor) depended very little on the soft layer depth but increased with its stiffness.
7. The isolated deck did not follow the trend defined by the stiffness of the soft material. To understand this, please note how, with an infinitely stiff soft layer material, the analyzed model would still include deformable piers and abutments.
8. The previous conclusion highlights the importance of including not only the surrounding terrain but also the main substructure (i.e., piers and abutments) in the model.

Declaration of competing interest

The authors declare that they have no known competing financial interests or personal relationships that could have influenced the study reported in this paper.

Acknowledgments

The authors would like to acknowledge the financial support provided for this research by the Spanish Ministry of THE Economy and Competitiveness within the framework of project PID2023-147971OB-C32. D. Suescum-Morales would also like to acknowledge the financial support from the Spanish Ministry of Education (http://www.mecd.gob.es/educacion-mecd/) through grant FPU 17/04329.

References

[1] G. Diana, Dynamic interaction of railway systems with large bridges, Vehicle System Dynamics 18 (1989) 71–106. https://doi.org/10.1080/00423118908968915.

[2] Ladislav. Frýba, Vibration of solids and structures under moving loads, Springer Netherlands, 1999.

[3] M. Klasztorny, Vertical vibrations of a multi-span beam steel bridge induced by a superfast passenger train, Structural Engineering and Mechanics 12 (2001) 267–281. https://doi.org/10.12989/sem.2001.12.3.267.

[4] H. Xia, N. Zhang, G. De Roeck, Dynamic analysis of high speed railway bridge under articulated trains, 81 (2003) 2467–2478. https://doi.org/10.1016/S0045-7949(03)00309-2.

[5] M. Shamsi, A. Ghanbari, Nonlinear dynamic analysis of Qom Monorail Bridge considering Soil-Pile-Bridge-Train Interaction, Transportation Geotechnics 22 (2020) 100309. https://doi.org/10.1016/j.trgeo.2019.100309.

[6] J. Shen-Haw, Resonance characteristics of high-speed trains passing simply supported bridges, J Sound Vib 267 (2003) 1127–41.

[7] C. Johansson, C. Pacoste, R. Karoumi, Closed-form solution for the mode superposition analysis of the vibration in multi-span beam bridges caused by concentrated moving loads, Comput Struct 119 (2013) 85–94. https://doi.org/10.1016/j.compstruc.2013.01.003.

[8] ERRI D214, Rail bridges for speeds > 200 Km/h. Final report. Part A: Synthesis of the results od D214 research, European Rail Research Institute, 1999.

[9] E. 1998-1 CEN, Eurocode 1: Actions on Structures-Part 2 : Traffic Loads on Bridges, (2003).

[10] Ministerio de Fomento, Code for actions for the Design of Railway Bridges, (2010).

[11] C. Svedholm, Efficient Modelling Techniques for Vibration Analyses of Railway Bridges, (2017) 1–90.

[12] C. Johansson, N.Á.N. Nualláin, C. Pacoste, A. Andersson, A methodology for the preliminary assessment of existing railway bridges for high-speed traffic, Eng Struct 58 (2014) 25–35. https://doi.org/10.1016/j.engstruct.2013.10.011.

[13] J.M. Goicolea, F. Gabaldón, F. Riquelme, Design Issues for Dynamics of High Speed Railway Bridges, Dynamics of High-Speed Railway Bridges (2005).

[14] M. Majka, M. Hartnett, Effects of speed, load and damping on the dynamic response of railway bridges and vehicles, Comput Struct 86 (2008) 556–572. https://doi.org/10.1016/j.compstruc.2007.05.002.

[15] S.G.M. Neves, A direct method for analyzing the vertical vehicle-structure interaction, Eng Struct 34 (2012) 414–420. https://doi.org/10.1016/j.engstruct.2011.10.010.

[16] K. Knothe, S.L. Grassie, Modelling of Railway Track and Vehicle/Track Interaction at High Frequencies, 1993. https://doi.org/10.1080/00423119308969027.

[17] E.Esmailzadeh, Vehicle–passenger–structure interaction of uniform bridges traversed by moving vehicles, J Sound Vib 260(4) (2003) 611–635.

[18] Y.B.Q.P. Hongye Gou; Chang Liu; Hui Hua, Mapping relationship between dynamic responses of high-speed trains and additional bridge deformations, (2020). https://doi.org/https://doi.org/10.1177/1077546320936899.

[19] M. Szafrański, A dynamic vehicle-bridge model based on the modal identification results of an existing EN57 train and bridge spans with non-ballasted tracks, Mech Syst Signal Process 146 (2021). https://doi.org/10.1016/j.ymssp.2020.107039.

[20] A. Martínez-De la Concha, H. Cifuentes, F. Medina, A Finite Element Methodology to Study Soil–Structure Interaction in High-Speed Railway Bridges, J Comput Nonlinear Dyn 13 (2018) 031010. https://doi.org/10.1115/1.4038819.

[21] H. Li, Z. Yu, J. Mao, L. Jiang, Nonlinear random seismic analysis of 3D high-speed railway track-bridge system based on OpenSEES, Structures 24 (2020) 87–98. https://doi.org/10.1016/j.istruc.2020.01.003.

[22] A. Zangeneh, A. Andersson, C. Pacoste, Identification of soil-structure interaction effect in a portal frame railway bridge through full-scale dynamic testing, 159 (2018) 299–309. https://doi.org/10.1016/j.engstruct.2018.01.014.

[23] B. Takemiya, Shinkansen high-speed train induced ground vibrations in view of viaduct–ground interaction, Soil Dynamics and Earthquake Engineering 27(6) (2007) 506–20.

[24] M. Ülker-Kaustell, R. Karoumi, C. Pacoste, Simplified analysis of the dynamic soil-structure interaction of a portal frame railway bridge, Eng Struct 32 (2010) 3692–3698. https://doi.org/10.1016/j.engstruct.2010.08.013.

[25] J. Vega, A. Fraile, E. Alarcon, L. Hermanns, Dynamic response of underpasses for high-speed train lines, J Sound Vib 331 (2012) 5125–5140. https://doi.org/10.1016/j.jsv.2012.07.005.

[26] A. Zangeneh, C. Svedholm, A. Andersson, C. Pacoste, R. Karoumi, Dynamic Stiffness Identification of Portal Frame Bridge – Soil System using Controlled Dynamic Testing, Procedia Eng 199 (2017) 1062–1067. https://doi.org/10.1016/j.proeng.2017.09.293.

[27] A. Romero, M. Solís, J. Domínguez, P. Galvín, Soil-structure interaction in resonant railway bridges, Soil Dynamics and Earthquake Engineering 47 (2013) 108–116. https://doi.org/10.1016/j.soildyn.2012.07.014.

[28] A. Doménech, M.D. Martínez-Rodrigo, A. Romero, P. Galvín, Soil–structure interaction effects on the resonant response of railway bridges under high-speed traffic, International Journal of Rail Transportation 3 (2015) 201–214. https://doi.org/10.1080/23248378.2015.1076621.

[29] J. Domínguez, J. Roesset, Dynamic stiffness of rectangular foundations, MIT Research Report R Cambridge (1978).

[30] S.-H. Kim, M. Shinozuka, Development of fragility curves of bridges retrofitted by column jacketing, Probabilistic Engineering Mechanics 19 (2004) 105–112. https://doi.org/10.1016/j.probengmech.2003.11.009.

[31] J.-W. Lin, C.-W. Chen, S.-H. Chung, Modeling and assessment of bridge structure for seismic hazard prevention, Natural Hazards 61 (2011) 1115–1126. https://doi.org/10.1007/s11069-011-9969-3.

[32] K.-J. Bathe, Finite Element Procedures, Prentice Hall, 1996.

[33] A. Martínez-de la Concha, J.D. Ríos, H. Cifuentes, Numerical Study of the Shear Behavior of Ultra-High-Performance Concrete Beams, Hormigon y Acero 75 (2024) 157–162. https://doi.org/10.33586/hya.2023.3119.

[34] L. Cañizo, B. Escario, C. Faraco, L. Fort, J.A. Jiménez Salas, J.L. Justo Alpañés, M. Llorens, C. Lorente de No, R. Marsal, R. Molina, F. Muzas, C. Oteo, J.M. Rodríguez Ortiz, M. Romana, A. Serrano, A. Soriano, A. Uriel, S. Uriel, Geotecnia y cimientos, Servicio de Publicaciones de alumnos, Madrid, 1970.

[35] Ministerio de Fomento, Norma de Construcción Sismorresistente : Puentes (NCSP-07), (2008).

[36] L. Frýba, Traffic loads on railway bridges, Dynamics of Railway Bridges (1996) 183–198. https://doi.org/10.1680/dorb.34716.0010.

[37] A. Romero, P. Galvín, J. Domínguez, Comportamiento dinámico de viaductos cortos considerando la interacción vehículo-vía-estructura-suelo, Revista Internacional de Metodos Numericos Para Calculo y Diseno En Ingenieria 28 (2012) 55–63. https://doi.org/10.1016/j.rimni.2011.11.004.

[38] M.D. Martínez-Rodrigo, Atenuación de vibraciones resonantes en puentes de ferrocarril de Alta Velocidad mediante amortiguadores fluido-viscosos, (2009). https://doi.org/10.1200/JCO.2009.26.8789.

[39] ADIF, IGP-5 Instructions and recommendations on Spanish Railway Structures, (2011).

[40] Y.B. Yang, H.H. Hung, Wave Propagation for Train-Induced Vibrations, World Scientific, 2009.

[41] Ministerio de Fomento, Norma de Construcción Sismorresistente : Puentes (NCSP-07), (2008).

[42] CEN, EN 1998-1: Eurocode 8 Design of structures for earthquake resistance. Part 1 : General rules, seismic actions and rules for buildings, (2011).

[43] Asce/Sei, Minimum design loads for buildings and other structures, ASCE Standard (2010) 608. https://doi.org/10.1061/9780784412916.

[44] B.H. Kim, J. Lee, D.H. Lee, Extracting modal parameters of high-speed railway bridge using the TDD technique, Mech Syst Signal Process 24 (2010) 707–720. https://doi.org/10.1016/j.ymssp.2009.11.010.

[45] J.M. Proença, H. Casal, M. Neves, Effect of the type of track on the dynamic behaviour of high speed railway brigdes, 3rd International Conference on Computational Methods in Structural Dynamics and Earthquake Engineering: An IACM Special Interest Conference, Programme (2011) 25–28.

Disponible en **www.hormigonyacero.com**
https://doi.org/10.33586/hya.2024.3135

Analytical Approach for Serviceability Assessment of Prestressed Concrete Girders Consisting of a Precast Beam and a Cast-in-place Slab

Enfoque analítico para la evaluación del Estado Límite de Servicio de vigas de hormigón pretensado que constan de una viga prefabricada y una losa hormigonada in situ

Mª Carmen Beteta[a], Luis Albajar[b], Carlos Zanuy[c]

[a] *PhD Structural Engineer at INECO*
[b] *Former Associate Professor, Dept. Continuum Mechanics and Structures, Universidad Politécnica de Madrid, Madrid, Spain*
[c] *Professor, Dept. Continuum Mechanics and Structures, Universidad Politécnica de Madrid, Madrid, Spain*

Recibido el 4 de enero de 2024; revisado el 18 de abril de 2024, aceptado el 18 de abril de 2024

ABSTRACT

This paper is focused on the assessment of the Serviceability Limit State of bridge girder cross-sections consisting of a precast, prestressed concrete beam and a cast-in-place top slab, which will be referred to as composite concrete sections because of the presence of more than one concrete within the section. Various methodologies for non-composite (i.e., with only one concrete within the section) concrete sections have been proposed by different authors to address the issue of stress assessment and crack control, mostly making use of analytical neutralization methods. In the present study, the neutralization method is extended and adapted to composite sections involving two concretes cast at different times. The proposed method is validated by comparison with a direct calculation method and commercial software. Three scenarios have been analyzed in the paper: midspan sections subjected to positive bending with cracking of the precast beam, sections at support regions of bridge girders subjected to negative bending in which the top slab is uncracked under permanent loads but undergoes cracking with the application of live loads, and sections at support regions in which the top slab is already cracked under permanent loads. Additionally, worked examples from real projects are provided.

KEYWORDS: prestressed concrete bridges, staged construction, cracking, composite sections, neutralization method.

RESUMEN

Este artículo se centra en la evaluación del Estado Límite de Servicio de secciones de puentes, consistentes en una viga prefabricada pretensada y una losa hormigonada in situ, que se denominarán secciones compuestas por la presencia de más de un hormigón en la sección. Diferentes autores han propuesto distintas metodologías para secciones homogéneas formadas por un solo hormigón, para abordar el cálculo de tensiones y el control de fisuras en su mayoría mediante el empleo de métodos analíticos basados en la neutralización. En el presente estudio, el método de neutralización se amplia y se adapta a secciones compuestas formadas por dos hormigones, hormigonados a diferentes edades. El método propuesto se valida mediante comparación con un método de cálculo directo y con el uso de un programa de cálculo comercial. Se han analizado tres escenarios: secciones de centro de vano sometidas a un momento flector positivo con fisuración de la viga prefabricada, secciones de apoyo sometidas a momento flector negativo donde la losa superior se fisura bajo la acción de la sobrecarga de uso, pero permanece comprimida bajo la acción de las cargas permanentes y secciones de apoyo donde la losa superior ya está fisurada bajo la acción de las cargas permanentes. Además, se añaden ejemplos de puentes de proyectos reales.

PALABRAS CLAVE: puentes de hormigón pretensado, construcción evolutiva o por fases, fisuración, secciones compuestas, método de neutralización.

* Persona de contacto / *Corresponding author*:
Correo-e / *e-mail*: maria.beteta@ineco.com (María Beteta)

Cómo citar este artículo: Beteta, M.C., Albajar, L., & Zanuy, C. (2025). Analytical Approach for Serviceability Assessment of Prestressed Concrete Girders Consisting of a Precast Beam and a Cast-in-place Slab. *Hormigón y Acero*. 76(306):47-63. https://doi.org/10.33586/hya.2024.3135

NOTATION

A Area of the cross section.
$A_{c,eff}$ Effective area of concrete in tension surrounding the reinforcement or prestressing tendons.
As_i Area of reinforcement steel of the layer i of reinforcement of the section.
Ap_i Area of prestressing steel of the layer i of prestressing of the section.
$B(x)$ First moment of inertia of the cracked transformed composite section at infinite time in relation to the fiber x of the cracked section.
$b(y)$ Width of the section.
$E_{cb}(t_\infty)$ Instantaneous Modulus of Elasticity of the concrete of the beam at end of time.
E_c Instantaneous Modulus of Elasticity of the concrete.
E_s Modulus of Elasticity of the reinforcement steel.
$I(x)$ Second moment of inertia of the cracked transformed composite section at infinite time in relation to the fiber x of the cracked section.
PN Neutralization Force.
c.o.g Center of gravity.
d_{pi} Distance from the layer "i" of prestressing steel to the top fiber of the section.
d_{si} Distance from the layer "i" of reinforcement steel to the top fiber of the section.
e Eccentricity of the neutralization force with respect to the center of gravity of the section.
e' Eccentricity of the neutralization force with respect to the center of gravity of the prestressing reinforcement of the beam.
e'' Eccentricity of the neutralization force with respect to the center of gravity of the prestressing reinforcement of the slab.
f_{ck} Compressive strength in the concrete.
$f_{ct,eff}$ Mean value of the tensile strength of the concrete effective at the time when the cracks may first be expected to occur.
k_1 Coefficient which takes into account of the bonded properties of the bonded reinforcement.
k_2 Coefficient which takes into account the distribution of strain.
k_3, k_4 Coefficients depending of National Annex.
k_t Factor dependent on the duration of the load.
n Relation between Modulus of Elasticity.
s_{rmax} Maximum crack spacing.
x Depth of neutral fiber of the cracked section.
y_g Position of the c.o.g referred to the bottom of the section.
$\Delta\varepsilon_{ci}$ Increase of strain in each fiber of concrete from state under permanent loads to zero stress plane in concrete.
ΔM Increment of bending moment due to live loads with respect to the permanent loads bending moment.
$\Delta\sigma_c$ Increase in stress in the concrete of the beam with respect to the concrete of the slab due to permanent loads at end time.
α_e Ratio between the Modulus of Elasticity of the reinforcement steel and the concrete.
ε_{sm} Mean strain in the reinforcement.
ε_{cm} Mean strain in the concrete between cracks.
ρ_{peff} Ratio between the area of bonded reinforcement and prestressing within Aceff.
σ_{bbct} Bottom beam concrete stress under permanent loads.
σ_{tbct} Top beam concrete stress under permanent loads.
σ_{bsct} Bottom slab concrete stress under permanent loads.
σ_{tsct} Top slab concrete stress under permanent loads.
σ_{ct} Concrete stress under permanent loads.
σ_c Concrete stress under permanent plus live loads.
σ_{pit} Prestressing steel stress under permanent loads.
σ_{sit} Reinforcement steel stress under permanent loads.
σ_{p0} Initial prestressing steel stress.
σ_{pi} Increase of stress in the prestressing steel due to live loads from zero stress plane in concrete.
σ_{si} Increase of stress in the reinforcing steel due to live loads from zero stress plane in concrete.
σ_{piN} Prestressing steel stress due to permanent loads at end time and neutralization forces.
σ_{siN} Reinforcement steel stress due to permanent loads at end time and neutralization forces.

1. INTRODUCTION

Many structural typologies of bridges rely on girder designs consisting of composite concrete sections (i.e., with more than one concrete within the section, typically manufactured at different times) affected by staged construction processes. Efficient structural systems may involve the utilization of precast, prestressed concrete beams and cast-in-place concrete top slabs, which are affected by time-dependent effects of the two concretes leading to progressive redistribution of stresses. The instantaneous effects produced by live loads might also induce cracking, which must be considered at the design stage [1][2] . Though composite sections consisting of a prestressed concrete beam and a reinforced concrete slab built at different times are mostly designed so that concrete stresses under the frequent load combination are lower than the concrete tensile strength to avoid the explicit calculation of crack widths, this assumption does not ensure that the sections remain uncracked under the actuation of eventual overloads or full live loads (i.e., the characteristic combination of loads). In the previous situation, the section might come back to fully compressed state after removal of live loads, but the previous decompression cancels the further ability to carry tensile stresses under new load increments including the frequent load combination. Moreover, partially prestressed composite sections also require crack width estimation in the serviceability verifications. Accordingly, consistent analytical methods to assess stress state and crack control of composite concrete sections are necessary.

Serviceability Limit State (SLS hereafter) of cracking in composite sections consisting of a precast, prestressed concrete beam and a cast-in-place top slab was discussed in the first au-

thor's PhD Thesis [3]as a complement to the main aim of the thesis, which was to develop a simplified method for time-dependent effects in statically indeterminate concrete bridges with connected precast beams with evolutive cross-sections, also detailed in [4]. The necessity of analytical models was discussed and highlighted. The problem of a non-composite (i.e. with only one concrete within the section) prestressed concrete section which is fully compressed under permanent loads but undergoes cracking with the additional application of live loads -partially prestressed concrete section- has been addressed by several authors. Nilson [5] and Dilger *et al.* [6] used approaches based on the neutralization of prestressing stresses. Ghali [7] proposed the neutralization of the stresses produced by permanent loads. Karayannis *et al.* [8] proposed a simplified method mainly for T-sections and completed a parametric study focused on the amount of prestressing to study the crack width. Lee *et al.* [9] suggested a simplified method for the calculation of stress increase in passive reinforcement and performed a parametric study on T and inverted T sections to check that tensile stress of prestressing strands is under 250 MPa due to ACI 318 code [2] formulation.

Cracking of composite sections has been addressed by various authors. Amongst others, Naaman *et al.* [10] firstly solved the composite section without considering time-dependent effects (shrinkage, creep and relaxation) or the variation over time of the concrete modulus of elasticity. In subsequent research, Naaman *et al.* [11] updated the direct method for instantaneous actions with the use of elastic deformations for equilibrium conditions and total deformations (instantaneous and delayed) for compatibility conditions. Despite of the quality of the paper, three drawbacks can be highlighted: compatibility conditions should be extended to total curvatures (elastic and time-dependent), the instantaneous modulus of elasticity of concrete was assumed constant for all periods (neglecting the initial value at time of prestressing, notably lower), and the fact of combining as a single stage the delayed effect of casting the top slab, the application of superimposed loads and the instantaneous effect of the live load that causes cracking, which are clearly different phenomena. Pokharel [12] relied on the general recommendations and assumptions from Naaman *et al.* [11] however without providing details of the calculation steps for the analysis of cracking of the composite section.

The most extended analytical solution so far is based on the neutralization method in order to overcome the inconsistency of applying superposition to load sequences governed by the nonlinearity of concrete cracking: in a first stage, the permanent stress state of the concrete is cancelled with the application of a couple of neutralization sectional forces (an axial force and a bending moment, i.e. an eccentric neutralization axial force); in a subsequent second stage, neutralization forces are applied in opposite direction together with the sectional forces produced by live loads to a composite section in which the concrete does not carry tensile stresses (cracked section analysis). The extension of the neutralization method to composite sections including more than one concrete (typical of bridge girders consisting of a precast beam and a cast-in-place slab, manufactured at different times) is not straightforward. Even though Ghali *et al.* [13] pointed out that the problem can be solved with neutralization forces by cancelling the stresses of the concrete which cracks, the subsequent calculation steps were not described, and no practical examples were provided. In practice, commercial software for the calculation of cracking in prestressed sections formed by one or several layers of concrete are available [14]-[19] but the accuracy of the analysis will depend on the correct definition of assumptions, mechanical properties of materials and loading conditions within the software. Although some software tools do not have a specific function for cracking assessment, detailed structural analysis can be performed to evaluate stresses and strains in composite sections and the occurrence of cracking can be inferred from the calculated stress and strain distribution; however, the introduction of the previous creep and shrinkage of concrete layers is not always obvious.

In the present paper, the neutralization method has been extended and adapted to composite sections consisting of a prestressed concrete beam and a cast-in-place concrete slab [3], i.e. with two concretes cast at different times. A summary of the neutralization method for prestressed concrete sections with one concrete is presented in Section 2 based on [20]. In Section 3, the application to the most relevant cases of bridge girders with two concretes within the section is detailed: mid-span region sections subjected to positive bending moment (cracking of the precast beam), support region sections subjected to negative bending moment in which the top concrete slab is uncracked under permanent loads but cracks due to the application of live loads, and support region sections where the top slab is already cracked under permanent loads. Section 4 is dedicated to validating the proposed method for composite sections. This involves comparing results with direct calculations and commercial software [14]. Section 5 encompasses practical examples derived from real projects. In Section 6, the attention is paid at the influence of the modulus of elasticity of the concrete which can be used for the cracked section analysis (either instantaneous or delayed). Lastly, conclusions are drawn in Section 7 of the paper.

2. BACKGROUND TO THE NEUTRALIZATION METHOD FOR PRESTRESSED CONCRETE SECTIONS

The stress state development of a prestressed concrete section with one concrete and two types of embedded steel layers (reinforcing and prestressing, both perfectly bonded to the concrete), subjected to the subsequent action of permanent and live loads is a common problem in the structural analysis of prestressed concrete girders for serviceability verification. According to design codes, stress state assessment and crack control must be verified for different fractions of the live loads: quasi-permanent, frequent and/or characteristic load combinations [1]. Typically, the section is fully compressed under permanent loads but undergoes cracking at the most tensioned side with the actuation of a fraction of the live loads. The application of the superposition method to add the stresses caused by permanent and live loads is not consistent due to the nonlinearity which arises when concrete cracks. As an alternative to numerical non-linear approaches, the problem can be solved analytically in two stages with the help of the neutralization method [20]. In Figure 1, the stress

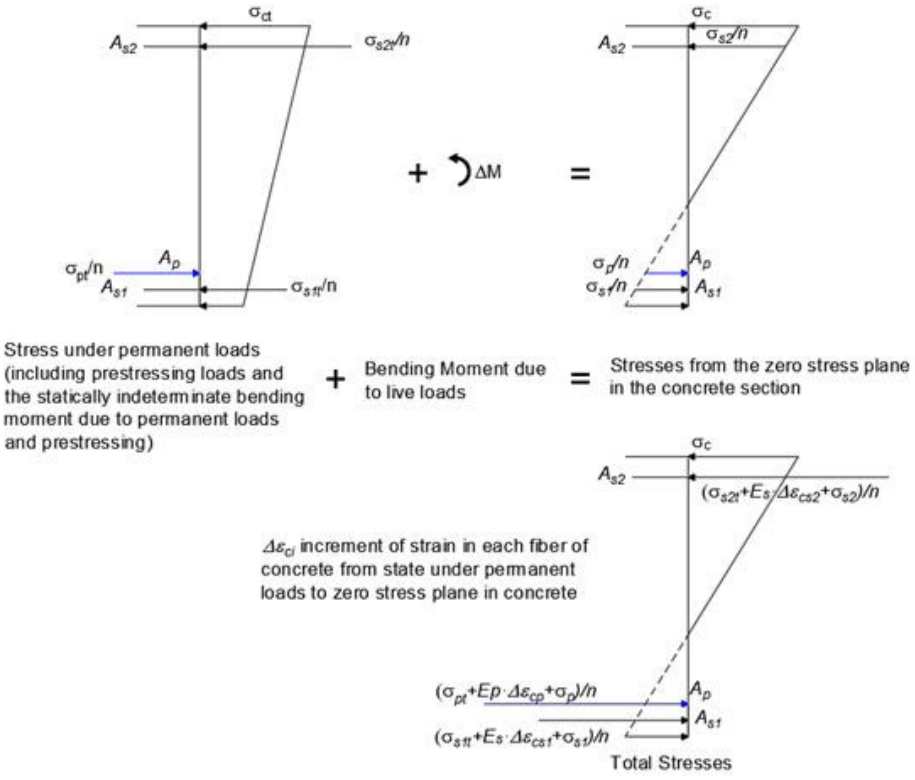

Figure 1. Stress development in a prestressed concrete section from the permanent stress state after the application of live load.

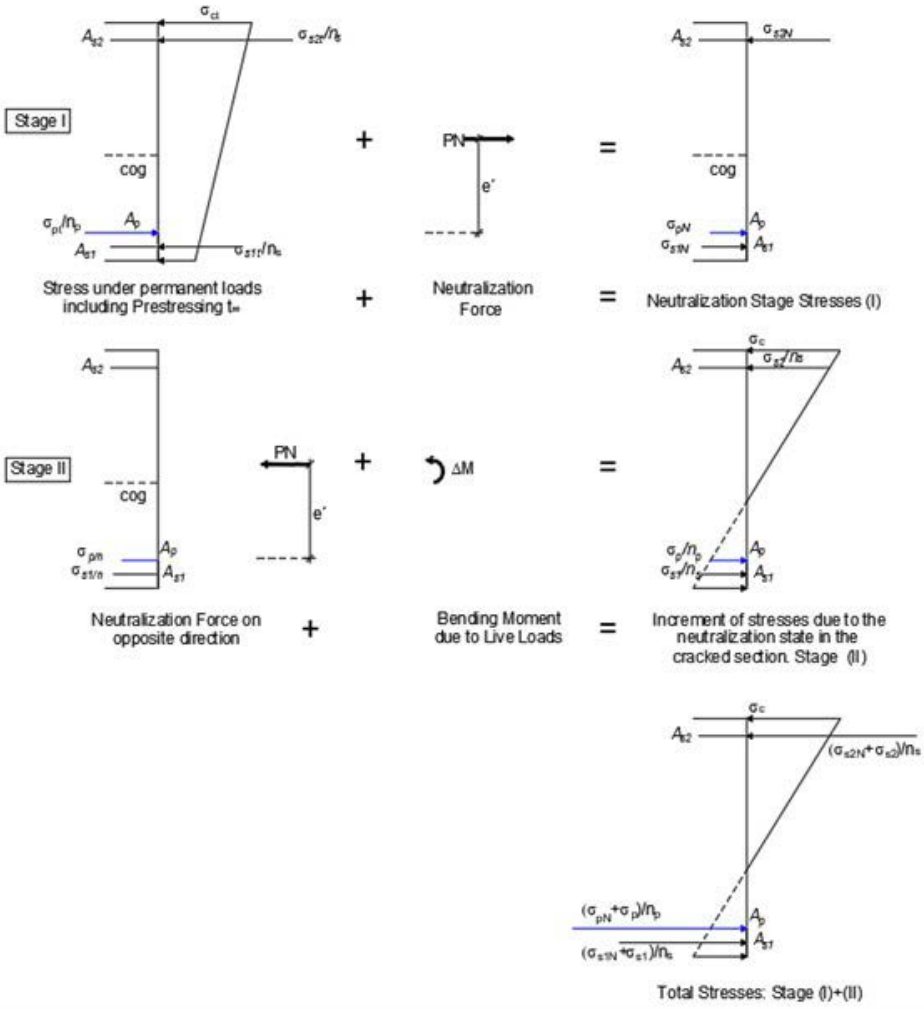

Figure 2. Neutralization method. Decomposition of stresses.

development of the prestressed concrete section is shown. The change of stresses from the uncracked permanent state to the cracked situation under live loads can be addressed with the neutralization method, by the decomposition of the process in two steps (Figure 2.

In the first step (Stage I in Figure 2), the neutralization force PN, applied with an eccentricity e' with respect to the centroid of the prestressing steel, is obtained by cancelling the permanent concrete stresses with use of the transformed section properties: the total area of the section is a result of the concrete area plus the area of each steel layer (Asi and Api) multiplied by the corresponding modular ratio with respect to concrete ($As_i \cdot Es/Ec$ and $Ap_i \cdot Ep/Ec$ respectively). The resulting concrete stresses are zero in the so-called neutralization plane, but not zero in the prestressing and non-prestressing steels, so that they balance the system of forces formed by the permanent loads plus the neutralization force.

In the second step (Stage II in Figure 2), the neutralization force is applied in opposite direction plus the bending moment caused by live loads from the neutralization plane. The solution to Stage II can be obtained with the traditional assumptions of the cracked transformed section: plane sections remain plane, linear elastic behaviour of the steels and the concrete in compression, and concrete cannot carry tensile stresses.

The basis of the method is to cancel concrete stresses in the neutralization state, which allows the stresses of Stages I and II for steel and concrete to be superimposed, since the non-linearity of concrete (which would prevent the addition) is cancelled as the first term of the sum is zero and cracking appears automatically (zero-stress layers) in Stage II. In the case of concrete, as the neutralization stresses from Stage I are zero, the stress increments of Stage II coincide with the final stresses and directly include the non-linear effect of cracking through the zero-stress zone at the bottom of the section. For prestressing and non-prestressing steels, final stresses are the sum of those corresponding to the neutralization Stage I plus those of Stage II. This sum is possible because in service the steels behave elastically without yielding. Stage II can be easily solved as a concrete section with several layers of reinforcement subjected to an axial force and a bending moment (Figure 3).

According to the classical theory, applying sectional equilibrium of axial force and bending moment with respect to the point of zero stresses, referred to as 0 in Figure 3:

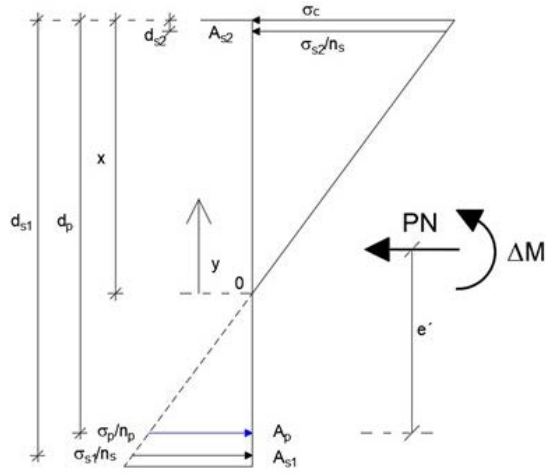

Figure 3. Cracked section analysis from the neutralization state.

$$PN = \frac{\sigma_c}{x}\int_0^x b(y)y\,dy + n\frac{\sigma_c}{x}A_{s2}(x-d_{s2}) - n\frac{\sigma_c}{x}A_{s1}(d_{s1}-x) - n\frac{\sigma_c}{x}A_p(d_p-x) \quad (1)$$

$$\Delta M - PN(d_p - e' - x) = \frac{\sigma_c}{x}\int_0^x b(y)y^2\,dy + n\frac{\sigma_c}{x}A_{s2}(x-d_{s2})^2 - n\frac{\sigma_c}{x}A_{s1}(d_{s1}-x)^2 - n\frac{\sigma_c}{x}A_p(d_p-x)^2 \quad (2)$$

Equations (1) and (2) can be written in a simplified form:

$$PN = B(x)\frac{\sigma_c}{x} \quad (3)$$

$$\Delta M - PN(d_p - e' - x) = I(x)\frac{\sigma_c}{x} \quad (4)$$

where $B(x)$ and $I(x)$, are the first and second moment of inertia of the transformed cracked section with respect to the neutral axis. The former system of equations is general for any section shape with a vertical axis of symmetry and several layers of prestressing and reinforcing steel. It allows obtaining the neutral axis depth (x) and the top concrete stress (σ_c). Hence, by compatibility, the complete distribution of stresses at the section can be derived. It must be noted that the transformed section in Stage I is homogenized to the instantaneous modulus of elasticity of concrete because first cracking takes place due to the action of the frequent or the characteristic combination of loads, which is an instantaneous phenomenon. Moreover, the same modulus of elasticity must be used in the two stages I and II for the sake of consistency in the addition.

3. EXTENSION OF THE NEUTRALIZATION METHOD TO COMPOSITE SECTIONS WITH MORE THAN ONE CONCRETE

In this Section, the neutralization method is extended to composite sections including more than one concrete, which is useful for prestressed concrete girders constructed sequentially. In particular, the attention is paid at the SLS verification of composite sections consisting of a precast, prestressed concrete beam and a reinforced concrete cast-in-place top slab. In practice, there are methods [5][6] to neutralize prestressing stresses which are valid for prestressed sections with only one type of concrete, but they are not generally correct for composite sections. In particular, the attention is paid at sections consisting of a precast, prestressed concrete beam and a top cast-in-place concrete slab. Three different cases are addressed, including sections subjected to positive and negative bending moments:

- Case A: sections at midspan regions of bridge girders subjected to positive bending with cracking of the precast beam.
- Case B: sections at support regions of bridge girders subjected to negative bending in which the top slab is uncracked under permanent loads but undergoes cracking with the application of live loads.
- Case C: sections at support regions of bridge girders subjected to negative bending in which the top slab is already cracked under permanent loads.

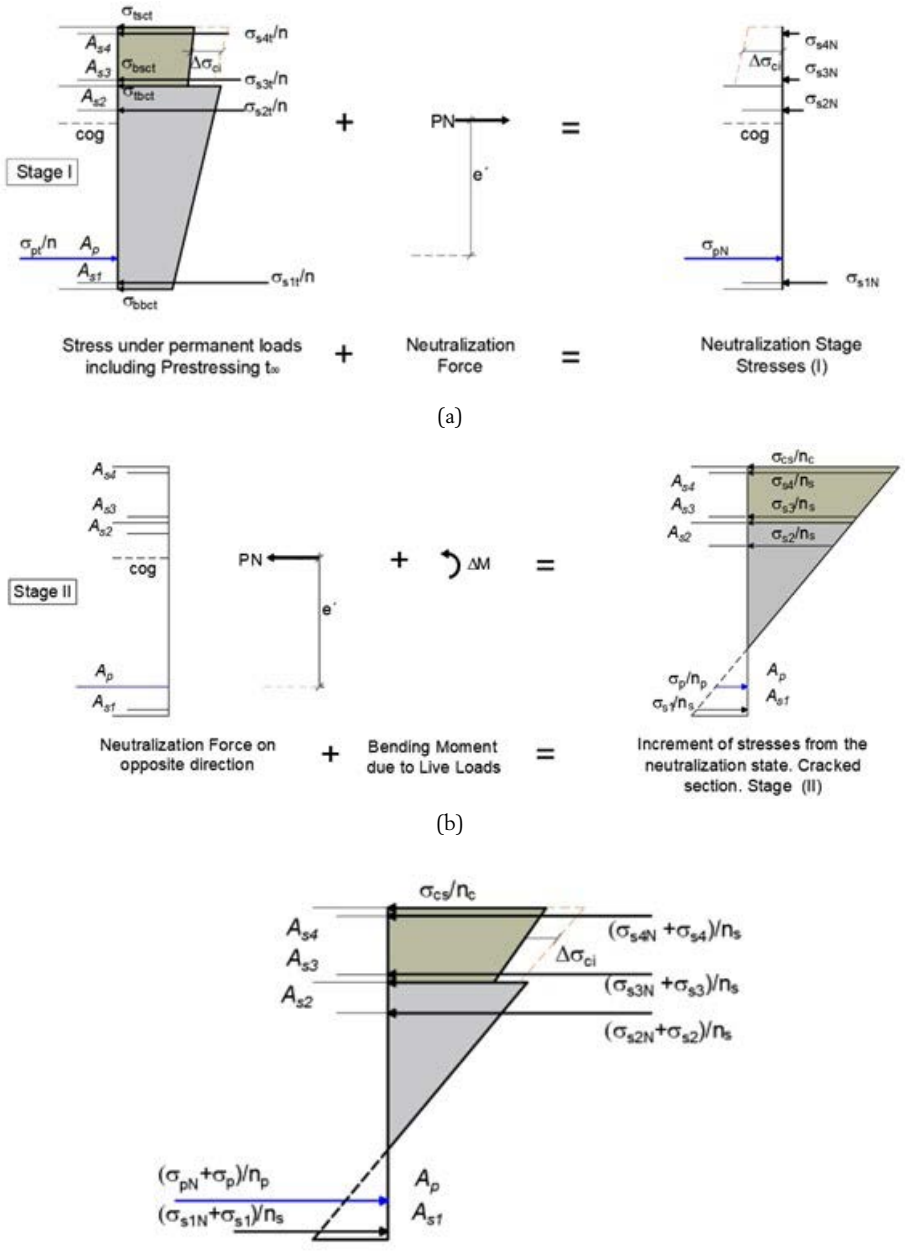

Figure 4. Composite section at midspan regions subjected to positive bending moment with cracking of the precast beam. (a) Stage I: Neutralization of permanent concrete stresses at the precast beam. (b) Stage II: Increment of stresses from neutralization state due to application of neutralization forces in opposite direction and live loads. (c) Total Stresses: Stages I + II.

3.1. *Case A*

In this case, the actuation of positive (sagging) bending moment at midspan regions of bridge girders decisive for cracking at the bottom of the precast prestressed beam under live loads is studied, whereas the top slab remains in compression under all combinations of loads (quasi-permanent, frequent, and characteristic). The application of the neutralization method to obtain the stress change due to the application of live loads can be explained with the help of Figure 4.

Under these conditions, the permanent stress state at end time is a result of permanent loads, including prestressing forces, and time-dependent effects of the two concretes and their interaction [3][4]. Concrete stresses at the top and bottom of the slab are referred to as σ_{tsct} and σ_{bsct}, concrete stresses at the top and bottom of the precast beam are σ_{tbct} and σ_{bbct}, and the non-prestressing and prestressing steel stresses are σ_{sit} and σ_{pt} respectively. From such permanent state, Figure 4a summarizes the process of stress neutralization (Stage I). The neutralization force (PN) and its eccentricity (e') with respect to the centroid of the prestressing layer are obtained in the transformed composite section by cancelling the permanent concrete stresses of the precast beam.

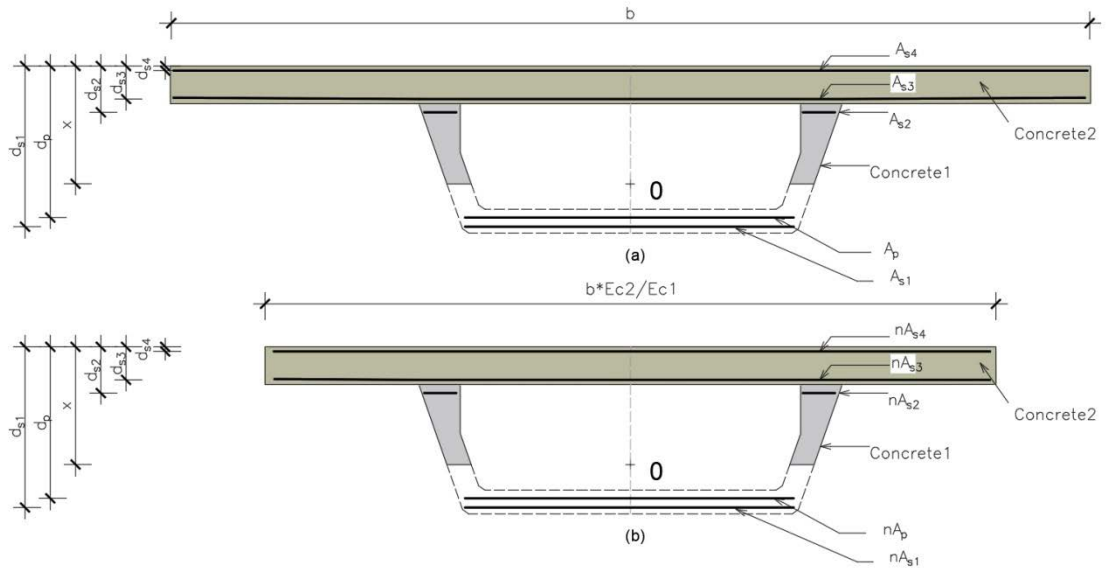

Figure 5. (a) Cracked section (b) Transformed cracked section.

The stresses in prestressing and reinforcing steels obtained in the neutralized state are σ_{piN} and σ_{siN} respectively. Non-zero stresses also result in the concrete of the top slab in the situation of neutralization of stresses. The value of $\Delta\sigma_{ci}$ in Figure 4a is the difference between the concrete stresses at the top slab and those at the precast beam multiplied by their modular ratio. This value is constant for each fiber of the concrete of the slab throughout the process as the process assumes different strain planes (the difference of concrete stresses of the precast beam multiplied by the modular ratio is shown by the dashed orange line in the Figure 4a). In Figure 4b, Stage II of the method is schematized: the neutralization force is applied in opposite direction in addition to the bending moment due to live loads. The properties of the section are those corresponding to a transformed section where the concrete slab is homogenized with its modular ratio with respect to the concrete of the precast beam, (Figure 5).

This stage provides the stress increase from the neutralization plane. At this stage, cracking of the concrete beam occurs. The transformed cracked section method explained in Section 2 for Stage II can be applied, as mentioned above, with the top concrete slab playing a similar role as other layer of prestressing steel (the analogy makes sense, as the initial strain of the prestressing steel, would be analogous to the strain difference which initially exists between the concrete of the top slab and that of the precast beam due to the effect of the self-weight of the top slab on the beam while the concrete of the top slab hardens, as well as other initial strains of the precast beam). Figure 6 shows the stresses in the cracked transformed section in Stage II. The calculation of the neutral axis depth, (x in Figure 6) is carried out by applying the equilibrium, Equations (3) and (4). In this case, $B(x)$ and $I(x)$ are the first and second moment of inertia of the cracked transformed section with respect to the neutral axis and sc is the concrete stress at the top slab divided by n_c –ratio of E_i of both concretes–, and d_p and x are measured from the top of the slab.

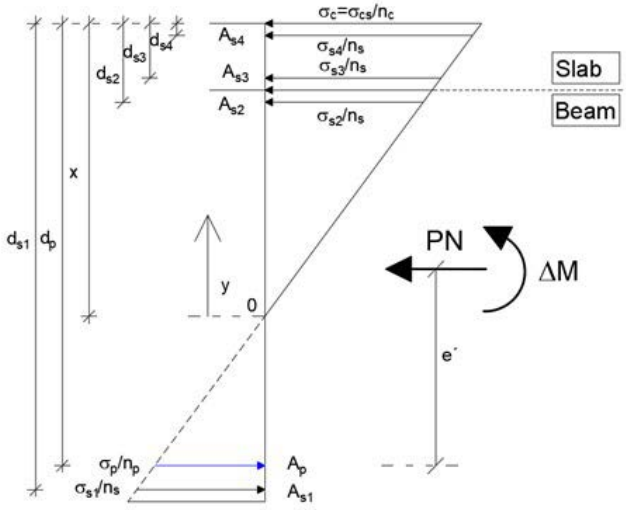

Figure 6. Stage II for Case A. Cracked section analysis.

The final total stresses (Figure 4c) are those of Stage II for the concrete of the precast beam (zero stresses in the neutralization process), while the stresses for the concrete of the top slab, the reinforcing and prestressing steels are the sum of the stresses of Stages I and II. The method is valid because the reinforcing and prestressing steels behave linear-elastically, as well as the concrete of the top slab as long as it is always compressed.

3.2. Case B

A composite section subjected to negative bending in which the top slab is uncracked under permanent loads is studied here. Such a situation might occur when the top slab is prestressed, though such sections are usually oversized, and cracking does not occur normally.

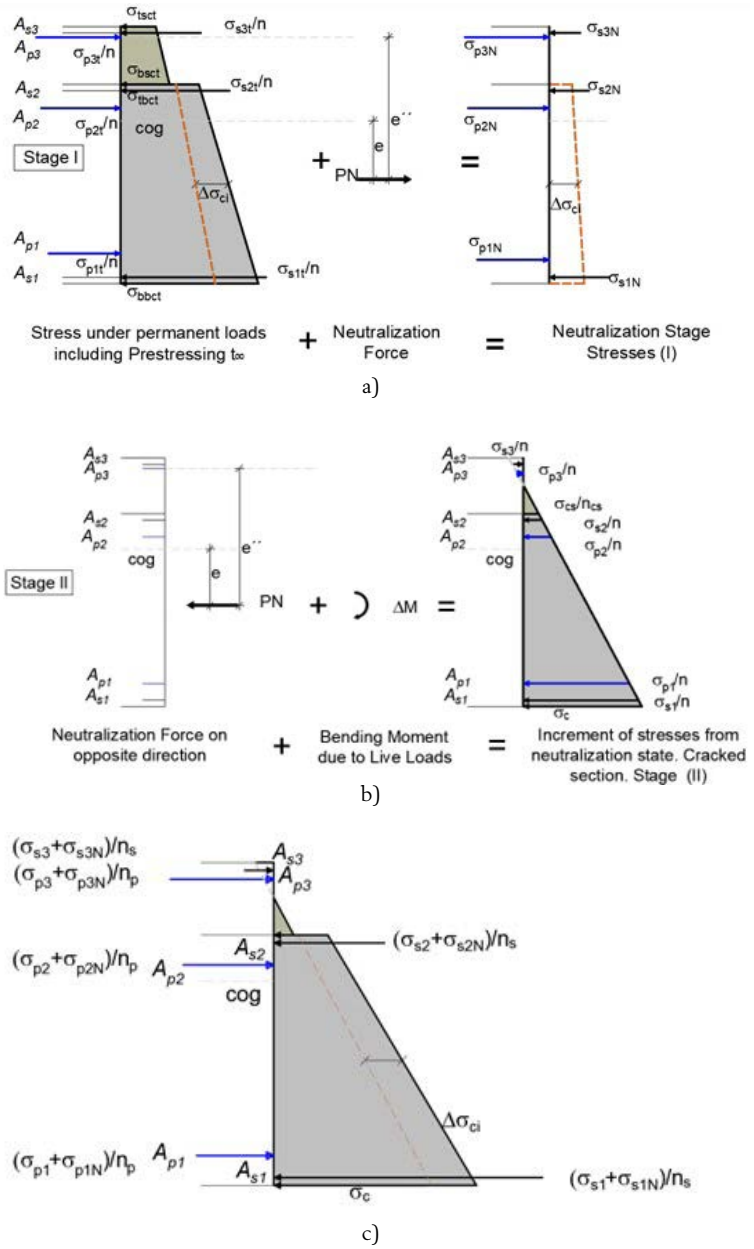

Figure 7. Composite section at support regions girders subjected to negative bending moment in which the top slab is uncracked under permanent loads but undergoes cracking with the application of live loads. (a) Stage I: Neutralization of permanent concrete stresses at the top slab (b) Stage II: Increment of stresses from neutralization state due to application of neutralization forces in opposite direction and live loads (c) Total Stresses: Stages I + II.

The solution thus is based on the procedure explained in Section 3.1 with the top prestressed concrete slab playing the same role as the prestressed beam in Case A. Stage I consists of the introduction of an eccentric neutralization force PN to cancel the permanent concrete stresses of the top slab Figure 7a.

Stage II (Figure 7b) corresponds to the application of the neutralization force in opposite direction to the cracked transformed section plus the bending moment due to live loads. Concrete stresses at the top slab after the neutralization are zero, while the stress increase of the concrete of the precast beam with respect to the concrete of the top slab multiplied by the modular ratio between both concretes ($\Delta\sigma_{ci}$) remains constant throughout the process in each fiber of the concrete of the beam. It is necessary to verify that concrete stresses at the precast beam remain in compression during the whole process. Cracking of the top slab occurs in Stage II. Total stresses due to permanent and live loads are obtained by adding those from the Stages I and II (Figure 7c).

In this case, the cracked section is solved by applying the scheme shown in Figure 8. The system of equations is the same as the one defined by Eqs. (3)-(4) but replacing d_p and e´ with d_{p3} (distance from the prestressing steel of the top slab to the bottom of the precast beam) and e'' (eccentricity of the neutralization force with respect to the prestressing steel of the top slab), respectively.

It might occur that the neutral axis depth goes into the beam in Stage II. In such a situation, the concrete of the beam between the neutralization Stage I to Stage II remains compressed. This results in a decrease of compressive stresses in the beam (Figure 9), which is represented by some tensile

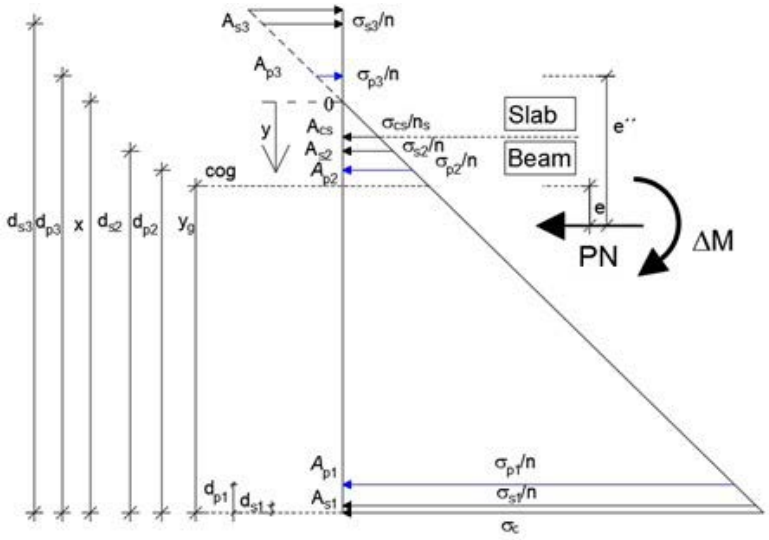

Figure 8. Cracked section analysis from the neutralization state for a section subjected to negative bending moment.

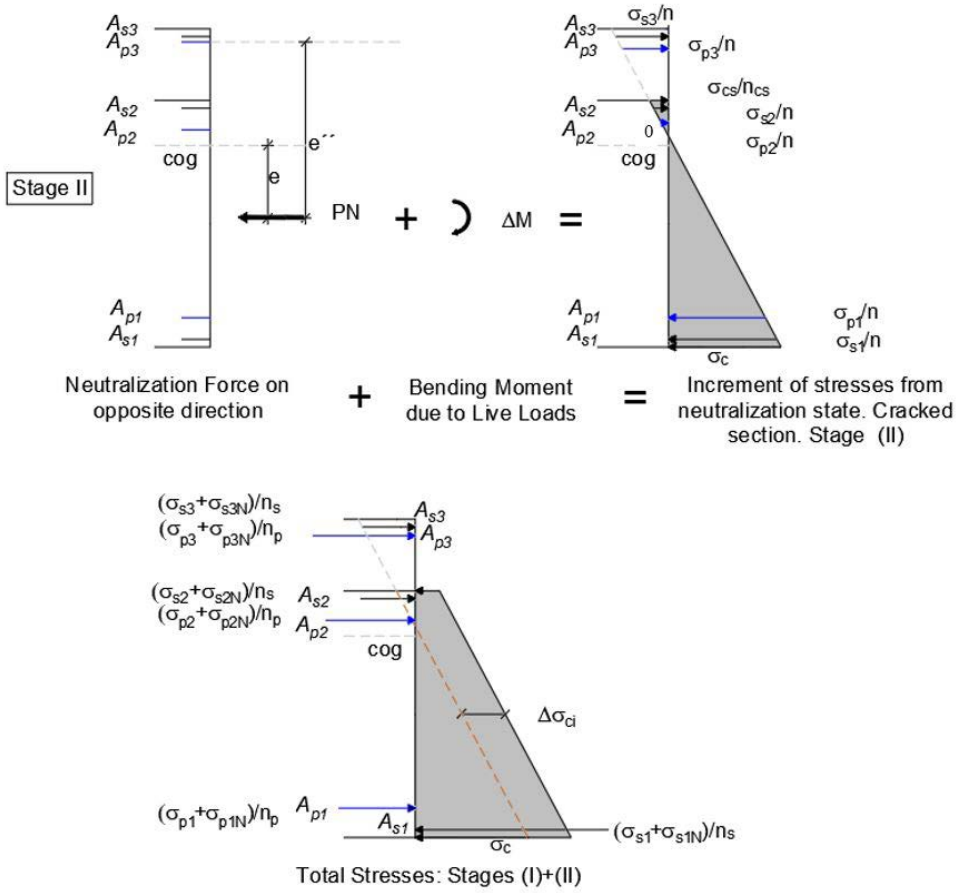

Figure 9. Figure 7b and 7c modified with neutral fiber x inside the depth of the precast beam.

stresses in the concrete of the upper zone of the beam up to the neutral axis (Stage II is an incremental process starting from the plane of neutralization of the stresses in the slab). Figure 9 shows Stage II and the total stresses sum of Stages I (the same as Figure 7a) and II.

The mechanical effect of the tensile stresses of the concrete of the beam can be introduced in the calculations by including it in the equilibrium conditions in Stage II. Equations (3) and (4) can be used, applying sectional equilibrium of axial force and bending moment with respect to the point of zero stresses, referred to as 0, see Figure 9. In addition, the expressions for *B(x)* and *I(x)*, the first and second moment of inertia of the cracked transformed section with respect to the neutral axis, must include the contribution of the complete area of the beam.

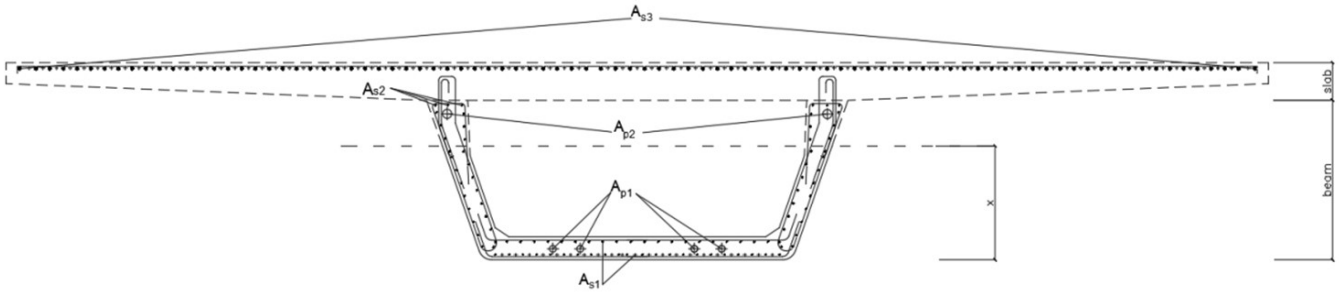

Figure 10. Cracked Composite Section. Case C.

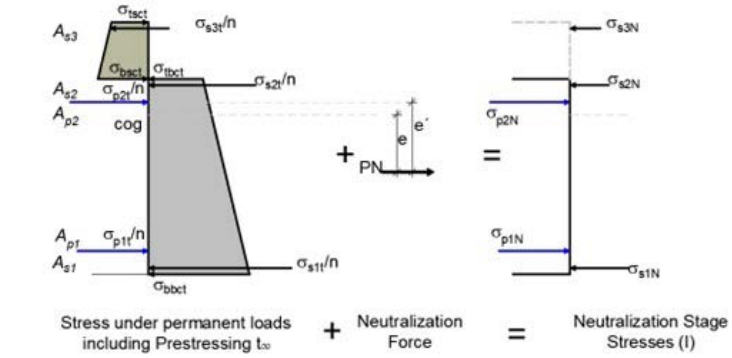

(a)

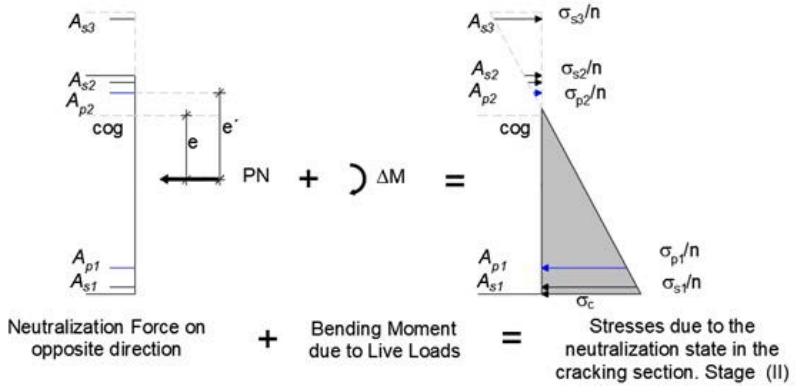

(b)

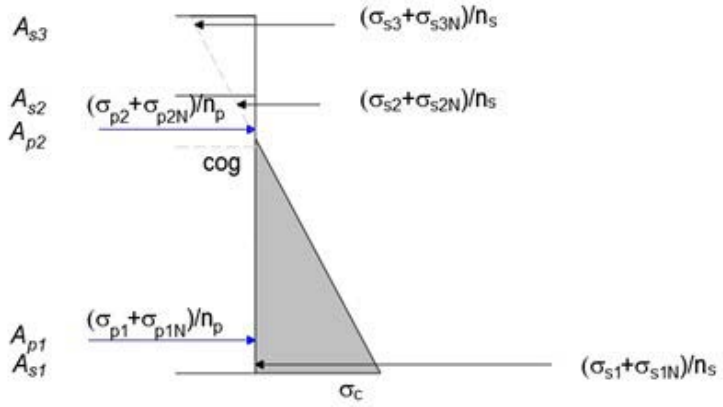

(c)

Figure 11: Composite sections at support regions subjected to negative bending in which the top slab is cracked under permanent loads. (a) Stage I: Neutralization of the permanent concrete stresses at the precast beam. (b) Stage II: Increment of stresses from neutralization state due to application of neutralization forces in opposite direction and live loads. (c) Total Stresses: Stages I + II.

3.3. *Case C*

This Section analyzes the case of a composite section consisting of a precast prestressed beam and a cast-in-place top slab subjected to negative bending moment, in which the top slab is cracked under permanent loads at infinite time.

In this case the concrete of the top slab is considered ineffective, so the considered section is a prestressed concrete section with only one concrete and the reinforcing steel of the top slab outside the concrete (Figure 10).

The application of the method consists, in Stage I, of the neutralization of the permanent concrete stresses in the precast beam (including prestressing loads) at end time (Figure 11a). Stage II (Figure 11b) corresponds to the application of the neutralization force in opposite direction plus the bending moment due to live loads to the cracked transformed section. Total stresses due to permanent and live loads are obtained by adding those of Stages I and II (Figure 11c).

The cracked section is solved by applying the scheme shown in Figure 12 and the system of equations is the same as the one defined in Eqs. (3) and (4) but referring d_p and e' to the prestressing steel of the precast beam (A_{p2}).

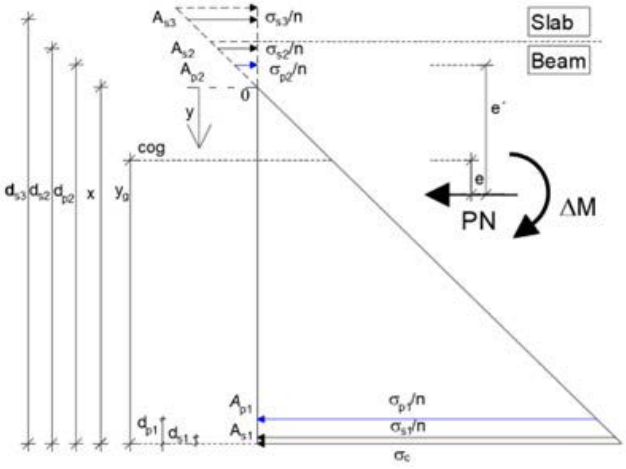

Figure 12: Cracked section analysis from the neutralization state for a section subjected to negative bending moment in which the top slab is cracked under permanent loads.

4. VALIDATION

In this Section, the capabilities of the proposed approach based on the neutralization method are verified by a comparison of the results with a direct calculation and the commercial software FAGUS [14]. FAGUS is part of CUBUS Engineering Software which allows for the cross-sectional analysis of structural elements and gives the stress distribution for a given combination of sectional forces. A reference example is studied to validate the neutralization method for composite sections.

4.1. *Reference example*

An example is studied of a composite section consisting of a rectangular pre-tensioned concrete beam of 1.0 m (height) x 0.3 m (width) and a top concrete slab of 0.25 m (thickness) x 0.3 m (width), refer to Figure 13. The composite section is supposed to be at the midspan region of a structural element subjected to positive bending which is compressed under permanent loads but cracks with the application of live loads. The initial stress at the prestressing steel is σ_{p0} = 1400MPa, the area of prestressing steel A_p is 3.46 cm² and is located 5 cm from the bottom of the beam. For simplicity, both components of the cross-section (beam and slab) have the same concrete and the modular ratio of the prestressing steel (Ep/Ec) is 6.0. Reinforcing steel and rheological effects of concrete are not considered for the sake of simplicity of the example.

The relevant mechanical properties (area, second moment of inertia and distance of the centroid to the bottom of the transformed section) of the beam section and the composite section, both homogenized to concrete as reference material, are as follows:

Transformed beam section:
A = 0.30173 m², I = 0.02534 m⁴, y_g = 0.4974 m.

Transformed composite section:
A = 0.37673 m², I = 0.04939 m⁴, y_g = 0.6223 m.

The beam is subjected to positive bending moments due to its self-weight and the weight of the slab of 210 kN·m and 53 kN·m, respectively. The composite section is subjected to a bending moment due to live loads of 190 kN·m. As there are no shrinkage and creep effects, there is no stress redistribution and, therefore, the slab has no stresses before the application of live loads.

4.2. *Direct calculation*

The stresses in the beam due to prestressing and its self-weight are -1.469 and -1.745 MPa at the top and at the bottom of the section, respectively, which can be easily obtained from Navier's equations with the use of the mechanical properties of the transformed beam section because the beam section is fully compressed.

The additional stresses caused by the self-weight of the cast in place slab modify the stresses of the beam so that the total stresses due to permanent loads are -2.520 and -0.704 MPa at the top and at the bottom of the beam, respectively (Figure 13a, note that the self-weight of the slab is totally carried by the beam because the fresh concrete of the slab does not contribute yet). Once the top slab has hardened, the bending moment due to live loads is applied to the composite section. Since such additional bending moment leads to cracking of the beam, the superposition principle cannot be applied to sum the stresses due to dead loads and live loads, as shown in Figure 13. Direct application is possible since concrete creep and shrinkage are not included in the example. For the application of a direct calculation, the following assumptions have been made:

- The plane of zero stresses coincides with the plane of zero strain. Therefore, the pre-tensioned steel stress is 1400 MPa at the zero-stress plane.
- As plane sections remain plane, the compression resultant at the slab (C), which is the continuation of the beam

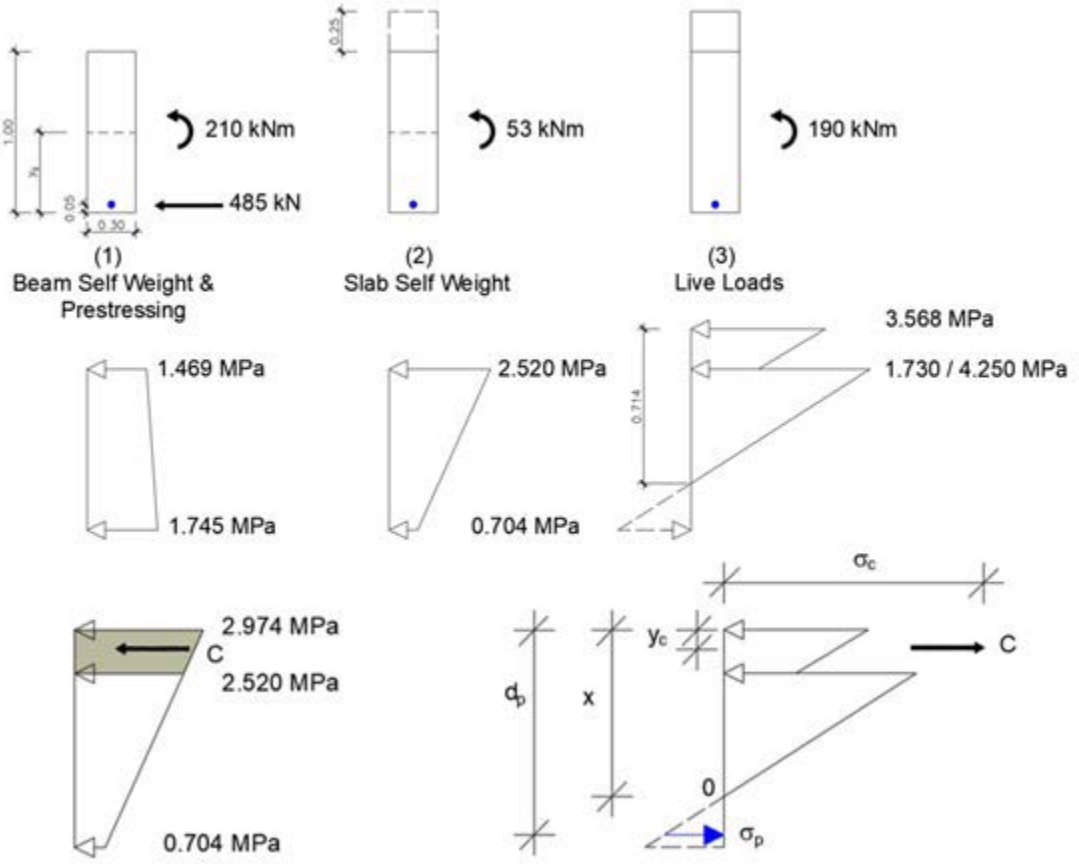

Figure 13. Validation example. Stresses direct calculation.

stresses at permanent loads are discounted in the calculation of final stresses.

The problem is solved by applying sectional equilibrium of axial force and bending moment with respect to the point of zero stresses, referred to as 0 in Figure 13. The axial force in the example is zero and the bending moment (M) is the sum of the bending moment due to dead loads and live loads:

$$0 = \frac{\sigma_c \cdot x \cdot b}{2} - C - \left(P + n \frac{\sigma_c}{x} A_p (d_p - x) \right) \quad (5)$$

$$M = \frac{\sigma_c \cdot x^2 \cdot b}{6} - C(x - y_c) + \left(P_p + n \frac{\sigma_c}{x} A_p (d_p - x) \right) (d_p - x) \quad (6)$$

where b is width of the cross section, C is the stress resultant at the slab from continuation of the beam stresses at permanent loads (Figure 13), yc is the distance from the centroid of the stress resultant C to the top of the slab, and σ_c is the stress at the top of the slab considering the value of C, Figure 13.

Solving Eqs. (5) and (6) yields a neutral axis depth of x = 0.7136 m and a compressive stress at the top of σ_c = 6.542 MPa. Therefore, the stresses at the top and bottom of the slab, and the top of the beam, are -3.568, -1.730 MPa and -4.250 MPa, respectively.

4.3. *Neutralization method*

Stage I of the neutralization method consists of the calculation of the neutralization force PN and its eccentricity e' with respect to the prestressing steel layer, so that the permanent concrete stresses in the beam are cancelled (-2.520 MPa and -0.704 MPa at the top and the bottom of the beam, respectively) with the use of the transformed composite section properties. The resulting neutralization force is PN = 691.02 kN with an eccentricity e´ = 0.702 m. With the neutralization forces, the resulting stresses at the top and the bottom of the slab are tensile stresses 2.974 MPa and 2.520 MPa, respectively (see Figure 14).

In Stage II, the neutralization force is applied in opposite direction in addition to the bending moment due to live loads. With the equilibrium equations (3) and (4), the resulting neutral axis depth and concrete compressive stress at the top of the composite section (x and σ_c in Figure 6) are 0.7082 m and 6.594 MPa, respectively. Therefore, the total stresses at the top and the bottom of the slab, and at the top of the beam are -3.620, -1.746 MPa and -4.266 MPa, respectively. The neutralization method with its two stages is depicted in Figure 14.

4.4. *Commercial software program FAGUS*

FAGUS is a program for the definition and design of cross-sections used in the general CUBUS software framework [14]. FAGUS analysis method enables the calculation of stresses based on specified strains or forces. In the first scenario, known the strain plane allows for a straightforward integration of stresses over the cross-section to determine the section forces. Assumptions include that cross-sections remain plane (Bernoulli hypothesis), complete bonding between concrete and steel, and zero concrete tensile strength (implying a cracked

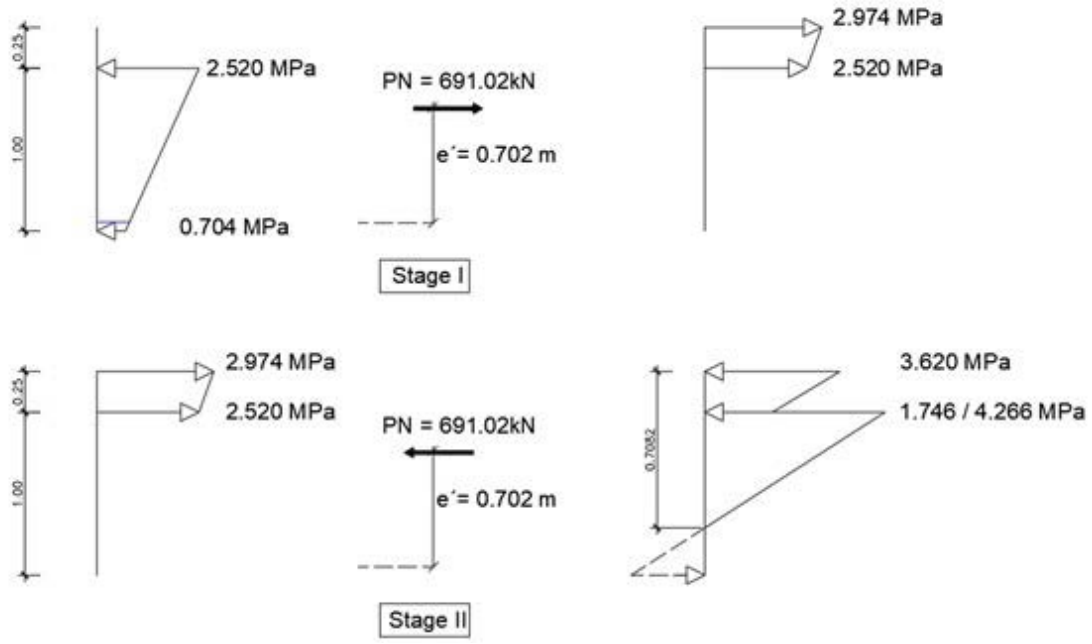

Figure 14. Validation example. Neutralization method.

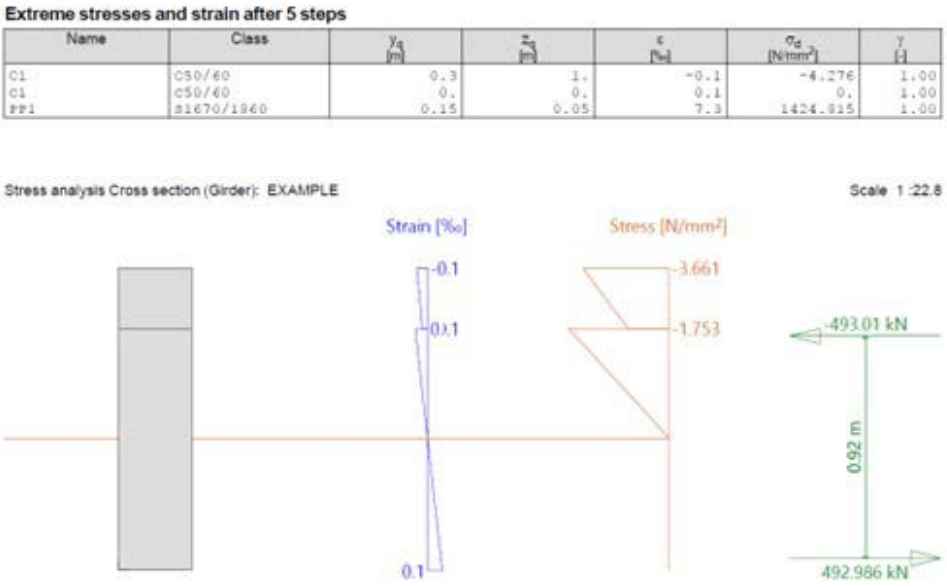

Figure 15. Validation example. Calculation with Fagus.

concrete tensile zone). In the second scenario, analyzing stresses for given forces demands additional computational effort. Determining the associated strain plane an iterative process which involves assuming a strain plane, calculating internal forces and moments (cross-section integration), and then comparing external and internal forces. If discrepancies are significant, the iteration is repeated with an improved strain plane.

FAGUS can conduct stress checks for any composite cross-section type via batch analysis, gradually introducing loads or deformations on selective partial sections that can be activated or deactivated at each step.

In the reference example, the stresses at the top and at the bottom of the slab resulting from the analysis with FAGUS are -3.661 and -1.753 MPa, respectively. The stress at the top of the beam is -4.276 MPa, as shown in Figure 15. Therefore, the neutral axis depth x is equal to 0.7021 m.

TABLE 1.
Validation. Example

	Direct Calculation	Direct Calculation/ FAGUS	Neutralization Method	Neutralization Method/ FAGUS	FAGUS
X(m)	0.7136	1.017	0.7082	1.009	0.7020
σ_{tsc} (MPa)	3.568	0.975	3.620	0.989	3.661
σ_{bsc} (MPa)	1.730	0.987	1.746	0.996	1.753
σ_{tbc} (MPa)	4.250	0.994	4.266	0.998	4.276

The results are shown in Table 1, which compares the neutral axis depth and the concrete stresses at the top and bottom of the slab, and at the top of the beam, with the three methods studied: direct calculation, neutralization method, and FAGUS software. Both direct calculation and neutralization method give

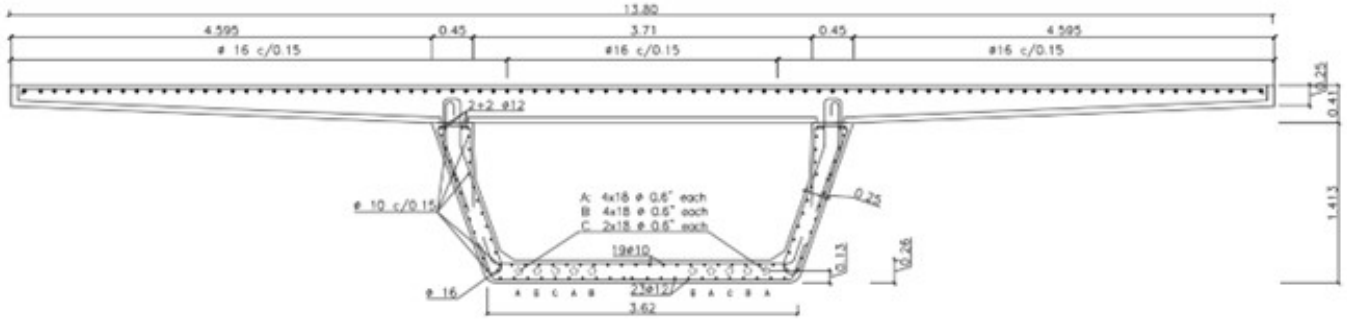

Figure 16. Cross section at midspan. Section 1.

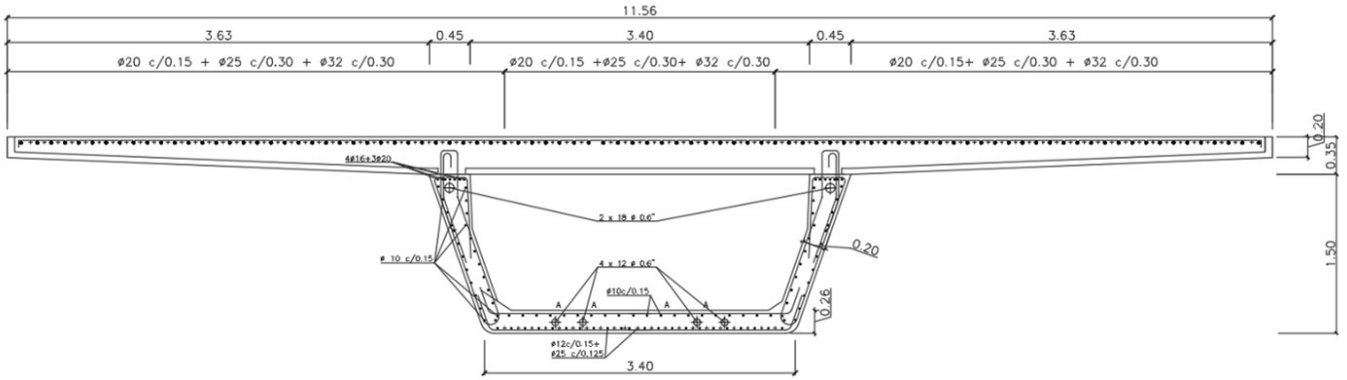

Figure 17. Cross section at pier 1. Section 2.

accurate results in terms of depth fiber and stresses in the slab and in the beam when they are compared with the FAGUS calculation. Differences between the FAGUS software and the neutralization method are less than 1% and differences between FAGUS software and direct calculation are less than 2.5%.

The neutralization method presents advantages in complex cases compared to other methods such as the direct method or using Fagus software. Direct method and Fagus software either do not consider delayed phenomena or it is difficult to introduce or consider them. Neutralization method has lower possibility of error and presents clear advantages for introducing sections of complex geometry such as composite sections consisting of a prestressed concrete beam and a cast-in-place concrete slab with two concretes cast at different times in statically indeterminate concrete bridges with connected precast beams.

5. WORKED EXAMPLES

5.1. Case A

The methodology proposed in the paper is applied to the midspan section of one of the multiple spans of the Viaduct over the Abion River studied in [3]. The structure is a 250 m long continuous bridge with six spans of 25,0 + 40,0 + 3 x 50,0 + 35,0 m. The deck cross-section is a spliced U-shape precast post-tensioned girder with variable depth and a cast-in-place concrete top slab. The analyzed cross-section (referred to as section 1 hereafter) consists of a precast U beam with a depth of 1.41 m and a cast-in-place slab of 13.80 m width and 0.41 m maximum thickness. The characteristic compressive strengths of concrete at 28 days are 50 MPa and 35 MPa, for the beam and the slab, respectively. The layers of prestressing (Y1860S7 according to [3]) and non-prestressing steel (B500S according to [3]) are shown in Figure 16. The area, centroid position and inertia moment about the centroid's horizontal axis of the transformed composite section are A = 6.160 m², y_g = 1.305 m and I = 2.175m⁴, respectively.

The permanent loads at infinite time considered are the self-weight of the precast beam and the top slab, the prestressing force at the precast beam at infinite time including prestressing losses, and rheological effects. Also, the statically indeterminate bending moment due to permanent loads and prestressing and superimposed loads are considered. The resulting permanent stresses over time have been calculated using the stress redistribution method described in [3] [4], and are shown in table 2. If the live load fraction corresponding to the frequent load combination (ΔM_{Freq} = 11866 m·kN according to [3]) is applied over the permanent stress state, a tensile stress of 2.00 MPa is obtained at the bottom of the precast beam, which is still smaller than the considered tensile strength of concrete (ΔM_{cr} = 15134 m·kN,[3]). Nevertheless, under characteristic load ($\Delta M_{characteristic}$ = 19367 m·kN, [3]) the section would be cracked and not able to support tensile stresses under subsequent frequent load combination. Thus, a

consistent analysis requires consideration of cracking for the SLS assessment.

TABLE 2.
Stresses under permanent loads at end time

Location	Section 1 Mid span	Section 2 At pier	Section 3 Mid span
σ_{tsct} (MPa)	-2.79	3.57	-4.93
σ_{bsct} (MPa)	-2.06	2.60	-3.18
σ_{tbct} (MPa)	-7.16	-0.38	-11.76
σ_{bbct} (MPa)	-5.01	-6.61	0.00

To account for cracking, the neutralization method is applied. In Stage I, a neutralization force of PN = 43088.4 kN with an eccentricity of e´ = 1.251 m is necessary to cancel the concrete permanent stresses of the precast beam. Solving equations (3) and (4), with the value of ΔM_{Freq} = 11 866 m·kN yields a neutral axis depth of x = 1.175 m, with $B(x)$ = 4.56 m³, σ_c /x = PN/$B(x)$ = 9448 kN/m³ and σ_{s1} = 23.59 MPa.

The crack width under frequent load combination, relevant for SLS cracking verification, can be calculated with the equations given in Appendix A [EN 1992], which provides (εsm- εcm) = 0.000071, srmax= 313 mm and wk = 0.022 mm (less than 0.2 mm, maximum value according to the corresponding exposure class [1]).

Furthermore, the section is fully compressed under quasi-permanent load combination; so it does not crack and the concrete at the level of the presstressing steel of the beam is in compression.

5.2. Case C

In this case, the studied cross-section is the one located over pier 1 of the Viaduct 2+130 of the Project of Enlargement of Road BI-630 (Spain), refer to [3]. The structure is a continuous 79.0 m long viaduct with three spans of 22.0 + 35.0 + 22.0 m. The deck type is a spliced U-shape precast post-tensioned girder with constant depth and a cast-in-place concrete top slab. The analyzed cross section, named section 2 hereafter, is a precast U beam with a depth of 1.50 m and a slab of 11.56 m width and 0.35 m maximum thickness. The characteristic compressive strengths of concrete at 28 days are 50 MPa and 30 MPa for the beam and the slab, respectively. All layers of prestressing (Y1860S7) and non-prestressing steels (B500S) are shown in Figure 17. The area, the centroid position and inertia moment about the horizontal axis on the centroid of the cracked transformed composite section (neglecting the concrete of the slab but considering the non prestressing steel of the slab) are A = 2.102 m², y_g = 0.745 m and I = 0.948 m⁴ respectively.

Under frequent load combination, the concrete stress at the top of the beam is 2.30 MPa and the concrete of the slab is cracked under permanent loads. Stresses due to permanent loads at end time in section 2, are shown in table 2 (the beam is in compression). Thus, the neutralization force and the eccentricity which cancel the stresses of the concrete of the beam due to permanent loads are PN = 7392,9 kN and e´ = 1.138 m. In this case, the following checks must be done at SLS according to EN 1992 [1]: assessment of the crack width at the top of the beam under frequent load combination; and verification that the concrete at the level of the top prestressing steel of the beam is in compression under quasi-permanent load combination.

Solving equations (3) and (4) with the value of ΔM_{Freq} = -5485 m·kN, the neutral axis depth is x = 0,975 m (measured from the bottom of the beam), and the relevant parameters are as follows: B = 0,68 m3, σ_c /x = PN/$B(x)$ = 10950 kN/m³ and σ_{s2} = 24,64 MPa. Introducing these values in equations (5)-(7), the crack control leads to (ε_{sm}- ε_{cm}) = 0.000074, s_{rmax}= 238 mm and w_k = 0,018 mm (at the top of the beam), which is less than 0.2 mm (maximum value according to concrete exposure class [1]).

Following the same procedure under quasi-permanent load combination (ΔM_{quasi} = -1063 m·kN) the neutral axis depth is x = 1,37 m from the bottom of the beam, so the concrete at the level of the top prestressing steel of the beam is in compression.

6. INFLUENCE OF THE DEFINITION OF THE CONCRETE MODULUS OF ELASTICITY

All the above calculations of the transformed section have been carried out using the instantaneous modulus of elasticity of concrete at infinite time, E_{cb} (t_∞). Nevertheless, it is not totally clear which definition of the modulus of elasticity (either instantaneous or age-adjusted) is conceptually more consistent due to the fact that cracking under both quasi-permanent and frequent loads is not an instantaneous event. In principle, the real modulus of elasticity of the concrete for quasi-permanent loads seems close to the age-adjusted modulus, but an intermediate value between the age-adjusted and instantaneous moduli seems more reasonable for frequent actions.

The choice of the most accurate definition of the concrete modulus for each case is not an easy question and a sensitivity analysis has been carried out in this Section to check the influence of such a parameter, used for the cracked section analysis of Stage II. The same value of the modulus of elasticity must be taken for Stages I and II so that superposition can be applied. Five cases have been studied, including the instantaneous modulus of elasticity at 28 days and end time, and the age-adjusted modulus of elasticity at 1, 2 and 3 years. In order to determine the age-adjusted modulus of elasticity between two-time instants $t_1 < t_2$, the following formulation [3] is applied:

$$E_c(t_2, t_1) = \frac{E_c(t_1)}{1 + \chi(t_2, t_1)\,\varphi(t_2, t_1)} \qquad (7)$$

where $\chi(t_2, t_1)$ and $\varphi(t_2, t_1)$ are the aging and the creep coefficient in the period (t_2, t_1).

The study is applied to the midspan cross-section of the Viaduct 2+130 of the Project of Enlargement of Road BI-630 (Spain) [3]. The analyzed cross-section, named section 3 hereafter, is a precast pre-tensioned U-shaped beam with a depth of 1.50 m and a cast-on-site slab of 11.56 m width and 0.35 m maximum thickness. The geometry of the cross-section is represented in Figure 16. The values of the modulus of elasticity are shown in Table 3.

TABLE 3.
Modulus of elasticity of the concrete

Modulus of Elasticity	Ec Instantaneous t = ∞	Ec Instantaneous t = 28 days	Ec Delayed t = 1 year	Ec Delayed t = 2 year	Ec Delayed t = 3 year
E_{cbeam} (MPa)	43544	38640	17117	16142	15746
E_{cslab} (MPa)	37819	33560	12937	12006	11618

The area, the position of the centroid and the inertia moment about the horizontal axis at the centroid of the transformed composite section are shown in Table 4 depending on the different value of the modulus of elasticity of the concrete. Permanent concrete stresses at the slab and the beam are shown in Table 2. It should be noted that the permanent loads have been increased with respect to the values of the project to obtain zero stress at the bottom of the beam as in the real situation the section is fully compressed.

Table 4 summarizes the neutralization forces (PN, e´) for section 3 depending on the value of the modulus of elasticity. As it is shown, the highest neutralization forces are obtained with the instantaneous modulus of elasticity at end time, while the lowest values are obtained with the age-adjusted modulus at 3 years, but the difference between extreme values is around 7%.

The increase of the bending moment due to quasi-permanent and frequent combination of loads are 2356 and 8637 m·kN respectively. The neutral axis depth (x) under frequent load combination, measured from the top of the section, is shown in Table 4. It should be noted that the smallest values correspond to instantaneous modulus of elasticity and the highest values correspond to age-adjusted modulus of elasticity of concrete, which means that the higher the modulus of elasticity, the lower the position of the neutral axis.

Regarding crack width control of the beam, it can be observed from Table 4 that the values are very similar, being the difference between extreme values 4%. The highest values correspond to the instantaneous modulus of elasticity at end time. Regarding checking under quasi-permanent load combination, the cross-section remains fully compressed when the age-adjusted modulus of elasticity is used, whereas is used, the bottom of the beam is tensioned if the instantaneous modulus of elasticity is considered. Nevertheless, the concrete at the layer of the prestressing steel of the beam is compressed, as shown in Table 4.

TABLE 4.
Analysis of the section with different values of modulus of elasticity of the concrete

	Ec Instantaneous t = ∞	Ec Instantaneous t = 28 days	Ec Delayed t = 1 year	Ec Delayed t = 2 year	Ec Delayed t = 3 year
A(m²)	4.791	4.815	4.685	4.671	4.663
I (m⁴)	1.924	1.936	1.995	2.001	2.003
yg(m)	1.291	1.290	1.248	1.244	1.241
PN (kN)	48471	48687	45833	45534	45370
e´ (m)	1.472	1.472	1.460	1.458	1.457
X(m) Freq Comb	0.835	0.875	1.125	1.150	1.160
w_k (mm)	0.0865	0.0856	0.0852	0.0827	0.0818
X(m) Quasi Comb	1.750	1.775	1.800	1.800	1.800
σ_p (MPa) Quasi Comb	-1.00	-2.04	-6.29	-6.66	-6.82

As a conclusion, the use of the instantaneous modulus of elasticity is on the safe side as it leads to higher values of crack width of the beam and higher neutral axis depth under both quasi-permanent and frequent load combinations. Despite the higher compressive stresses, they remain far below the established stress check limits. However, it is proved that the results have a very limited dependence of the value of the modulus of elasticity of the concrete.

7. CONCLUSIONS

This paper has presented an analytical method for serviceability and crack control in composite sections consisting of a prestressed concrete beam and a cast-on-site concrete slab, both cast at different times. The approach is based on the neutralization method for prestressed concrete sections [7] 20] and has been extended and adapted to composite sections with more than one concrete. The neutralization method provides good agreement regarding the depth of neutral fiber and the stresses in the slab and beam.

The proposed method's key advantage lies in its applicability to composite sections, accounting for prior stress redistribution from concrete shrinkage, creep, and prestressing steel relaxation while also providing a quick tool for assessing the serviceability analysis and offering an alternative to more complex approaches.

The method has been exposed for three cases of practical relevance: midspan sections subjected to positive bending with cracking of the beam, support sections subjected to negative bending in which the top slab is uncracked under permanent loads but undergoes cracking with the application of live loads, and support sections subjected to negative bending in which the top slab is already cracked under permanent loads.

When dealing with cracked positive moment areas, the 'in situ concrete layer' assumes the role of prestressing steel during the neutralization process, requiring consideration of its dimensions using the transformed section method. This approach results in zero stresses only within the precast beam, simulating a homogeneous section. Similarly, support sections experiencing negative bending moments with an uncracked slab under permanent loads follow a comparable methodology, considering the concrete of the beam as "the in situ concrete layer" in positive moment areas, because the concrete of the beam is compressed in all stages.

Conversely, support sections encountering negative bending moments with a cracked slab under permanent loads are approached differently. In this scenario, considering the concrete of the slab as ineffective leads to treating the section as prestressed non-composite, with the reinforcement steel of the slab positioned externally to the concrete. This strategy allows for the treatment of the section as a homogeneous one, distinct from the former cases due to the inefficacy of the cracked slab's concrete.

The influence of the choice of the modulus of elasticity of the concrete has been analyzed, showing that its influence on the results is rather limited. Moreover, the use of the instanta-

neous modulus of elasticity gives results of neutral axis depth and crack width on the safe side compared to the values obtained with the age-adjusted modulus of elasticity. Thus, it can be concluded that it is not necessary to deal with the inherent difficulties to determine the age-adjusted modulus of elasticity of the concrete for permanent or frequent situations.

Acknowledgements

To Miguel Estaún Ibañez, Civil Engineer, and Director of StrucREs, an engineering company specialized in continuous precast bridges, for providing all the documentation related to two examples of continuous precast projects: Project of the Viaduct over the Abion River and the Viaduct located in chainage 2+130 of the Project of Enlargement of Road BI-630 (Spain).

Appendix A. Crack width calculation according to EN 1992

In order to calculate crack width, the following formulation of the Eurocode 2 EN 1992 [1] is applied:

$$\omega_k = s_{rmax}\,(\varepsilon_{sm} - \varepsilon_{cm}) \tag{8}$$

$$s_{rmax} = k_3 \cdot c + k_1 \cdot k_2 \cdot k_3 \cdot k_4 \,\frac{\Phi}{\rho_{p,eff}} \tag{9}$$

$$(\varepsilon_{sm} - \varepsilon_{cm}) = \frac{\sigma_c - k_t \,\frac{f_{cteff}}{\rho_{p,eff}}\,(1+\alpha_e \cdot \rho_{p,eff})}{E_S} \geq 0.6 \cdot \frac{\sigma_s}{E_s} \tag{10}$$

References

[1] CEN. Eurocode 2 EN 1992-1-1:2012. 2012. Design of concrete structures - Part 1: General rules and rules for buildings. Brussels, 2012.

[2] American Concrete Institute (2019). ACI 318: Building Code Requirements for Structural Concrete.

[3] Beteta Cejudo, Mª Carmen (2022). "Comportamiento de puentes prefabricados de viga artesa: Influencia del ambiente y del proceso constructivo". PhD Thesis. Universidad Politécnica de Madrid

[4] Beteta Cejudo, MªC, Albajar, L; Zanuy & C; Estaún, M (2022) "Simplified method for time-dependent effects in statically indeterminate concrete bridges with connected precast beams". Informes de la Construcción 74 (568) https://doi.org/10.3989/ic.91246

[5] Nilson, A.H (1976) "Flexural stresses after cracking in partially prestressed beams". PCI Journal, 21(4), pp 72-81, https://doi.org/10.15554/pcij.07011976.72.81

[6] Dilger, W.H. & Suri, K.M, (1986) "Steel stresses in partially prestressed concrete members". PCI Journal, 31(3), pp 88-112, http://doi.org/10.15554/pcij.05011986.88.112

[7] Ghali, A. (1986) "A unified approach for serviceability design of prestressed and non-prestressed reinforced concrete structures". PCI Journal, 31(2), pp 118-137, https://doi.org/10.15554/pcij.03011986.118.137

[8] Karayannis, C.G.& Chalioris C.E (2013) "Design of partially prestressed concrete beams based on the cracking control provisions". Engineering Structures, 48, pp 402-416 https://doi.org/10.1016/j.engstruct.2012.09.020

[9] Lee, D.H., Han, SJ., Joo, HE. et al. (2018) "Control of tensile stress in prestressed concrete members under service loads". International Journal of Concrete Structures and Materials, 12, 38 https://doi.org/10.1186/s40069-018-0266-3

[10] Al-Zaid, R.J.& Naaman A.E. (1986) "Analysis of partially prestressed composite beams". Journal of Structural Engineering, 112(4), 709-725.

[11] Al-Zaid, R. Z., Naaman, A. E., & Nowak, A. S. (1988). "Partially prestressed composite beams under sustained and cyclic loads". Journal of Structural Engineering, 114(2), 269-291.

[12] Pokharel, H. P. (2014, October). Effect of crack control measures in AS5100. 5 on partially prestressed Super-T girder bridges. In Austroads Bridge Conference, 9th, 2014, Sydney, New South Wales, Australia (No. 3.2).

[13] Ghali, A., Favre, R., & Elbadry, M. (2019). Concrete Structures: Stresses and Deformations. (4th ed) Spon London.

[14] Cubus, AG (2023) Fagus (v9). Structural analysis software.

[15] Computers and Structures, Inc (2023) SAP2000 (v 25.0.0). Structural analysis software.

[16] Computers and Structures, Inc (2023) ETABS (v 21.0.0). Structural analysis software.

[17] Autodesk, Inc (2023) Robot Structural Analysis (2024). Structural analysis software.

[18] Bentley Systems, Inc (2023) Staad.Pro (v 22). Structural analysis software.

[19] Sofistik, AG (2023) Sofistik (2024). Structural analysis software.

[20] Gil Martín L. M; Albajar Molera et al (2011). "Problemas Resueltos de Elementos Estructurales de Hormigón Armado y Pretensado según EHE-08 y EC-2. España". Colegio de Ingenieros de Caminos.

ACHE

MONOGRAFÍAS

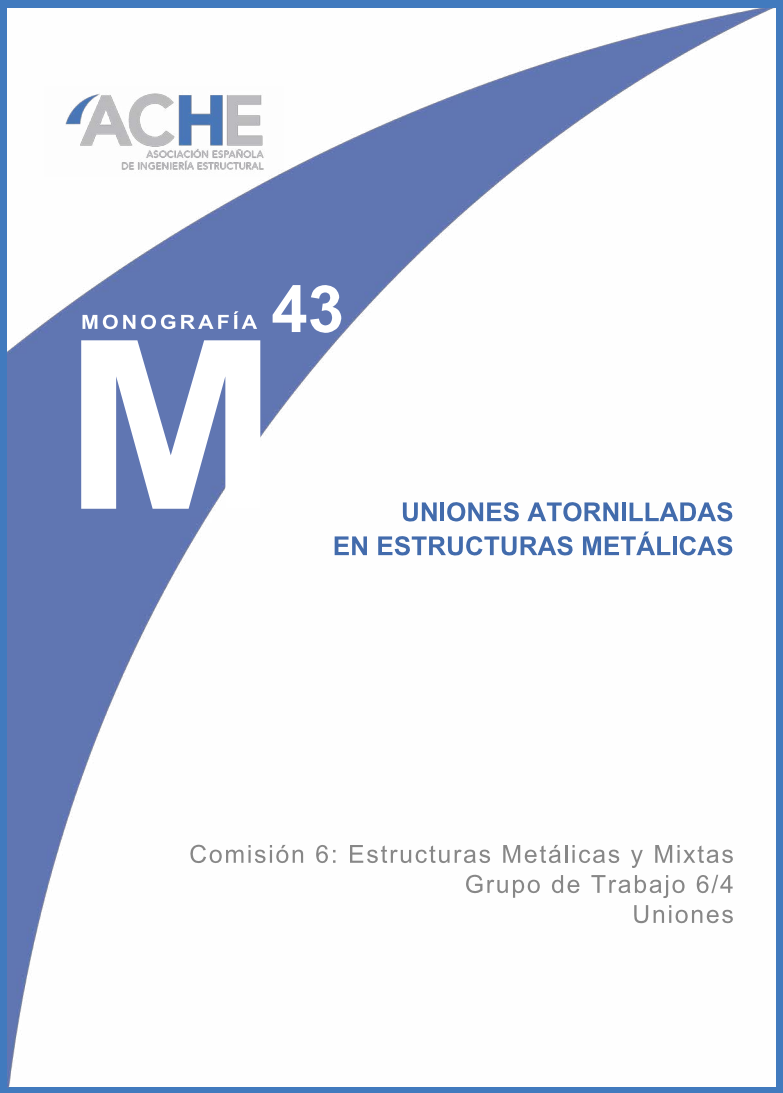

SECRETARÍA DE ACHE
Tel.: 91 336 66 98
www.e-ache.com

Disponible en **www.hormigonyacero.com**
https://doi.org/10.33586/hya.2025.4089

The Impact of Steel Fiber Length and Dosage on Microstructure and Mechanical Performance in UHPFRC: A Hybrid Approach

El impacto de la longitud y la dosificación de la fibra de acero en la microestructura y el rendimiento mecánico en UHPFRC: un enfoque híbrido

J.D. Ruiz Martínez[a], J.D. Ríos[b], E.M. Pérez-Soriano[c], H. Cifuentes[b], C. Leiva[a,*]

[a] *Department of Chemical and Environmental Engineering, Escuela Técnica Superior de Ingeniería, Universidad de Sevilla.*
[b] *Department of Continuum Mechanics and Structural Analysis, Escuela Técnica Superior de Ingeniería, Universidad de Sevilla.*
[c] *Department of Materials Science and Engineering and Transport, Escuela Politécnica Superior, Universidad de Sevilla.*

Recibido el 11 de febrero de 2025; revisado el 6 de mayo de 2025, aceptado el 26 de mayo de 2025

ABSTRACT

This study evaluates the effects of steel fiber length (6 and 13 mm) and dosage on the microstructural and mechanical properties of an ultra-high-performance fiber-reinforced concrete (UHPFRC). The incorporation of 6 mm fiber significantly improved the material's workability characteristics. Microscopic evidence indicates better alignment and distribution of 13 mm fibers within the concrete matrix compared to 6 mm fibers, resulting in reduced porosity and enhanced matrix-fiber interaction. Mechanical testing confirmed that the inclusion of 13 mm steel fibers at various dosages consistently outperformed 6 mm fibers in enhancing compressive and flexural strengths. The optimal dosage, among those tested, for compressive strength was found to be 196 kg/m³ with 13 mm fibers, while the best performance in flexural strength was observed at 226 kg/m³. To address the challenges inherent in UHPFRC—specifically the intricate metallic fiber distribution and limited workability prompted a comprehensive investigation into fiber mixture optimization strategies. Hybrid fiber approach was explored by substituting 10%, 20%, and 30% of the 13 mm fiber dosage (196 kg/m³) with 6 mm steel fibers. Among these, the mix containing 80% of 13 mm steel fibers and 20% of 6 mm steel fibers demonstrated the highest flexural strength, even than those with higher steel fiber content (226 kg/m³). This hybridization suggests an optimized combination of fiber lengths for enhanced flexural performance without compromising compressive strength, providing insights into effective fiber-reinforcement strategies for UHPFRC applications.

KEYWORDS: Ultra-high-performance concrete; steel fiber-reinforced concrete; fiber length; fiber hybridization; fiber-matrix interaction.

RESUMEN

Este estudio evalúa los efectos de la longitud (6 y 13 mm) y la dosificación de fibras de acero sobre las propiedades microestructurales y mecánicas de un hormigón reforzado con fibras de ultra altas prestaciones (UHPFRC). La incorporación de fibras de 6 mm mejoró significativamente la trabajabilidad del material. La evidencia microscópica indica una mejor alineación y distribución de las fibras de 13 mm dentro de la matriz del hormigón en comparación con las fibras de 6 mm, lo que se traduce en una menor porosidad y una interacción matriz-fibra más eficaz. Los ensayos mecánicos confirmaron que la inclusión de fibras de acero de 13 mm, en distintas dosificaciones, superó consistentemente a las de 6 mm en términos de resistencia a compresión y a flexión. La dosificación óptima para la resistencia a compresión fue de 196 kg/m³ con fibras de 13 mm, mientras que el mejor comportamiento en flexión se obtuvo con 226 kg/m³. Para abordar los desafíos de colocación característicos del UHPFRC —en particular la compleja distribución de fibras metálicas y la limitada trabajabilidad— se llevó a cabo una investigación exhaustiva sobre estrategias de optimización de mezclas con fibras. Se exploró un enfoque híbrido mediante la sustitución del 10%, 20% y 30% de la dosificación de fibras de 13 mm (196 kg/m³) por fibras de acero de 6 mm. Entre estas, la mezcla con un 80% de fibras de 13 mm y un 20% de fibras de 6 mm mostró la mayor resistencia a flexión, incluso superior a la de mezclas con mayor contenido total de fibra (226 kg/m³). Esta hibridación sugiere una combinación optimizada de longitudes de fibras para mejorar el comportamiento a flexión sin comprometer la resistencia a compresión, ofreciendo así nuevas perspectivas para el diseño eficiente de UHPFRC.

PALABRAS CLAVE: Hormigón de ultra altas prestaciones, hormigón reforzado con fibras metálicas, longitud de la fibra, hibridación de fibras, interacción matriz-fibra.

* Persona de contacto / *Corresponding author*:
Correo-e / *e-mail*: cleiva@us.es (Carlos Leiva Fernández)

Cómo citar este artículo: Ruiz, J.D., Ríos, J.D., Pérez, E.M., Cifuentes, H., & Leiva, C. (2025). The Impact of Steel Fiber Length and Dosage on Microstructure and Mechanical Performance in UHPFRC: A Hybrid Approach.. *Hormigón y Acero*. 76(306):65-76. https://doi.org/10.33586/hya.2025.4089

1. INTRODUCTION

Over the past 20 years, ultra-high performance concrete (UHPC) has gained popularity for its exceptional mechanical properties, even competing with structural steel [1,2]. UHPC boasts a minimum compressive strength of 130 MPa and a flexural tensile strength over 12 MPa, with a notable opportunity for improvement in ductility [3,4]. Because of its nearly complete porosity, it is extremely resistant to aggressive and acidic substances penetrating into its matrix [5–7]. UHPC usually offers more than three times the compressive strength and approximately six times the flexural tensile strength of ordinary concrete, enhancing its ductility and energy absorption capacity [8]. It has also been widely employed in pavements, airport runways, and long-span bridge decks, which require excellent performance under flexural strain [9]. The use of UHPC allows for the reduction in the size of structural components and, consequently, the overall weight of the structure. This reduction leads to lower labor, maintenance, and shipping expenses, contributing to sustainability [10]. UHPC manufacturing presents substantial processing challenges, primarily attributed to its restricted water-to-binder proportion, intricate macro metallic fiber distribution, and markedly diminished workability [11,12].

The steel fibers are used for improved structural performance, typically employed for UHPC at a content of 2% to 3% by volume. According to Skazlić and Bjegovic [13], when the fiber volume content is 3%, the flexural behavior of Ultra High Performance Fiber Reinforced Concrete (UHPFRC) deteriorates with the use of long steel fibers due to poor fiber dispersion and fiber balling. Steel fibers with dimensions of 13 mm in length and 0.20 mm in diameter are the most widely utilized sizes [14]. As a result, is a composite material in which the inclusion of fibers improves the mix's characteristics, particularly its tensile and fracture qualities, but also has the potential to create voids and encourage the initiation and development of microcracks within the matrix [15–19]. In UHPFRC, the effectiveness of the fiber in improving mechanical properties, such as strength and ductility, through effective stress transfer and crack bridging mechanisms is typically only 30% and fiber orientation is erratic [20]. Experimental results affirmed that better fiber alignment correlates with increased flexural strength and toughness in UHPFRC [21]. Minimizing the fiber reinforcement volume without sacrificing its performance is crucial since UHPFRC places a strong emphasis on sustainability and economic efficiency [22,23].

Hybridization of different steel fiber lengths to improve use efficiency and fiber quantity presents a promising opportunity for further development. It has been demonstrated that combination of short (13 mm) and medium length (19.5 mm) stainless steel fibers significantly improves the flexural performance of UHPFRC [24]. Yoo et al. [25] found that hybrid of long and medium-length fibers improves flexural performance of UHPFRC. The length of the fibers is a critical factor: shorter fibers may not bond effectively with the matrix, potentially leading to slippage and reduced crack resistance, whereas longer fibers increase the contact area and strengthen the bond [26]. Outcomes in line with Rios et al. [18] found that the hybrid reinforced mix of steel fibers produced better fracture behavior because the presence of straight fibers (13 mm) increased the matrix's cracking strength and caused larger deformations prior to the hooked end fibers (30 mm) debonding.

The aim of this work is to study the influence and effectiveness of straight steel fibers of different lengths (some are under explored as 6 mm) on the flexural and compressive properties of UHPFRCs. Complementarily, the workability of fresh concrete, key factor for the on-site application of this type of concrete, as well as the porosity of the compositions were investigated to establish a correlation with their mechanical properties. Evidence was also extracted with a stereomicroscope of the dispersion and orientation of the fibers when casting fresh concrete. Based on comprehensive experimental results and with the objective of enhancing workability without compromising mechanical performance, the best dosage of hybridization to reinforce the UHPFRC was established.

2. MATERIALS AND SPECIMEN PREPARATION

2.1. Materials

For the cementitious matrix, a mix of three binders were used in this study. Type I cement 52.5 R/SR (Portland Valderrivas, Spain) complies with EN 197-1:2011 [27]. The ground-granulated blast-furnace slag (GGBS) provided by Arcelor-Mittal, and the silica fume (SF) S-92-D provided by SIKA. Two varieties of quartz sand were used as aggregates: the finest sand (FS) had a maximum particle size of 0.315 mm, while the coarse aggregate (CS) had particles less than 0.800 mm [12]. Bekaert provided two type of the steel fibers, which were 6 and 13 mm in length (designated as F6 and F13) and 0.15 mm and 0.2 mm in diameter respectively (Table 1). Sika supplied the superplasticizer (20HE).

2.2. Mix proportions and sample preparation

Initially twelve different mixes of UHPFRC that differed only in steel fiber type and content were manufactured. Ta-

TABLE 1.
Properties of Steel Fiber

Fiber	Diameter (d_f) (mm)	Length (l_f) (mm)	Aspect ratio (l_f/d_f)	Density (g/cm³)	Tensile strength (MPa)	Elastic Modulus (GPa)
F6	0.15	6	6/0.15 = 40	7.8	2500	200
F13	0.2	13	13/0.2 = 65	7.8	2500	200

ble 2 shows the designation of the mixes and the proportion of constituents of each.

The manufacturing process of these types of concretes plays a crucial role in the final properties of the matrix, which is why it is detailed below. The solid materials – cement, SF, GGBS, FS and CS – were mixed for 5 minutes in a vertical mixer to achieve a homogeneous solid mix. Subsequently, the super-plasticizer and water were added and mixed for 20 minutes to achieve a workable consistency. Finally, steel fibers were added and mixed for five more minutes. For each of the mixes, three 40x40x160 mm³ prisms were cast. After 24 hours, the samples were demolded and subjected to a further curing period of 26 days submerged in water at room temperature. Finally, the samples were left to dry for 48 hours. The selected fiber volume fractions ranged from 2.24% to 2.88%, consistent with values reported in the literature for structural-grade ultra-high-performance fiber-reinforced concrete (UHPFRC). This dosage range ensures sufficient performance for structural applications while promoting uniform fiber dispersion and mitigating workability issues such as fiber balling or excessive mix stiffness–challenges typically encountered at higher fiber contents. Given that UHPFRC must inherently exhibit self-compacting behavior, maintaining this range is critical. Furthermore, over the past decade, our research group has conducted extensive investigations on fiber-reinforced UHPC, consistently achieving optimal mechanical performance within this dosage interval. [28,29]

2.2.1. Hybrid Mix proportions and sample preparation

The proposal has been based on the dosage of 196 kg/m³ of 13 mm fiber for its better performance in porosimetry and consequently compressive strength. Concerted percentages are replaced by 6 mm fibers to measure the effectiveness of hybridization. This decision balances performance and resource efficiency by avoiding the higher fiber dosage that, even though it offers improvements in flexural performance, presents problems related to fiber dispersion and possible bunching of the fiber that compromises compressive performance. Therefore, the 13 mm fiber mix with 196 kg/m³ was replaced by 10%, 20% and 30% with 6 mm fiber content, in order to observe its mechanical behavior.

3. EXPERIMENTAL PROGRAM

3.1. Workability

To assess the workability of fresh concrete, a downscaled slump test was developed in accordance with the guidelines provided in EN 12350-2:2020 [30] standard. A modified Abrams cone geometry with dimensions of 50 mm at the top, 100 mm at the bottom, and 150 mm in height was used as the setup for the mini-slump test in this work. The reduced

TABLE 2.
Mix proportions and designation.

	Constituent (kg/m³)								
Mix	**Cement**	**SF**	**GGBS**	**FS**	**CS**	**Water**	**SP**	**6 mm Steel fibers**	**13 mm Steel fibers**
F6_176	540	210	310	470	470	205	42	176	
F6_186								186	
F6_196								196	
F6_206								206	
F6_216								216	
F6_226								226	
F13_176									176
F13_186									186
F13_196									196
F13_206									206
F13_216									216
F13_226									226

TABLE 3.
Mix proportions and designation of fiber hybridization.

	Constituent (kg/m³)								
Mix (196 kg/m³)	**Cement**	**SF**	**GGBS**	**FS**	**CS**	**Water**	**SP**	**6 mm Steel fibers**	**13 mm Steel fibers**
F90/10								19.6	176.4
F80/20								39.2	156.8
F70/30								58.8	137.2

cone used has dimensions that are half those of the standard Abrams cone, resulting in approximately half the volume of concrete. Based on this, and following previous literature [31], a mini slump flow value of 275 mm was considered equivalent to the 550 mm limit used in the conventional slump flow test to classify a mixture as self-compacting.

3.2. Steel Fiber Dispersion and orientation

For the study of the dispersion and orientation of the fibers, slices of the prismatic molds were obtained by saw cutting. A cross-section measuring 20 × 20 mm² was obtained from the center of each prism of 40 x 40 mm², This central position was chosen to minimize boundary effects and ensure a representative measurement of fiber distribution.. Based on previous literature [32] who have used ellipse-based image analysis techniques to quantify orientation with higher precision, our approach relies on optical microscopy and visual examination to assess horizontal alignment trends in fiber distribution. The samples were subsequently roughened, finely ground, and polished to achieve a smooth surface for analysis. A Nikon Microscope eclipse (MA100N, New York, USA), coupled with a PC running NIS-Elements BR image capture software, was utilized. This setup enabled detailed microscopic observations of the fiber alignment and their interactions with the cementitious matrix [33,34].

3.3. Porosity

A Micromeritics Autopore IV mercury intrusion porosimeter (Norcross, USA) was used to measure porosity. Pore sizes varied between 150 µm and 0.007 µm. The 5 mm pellets were obtained from the tested samples and drying them in an oven at 105 °C to remove moisture.

3.4. Mechanical properties

3.4.1. Compressive strength

For each type of mix, six 80x40x40 mm³ samples were tested to evaluate compressive strength in compliance with EN 12390-3 [35]. This test was conducted using a servo-hydraulic testing apparatus with a 3000 kN load capability.

3.4.2. Flexural strength

Three-point bending tests were performed on each of the concrete designs used in this study. The tests were carried out in compliance with EN 14651[36]. The specimens prepared for these testing have the following dimensions: 40x40x160 mm³. A central notch was made in each specimen to a depth equal to one-sixth of its height. A 5-mm clip-on displacement gage was used to measure the crack mouth opening displacement (CMOD) during the test, and a 10-mm vertical transducer was used to record the deflection at the specimen's center. Servo hydraulic bending testing machine with CMOD displacement control that can resist a maximum load of 200 kN was used for the studies, The f_L value was identified as the maximum flexural strength within the 0.05 mm CMOD range, as defined by EN 14651 [36]. The f_L value, which represents the cracking strength, triggered tensile cracking in the UHPFRC beam, also referred to as Limit of Proportionality (LOP).

The residual strength is determined using equation (1), and the tests and outcomes were carried out in accordance with EN 14651 standard [36]:

$$f_{Rj} = \frac{3P_jL}{2bh_{sp}^2} \quad (1)$$

where f_{Rj} and P_j, which correlate to $CMOD_j$, stand for the applied load and residual flexural tensile strength, respectively. More specifically, the corresponding CMOD values of 0.5 mm, 1.5 mm, 2.5 mm, and 3.5 mm were used to determine f_{R1}, f_{R2}, f_{R3}, and f_{R4}. Equation (1) uses b for the beam's width, hsp for the beam's height (not including the notch height), and L for the span length.

4. RESULTS

4.1. Workability

The workability test was conducted on mixes with varying dosages (176, 196, 226 kg/m³) of two different lengths of steel fibers. The results indicated a clear trend: as the steel fiber content increased, the slump diameter decreased. Additionally, the results demonstrated that larger fibers resulted in lower workability for the same content. The results of the slump tests for each mix are depicted in Figure 1.

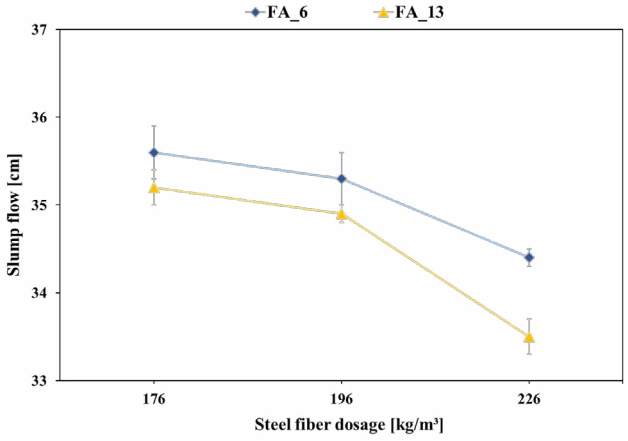

Figure 1. Mini slump flow images for representative mixes.

As shown in Figure 1, mixes with shorter fiber lengths exhibit larger slumps diameters, suggesting less fiber entanglement due to the shorter fibers. Furthermore, as illustrated in Figure 2, all mixes demonstrated self-compacting characteristics, achieving a diameter slump greater than 30 cm without deformation or segregation. This indicates that even with substantial reinforcement, the UHPFRC can flow and fill formwork under its own weight without the need for vibration, maintaining a consistent consistency throughout [37].

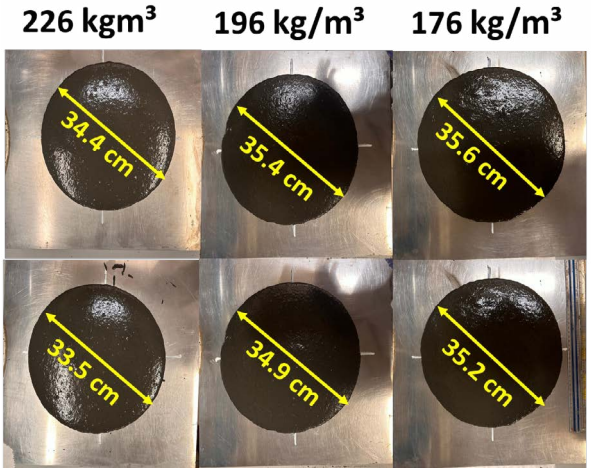

Figure 2. Mini slump flow measurements were conducted on UHPFRC samples containing varying steel fiber dosages and lengths.

4.2. Steel Fiber Dispersion and Orientation

Figure 3 shows images of the interaction between the steel fibers and the cementitious matrix after the curing process obtained from the cut samples. A microscopic approximation of the specially fabricated samples is made, with the focus on the orientation and dispersion of the fiber as the concrete is cast.

Previous research states that there is a positive correlation between the orientation and the UHPFRC's tensile characteristics. In steel fiber reinforced UHPC, the orientation of the fiber should be perpendicular to the fracture orientation, this allows steel fibers to efficiently bridge the crack and support the load [14,18,38,39].

The Figure 3 comparison reveals that, with the same dosage of steel fibers, the shorter fibers (6 mm) are more frequently observed due to their greater quantity (F13:118 – F6:136) compared to the longer fibers (13 mm). However, the 6 mm fibers appear to be less horizontally aligned, in the direction perpendicular to, with a noticeable increase in vertically oriented fibers. Additionally, the distribution of the 6 mm fibers seems inadequate, as certain areas lack any visible fibers, indicating a non-uniform dispersion within the matrix.

The longer fibers, due to their larger contact surface, and therefore higher surface tension, tend to settle more easily into a horizontal position under the influence of gravity. In contrast, the shorter 6 mm fibers, lighter and smaller, can remain more randomly oriented, often vertical.

Figure 4 compares the steel fibers of 13 mm length at dosages of 196 kg/m³ and 226 kg/m³. As expected, the figure corresponding to 226 kg/m³ exhibits a higher density of fiber points (F13_226:153 – F13_196:118). However, it also shows poorer longitudinal alignment of fibers (perpendicu-

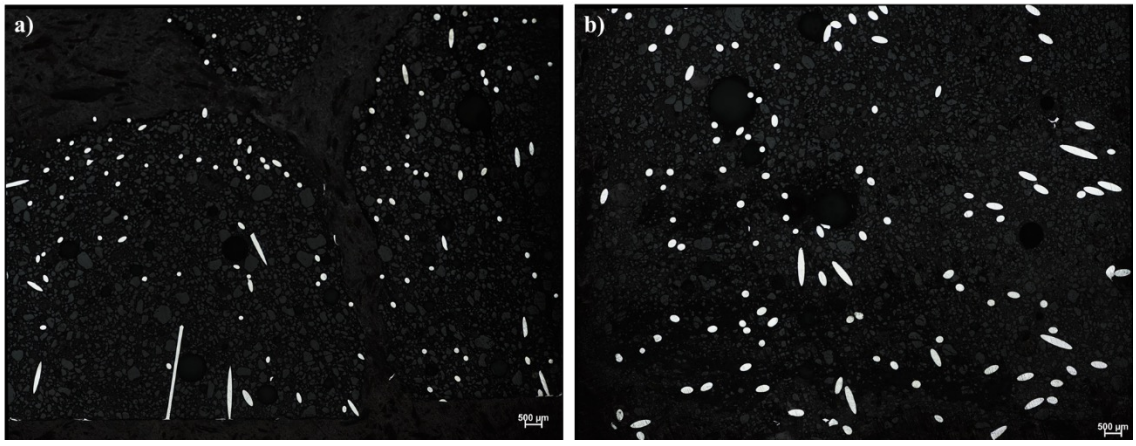

Figure 3. Comparison of Steel Fiber Orientation and Dispersion of a) F6_196 and b) F13_196.

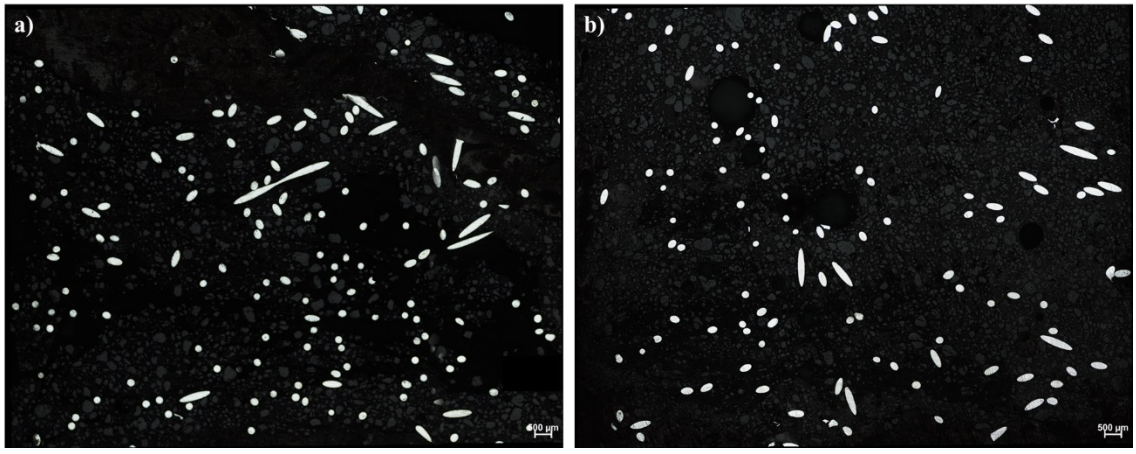

Figure 4. Comparative Image of steel fiber orientation and dispersion of a) F13_226 and b) F13_196.

lar to the bending stress), which, as previously mentioned, reduces their efficiency. Furthermore, the reduction in workability, as illustrated in Figures 1 and 2, is linked to the impaired orientation and dispersion of the steel fibers.

4.3. Porosity

Porosity is a crucial factor in determining the mechanical properties of concrete. Increased porosity in a concrete matrix reduces the solid surface contact area between particles [40]. As shown in Figure 5 and table 4, there are three different pore ranges: capillary pores (less than 0.1 µm in diameter), micropores (0.1–10 µm in diameter), and macropores (greater than 10 µm in diameter). The three main parameters in the pore distribution are: 1) the pore size, 2) pore volume, and 3) Steel Fiber dosage.

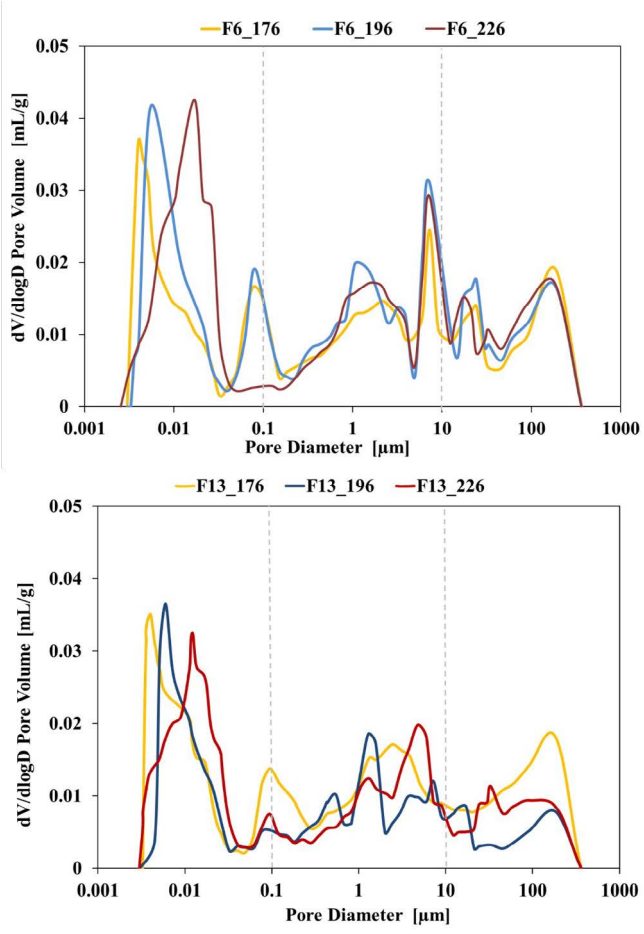

Figure 5. Pore size distribution of representative mix containing 6mm and 13mm steel fiber.

The porosimetry results in Figure 5 and Table 4 reveals the pore distribution across the different UHPFRC mixes. Figure 5 shows that most of the pores are capillary pores in all dosages, especially in the 6 mm composites. F6_176 has a higher amount of macropores compared to other quantities of steel fibers in both lengths. Ríos et al. [18,19] demonstrated by X-ray tomography that micro pores and voids are mostly concentrated around the steel fibers, because the fibers act as blades that divide the macropores into micropores and capillary pores, so it would be logical that the higher the amount of fiber, the higher the capillary pores. However, the 226 kg/m³ mix shows a slightly larger quantity of micropores than 196 kg/m³, probably due to bunching or excess fiber distribution (Figure 4).

TABLE 4.
Pore volume of representative mix containing 6mm and 13mm steel fiber.

	Pore Volume (mL/g)		
Mix	**<100 nm**	**100–10000 nm**	**>10000 nm**
F6_176	0.233	0.214	0.122
F6_196	0.269	0.246	0.106
F6_226	0.297	0.225	0.117
F13_176	0.163	0.223	0.096
F13_196	0.187	0.202	0.053
F13_226	0.195	0.193	0.060

Regarding capillary pores, the addition of more steel fibers increases the pore volume by 27.3% for F6, while for F13 it increases pore volume by 19.4%. While talking about macro porosity, the effect experienced is adverse, reducing the pore volume by –12.7% for F6 and –37.4% for F13 in the dosages with the lowest macro porosity (196 kg/m³). This could be explained by the effect of the fiber in dividing the large pores into micro and capillary pores.

4.4. Mechanical and fracture properties

4.4.1. Compressive strength

Figure 6 compares the effect of different dosages and fiber lengths on the compressive strength of UHPFRC. The 6 mm fibers exhibit a consistent upward trend in compressive strength as fiber dosage increases. The best performance was shown by the dosage of 216 kg/m³, the compressive strength peaks at 151 MPa. Overall, an increase of 14% is observed compared to the initial dosage. However, the highest dosage (226 kg/m³) shows an adverse trend by dropping to 135 MPa (-10.2%), due to a fiber saturation that does not allow the fibers to take the horizontal position to develop their mechanical function, as shown in Figure 3a.

For the 13 mm fibers, the results do not follow a clear upward trend. The best result is obtained at 196 kg/m³, where the strength reaches 161 MPa, marking an additional 12% increase compared to the lower dosage. However, beyond this point, a decline is noted. At 206 kg/m³, the strength drops back to 149 MPa and remains almost stable at 226 kg/m³ with 146 MPa. It is remarkable that compression mechanisms are clearly related to porosity (Figure 5), where the dosage with the lowest amount of macropores showed the best results in compression (196 kg/m³).

Across the range of dosages, 13 mm fibers generally outperform the 6 mm fibers. The maximum compressive strength for 13 mm fibers is 161 MPa, whereas the maximum for 6 mm fibers is 151 MPa. However, the 13 mm fibers peak earlier, at 196 kg/m³, while the 6 mm fibers show steady improvement up to 226 kg/m³.

On average, the 13 mm fibers show approximately 10% higher performance compared to the shorter fibers across most

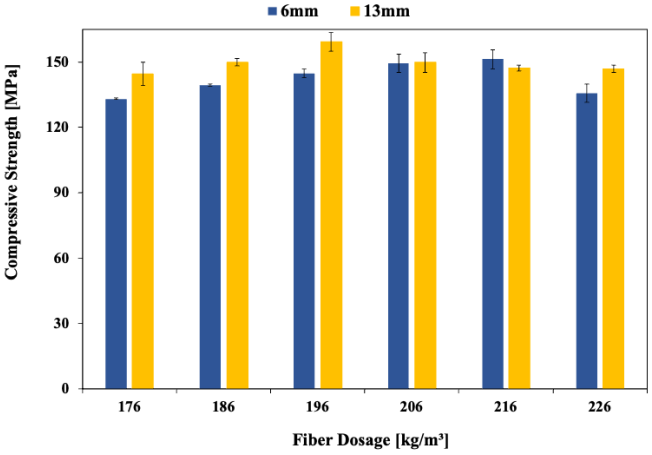

Figure 6. Compressive strength results of each mix.

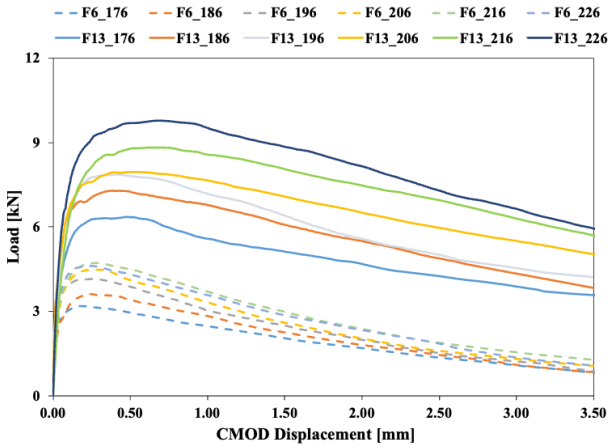

Figure 7. Average Load-CMOD curves for all mixes.

TABLE 5.
Limit of proportionality and residual strengths for each mix.

Mix	LOP, f_L (MPa)	f_{R1} (MPa)	f_{R2} (MPa)	f_{R3} (MPa)	f_{R4} (MPa)
F6_176	9.3	10.0	6.9	4.6	2.7
F6_186	9.8	12.1	8.2	5.5	3.4
F6_196	11.1	13.8	8.7	5.4	3.6
F6_206	11.6	14.9	8.7	5.4	3.6
F6_216	11.9	16.7	10.9	6.9	4.7
F6_226	11.6	14.5	9.6	6.2	3.6
F13_176	13.7	19.1	15.6	13.0	11.0
F13_186	15.9	23.8	19.9	16.2	13.5
F13_196	16.4	26.0	21.2	16.6	13.9
F13_206	17.3	27.8	22.9	19.1	16.0
F13_216	18.5	29.7	27.2	23.4	19.2
F13_226	19.4	32.7	29.8	24.6	20.1

dosages, except at the highest dosage of 216 kg/m³, where the 6 mm fibers slightly surpass the 13 mm fibers. This behavior suggests that while 13 mm fibers are more effective at lower dosages, 6 mm fibers offer a more reliable improvement in compressive strength as the fiber content increases, except for the highest dosage. This compressive strength behavior is in line with the porosimetry results (Table 4), especially linked to the macropore volume.

4.4.2. Evaluation of residual flexural strength and LOP

The experimental findings for the proportional limit and residual strengths derived from three-point bending tests are shown in Table 5 and Figure 7.

Fracture curve models are essential for calculating the propagation of cracks and have been used to describe both pre- and post-cracking behavior in concrete [41,42]. The references mentioned state that there are three distinct stages in the UHPFRC failure process. 1) Linear or elastic phase: the fibers and cement matrix cooperate to withstand applied loads during this first stage, reflected in the LOP. 2) Cracking zone or nonlinear phase: microcracks form during this phase. The growth of these microcracks is gradually resisted by the fibers incorporated into the matrix, behavior reflected in fR1. 3) Stable propagation phase, also known as the post-cracking zone, during which the load is supported by the fibers at the macrocrack surface, ultimately resulting in total fiber detachment, which is reflected in the different highly correlated values of fR2, fR3 and fR4. The behavior of fiber pull-out is mostly associated with the mechanical performance of the UHPFRC mixes in the post-cracking regime [43,44].

Figure 7 presents the Load–CMOD curves for all tested mixes, obtained from the three-point bending test. These curves provide a detailed representation of the flexural behavior, including peak load capacity and post-peak softening response. As observed, the incorporation of 13 mm fibers (solid lines) significantly improves both the maximum load-bearing capacity and the residual load-carrying ability after cracking, in comparison with the mixes containing 6 mm fibers (dashed lines). This graphical representation complements the tabulated data and may serve as a useful reference for the calibration and validation of numerical models.

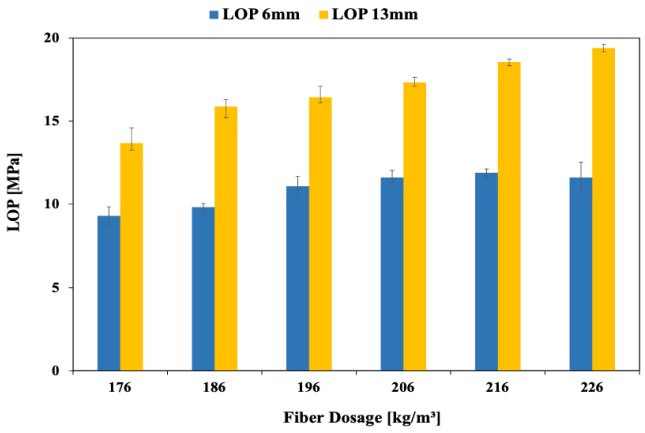

Figure 8. LOP values for the different dosages of 6 and 13 mm fibers.

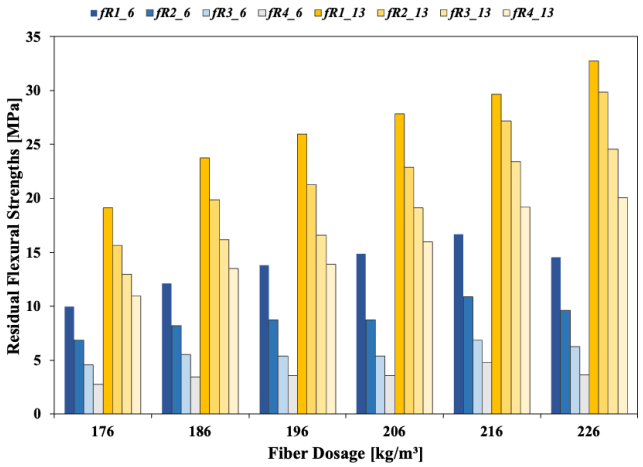

Figure 9. Residual strengths of each composition.

The data provided in Figure 8 shows the LOP values for the different dosages and lengths. It reveals a significant improvement within the efficiency of 13 mm fibers compared to the fibers with lengths of 6 mm, specifically within high dosages. The highest difference in the two strands is reflected at the dosage of 226 kg/m³, where the 13 mm stands at a strength of approximately 19.4 MPa. This is substantially much higher than that of 6 mm, which is 11.6 MPa. This underlines the improved capability of the extended fibers to increase the flexural properties of the material when used at higher dosages.

In the case of the 6 mm fibers, there is a gradual rise in the LOP values with the increase in fiber dosage. As in compressive strength (Figure 6), the peak performance occurs at 216 kg/m³ dosage, where the LOP is about 11.9 MPa. This reflects a gain of 15%, compared to the LOP value recorded at the lowest dosage of 176 kg/m³, which starts at approximately 9.3 MPa. Notwithstanding this enhancement, the 6 mm fibers exhibit a more conservative pattern in comparison to the 13 mm fibers, suggesting that the shorter fibers are less efficient in markedly elevating the material's proportionality limits when subjected to load.

In contrast, the 13 mm fibers exhibit clear linearity in growth with fiber dosage. Starting with a dosage of 176 kg/m³, where the LOP is 13.7 MPa, as the fiber dosage increases, reaching a peak of 19.4 MPa (+41%) at the highest dosage level of 226 kg/m³. This progressive improvement shows that higher percentages of these fibers directly benefit the LOP values by showing their capability to sustain higher relative stresses before yielding or the onset of cracking.

4.4.3. Influence of LOP on residual flexural strengths

A matrix with a high LOP corresponds to an improvement in initial linear-elastic properties and a higher residual strength of the concrete. This is because steel fibers act against the first instances of microcracking, forcing the cracks to follow much more complicated routes that are many times more energy-intensive. These fibers help in sustaining the integrity of the matrix due to the difficulty of crack propagation, hence giving higher residual strength even past attainment of the LOP in the matrix where microcracks have started to appear [45–47].

In this phase a strong relation occurs between LOP and residual strengths determined at f_{R1} (0.5 mm CMOD) and f_{R2} (1.5 mm CMOD). The residual strength curves exhibited sharp rises in the early stages within the region of lower values of CMOD which is indicative of the resistance of the matrix to cracking, enhanced by the fibers.

Nevertheless, when crack openings exceed 2.5 mm CMOD (f_{R3}), there is a noticeable reduction in the rate of increase of residual strength. This phenomenon occurs as the matrix's capacity to support loads diminishes progressively with the widening of the cracks, resulting in a redistribution of stress toward the fibers. At this juncture, the fibers assume a more prominent function in spanning the cracks and supporting the loads [19,48]. In fact, the transition of forces can be realized from the f_{R4} (3.5 mm CMOD) measurements, as the residual strength gain plateaus out after the previous stages. Thus, even though the matrix dominates the initial stages of crack development, the fibers dominate the later stages of crack growth and, hence, significantly control the further crack growth and enable an enhancement in residual strength in the composite material.

As can be seen in Figure 9, 13 mm fibers show higher performance than that of 6 mm with most significant gap between them at the highest fiber dosage of 226 kg/m³. In this dosage, f_1 and f_{R2} for the 13 mm fibers reach up to about 30 MPa, whereas for the 6 mm fibers, the residual strength is substantially lower, with a maximum residual strength value of around 16 MPa. This behavior of the longer fibers is correlated with the results reflected in Figure 3, where better horizontality and distribution of those longer fibers were seen within the UHPFRC matrix. This improved distribution enables the 13 mm fibers to bridge the macrocracks more effectively, allowing better stress transfer across the fibers [40,49].

Since these observations are related to the trends in LOP given in Figure 8, it is obvious to note that the 13 mm fibers showing improved LOP behavior also exhibit better residual strength behavior in the whole range of CMOD. With further crack propagation, the contribution of the matrix be-

comes small, and the fibers become the main load-carrying elements, primarily the longer 13 mm fibers. This explains why the residual strengths of the 13 mm fibers increase linearly with increasing dosage, whereas the 6 mm fibers reach a peak earlier (lower dosage).

It is also worth mentioning that on average, the percentage variation between the LOP of F6 and F13 is 55%, but this value increases in the residual forces, reaching an average of 95% in f_{R1} and reaching a percentage variation of 330% in f_{R4}. These findings provide critical insights into fiber performance mechanisms. Short fibers demonstrate effectiveness in mitigating microcracks and dissipating energy prior to initial crack formation. Conversely, long fibers exhibit superior performance throughout the entire testing process, with exceptional capabilities in resisting macro-crack propagation.

5. FIBER HYBRIDIZATION APPROACH

Based on the obtained results and previous research, proven the ability of small fibers to delay fracture initiation while long fibers are able to reduce fracture propagation, hybrid composites were prepared with fibers of different lengths to further improve their performance and effectiveness.

This series of research focuses on hybridizing fibers of different lengths for their microstructural implications and its consequence on the flexural and compressive properties, with a view to optimizing the strength of both fiber types in seeking an optimal balance between workability, crack mitigation, and load-bearing capacity.

The workability of hybrid compositions, as shown in Figure 10, follows the expected trend. As the proportion of shorter fibers within the 196 kg/m³ dosage increases, a slight improvement in workability is observed. This is consistent with the behavior observed in the previous test, where smaller fibers contributed to a smoother mix. By increasing the percentage of shorter fibers, the matrix flows more easily, facilitating better fiber dispersion and improving overall workability. This is important as it represents an advantage in the civil implementation [6].

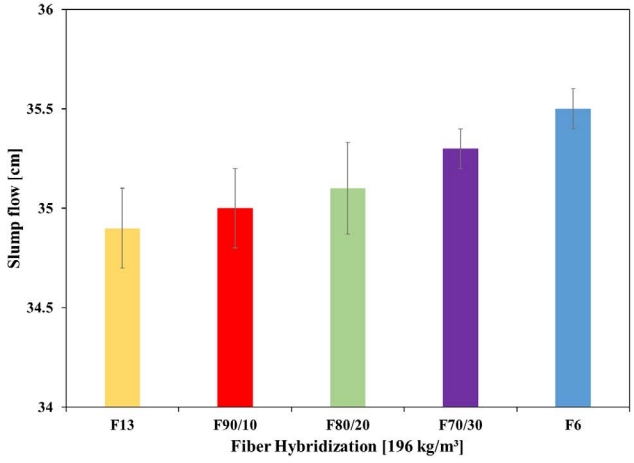

Figure 10. Mini slump flow diameter for hybridization mixes.

Figure 11 illustrates the distribution and orientation of fibers in the hybridization configuration 80/20, which subsequently demonstrated better performance, compared to image containing only 13 mm fibers (Figure 4b).

It is evident that in hybridization, the shorter fibers (smaller white circles) are properly integrated with the longer fibers (larger white circles) and are more evenly distributed within the matrix. In addition, the horizontal alignment of the fibers, which can be seen in the circularity of the white dots, indicates a more efficient working of the fiber flexural stresses, and is noticeably better in the hybrid configuration (Figure 11) than in the F13_226 mix (Figure 4a), even better than in the F13_196 mix (Figure 4b).

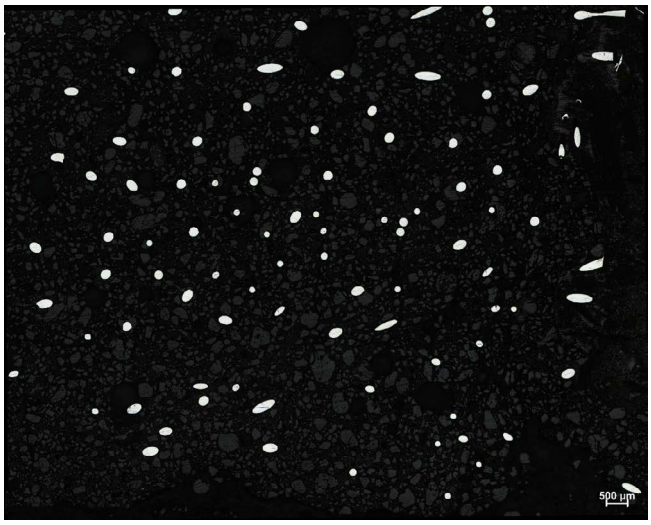

Figure 11. Image of Steel Fiber Orientation and Dispersion of F80/20_196 Mix.

Figure 12 illustrates the porosity of different proportions of fiber hybridization with varying fiber lengths. As seen in Table 6, in terms of porosity, no significant improvement has been achieved compared to the reference dosage of 13 mm.

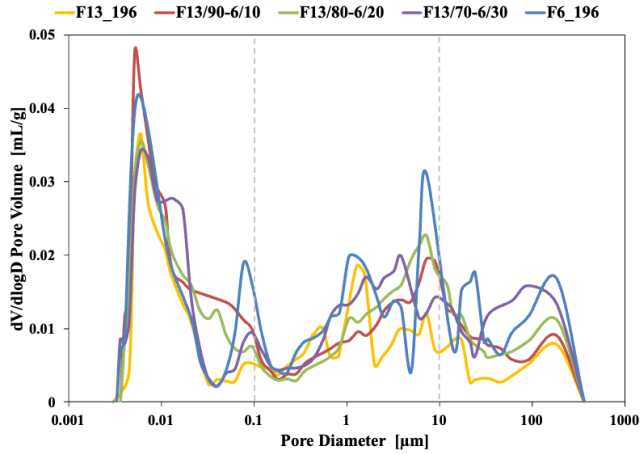

Figure 12. Porosimetry analysis for hybridization mixes.

The results indicate that the amount of macropores (with diameters larger than 100 µm) is higher in all hybrid mixes

compared to the reference, but as expected, they improve the macroporosity of the 6 mm fiber composition, with the 90/10 composition showing the best performance among the three hybrid mixes regarding total porosity. In terms of micropore distribution (diameters less than 0.1 µm), the 90/10 and 13 mm mix outperform as a consequence of the large pores divided into small pores. Among the other compositions, there are no evident differences.

TABLE 6.
Pore volume of hybrid and reference mix (196 kg/m³).

	Pore Volume (mL/g)		
Mix	<100 nm	100–10000 nm	>10000 nm
F6_196	0.269	0.246	0.106
F_70/30	0.312	0.222	0.104
F_80/20	0.316	0.220	0.102
F_90/10	0.321	0.201	0.097
F13_196	0.187	0.202	0.053

Figure 13 presents the compressive strength results for different hybrid fiber compositions, with a 196 kg/m³ dosage. The three hybrid mixes displayed very similar results to each other, maintaining comparable compressive strengths slightly below the reference but still higher than the mix containing only 6 mm fibers.

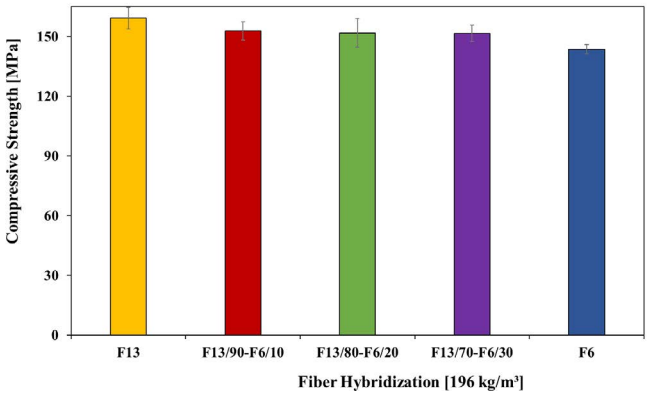

Figure 13. Compressive Strength for hybridization mixes.

The consistency in the results across the hybrid mixes can be linked to the macroporosity findings. As discussed previously (Figure 11), the F13 mix showed fewer macropores, explaining its superior compressive strength. The hybrids, while not reducing macroporosity as effectively, still managed to significantly improve compressive behavior compared to the F6 mix, which had the lowest performance in both porosity and strength. This indicates that the combination of fiber lengths achieves a balance, where microstructural improvements such as reduced macropore formation may not be fully realized, but the hybrid fibers still contribute positively to maintaining compression strength.

Figure 14 presents the LOP and residual flexural strength (f_R) for different hybrid fiber compositions at a dosage of 196 kg/m³. When comparing these hybridized mixes to the reference mix containing only 13 mm fibers (F13), it is evident that all hybridizations improve flexural performance. Specifically, the F 90/10 mix shows a modest 4% increase in strength, while the 80/20 hybridization achieves a more substantial 25% improvement in LOP. This proves that incorporating a controlled ratio of shorter fibers enhances the ductility of the matrix more effectively than using only one length steel fibers.

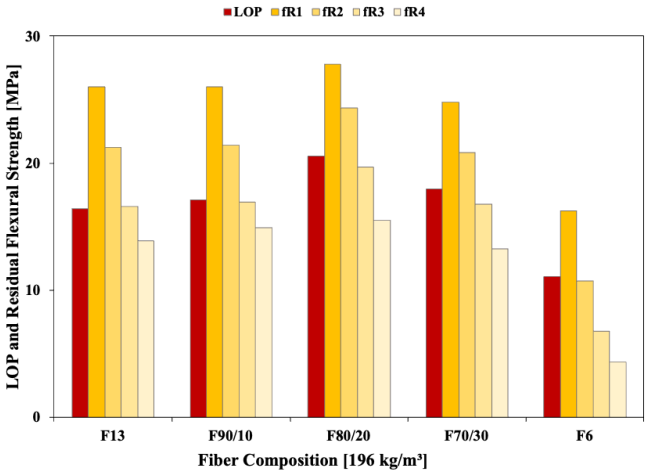

Figure 14. Limit of Proportionality (LOP) and Residual Flexural Strength (fR) for different hybrid fiber compositions at a dosage of 196 kg/m³.

Notably, the highest peak in LOP is achieved by the 80/20 hybrid mix, reaching 20.5 MPa, which even surpasses the performance of a higher fiber dosage of 226 kg/m³ that had a LOP of 19.4 MPa. This exceptional result highlights the efficiency of the 80/20 composition in optimizing initial flexural strength, making it the most effective among the tested mixes. This results in a more even fiber distribution and greater alignment of the fibers along the longitudinal plane (perpendicular to the bending stress) (as seen in Figure 12).

The behavior of the residual flexural strength (f_{R1} to f_{R4}) also reveals important insights. As the proportion of shorter fibers decreases, the gap between the LOP and the residual strengths becomes bigger, (86% for F90/10 against 74% for 70/30 between f_{R1}-f_{R4}) indicating that while the hybridization improves the elastic performance, its impact on residual strengths capacity is less effective. Explained because the presence of short fibers enhances the matrix's performance, increasing the toughening effect of the fibers on the matrix, thereby improving its cracking strength. On the other hand, the presence of longer fibers improves their adherence to the matrix, providing greater deformability to the material, which explains the reduction in the residual strengths.

6. CONCLUSIONS

This research explored the impact of the length and amount of steel fibers in the UHPFRC matrix to assess its effect. Once the most effective dosage and length were determined,

hybridization was carried out to determine whether it can help maintain or improve mechanical properties by reducing the total amount of steel used. The following conclusions were drawn from this research:

- Microscopic analysis shows that 13 mm steel fibers achieve better alignment and distribution within the UHPFRC matrix, resulting in an optimized bridging effect across cracks compared to 6 mm fibers. This enhanced alignment contributes to improved mechanical properties, especially in flexural strengths.
- Porosimetry analysis indicates that the mix with 196 kg/m³ of 13 mm fibers has the lowest macroporosity, which positively correlates with higher compressive strength. The improved pore distribution in this dosage appears critical in reducing structural weakness.
- The workability tests revealed a linear trend where increasing fiber dosage decreased slump flow, indicating lower workability. However, all mixes maintain the parameters of self-compaction, and did not directly impact mechanical performance, allowing for higher fiber dosages without compromising strength.
- Across all compositions, 13 mm fibers consistently provided superior compressive and flexural properties compared to 6 mm fibers, making them more effective at enhancing UHPFRC's mechanical performance. The optimal dosage for compressive strength was 196 kg/m³ of 13 mm fibers, achieving the highest compressive resistance, while the flexural strength peaked at 226 kg/m³. These findings guided the choice of 196 kg/m³ as the baseline for hybridization.
- Among the hybridization mixes the 80/20 mix exhibited the highest flexural strength among all tested compositions reaching 25% LOP than F13_196, even surpasses the performance of a higher fiber dosage of 226 kg/m³. This hybrid mix maintained compressive strength stable to the 13 mm-only mix at 196 kg/m³, demonstrating that hybrid fiber combinations can optimize flexural performance in UHPFRC applications without compromising compressive strength, therefore proves to be the best in terms of flexural strength and cost effectiveness.

Acknowledgments

This research was funded by the Ministerio de Ciencia e Innovación of Spain under project number PID2019-110928RB-C33 and PID2023-147971OB-C32.

References

[1] Z. Fang, L. Hu, H. Jiang, S. Fang, G. Zhao, Y. Ma, Shear performance of high-strength friction-grip bolted shear connector in prefabricated steel–UHPC composite beams: Finite element modelling and parametric study, Case Stud Constr Mater 18 (2023) e01860. https://doi.org/10.1016/J.CSCM.2023.E01860.

[2] X. Shao, L. Deng, J. Cao, Innovative steel-UHPC composite bridge girders for long-span bridges, Front Struct Civ Eng 13 (2019) 981–989. https://doi.org/10.1007/s11709-019-0531-9.

[3] B. MacDougall, H. Hajiloo, S. Sarhat, J. Kabanda, M. Green, The Compressive Strength of Ultra-high Performance Concrete at Elevated Temperatures, in: R. Gupta, M. Sun, S. Brzev, M.S. Alam, K.T.W. Ng, J. Li, A. El Damatty, C. Lim (Eds.), Proceedings of the Canadian Society of Civil Engineering Annual Conference 2022, Springer Nature Switzerland, Cham, 2024: pp. 895–906. https://doi.org/https://doi.org/10.1007/978-3-031-35471-7_63.

[4] F. de Larrard, T. Sedran, Optimization of ultra-high-performance concrete by the use of a packing model, Cem Concr Res 24 (1994) 997–1009. https://doi.org/10.1016/0008-8846(94)90022-1.

[5] P. Richard, M. Cheyrezy, Composition of reactive powder concretes, Cem Concr Res 25 (1995) 1501–1511. https://doi.org/10.1016/0008-8846(95)00144-2.

[6] S. Abbas, A.M. Soliman, M.L. Nehdi, Exploring mechanical and durability properties of ultra-high performance concrete incorporating various steel fiber lengths and dosages, Constr Build Mater 75 (2015) 429–441. https://doi.org/10.1016/J.CONBUILDMAT.2014.11.017.

[7] J.D.R. Martínez, J.D. Ríos, H. Cifuentes, C. Leiva, Multi-Scale Toughening of UHPC: Synergistic Effects of Carbon Microfibers and Nanotubes, Fibers 13 (2025). https://doi.org/10.3390/fib13040049.

[8] D. Wang, C. Shi, Z. Wu, J. Xiao, Z. Huang, Z. Fang, A review on ultra high performance concrete: Part II. Hydration, microstructure and properties, Constr Build Mater 96 (2015) 368–377. https://doi.org/10.1016/J.CONBUILDMAT.2015.08.095.

[9] Y. Niu, J. Wei, C. Jiao, Crack propagation behavior of ultra-high-performance concrete (UHPC) reinforced with hybrid steel fibers under flexural loading, Constr Build Mater 294 (2021) 123510. https://doi.org/10.1016/J.CONBUILDMAT.2021.123510.

[10] Y. Aydın, C. Cakiroglu, G. Bekdaş, Z.W. Geem, Explainable Ensemble Learning and Multilayer Perceptron Modeling for Compressive Strength Prediction of Ultra-High-Performance Concrete, Biomimetics 9 (2024). https://doi.org/10.3390/biomimetics9090544.

[11] M. Amran, S.S. Huang, A.M. Onaizi, N. Makul, H.S. Abdelgader, T. Ozbakkaloglu, Recent trends in ultra-high performance concrete (UHPC): Current status, challenges, and future prospects, Constr Build Mater 352 (2022) 129029. https://doi.org/10.1016/J.CONBUILDMAT.2022.129029.

[12] S. Abbas, M.L. Nehdi, M.A. Saleem, Ultra-High Performance Concrete: Mechanical Performance, Durability, Sustainability and Implementation Challenges, Int J Concr Struct Mater 10 (2016) 271–295. https://doi.org/10.1007/s40069-016-0157-4.

[13] M. Skazlić, D. Bjegović, Toughness testing of ultra high performance fibre reinforced concrete, Mater Struct 42 (2009) 1025–1038. https://doi.org/10.1617/s11527-008-9441-3.

[14] H. Huang, X. Gao, K.H. Khayat, Contribution of fiber alignment on flexural properties of UHPC and prediction using the Composite Theory, Cem Concr Compos 118 (2021) 103971. https://doi.org/10.1016/J.CEMCONCOMP.2021.103971.

[15] J.P. Hwang, M. Kim, K.Y. Ann, Porosity generation arising from steel fibre in concrete, Constr Build Mater 94 (2015) 433–436. https://doi.org/10.1016/J.CONBUILDMAT.2015.07.044.

[16] C. Jiang, K. Fan, F. Wu, D. Chen, Experimental study on the mechanical properties and microstructure of chopped basalt fibre reinforced concrete, Mater Des 58 (2014) 187–193. https://doi.org/10.1016/J.MATDES.2014.01.056.

[17] E. Poveda, G. Ruiz, H. Cifuentes, R.C. Yu, X. Zhang, Influence of the fiber content on the compressive low-cycle fatigue behavior of self-compacting SFRC, Int J Fatigue 101 (2017) 9–17. https://doi.org/10.1016/J.IJFATIGUE.2017.04.005.

[18] J.D. Ríos, C. Leiva, M.P. Ariza, S. Seitl, H. Cifuentes, Analysis of the tensile fracture properties of ultra-high-strength fiber-reinforced concrete with different types of steel fibers by X-ray tomography, Mater Des 165 (2019) 107582. https://doi.org/10.1016/J.MATDES.2019.107582.

[19] J.D. Ríos, H. Cifuentes, C. Leiva, S. Seitl, Analysis of the mechanical and fracture behavior of heated ultra-high-performance fiber-reinforced concrete by X-ray computed tomography, Cem Concr Res 119 (2019) 77–88. https://doi.org/https://doi.org/10.1016/j.cemconres.2019.02.015.

[20] H. Huang, X. Gao, K.H. Khayat, A. Su, Influence of fiber alignment and length on flexural properties of UHPC, Constr Build Mater 290 (2021) 122863. https://doi.org/10.1016/J.CONBUILDMAT.2021.122863.

[21] H. Huang, X. Gao, L. Li, H. Wang, Improvement effect of steel fiber orientation control on mechanical performance of UHPC, Constr Build Mater 188 (2018) 709–721. https://doi.org/https://doi.org/10.1016/j.conbuildmat.2018.08.146.

[22] Z. Wu, C. Shi, W. He, D. Wang, Static and dynamic compressive properties of ultra-high performance concrete (UHPC) with hybrid steel fiber reinforcements, Cem Concr Compos 79 (2017) 148–157. https://doi.org/10.1016/J.CEMCONCOMP.2017.02.010.

[23] D.J. Kim, S.H. Park, G.S. Ryu, K.T. Koh, Comparative flexural behavior of Hybrid Ultra High Performance Fiber Reinforced Concrete with different macro fibers, Constr Build Mater 25 (2011) 4144–4155. https://doi.org/10.1016/J.CONBUILDMAT.2011.04.051.

[24] B. Chun, D.Y. Yoo, Hybrid effect of macro and micro steel fibers on the pullout and tensile behaviors of ultra-high-performance concrete, Compos B Eng 162 (2019) 344–360. https://doi.org/10.1016/J.COMPOSITESB.2018.11.026.

[25] D.Y. Yoo, S.W. Kim, J.J. Park, Comparative flexural behavior of ultra-high-performance concrete reinforced with hybrid straight steel fibers, Constr Build Mater 132 (2017) 219–229. https://doi.org/10.1016/J.CONBUILDMAT.2016.11.104.

[26] W. Chen, Y. Wen, Experimental study on mechanical and durability properties of concrete incorporating various polyvinyl alcohol fiber lengths and dosages, Mater Construcc74 (2024) e349. https://doi.org/10.3989/mc.2024.368923.

[27] European Committee for Standarization (CEN), EN 197-1: Cement - Part 1: Composition, specifications and conformity criteria for common cements, Brussels, Belgium, 2011.

[28] D.Y. Yoo, J.H. Lee, Y.S. Yoon, Effect of fiber content on mechanical and fracture properties of ultra high performance fiber reinforced cementitious composites, Compos Struct 106 (2013) 742–753. https://doi.org/10.1016/J.COMPSTRUCT.2013.07.033.

[29] J.D. Ruiz Martínez, J.D. Ríos, E.M. Pérez-Soriano, H. Cifuentes, C. Leiva, Enhancing the matrix-fiber bond in ultra-high-performance fiber-reinforced concrete using a high performance plasticizer. Impact on the flowability, physical and mechanical properties, Constr Build Mater 470 (2025) 140683. https://doi.org/10.1016/J.CONBUILDMAT.2025.140683.

[30] European Committee for Standardization (CEN), EN 12350-2: Testing fresh concrete - Part 2: Slump test., Brussels, Belgium, 2020.

[31] E. Nguyen Amanjean, M. Mouret, T. Vidal, Effect of design parameters on the properties of ultra-high performance fibre-reinforced concrete in the fresh state, Constr Build Mater 224 (2019) 1007–1017. https://doi.org/10.1016/J.CONBUILDMAT.2019.07.284.

[32] T. Park, S. Her, H. Jee, S. Yoon, B. Cho, S.H. Hwang, S. Bae, Evaluation of orientation and distribution of steel fibers in high-performance concrete column determined via micro-computed tomography, Constr Build Mater 270 (2021) 121473. https://doi.org/10.1016/J.CONBUILDMAT.2020.121473.

[33] J. Zhou, J. Lai, L. Du, K. Wu, S. Dong, Effect of directionally distributed steel fiber on static and dynamic properties of 3D printed cementitious composite, Constr Build Mater 318 (2022) 125948. https://doi.org/10.1016/J.CONBUILDMAT.2021.125948.

[34] J. Liu, M. An, L. Huang, Y. Wang, S. Han, Influence of vibrating compaction time on the strength and microstructure of ultra-high performance concrete, Constr Build Mater 409 (2023) 133584. https://doi.org/10.1016/J.CONBUILDMAT.2023.133584.

[35] European Committee for Standardization (CEN), EN- 12390-3: Testing hardened concrete - Part 3: Compressive strength of test specimens, Brussels, Belgium, 2020.

[36] European Committee for Standardization (CEN), EN 14651: Test method for metallic fibre concrete - Measuring the flexural tensile strength (limit of proportionality (LOP), residual), Brussels, Belgium, 2008.

[37] H. Abdolpour, P. Niewiadomski, Ł. Sadowski, A. Chowaniec, Self-compacting ultra-high performance mortars produced with waste catalysts from petrochemical industry: Rheological, mechanical and microstructural properties, J Clean Prod 369 (2022) 133225. https://doi.org/10.1016/j.jclepro.2022.133225.

[38] S.T. Kang, J.K. Kim, The relation between fiber orientation and tensile behavior in an Ultra High Performance Fiber Reinforced Cementitious Composites (UHPFRCC), Cem Concr Res 41 (2011) 1001–1014. https://doi.org/10.1016/J.CEMCONRES.2011.05.009.

[39] R. Mu, J. Chen, X. Chen, C. Diao, X. Wang, L. Qing, Effect of the orientation of steel fiber on the strength of ultra-high-performance concrete (UHPC), Constr Build Mater 406 (2023) 133431. https://doi.org/10.1016/J.CONBUILDMAT.2023.133431.

[40] J.D. Ruiz Martínez, J.D. Ríos, E.M. Pérez-Soriano, H. Cifuentes, C. Leiva, Effect of nano silicon nitride on the microstructural characteristics and mechanical properties of ultra-high-performance steel fiber reinforced concrete, Mater Struct 58 (2025) 103. https://doi.org/10.1617/s11527-025-02634-9.

[41] S.P. Shah, Determination of fracture parameters (K Ic s and CTOD c) of plain concrete using three-point bend tests, Mater Struct 23 (1990) 457–460. https://doi.org/https://doi.org/10.1007/BF02472029.

[42] Z.P. Bažant, M.T. Kazemi, Determination of fracture energy, process zone longth and brittleness number from size effect, with application to rock and conerete, Int J Fract 44 (1990) 111–131. https://doi.org/https://doi.org/10.1007/BF00047063.

[43] Z.P. Bažant, E. Becq-Giraudon, Statistical prediction of fracture parameters of concrete and implications for choice of testing standard, Cem Concr Res 32 (2002) 529–556. https://doi.org/10.1016/S0008-8846(01)00723-2.

[44] W. Meng, K.H. Khayat, Mechanical properties of ultra-high-performance concrete enhanced with graphite nanoplatelets and carbon nanofibers, Compos B Eng 107 (2016) 113–122. https://doi.org/10.1016/J.COMPOSITESB.2016.09.069.

[45] V. Ortega-López, A. García-Llona, V. Revilla-Cuesta, A. Santamaría, J.T. San-José, Fiber-reinforcement and its effects on the mechanical properties of high-workability concretes manufactured with slag as aggregate and binder, J Build Eng 43 (2021) 102548. https://doi.org/10.1016/J.JOBE.2021.102548.

[46] H. Zhang, B. He, X. Zhu, Q. Wang, Z. Jiang, The use of AE technique for identifying ductility degradation against cryogenic on flexural performance of UHPC at various temperature conditions, Cem Concr Compos 137 (2023) 104904. https://doi.org/10.1016/J.CEMCONCOMP.2022.104904.

[47] Y. Wang, S. Backer, V.C. Li, An experimental study of synthetic fibre reinforced cementitious composites, J Mater Sci 22 (1987) 4281–4291. https://doi.org/10.1007/BF01132019.

[48] J.D. Ríos, C. Leiva, A. de la Concha, M.P. Ariza, H. Cifuentes, Influence of Graphene Oxide Concentration and Ultrasonication Energy on Fracture Behavior of Nano-Reinforced Cement Pastes, Crystals (Basel) 14 (2024). https://doi.org/10.3390/cryst14080707.

[49] A. Martínez-de-la-Concha, J.D. Ríos, H. Cifuentes, Numerical Study of the Shear Behavior of Ultra-High-Performance Concrete Beams, Hormigón Acero 75 (2024) 157–162.

Disponible en **www.hormigonyacero.com**
https://doi.org/10.33586/hya.2024.3142

Formulación analítica para el cálculo de tableros bijácena con solicitación excéntrica

Analytical Formulation for the Calculation of Bi-Girder Decks With Eccentric Loading

Javier Henche Blanco[a,*]

[a] *GRAHEN INGENIEROS SL. Madrid. Spain*

Recibido el 15 de febrero de 2024; revisado el 12 de julio de 2024, aceptado el 22 de julio de 2024

RESUMEN

Se presenta un planteamiento analítico para la obtención de las deformaciones y solicitaciones en tableros con vigas gemelas, en especial los obtenidos a partir de secciones prefabricadas en artesa. Fue de inspiración y fundamento la fuerza de la descomposición de la función resistente en estados más simples, para la obtención de una formulación matemática. Se trata de una forma similar al planteamiento que realizó Javier Manterola en el memorable artículo "La sección abierta y cerrada bajo solicitación excéntrica" [1]. Para la resolución se efectuará una aproximación al formalismo matemático de las funciones de Green. El planteamiento requiere una serie de simplificaciones admisibles que aproximan con bastante rigor la solución, y permiten la evaluación directa de la acción de cargas móviles. Por último, se efectúa un análisis de la efectividad del reparto transversal conseguido con diversas condiciones de apoyo.

PALABRAS CLAVE: Tablero bijácena, viga artesa, función de Green, solicitación excéntrica.

ABSTRACT

This paper presents an analytical approach to determine the deformations and stresses in twin beam decks, commonly used with channel-shaped precast beams. The method is inspired by and founded on the efficiency of load decomposition into simpler cases and provides a mathematical framework to address the problem. This approach builds on the significant work of Javier Manterola in 'The open and closed section under eccentric loads' [1]. The resolution involves applying the mathematical formalism of Green's functions. The analysis incorporates a set of admissible simplifications that yield a fairly rigorous approximation of the solution, enabling the direct evaluation of the effects of moving loads. Finally, the paper examines the effectiveness of transverse load distribution achieved under various support conditions.

KEYWORDS: Twin girder deck, channel-shaped beam, Green's function, eccentric load.

* Persona de contacto / *Corresponding author*:
Correo-e / *e-mail*: javier.henche@grahen.es (Javier Henche Blanco)

Cómo citar este artículo: Henche, J. (2025). Formulación analítica para el cálculo de tableros bijácena con solicitación excéntrica. *Hormigón y Acero*. 76(306): 77-101. https://doi.org/10.33586/hya.2024.3142

1. INTRODUCCIÓN

Siempre tuvimos presente la referencia [1] de Don Javier Manterola *"La sección abierta y cerrada bajo solicitación excéntrica"*, acerca de cómo se podría extender la teoría de vigas, cuando, bajo ciertas condiciones, un tablero de puente se puede asimilar a un elemento lineal. Era sorprendente la elegancia del desarrollo matemático, para condensar, en unas ecuaciones diferenciales formalmente bastante simples, toda la complejidad de la solicitación excéntrica. Una de las lecciones más importantes que se aprenden allí, tal como nuestro maestro intentó transmitirnos en sus clases, es la potencia de la descomposición del problema en una superposición de estados más simples, como son la torsión, la distorsión y los alabeos ligados a ellas, que a su vez son muy útiles para entender mejor la función resistente completa. Antes de la llegada del desarrollo genera-

lizado del método de elementos finitos (MEF) para el cálculo de los tableros, fueron importantes las herramientas analíticas, que poseen una magnifica exposición y rigor en los trabajos de Don Avelino Samartin, en especial de las recopilaciones recogidas en [2] y [3]. Como referencia más reciente, mencionamos los importantes trabajos de Don Salvador Monleón y el equipo de la Universidad Politécnica de Valencia (UPV) referencias [4] y [5], que, a partir de métodos variacionales, alcanzan el mismo objetivo para cualquier directriz de viga.

Lo que aquí se presenta, pretende ser una pequeña aportación para la solución del mismo problema para un caso particular pero muy útil: obtener la solución analítica para el cálculo de deformaciones y solicitaciones en puentes con doble viga con carga excéntrica. Esta tipología es ampliamente utilizada, correspondiendo el caso más frecuente, a dos vigas principales prefabricadas de hormigón con sección en artesa y una losa de reparto. Para puentes estrechos, es posible utilizar una pareja de vigas prefabricadas de ala ancha; también se aplica a tableros mixtos con vigas metálicas armadas, con diversas configuraciones. Toda esta familia de tableros pueden englobarse en la denominación general de tableros bijácena.

En el presente artículo, partiendo de unas simplificaciones razonables del problema general, se consigue establecer unas ecuaciones diferenciales que rigen el reparto transversal de la carga excéntrica entre ambas vigas. Mediante el formalismo de la función de Green que la resuelve, es posible calcular las solicitaciones y las deformaciones, ante la aplicación de cualquier clase de sobrecarga sobre el tablero, ya sean ferroviaria o de carretera. Una referencia interesante para profundizar en el fundamento matemático utilizado se señala en [6]; es oportuno señalar que, de forma indirecta y poco conocida, los formularios clásicos de solicitaciones de vigas con cargas puntuales, son soluciones de la función de Green de la ecuación diferencial de la viga de Bernouilli – Navier, bajo las diversas condiciones de contorno.

Consideramos que el planteamiento es útil para el estudio de tableros ferroviarios de doble vía, con anchos los habituales entre 12.50 y 14.0m para vía convencional o LAV, para lo cual presentamos al final un ejemplo de aplicación.

Figura 1. Configuración tipo del tablero de puente FFCC.

2. CONSIDERACIONES INICIALES

Para la obtención de una solución analítica, algunas restricciones y simplificaciones deben ser aplicadas. Al final se hará mención a la extensión a puentes continuos o de apoyo oblicuo, y con losa de reparto con rigidez torsional. Las hipótesis requeridas son las siguientes:

1. Son tableros de sección constante, con dos vigas principales paralelas e iguales. Ello es obligado al utilizar en las ecuaciones las condiciones de simetría de eje central longitudinal.
2. La sección transversal de la viga posee la rigidez propia de torsión de Saint Venant (como sección abierta o cerrada).
3. No se considera ni el alabeo torsional ni la distorsión de la sección individual de viga, lo cual es válido de acuerdo a las dimensiones y formas habituales.
4. La vinculación transversal entre las vigas la proporciona únicamente la losa de reparto. Las cargas aplicadas sobre ella, se transmiten únicamente por flexión transversal a las vigas.
5. Las vigas se encuentran simplemente apoyadas en ambos extremos. Se estudiarán los casos de vigas con giro de torsión impedido -por riostra transversal o disposición de doble apoyo, más habitual en puentes ferroviarios-; y giro libre solo coaccionado por la losa de reparto. Este último caso es bastante habitual en puentes de carretera, al disponerse uno único con riostra propia en centro de la viga prefabricada.
6. Se considera como eje X el longitudinal de viga, el eje Y vertical hacia arriba, y el Z horizontal transversal, con triedro directo, para fuerzas y deformaciones. Como signo de solicitaciones, se considerarán positivas las correspondientes a las positivas en la cara frontal de la sección; y el de deformaciones, las positivas según ejes globales. Ello implica que algunas las fórmulas habituales de la teoría elemental de vigas cambien de signo, quedando por ejemplo:

$$q(x)=\frac{dV(x)}{dx};\ V(x)=\frac{dM(x)}{dx};\ M(x)=-EI.\frac{dw(x)}{dx};\ w(x)=-\frac{du(x)}{dx}$$

Siendo aquí la nomenclatura de acciones y solicitaciones de viga en flexión que luego utilizaremos:

q(x): Ley de carga vertical
u(x) y w(x): Deformación vertical y giro de flexión de viga.
M(x) y V(x): Solicitaciones de flexión y cortante de viga.

Estas condiciones permiten abordar analíticamente el estudio de tableros sencillos, y obtener de forma directa su cálculo con gran aproximación.

3. TRANSFORMACIÓN DEL TABLERO REAL AL MODELO ANALÍTICO

Previamente al establecimiento de las ecuaciones constitutivas, se requiere transformar la sección real a la de cálculo, de acuerdo a la siguiente descomposición:

1. Se considera cada viga referida a sus ejes longitudinales (X) propios que pasan por su CDG, y con una separación (S) entre ellos.
2. La losa reparte transversalmente. Para obtener las reacciones sobre cada viga, se considera la losa como viga continua en sentido transversal, suponiendo fijos los apoyos sobre las almas.

3. Las reacciones locales se transmitirán en sentido longitudinal, generándose distribuciones de acciones $P_{v1}(x)$, $M_{v1}(x)$, $P_{v2}(x)$ y $M_{v2}(x)$, de acuerdo al siguiente método:

- **En el caso de vigas artesa**, se materializa un apoyo en cada alma de viga. De esta forma, se obtienen dos reacciones por viga.

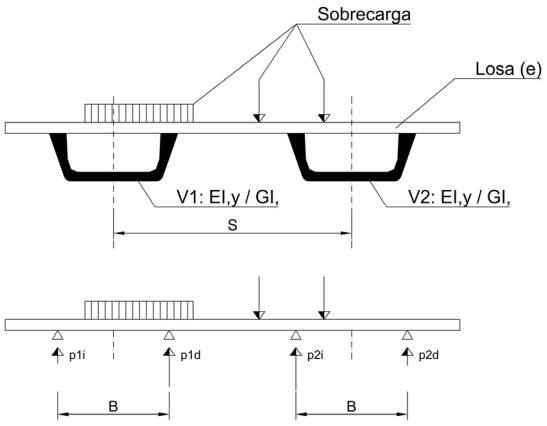

Figura 2. Obtención de reacciones unitarias en almas de vigas artesa.

Llamando B a la separación entre almas de vigas, se obtienen los valores de las reacciones equivalentes en eje de viga, en término de carga vertical y momento de eje viga:

$$P_{v1} = p_{1i} + p_{1d} \qquad M_{v1} = (p_{1d} - p_{1i}) \cdot B/2$$
$$P_{v2} = p_{2i} + p_{2d} \qquad M_{v2} = (p_{2d} - p_{2i}) \cdot B/2$$

- **En caso de vigas de alma única** se obtiene la reacción y el momento de las sobrecargas, de forma directa, considerando los puntos de apoyo en ejes de vigas como empotramientos perfectos.

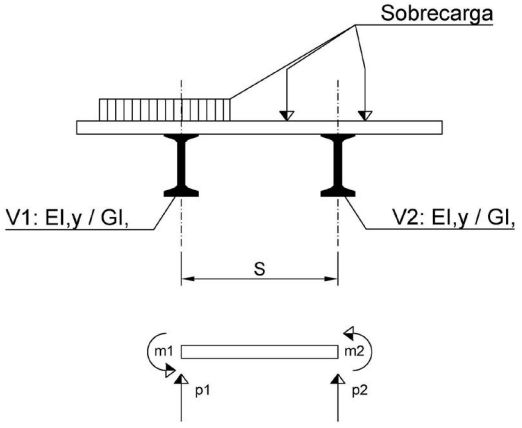

Figura 3. Obtención de reacciones unitarias en el almas de vigas doble T.

Con estos cuatro valores, se calculan cuatro estados de carga:

a) Carga vertical simétrica, abordada por teoría elemental de vigas -y por tanto sin reparto transversal- con acciones iguales a:

$$q_{,sim} = (P_{v1} + P_{v2}) / 2$$

b) Carga vertical antimétrica, igual y de signo contrario en cada viga, para la cual se obtendrá la solución analítica de la función de reparto (Apartado 4º)

$$q_{,ant} = (P_{v1} - P_{v2}) / 2$$

c) Momento de torsión simétrico – igual y de signo contrario en cada viga- que no provoca flexión en las vigas, solo reparto de torsión, que se estudiará analíticamente.

$$mt_{,sim} = (M_{v2} - M_{v1}) / 2$$

d) Momento de torsión antimétrico – de mismo signo en ambas vigas- que induce flexión y reparto de torsión (Apartado 5º)

$$mt_{,ant} = (M_{v2} + M_{v1}) / 2$$

Una vez obtenidas las solicitaciones de cada modelo analítico, la suma de los cuatro estados dará directamente las deformaciones y solicitaciones de las vigas.

e) Para obtener las solicitaciones en losa, en el caso de vigas artesa, con los resultados compuestos de deformaciones (giro y deformación vertical por vigas), se obtendrán las deformaciones verticales en cada alma. Aplicando un modelo de viga continua con aplicación de las deformaciones impuesta en cada apoyo de alma como asientos verticales, se obtendrán los esfuerzos de flexión y cortante de losa de reparto. Se le añadirán lógicamente los esfuerzos locales entre puntos de apoyo en almas fijas.

El esquema de la descomposición en los cuatro estados es el siguiente:

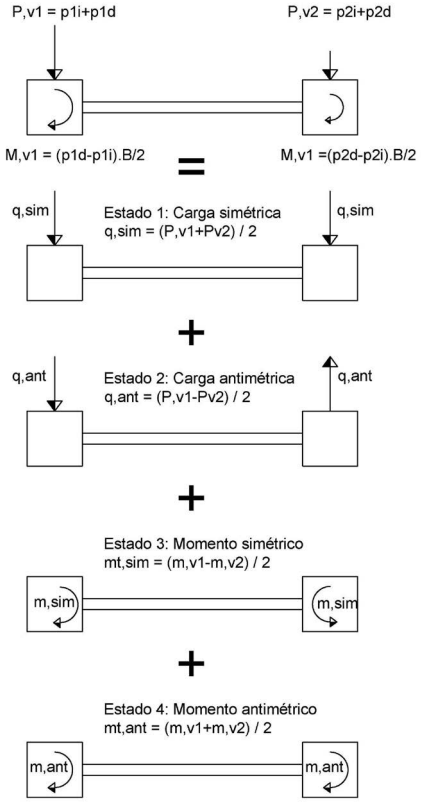

Figura 4. Descomposición de reacciones en unitarias en cuatro estados simples.

4.
ESTADO DE APLICACIÓN DE CARGA VERTICAL ANTISIMÉTRICA

El planteamiento de reparto transversal frente a carga vertical antisimétrica pura, se explica en el siguiente esquema, en el cual se establece una acción exterior q(x), en general variable a lo largo de cada viga. El problema trata de obtener la expresión, que definiremos como "función de descarga p(x)", a través de la losa, que el sistema distribuye transversalmente. Con el criterio de signos adoptado, posee valor negativo sobre la viga derecha:

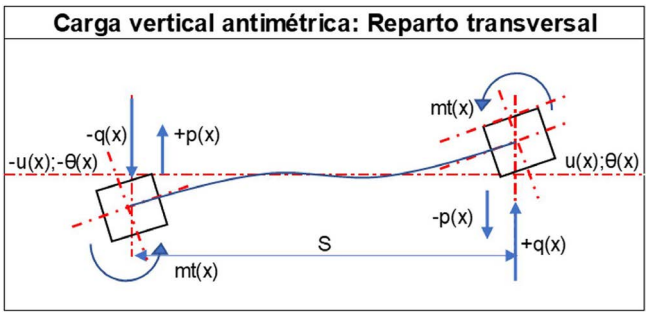

Figura 5. Nomenclatura de acciones, solicitaciones y deformaciones para carga vertical antimétrica.

El resto de variables definidas son:

- mt (x): Momento torsor repartido transmitido por losa por ml.
- Mt (x): Ley de torsión igual en cada viga.
- θ(x): Giro de torsión igual en cada viga.

Las ecuaciones que rigen las variables anteriores son las siguientes:

1. La primera ecuación es la general de flexión viga Bernoulli, que liga la deformación vertical con la carga neta aplicada que en este caso es la diferencia entre la exterior aplicada (+) y la descargada por reparto transversal (-), suponiendo inercia a flexión constante:

$$q(x)-p(x)=EI\ u^{IV} \qquad (4.1)$$

2. La segunda ecuación liga el giro de torsión con el momento por torsión de Saint Venant en vigas:

$$\frac{Mt(x)}{GI,t}=\theta'(x) \qquad (4.2)$$

3. La tercera ecuación liga, a través de los factores de rigidez de la losa, la carga de reparto transversal p(x), y las deformaciones y giros de sus extremos, que son los mismas que los de la vigas:

$$p(x)=2u(x)\cdot K_{uu}-2\theta(x)\cdot K_{u\theta} \qquad (4.3)$$

Siendo K_{uu} y $K_{u\theta}$ los factores de rigidez de losa, que para espesor constante valen $12EI_{,losa}/S^3$ y $6EI_{,losa}/S^2$

4. La última ecuación es la de equilibrio de losa:

$$mt(x)=-\frac{p(x)\cdot S}{2} \qquad (4.4)$$

Con ello, derivando dos veces (4.3) y una vez (4.2):

$$p''(x)=2u''(x)\cdot K_{uu}-2\theta''(x)\cdot Ku_{\theta} \qquad (4.5\text{-a})$$

$$\frac{Mt(x)}{GI,t}=\theta'(x) \qquad (4.2)$$

Y sustituyendo en (4.4) y luego en (4.5):

$$\theta''(x)=-\frac{p(x)\cdot S}{2GI,t}$$

$$p''(x)=2u''(x)\cdot K_{uu}+\frac{p''(x)\cdot S}{GI,t}\cdot K_{u\theta}$$

Derivando respecto a x dos veces:

$$p^{IV}(x)-2u^{IV}(x)\cdot K_{uu}+\frac{p''(x)\cdot S}{GI,t}\cdot K_{u\theta}$$

Sustituyendo en (4.1):

$$p^{IV}(x)-2\big(q(x)-p(x)\big)\frac{K_{uu}}{EI}-\frac{p''(x)\cdot S}{GI,t}\cdot K_{u\theta}=0$$

Simplificando, obtenemos la ecuación que rige el reparto transversal:

$$\mathbf{p^{IV}(x)-p''(x)\cdot\frac{K_{u\theta}\cdot S}{GI,t}+p(x)\cdot\frac{2K_{uu}}{EI}=2\frac{K_{uu}}{EI}\cdot p(x)} \qquad (4.6)$$

Que es una ecuación diferencial bicuadrada en p(x) de coeficientes constantes. Efectuando algunas transformaciones y denominando:

$$a=\frac{EI}{2K_{uu}} \qquad b=\frac{S\cdot K_{u\theta}\cdot EI}{2K_{uu}\cdot GI,t}$$

$$a\cdot p^{IV}(x)-b\cdot p''(x)+p(x)=q(x)$$

Se obtiene el polinomio característico de cuarto grado que se transforma de una forma sencilla en una de 2º grado:

$$at^4-bt^2+1=0$$

Usualmente el valor de b^2 es muy superior a 4a, con lo cual el discriminante es negativo y las cuatro raíces adoptan los valores de tipo $t = (+/-)\ u\ (+/-)\ i.v$, siendo los valores de u, y v los siguientes:

$$u=\frac{1}{2}\sqrt{\frac{2\sqrt{a}+b}{a}} \qquad v=\frac{1}{2}\sqrt{\frac{2\sqrt{a}-b}{a}}$$

Transformando las expresiones de variable compleja en funciones trigonométricas, la solución general de la ecuación homogénea, incluyendo las 4 variables de integración A1, A2, A3 y A4, es la siguiente:

$$\mathbf{p(x)=A1\cdot Cosh(ux)\cdot Cos(vx)+A2\cdot Cosh(ux)\cdot Sen(vy)+}$$
$$\mathbf{+A3\cdot Senh(ux)\cdot Cos(vx)+A4\cdot Senh(ux)\cdot Sen(vx)} \qquad (4.7)$$

4.1. Cálculo de deformaciones y solicitaciones en el caso general

La obtención de la solución de la función p(x) permite obtener todas las solicitaciones y deformaciones de viga, a partir de las derivaciones y cuadraturas propias de la teoría de vigas:

- **La ley de flexión transversal de losa** que es antimétrica, es la ecuación (4.4) que es también la de torsión repartida aplicada en cada viga mt(x) cambiada de signo.

- **La ley de flectores longitudinales** de vigas se obtiene a partir de las ecuaciones (4.4), y (4.5), con los parámetros a y b definidos anteriormente, y la relación directa entre curvaturas y momentos:

  $$\mathbf{M_f(x) = a\cdot p''(x) - b\cdot p(x)}$$

- **La ley de cortantes** se obtiene por derivación de la función anterior. En general:

  $$\mathbf{V(x) = -a\cdot p'''(x) + b\cdot p'(x)} = V(0) + \int_0^x p(x)dx - \int_0^x q(x)dx$$

  Particularizando en X = 0 y X = L se obtienen las reacciones en los extremos R_1 = -V(0) y R_2 = +V(L). La fórmula anterior también nos permite saber la función primitiva de p(x) directamente, que luego utilizaremos, y denominaremos P(x), sin necesidad de resolver la integral. Siendo obviamente P(0) = V(0), se obtiene:

  $$P(x)\ P(0) + \int_0^x p(x)dx = V(x) + \int_0^x q(x)dx$$

- **La ley de momentos torsores** en vigas se obtiene por integración de la ley de torsores repartidos según (4.4). Para ello es útil utilizar el valor de la integral obtenido anteriormente.

  $$\frac{dM_t(x)}{dx} = m_t(x) = p(x)\frac{s}{2} \rightarrow M_t(x) = M_t(0) + \frac{s}{2}[P(x) - P(0)]$$

  Las reacciones verticales de apoyo y el equilibrio global determinan el valor del torsor en el extremo. Considerando el valor de θ'(x), y siendo Q(x) la función primitiva de la ley de cargas exteriores q(x), establecemos la fórmula anterior modificada:

  $$GI,t.\theta'(x) = M_t(x) = M_t(0) + \frac{s}{2}[Q(x) + V(x) - V(0)]$$

  La integración de la ecuación anterior nos permite obtener la **ley de giros de torsión**, estimando las relaciones entre flectores y cortantes. Llamando QQ(x) la primitiva de la función Q(x):

  $$\theta(x) = \theta(0) = \frac{M_t(0)}{GI,t}\cdot x + \frac{S}{2GI,t}[QQ(x) - M_f(x) - xV(0)]$$

  A partir de la ecuación (4.3), y con la ley de giros de torsión se obtiene directamente la **ley de flechas**:

  $$u(x) = \frac{P(x)}{2K_{uu}} + \theta(x)\frac{K_{u\theta}}{K_{uu}}$$

Las expresiones analíticas generales p'(x), p"(x) y p"'(x), se presentan al final como apartado, incluyendo los valores de las primitivas de p(x) y P(x). Se calculan mediante una integral recurrente a partir de una doble integración por partes.

4.2. condiciones de contorno usuales

El cálculo de la expresión general (4.7) requiere determinar las cuatro variables de integración, de acuerdo a las condiciones de coacción al giro de torsión Los casos que aquí analizamos, que son los más frecuentes, corresponden a ambos extremos con giro de eje de viga impedido y giro libre; siempre con la condición de vigas apoyadas a flexión. Las condiciones de borde de las funciones analíticas anteriormente presentadas, que se utilizarán para tal fin son las siguientes:

a) Caso de extremos empotrados a torsión: Que es el caso más sencillo.

- Por condición de apoyo vertical:
  u(0) = u(L) = 0
- Por giro impedido a torsión:
  θ(0) = θ(L) = 0
- Con lo cual de acuerdo a ecuación (4.3):
  p(0) = p(L) = 0
- Por condición de flector nulo en los extremos:
  u"(0) = u"(L) = 0
- Con lo cual de acuerdo a ecuación (4.5):
  p"(0) = p"(L) = 0

Habiendo remarcado las cuatro condiciones de contorno del problema para el caso general.

b) Caso de extremos libres para el giro de torsión. Las cuatro condiciones son algo más complicadas. Se parte, al igual que antes de:

- Por condición de apoyo vertical:
  u(0) = u(L) = 0
- Por condición de flector nulo en los extremos
  u"(0) = u"(L) = 0.
- Con lo anterior se verifica que $p''(0) = -2K_\theta.\theta''(0)$. Aplicando la ecuación (4.5-b), se obtienen estas dos condiciones, en función de p(x) y su segunda derivada:

  $$\mathbf{p''(0) = p(0)\frac{K_\theta\cdot S}{GI,t} = p(0)\frac{b}{a}\ ;\ p''(L) = \frac{p(L)\cdot b}{a}}$$

- Las otras se obtienen considerando torsión nula en los extremos Mt(0) = Mt(L) = 0:
  - Aplicando la relación entre cortante y torsores en el extremo dorsal, y por condiciones de equilibrio general, obteniéndose una 3ª condición:

    $$\mathbf{0 = Q(L) + V(L) - V(0)}$$

    Esto nos dice que, aunque existe una redistribución transversal respecto a los esfuerzos isostáticos, ésta posee balance de suma cero, y por tanto podemos decir "lo que pasa en la viga se queda en la viga" para estados de carga puramente antisimétricos.
  - Por otra parte, derivando (4.3) y siendo θ'(0) = 0 por ser nulo el torsor, tenemos la siguiente condición en el extremo dorsal:

    $$p'(0) = 2\cdot u'(0)\ K_{uu} \qquad (4.8)$$

Es decir, necesitamos obtener una relación entre el del giro de flexión u'(0), y las funciones p y sus derivadas. Para ello se aplica la fórmula que obtiene el giro en extremo de viga biapoyada, en función de la integración del momento estático de la ley de curvaturas (2º Teorema de Mohr):

$$u'(0)\,L+\int_0^L (L-x)\cdot u''(x)\cdot d(x)=0 \qquad (4.9)$$

Conociendo la ley de curvaturas a partir de la ecuación (4.5):

$$\frac{p''(x)}{2K_{uu}}-\frac{p(x)\cdot S}{2GI,tK_{uu}}=K_{u\theta}=u''(x)$$

Con lo cual debemos calcular las integrales de p"(x)·(L-x) y p(x)·(L-x) para obtener la función de curvaturas. Integrando por partes y con alguna manipulación sencilla se obtiene:

$$\int_0^L (L-x)\cdot p(x)\cdot dx=(L-y)\cdot Q-P(0)\cdot L$$

$$\int_0^L (L-x)\cdot p''(x)\cdot dx=-L\cdot p'(0)+p(L)-p(0)$$

Siendo P(0) = V(0) el valor función primitiva de p(x) en el origen. Aplicando las fórmulas anteriores en (4.8) y (4.9) y despejando. se obtiene la cuarta condición de contorno:

$$-p(L)+p(0)-K_1\cdot L(0)=-K_1\cdot(L-y)\cdot Q$$

Siendo

$$K_1\frac{K_{u\theta}\cdot S}{GI,t}$$

En ambos casos, para condiciones de carga simétrica estas expresiones se simplifican notablemente, ya que la función de descarga p(x) también será simétrica, y solo requiere dos coeficientes a determinar por las condiciones anteriores en sus extremos, siempre que se considere el origen del eje X en el centro de la viga.

4.3. Caso de carga local: función de green

Es muy importante el caso en que la carga exterior es puntual (Q(y) aplicada en coordenada y), siendo entonces q(x) = **Q.δ(x-y)** siendo δ la función delta de Dirac. Se abre la posibilidad de aplicar el formalismo de funciones de Green para encontrar soluciones generales. En realidad los formularios de solicitaciones y deformaciones de vigas para carga puntual, son las funciones de Green G(X,Y) de doble variable: X la coordenada de viga e Y la posición de la carga. De hecho, el teorema de reciprocidad de Betti – Maxwell, es un corolario de la simetría en X e Y de la función de Green, al tratarse de un operador lineal. Si se conoce dicha función, para cualquier distribución de la carga exterior q(x), la solución puede obtenerse a partir de la fórmula siguiente

$$p(x)=\int_0^x G(x,y)\cdot q(y)\cdot dy$$

El planeamiento operativo pasa por obtener numéricamente la función G(x,y), y efectuar también numéricamente la integración. Otra propiedad útil es que si el funcional corresponde a un tipo

$$L[H(p(x)]=\delta(x-y)$$

Siendo L y H dos operadores diferenciales lineales, la función de Green será el producto de las funciones individuales de cada operador. Esto se verifica en nuestro caso, ya que la ecuación (4.6) se puede considerar la aplicación sucesiva de los operadores L = (k"- k) y H = (k" + k). La solución de cada una consta de dos términos de funciones trigonométricas ordinarias e hiperbólicas cuyo producto da la solución general (4.7).

El teorema de existencia considera que, si para condiciones de carga nula y de contorno homogéneas, no existe solución diferente de la trivial –lo cual se verifica siempre en estructuras elásticas–, existirá función de Green, y será formalmente similar a la expresada en (4.7), siendo los coeficientes (Ai) indeterminados, funciones de la posición de la carga (y). Para el caso de carga puntual –y en general la solución de función G(x,y)–, se establecen dos funciones a derecha e izquierda de la coordenada (y) de aplicación, siendo los cuatro coeficientes diferentes antes y después de la carga aplicada. Denominaremos A1 a A4 los aplicables por el lado izquierdo, y B1 a B4 a los del lado derecho de la viga, en relación al punto de aplicación. Hay por tanto 8 incógnitas a determinar en función de las condiciones de contorno y continuidad, de las cuales las cuatro primeras –**valores de contorno**– ya se han obtenido en el apartado anterior.

Las otras cuatro son las **condiciones de continuidad en el punto de aplicación de la acción**, que consisten en la propia continuidad de la función, y de sus dos primeras derivadas en la coordenada (y); la cuarta asigna valor del "salto" en ley de tercera derivada igual a -Q/a. La particularización de estos criterios a los resultados de solicitaciones y deformaciones es la siguiente:

- Las funciones Mf(x) y V(x) son diferentes para x<y x>y, siendo continua para x=y en el primer caso, y con salto de valor Q en el segundo. Esto es consecuencia de tratarse de la segunda y tercera derivada respectivamente de la función de descarga. Se obtienen por derivación según fórmulas (4.8) y (4.9).

- La integral de la función primitiva de p(x) se transforma en Q.H(x-y), siendo la función escalón de Heaviside en el punto de aplicación de la carga:

  $$P(x)=V(x)+H(x-y)$$

- En el caso de torsor no nulo en el extremo -caso de éste empotrado-, su valor se obtiene por equilibrio global: la mitad del momento isostático en el extremo, no recogido por el par de las reacciones, es el momento torsor en cada viga:

  $$M_t(0)=\frac{S}{2}\left[Q\left(\frac{Y}{L}-1\right)+V(0)\right]$$

  Con ello la ley de torsores sería, incluyendo el salto de la ley por la propia función H(x-y):

$$M_t(x) = M_t(0) + \frac{S}{2}\left[V(x) - V(0) + H(x-y)\right]$$

- Y la ley de giros de torsión, siendo HH(x-y) la función rampa igual a 0 para x<y e x-y para x>y:

$$\theta(x) = \theta(0) = \frac{M_t(0)}{GI,t}\cdot x + \frac{S}{2GI,t}\left[HH(x-y) - M_f(x) - xV(0)\right]$$

4.4. Caso de carga lineal uniforme

La solución de la ecuación diferencial (4.6) con valor de carga constante (q), consiste en la misma ecuación (4.7) como solución de la homogénea, más una solución particular que puede ser simplemente q, con lo cual queda:

$$p(x) = A1\cdot Cosh(ux).Cos(vx) + A2.Cosh(ux)\cdot Sen(vy) +$$
$$+A3\cdot Senh(ux)\cdot Cos(vx) + A4\cdot Senh(ux)\cdot Sen(vx) + q$$

Las expresión anterior se simplifica notablemente al considerar origen x'=0 el centro de la viga con lo cual los coeficientes A2 y A3 son nulos, ya que aportan componentes antisimétricas no compatibles con la solución. La ecuación posee por tanto solo 2 incógnitas a determinar con las dos condiciones de contorno en uno de los extremos, referentes a los valores de la función y de alguna de sus derivadas, dependiendo de las condiciones de apoyo. Las solicitaciones y deformaciones se obtienen de forma similar, siendo las expresiones de torsores y giros de torsión los siguientes:

$$M_t(x') = M_t\left(-\frac{L}{2}\right) + \frac{S}{2}\left(q\cdot[\![(x]\!]' + \frac{L}{2}\right) + V(x') - V\left(-\frac{L}{2}\right)\Big)$$

$$\theta(x') = \theta\left(-\frac{L}{2}\right) + \frac{M_t\left(-\frac{L}{2}\right)\cdot x'}{GI,t} + \frac{S\cdot[\![\left[\frac{q\cdot\left([\![x' + \frac{L}{2}\right)]\!]^2}{2} - M]\!]_f(x') - V\left(-\frac{L}{2}\right)\cdot\left(x' + \frac{L}{2}\right)\right]}{2GI,t}$$

4.5. Ánalisis de resultados para un caso tipo

Se ha aplicado las fórmulas anteriores, para un tablero con dos vigas artesas, con las siguientes características geométricas y mecánicas:

Luz de cálculo:	24.0m
Separación entre ejes de vigas:	5.50m (Plataforma 12m)
Canto tablero:	1.10 viga + 0.25 losa
Rigidez a flexión (EI) por viga:	14951 MNm²
Rigidez a torsión (GI,t) por viga:	14171 MNm²
Factor rigidez vertical losa (Kuu) =	2.56 MN/m²
Factor rigidez cruzada (Kuθ) =	7.04 MN/m
Factor K1 = Kuθ.S / GI,t =	0.00273 1/m²
Factor K2 = 2Kuu / EI =	0.00035 1/m⁴
Parámetro a = 1/K2 =	2849.3 m⁴
Parámetro b = K1/K2 =	7.79 m²

En los siguientes gráficos se presenta la función de Green de descarga p(X,Y) en kN/m para el caso de carga local de 1 kN (valor de p en coordenada X para carga situada en coordenada Y), para el caso de extremos fijos y libres a torsión:

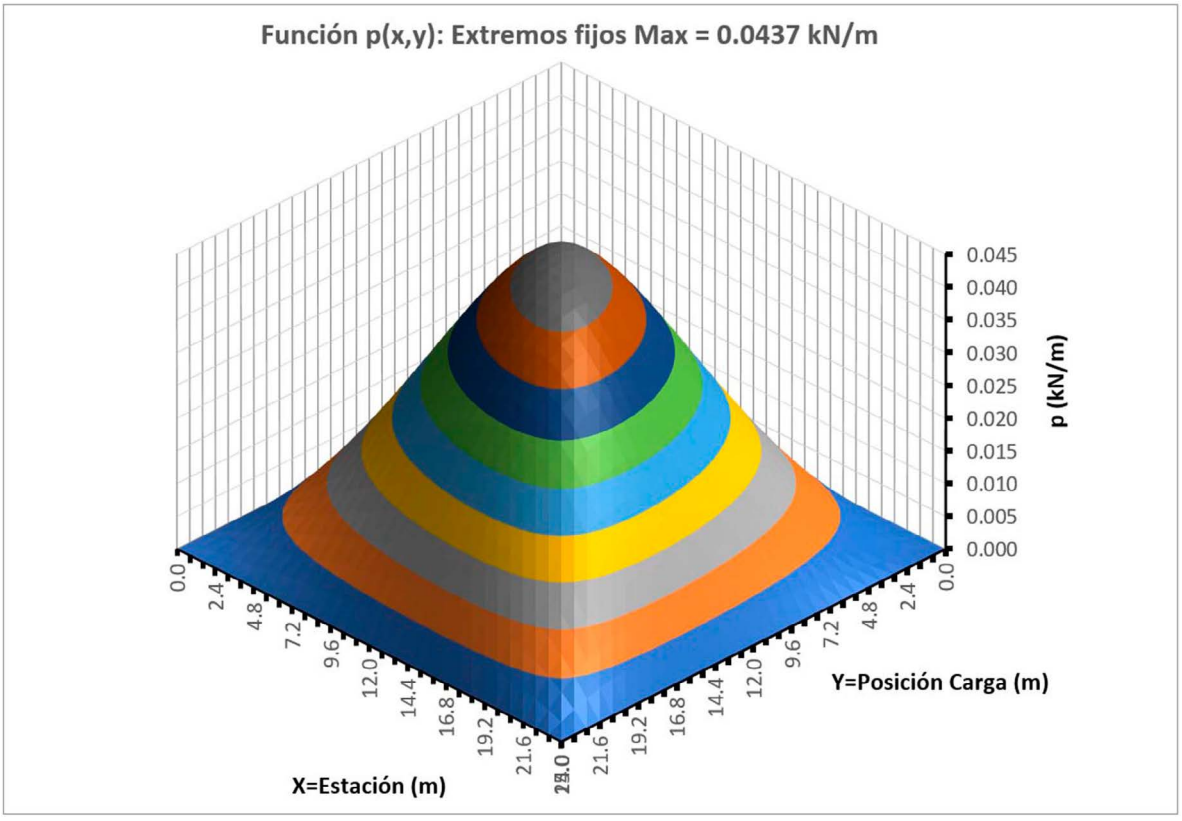

Figura 6: Función de Green de la función de descarga para carga antimétrica y apoyos fijos.

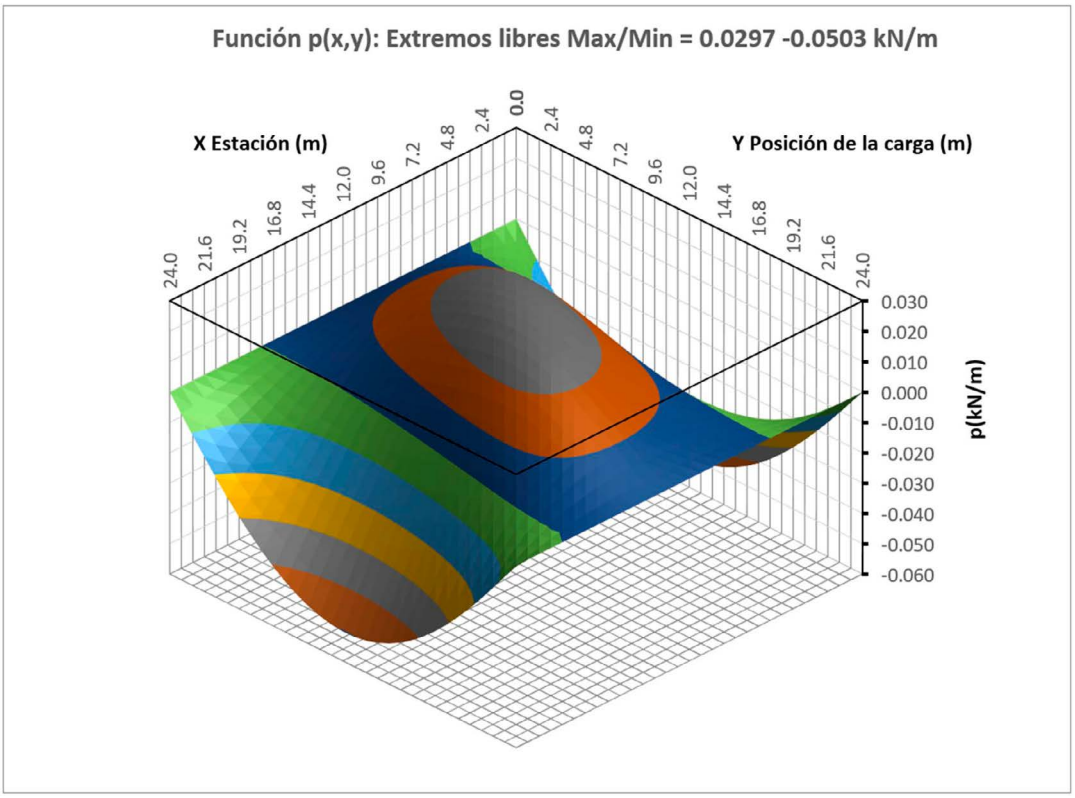

Figura 7. Función de Green de la función de descarga para carga antimétrica y apoyos libres.

Se presenta a continuación el diagrama de la función de descarga –en ambas condiciones de apoyo–, para el caso de carga lineal antimétrica:

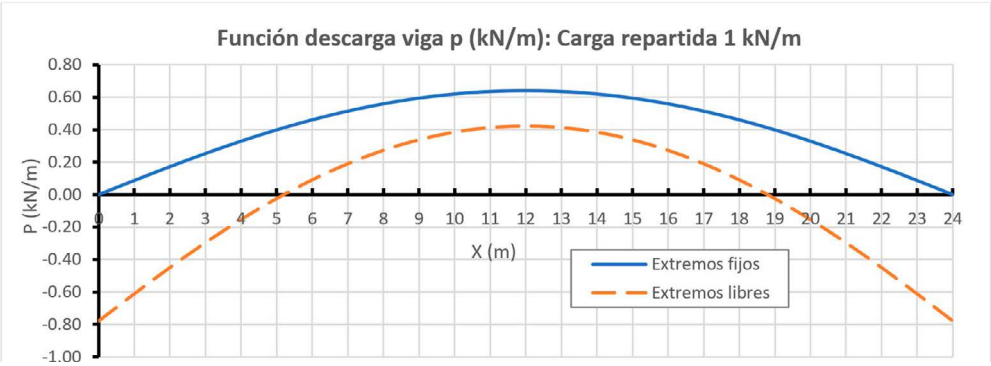

Figura 8. Función de descarga para carga repartida.

Y para el caso de carga puntual situada a 5.6m del apoyo:

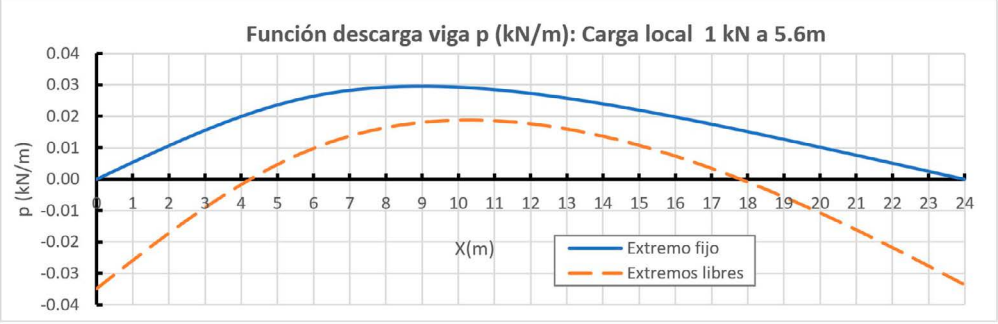

Figura 9. Función de descarga para carga local a ¼ luz.

Se observa la efectividad del reparto transversal, con un valor del 64.1% para el caso de extremos fijos frente al 42.3% del caso de extremos libres, en la situación de carga uniforme de viga. Es reseñable también, una inversión de la ley en el segundo caso en los extremos: el reparto solo es efectivo en los dos cuartos centrales, en donde se produce la mayor deformación; cuando esta se reduce en los extremos el efecto de giro de torsión es predominante, y se invierte el proceso. Como se ha observado anteriormente, se produce un reparto longitudinal con un balance de carga en apoyos cero. Esto se aprecia mejor en el diagrama de cortantes, en las que se compara además con la ley isostática sin reparto, observándose que su valor en el extremo es el mismo, solo obteniéndose una reducción, si los extremos están fijos.

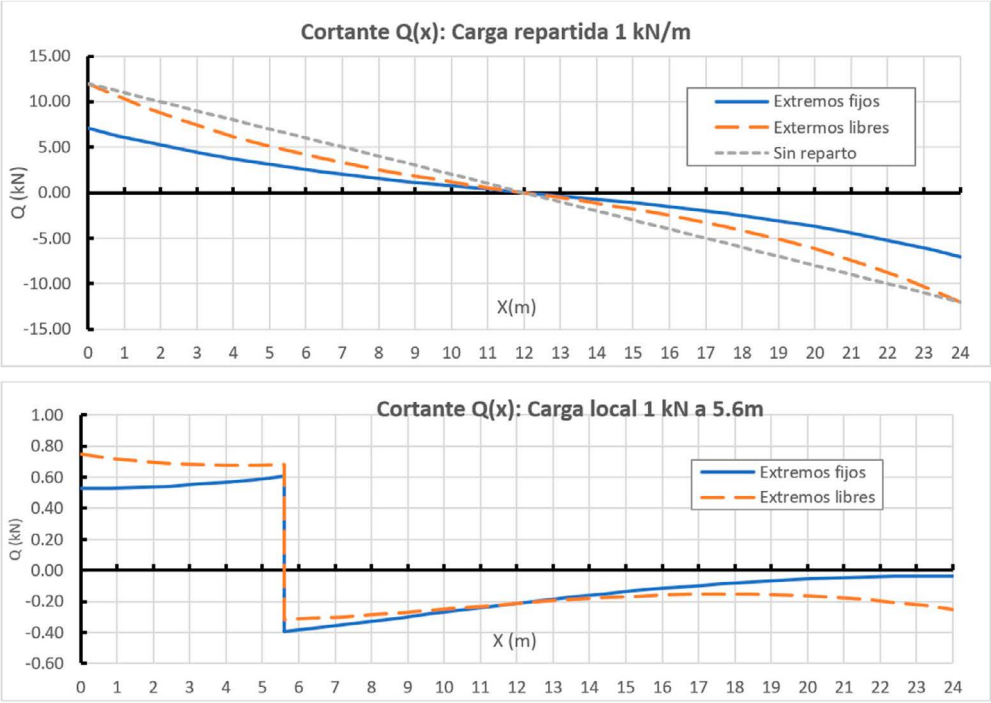

Figura 10. Cortantes para carga repartida y local a ¼ luz.

En términos de flectores, la reducción es apreciable: 52.3 % frente a 20.6%, tal como se aprecia en el siguiente gráfico.

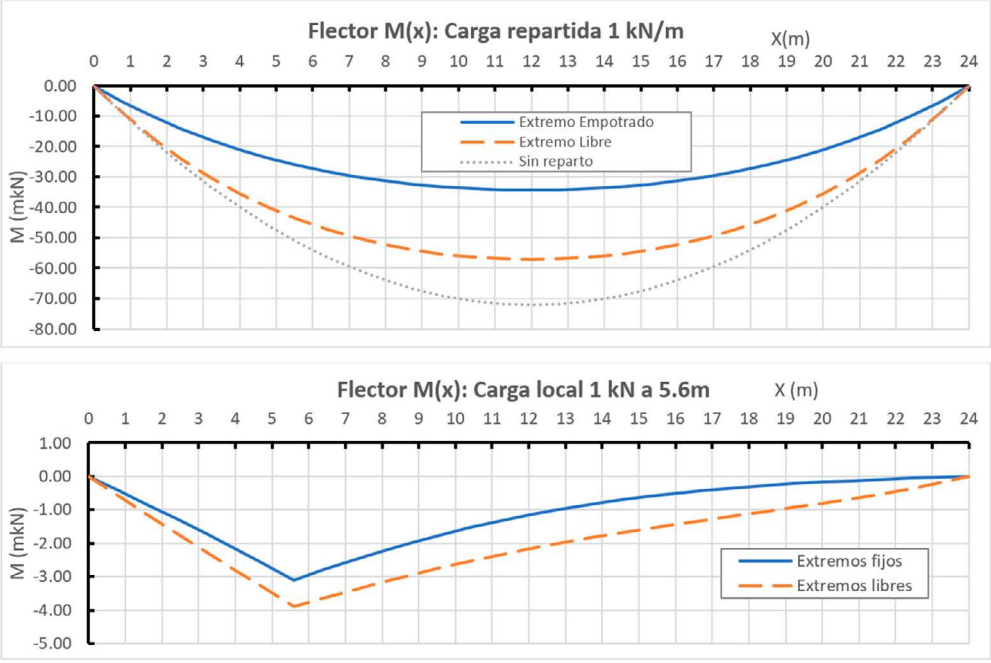

Figura 11. Flectores para carga repartida y local a ¼ luz.

En los siguientes gráficos se presentan de forma comparativa para ambos tipo de sustentación, los diagramas de torsores, deformaciones verticales y giros de torsión:

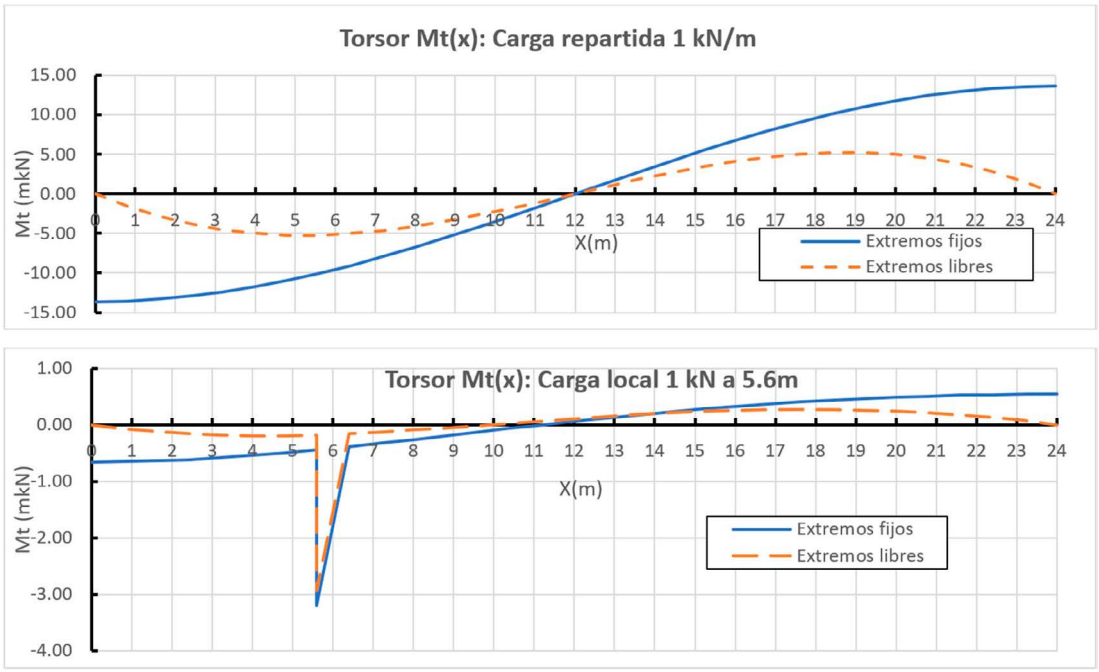

Figura 12. Torsores para carga repartida y local a ¼ luz.

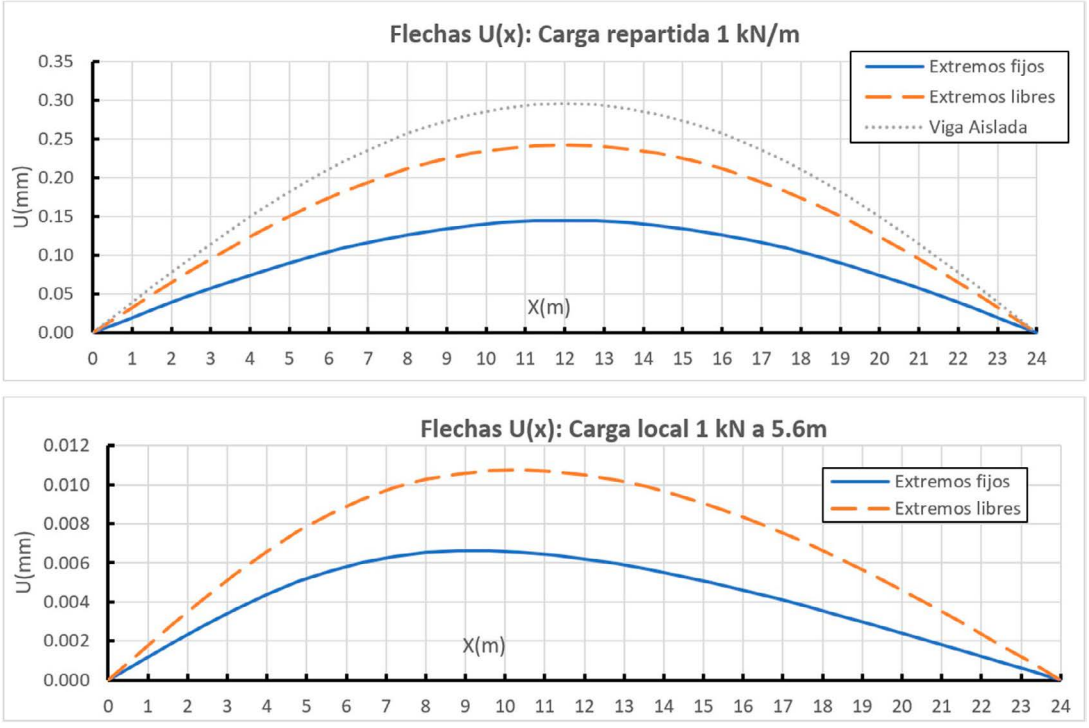

Figura 13: Diagrama de flechas para carga repartida y local a ¼ luz.

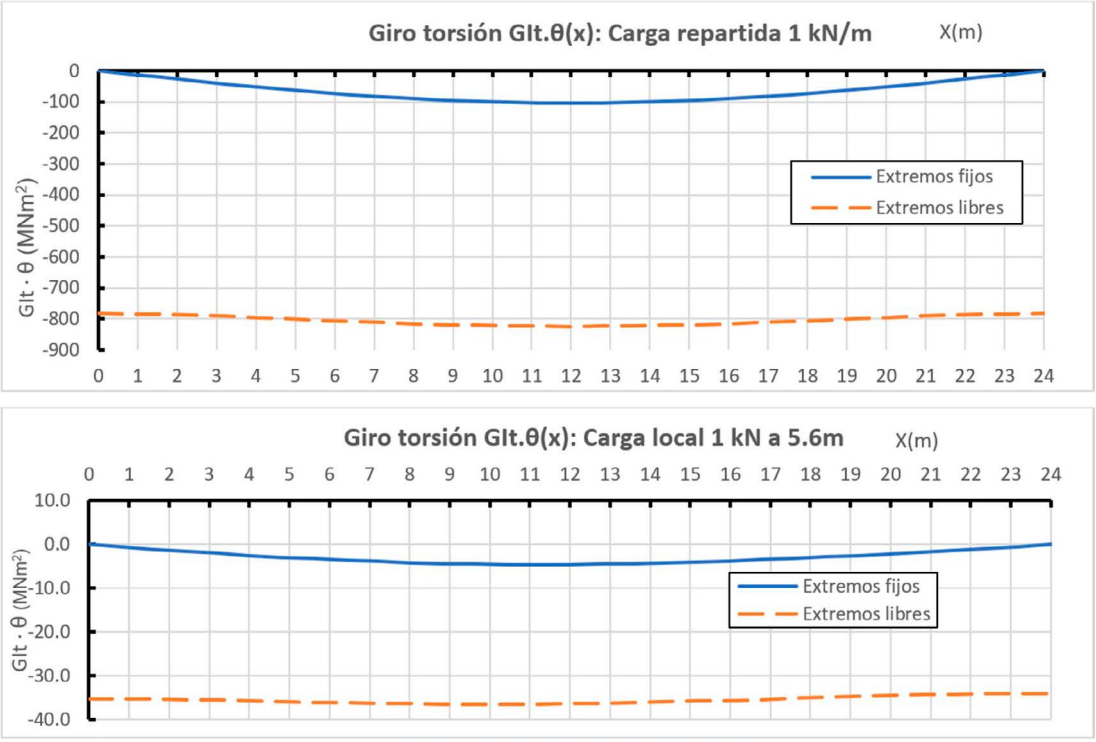

Figura 14.Diagrama de giros de eje viga para carga repartida y local a ¼ luz.

5. ESTADO DE APLICACIÓN DE MOMENTO TORSOR ANTISIMÉTRICO

El planteamiento de reparto transversal es bastante parecido, sin más que sustituir la función de carga q(x), por otra ma(x) –torsor repartido a lo largo de la viga–, para obtener como resultado la función de descarga p(x), de acuerdo al siguiente esquema:

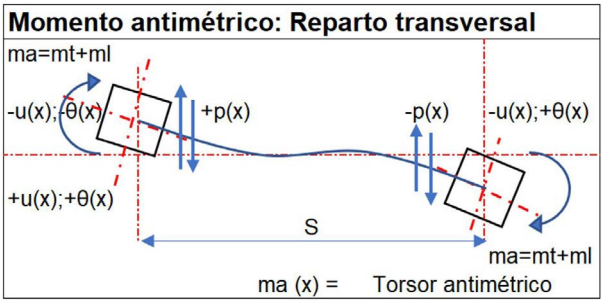

Figura 15. Nomenclatura de acciones, solicitaciones y deformaciones para momento antimétrico.

Para conservar la acción exterior positiva, la función de descarga posee signo negativo en ella, es decir, se trata en realidad de una función de recarga vertical hacia abajo que provocará deformación vertical negativa y flexión positiva en dicha viga. En este caso, la acción exterior ma(x) se repartirá en un torsor de viga mt(x) y una flexión de losa ml(x). La nomenclatura de las variables y los criterios de signos son los mismos que el caso anterior.

Las ecuaciones que relacionan dichas variables en este caso son las siguientes

1. La primera ecuación es la general de flexión viga Bernoulli, que en este caso carece de término de carga exterior aplicada, siendo negativo el signo al corresponder a la recarga de viga hacia abajo:

$$-p(x) = EI \cdot u^{IV} \tag{5.1}$$

2. Las ecuaciones (2.2) y (2.3) son las mismas que en el caso anterior, reproduciéndolas por conveniencia:

$$\frac{M_t(x)}{GI,t} = \theta'(x) \tag{5.2}$$

$$p(x) = 2u(x) \cdot K_{uu} - 2\theta(x) \cdot K_{u\theta} \tag{5.3}$$

3. La ecuación de equilibrio de losa cambia de signo, de acuerdo al criterio explicado. A dicha ecuación hay que añadir, el reparto del momento exterior entre viga y losa

$$ml(x) = +\frac{p(x) \cdot S}{2} \tag{5.4}$$

$$ma(x) = ml(x) + mt(x) \tag{5.5}$$

Con todo ello, entre (5.1), (5.3) y (5.4) se obtiene:

$$\frac{ml(x)}{S} = u(x) \cdot K_{uu} - \theta(x) \cdot K_{u\theta}$$

$$\frac{-2 \cdot ml(x)}{S} = EI \cdot u^{IV}$$

$$\frac{-EI \cdot u^{IV}}{2} = u(x) \cdot K_{uu} - \theta(x) \cdot K_{u\theta} \tag{5.6}$$

Entre (5.5), derivando (5.2), y sustituyendo en la anterior:

$$ma(x) = ml(x) + GI,t \cdot \theta''(x)$$

$$ma(x) = -\frac{EI \cdot S \cdot u^{IV}}{2} + GI,t \cdot \theta''(x) \qquad (5.7)$$

Despejando θ(x) de (5.6) y derivando dos veces:

$$\theta''(x) = u''\frac{K_{uu}}{K_\theta} + \frac{EI \cdot u^{IV}}{2K_{u\theta}}$$

Esta expresión se sustituye en (5.7), para obtener:

$$ma(x) = -\frac{EI \cdot S \cdot u^{IV}}{2} + GI,t\left[u''\frac{K_u}{K_{u\theta}} + \frac{EI \cdot u^{IV}}{2K_{u\theta}}\right]$$

Podemos efectuar un cambio de variable identificando el factor EI.u"(x) como mf(x), el flector longitudinal, con lo cual queda:

$$\frac{2ms(x)}{GI_t} = \frac{mf^{IV}(x)}{K_{u\theta}} - \frac{S \cdot mf''(x)}{GI_t} + \frac{K_{uu}}{EI \cdot K_{u\theta}} mf(x)$$

Reordenando los términos:

$$mf^{IV}(x) - \frac{K_\theta \cdot S}{GI_t} mf''(x) + \frac{2K_{uu}}{EI} mf(x) = \frac{2ma(x) \cdot K_{u\theta}}{GI_t} \qquad (5.8)$$

Que es exactamente la misma ecuación diferencial (4.7) que rige el reparto para carga vertical, salvo el cambio de factores de rigideces del término independiente. Denominando al igual que antes:

$$a = \frac{EI}{2K_{uu}} \qquad b = \frac{S \cdot K_{u\theta} \cdot EI}{2K_{uu} \cdot GI,t} \qquad c = \frac{K_{u\theta} \cdot EI}{K_{uu} \cdot GI,t}$$

$$a \cdot mf^{IV}(x) - b \cdot mf''(x) + mf(x) = c.ma(x) \qquad (5.9)$$

Por tanto, la solución general de esta ecuación diferencial en términos de mf(x), es idéntica a la obtenida anteriormente (5.10)

mf(x)=A1·Cosh(ux)·Cos(vx)+A2·Cosh(ux)·Sen(vy)+A3·Senh(ux)·Cos+A4·Senh(ux)·Sen(vx)

5.1. Cálculo de deformaciones y solicitaciones en el caso general

La obtención de la solución de la función mf(x) permite obtener expresiones sencillas del resto de solicitaciones y deformaciones mediante estos pasos:

- La ley de cortantes se obtiene por derivación de la ley de flectores, y la función de reparto por derivación de la ley de cortantes:

$$V(x) = -\frac{dmf(x)}{dx} \qquad p(x) = \frac{dV(x)}{dx} = -\frac{d^2mf(x)}{dx^2}$$

- Con las reacciones de apoyo y el equilibrio global, se calcula el valor del torsor en el extremo dorsal, en el caso de que estuviera empotrado. La ley de torsores repartidos se obtiene directamente a partir de la ley de reparto p(x) multiplicada por S/2. Con ello, el torsor en el extremo dorsal y la ley de torsores antisimétricos dato, se obtiene la ley de torsores en cualquier sección, siendo Ma(x) la función primitiva de la ley de momentos antisimétricos exteriores:

$$\frac{dM_t(x)}{dx} = -mx(x) = -ma(x) + ml(x) = -ma(x) + p(x)\frac{S}{2}$$

$$M_t(x) = M_t(0) - Ma(x) + [V(x) - V(0)]\frac{S}{2}$$

- La integración de la ecuación anterior nos permite obtener **la ley de giros de torsión**, estimando las relaciones entre flectores y cortantes. Siendo MMa(x) la función primitiva de Ma(x).

$$\theta(x) = \theta(0) + \frac{M_t(0)}{GI,t}x - \frac{MMa(x)}{GI,t} - \frac{S}{2GI,t}[M_f(x) + x \cdot V(0)]$$

- Con la función de descarga y con la **ley de giros de torsión** se obtiene directamente la ley de flechas:

$$u(x) = \frac{p(x)}{2K_{uu}} + \theta(x)\frac{K_{u\theta}}{K_{uu}}$$

Las expresiones analíticas generales de la funciones mf(x), sus derivadas y sus primitivas son idénticas a las presentadas para la función p(x) del caso anterior.

5.2. Condiciones de apoyo a torsión usuales

Análogamente, obtendremos las expresiones aplicadas a los casos de extremos analizados:

a) **Caso de extremos empotrados a torsión**:
   - Por apoyo simple a flexión:
     mf(0) = mf(L) = 0
   - Por giro impedido a torsión:
     θ(0) = θ(L) = 0
   - Por condición de apoyo vertical:
     u(0) = u(L) = 0
   - Con lo cual de acuerdo a ecuación (5.3):
     mf"(0) = mf"(L) = 0

Siendo las marcadas, las cuatro condiciones de contorno del problema para el caso general.

b) **Caso de extremos libres para el giro de torsión**. Las cuatro condiciones son algo más complicadas. Al igual que antes:
   - Por apoyo simple a flexión:
     mf(0) = mf(L) = 0
   - Por condición de apoyo vertical:
     u(0) = u(L) = 0
   - Por torsor nulo en los extremos:
     θ'(0) = θ'(L) = 0

La resultante global de torsión exterior se equilibra con los pares de torsión que general las reacciones en los extremos, las cuales se obtienen por el valor de la derivada de la mf(x) en los extremos. Se considera el caso general, de resultante exterior variable, en función de su primitiva en los extremos. Con ello tenemos la siguiente 3ª condición:

$$[mf'(0) - mf'(L)]\,\frac{S}{2} = Ma(L) - Ma(0)$$

- La cuarta condición es algo más complicada. En el extremo dorsal, al tener torsor nulo, $\theta'(0) = 0$, $p'(0) = -2K_u.u'(0)$ relación que nos proporcionará la solución, estableciendo las variables en función de los flectores: La función p' es la tercera derivada de la ley de flectores, particularizada en 0; u'(0) es el giro en el extremo de flexión de viga, que se puede sacar por integración de la ley de flectores (Teorema de Mohr) y la rigidez a flexión; aplicándolo de la misma manera que en la ecuación (4.8):

$$\int_0^L (L-x)\cdot mf(x)\cdot dx = mf_{der}(Y)\cdot(L-y) + mf_{izq}(Y)\cdot(L-y) - mf_{izq}(0)\cdot L + MMf_{der}(L) - MMf_{izq}(0) = -EI\cdot u'(0)\cdot L$$

  Siendo Mf(x) la función primitiva de mf(x) –que se relaciona con la ley de giros de flexión– y MMf(x) la segunda primitiva –que se relaciona con ley de flechas–. Hay que observar que la primera función puede no ser continua en x = y (caso de momento puntual), y debe contemplarse el salto mediante la aplicación de funciones diferentes por la izquierda y por la derecha en la integración por partes. En el caso de la segunda integral, ese salto no se produce.

Con los cual, se obtiene una expresión que relaciona la 3ª derivada de la función de flexión y sus primitivas, y que proporciona la 4ª condición.

$$m''(0) + \frac{2K_{uu}}{EI\left[mf_{izq}(0) + \frac{MMf_{izq}(0) - MMf_{der}(L)}{L} = Mf_{der}\left(1-\frac{Y}{L}\right) - Mf_{izq}\left(1-\frac{Y}{L}\right)\right.} = 0$$

Al igual que para carga vertical exterior, en caso de distribución simétrica, la solución solo requiere dos coeficientes a determinar por condiciones de apoyo de los extremos, si se dispone el origen del eje viga X en su centro.

5.3. *Caso de momento local: función de green*

Siguiendo la misma metodología que el caso de carga puntual, analizaremos la solución para la acción exterior $\mathbf{ma(x) = m_a\cdot\delta(x-y)}$, añadiendo a las cuatro condiciones de externo anteriormente obtenidas, las mismas condiciones de continuidad en el punto de aplicación, con la única diferencia es asignar el valor de "salto" en tercera derivada en valor $-c.m_a/a$ (siendo c el valor de la fórmula 5.9). Con ello se obtienen las 8 constantes de integración para obtener los resultados siguientes:

- Las funciones mf(x), V(x) y la función de descarga p(x), se obtienen de forma directa como primera y segunda derivada respectivamente; son continuas, pero diferentes para x<y x>y.
- En el caso de torsor no nulo en el extremo -caso de éste empotrado-, su valor se obtiene también por equilibrio global: la mitad del momento de reparto isostático en el extremo, no recogido por el par de las reacciones, es el momento torsor en cada viga:

$$M_t(0) = \frac{S}{2}\,V(0) + m_a\left(1-\frac{Y}{L}\right)$$

  Con ello la ley de torsores sería, incluyendo el salto de la ley por la propia función H(x-y):

$$M_t(x) = M_t(0) + \frac{S}{2}\,[V(x) - V(0)] - m_a\cdot H(x-y)$$

- Con la ley de giros de torsión, siendo HH(x-y) la función rampa igual a 0 para x<y e x-y para x>y, y la expresión

$$\theta(x) = \theta(0) + \frac{M_t(0)}{GI,t}\,x + \frac{S}{2GI,t}\cdot[M_f(x) - x\cdot V(0)] - m_a\cdot HH(x-y)$$

5.4. *Caso de momento torsor uniforme*

La solución de la ecuación diferencial (5.8) con valor de momento repartido de valor constante (m_a), se obtiene de igual manera añadiendo a la ecuación general, la solución particular ma de valor constante

$$mf(x) = A1\cdot Cosh(ux)\cdot Cos(vx) + A2\cdot Cosh(ux)\cdot Sen(vy) + A3\cdot Senh(ux)\cdot Cos(vx) + A4\cdot Senh(ux)\cdot Sen(vx) + c.m_a$$

Las solicitaciones y deformaciones se obtienen de forma similar, siendo las expresiones de torsores y giros de torsión los siguientes

$$M_t(x') = M_t\left(-\frac{L}{2}\right) - m_a\left(x'+\frac{L}{2}\right) + \frac{S}{2}\left[V(x') - V\left(-\frac{L}{2}\right)\right]$$

$$\theta(x') = \theta\left(-\frac{L}{2}\right) + \frac{M_t\left(x'+\frac{L}{2}\right)}{GI,t} + \frac{m_a\left(x'+\frac{L}{2}\right)^2}{2GI,t} - \frac{S\cdot\left[M(x')x'[\!+V\left(-\frac{L}{2}\right)\cdot\left(x'+\frac{L}{2}\right)\right]}{2GI,t}$$

5.5. *Análisis de resultados*

Para las mismas características de tablero que en el caso de cargas verticales anti métricas, se presentan a continuación los resultados para acciones de momentos. Se presentan a continuación las funciones de Green para extremos fijos y libres:

Los valores máximos obtenidos son de 0.124 en el primer caso (X=Y=12m), y 0.894 en el mismo punto, con una distribución que, como se observa, es muy poco dependiente de la posición de la carga. Los diagramas de momentos de flexión, que es la función de obtención directa, son los siguientes.

La comparación en este caso se realiza con la flexión inducida por una carga lineal de +/- 2m/S, sin torsión de vigas. Como se observa, la eficiencia del reparto es aquí muy grande para el caso de apoyos fijos (reducción del 93.1%) y muy reducida para apoyos libres (20.6%), superior al caso de carga lineal. Este efecto viene gobernado por la rigidez a torsión propia de la viga, y no por la transferencia de carga entre vigas; es por tanto determinante en este caso los factores de relación ancho – luz, y la relación de rigideces a flexión y torsión, además de las condiciones de apoyo de los extremos, como se aprecia bien en las funciones de descarga transversal (Fig. 20).

Los diagramas de cortantes y torsores están en relación con el argumento anterior: vigas muy poco solicitadas a cortante con extremos fijos, y muy solicitadas a torsión, y viceversa para extremos libres.

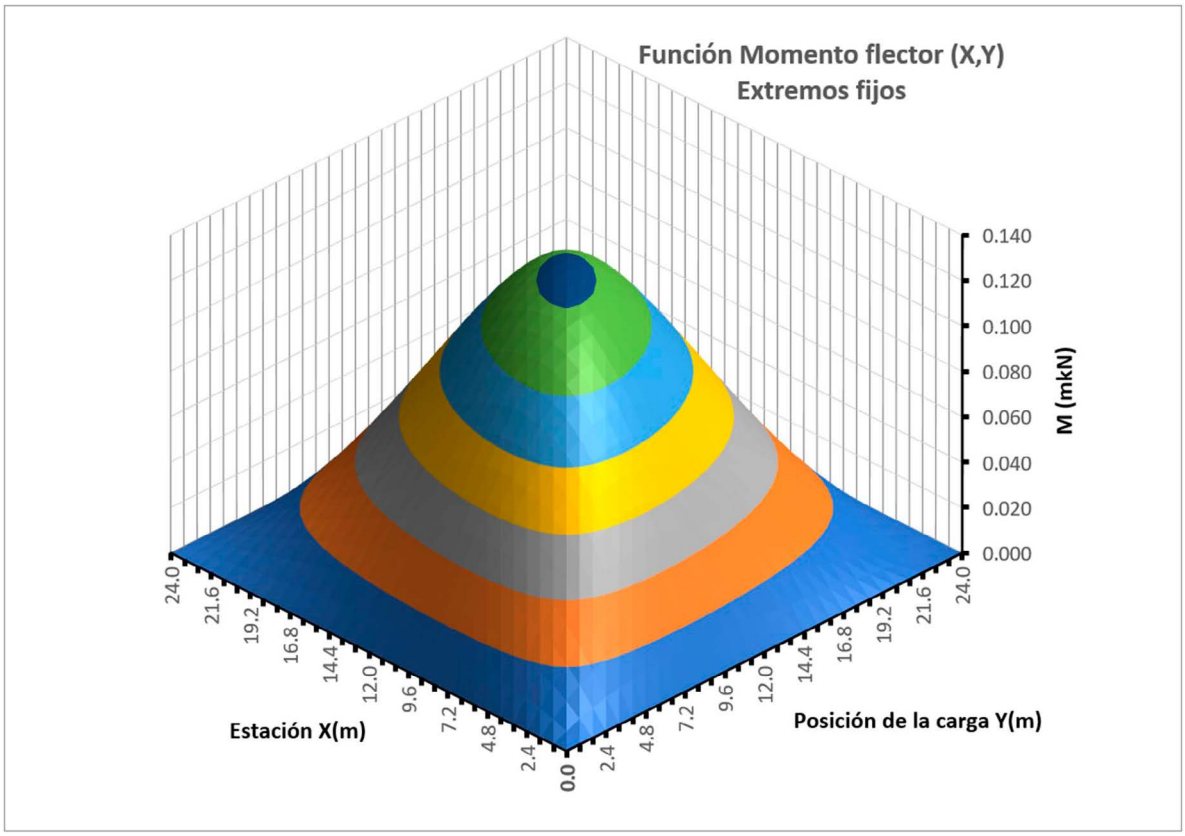

Figura 16. Función de Green de la función de descarga para momento antimétrico y apoyos fijos.

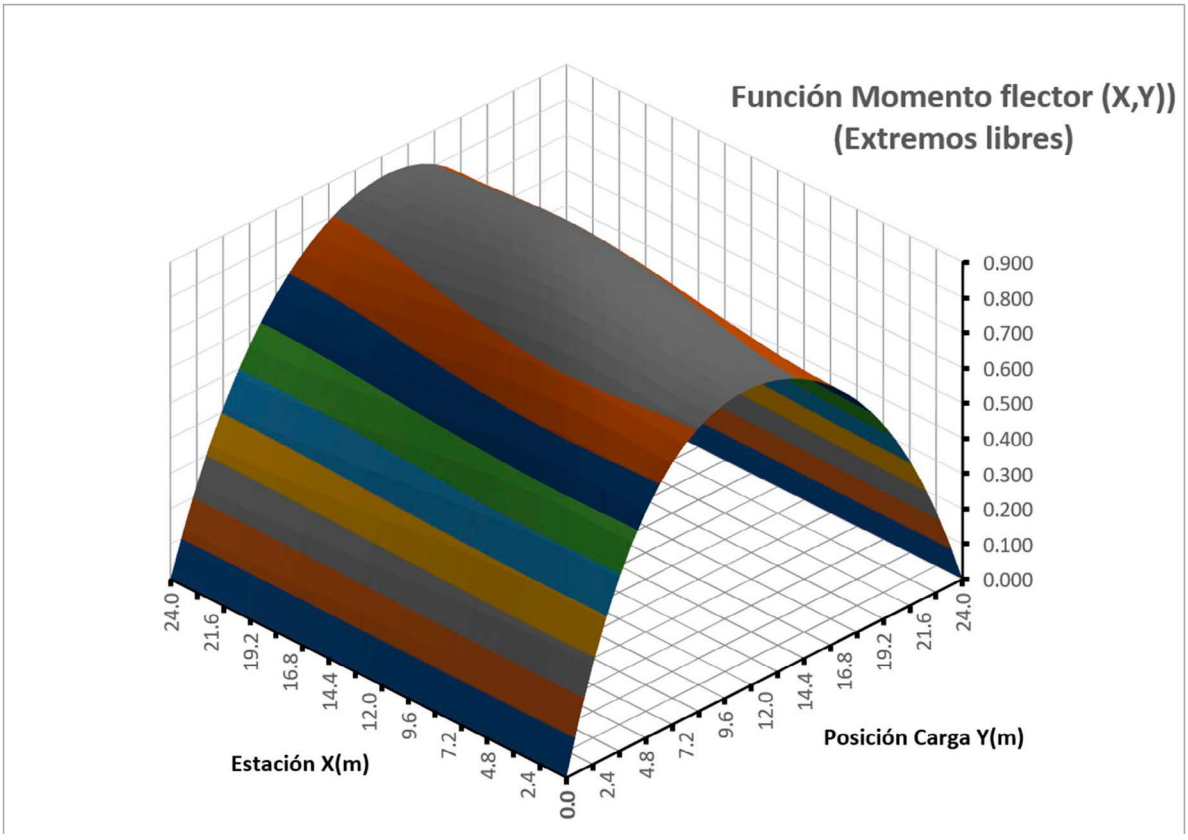

Figura 17. Función de Green de la función de descarga para momento antimétrico y apoyos libres.

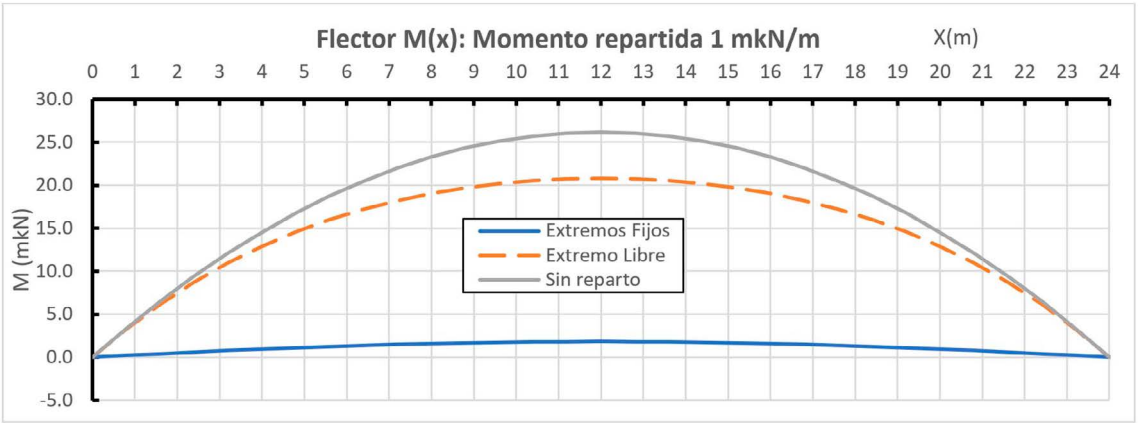

Figura 18. Flectores para momento repartido.

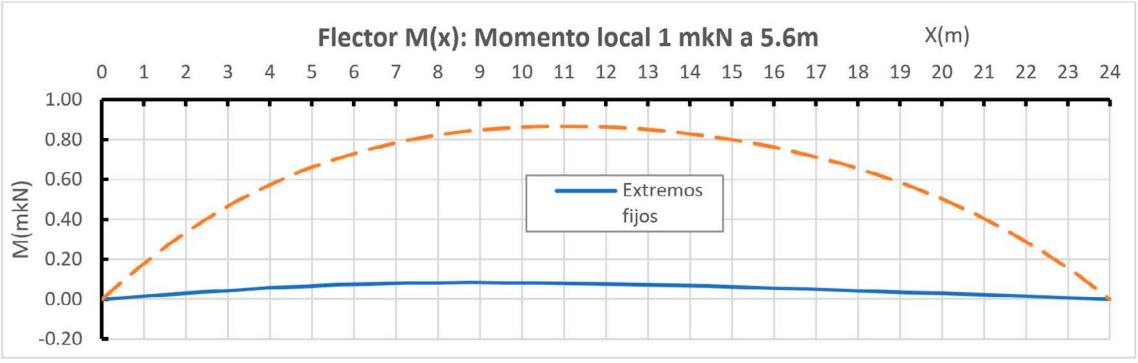

Figura 19. Flectores para momento local a ¼ luz.

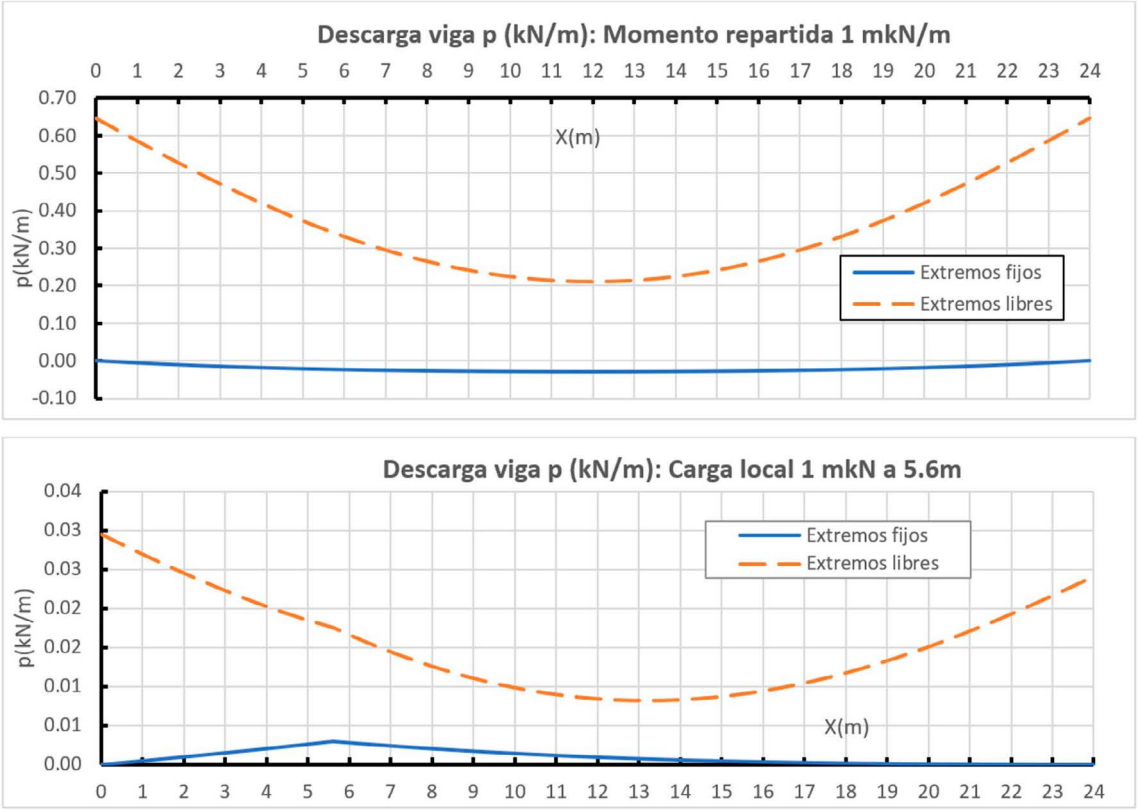

Figura 20. Función de descarga para momento repartido y local a ¼ luz.

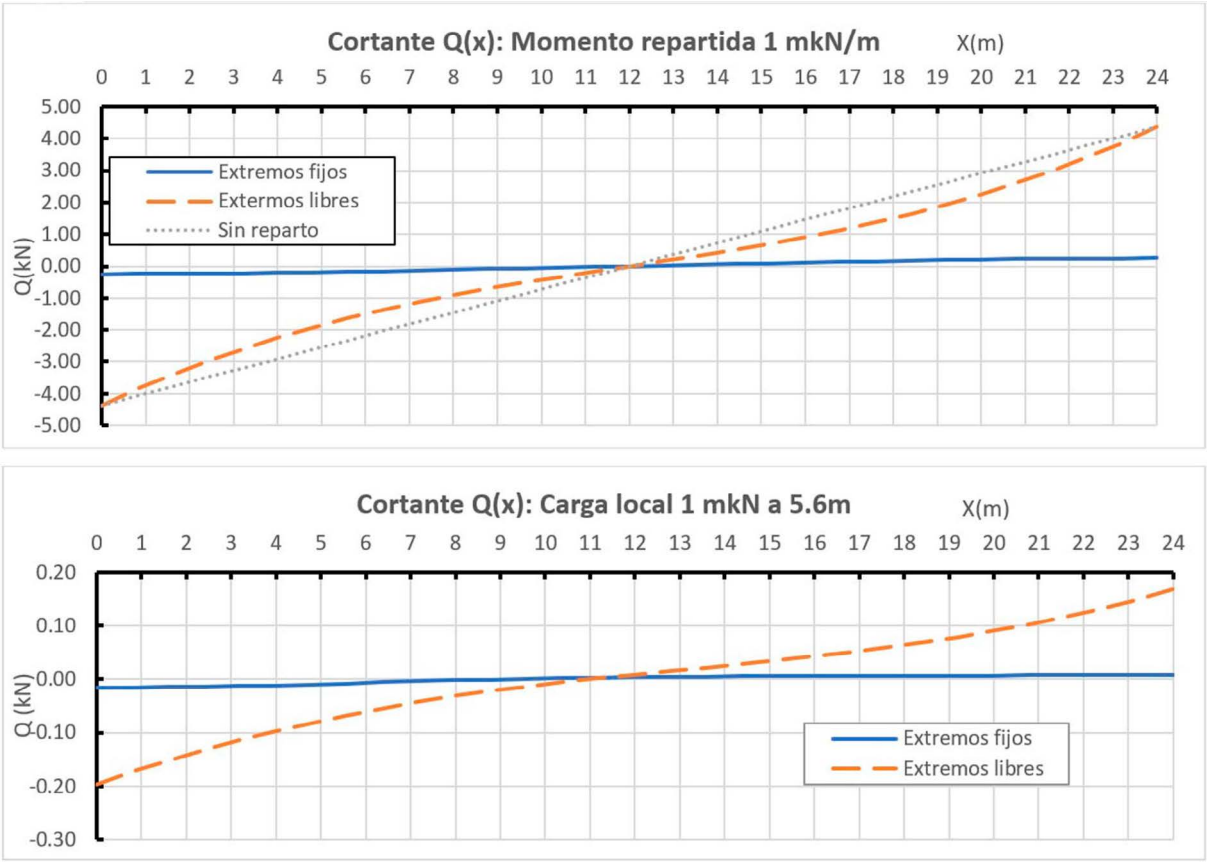

Figura 21. Cortante para momento repartido y local a ¼ luz.

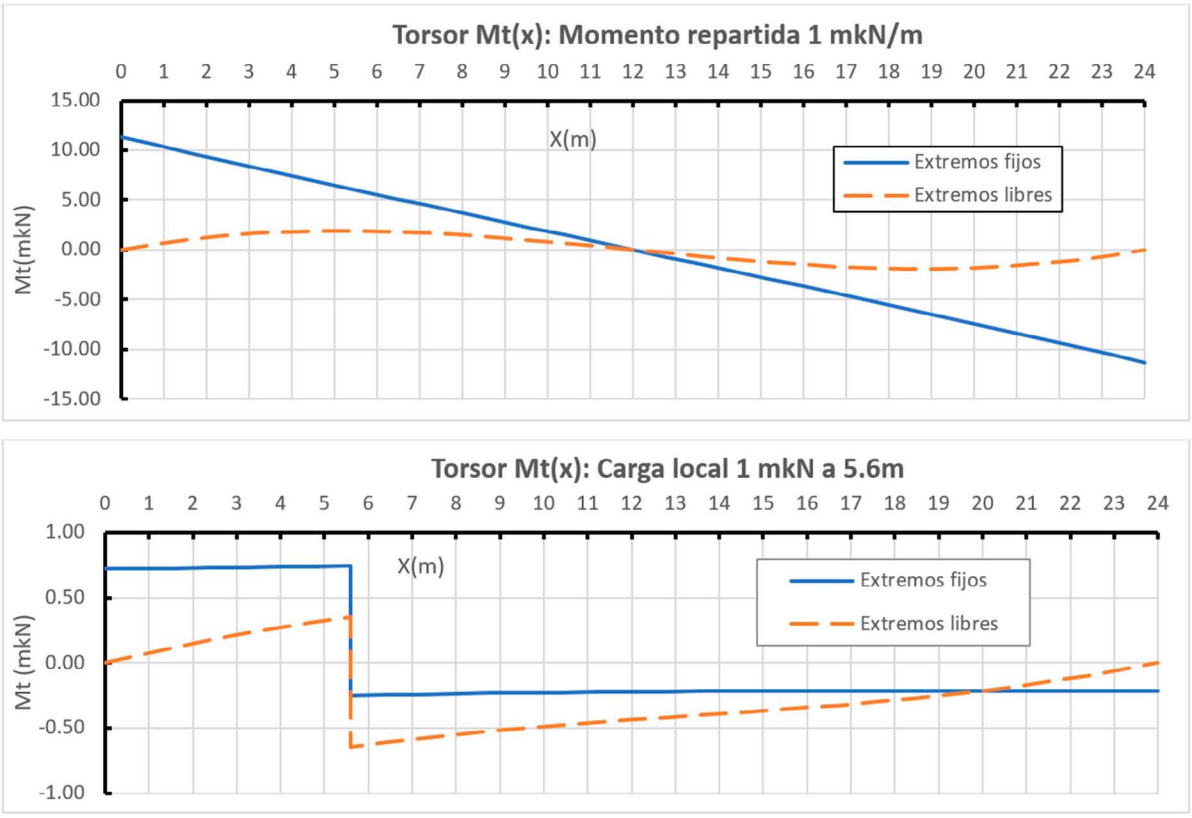

Figura 22: Torsor para momento repartido y local a ¼ luz.

Los diagramas de deformaciones (giros de eje viga y flechas) son los siguientes:

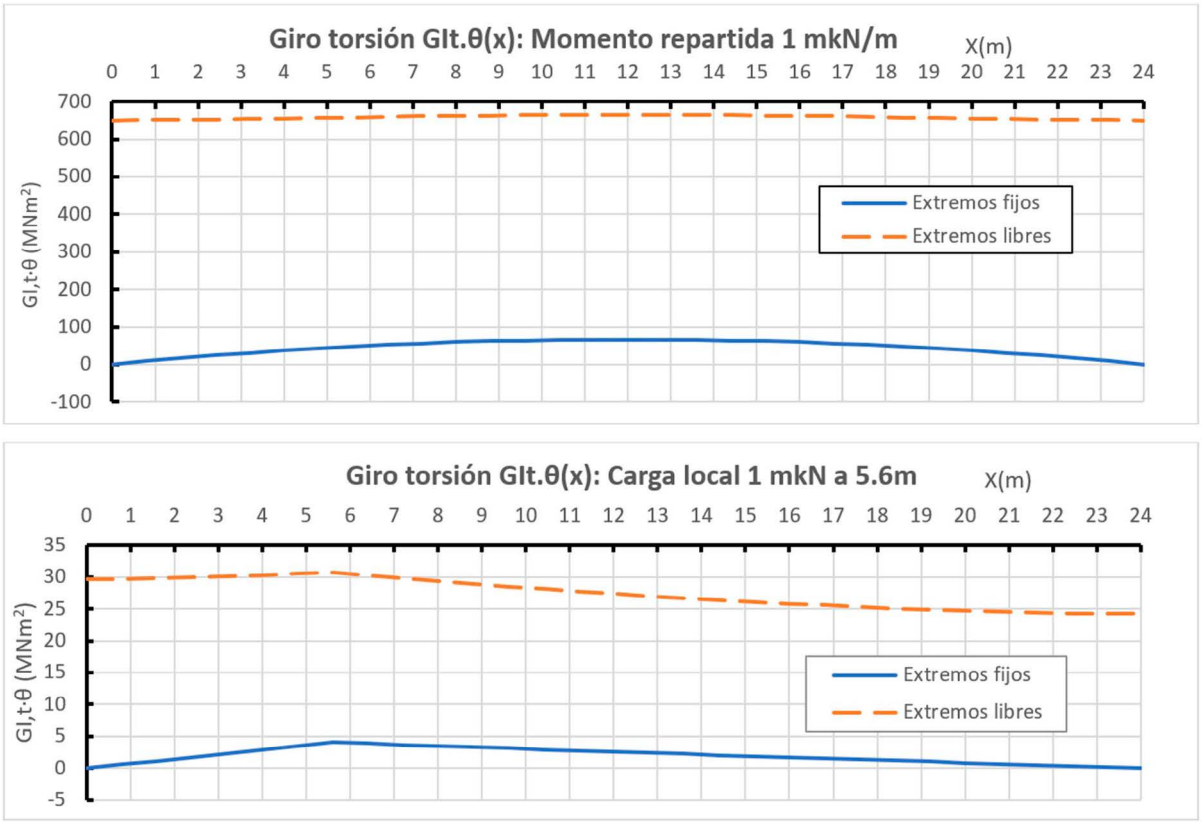

Figura 23. Giros de eje viga para momento repartido y local a ¼ luz.

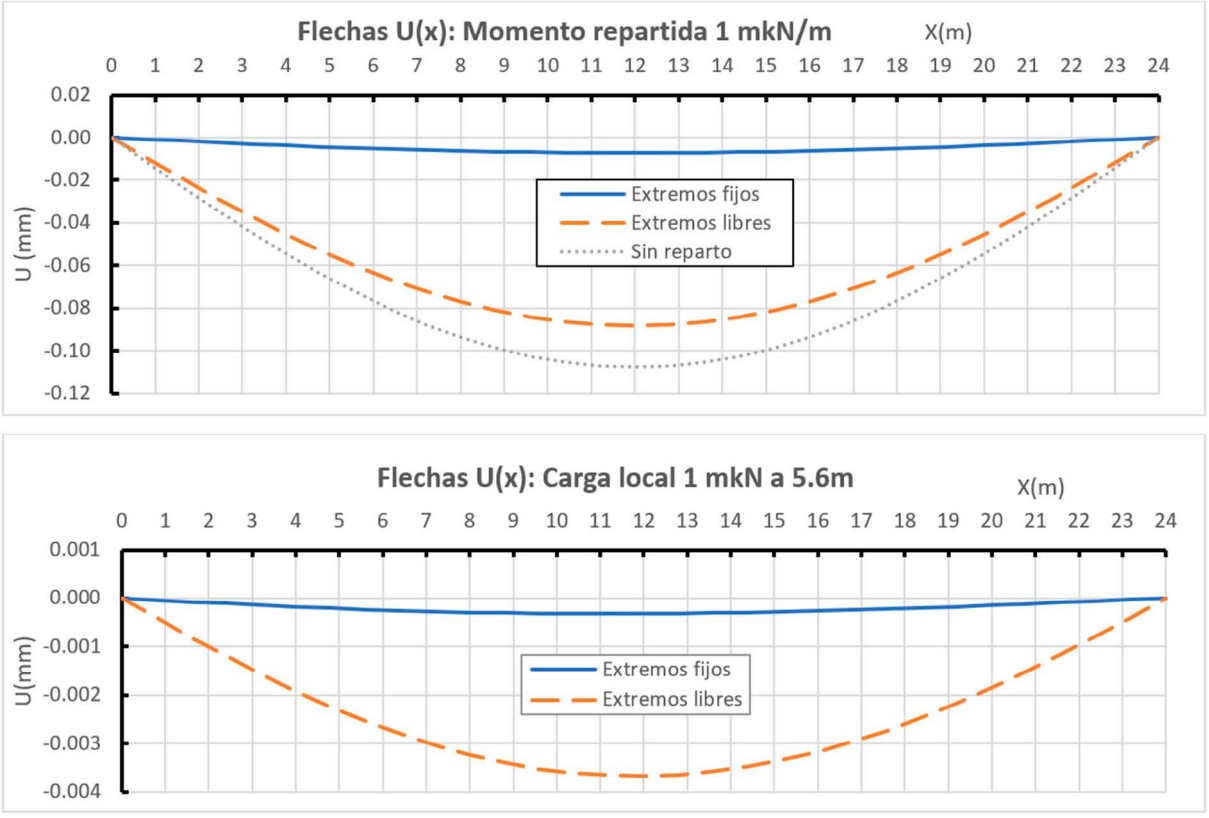

Figura 24. Diagrama de flechas de viga para momento repartido y local a ¼ luz.

Todo ello indica que la solicitación de torsión antimétrica se transforma casi en su totalidad en flexión longitudinal de cada viga en el caso de extremos libres, y en torsión de Saint Venant en el caso de extremos fijos, modulándose su valor con las propiedades mecánicas y geométricas del tablero.

6. ESTADO DE APLICACIÓN DE MOMENTO TORSOR SIMÉTRICO

Para terminar la descomposición de estados, se analiza a continuación la solicitación con función de momentos torsores simétricos respecto al eje de tablero. Esta situación no genera trabajo de flexión en viga, y sólo se produce un reparto longitudinal de torsores; de hecho el caso de torsor uniforme en ambas vigas con extremos libres es una solución trivial de flexión transversal solo en losa. En el caso general, vamos a plantear las ecuaciones de equilibrio y compatibilidad:

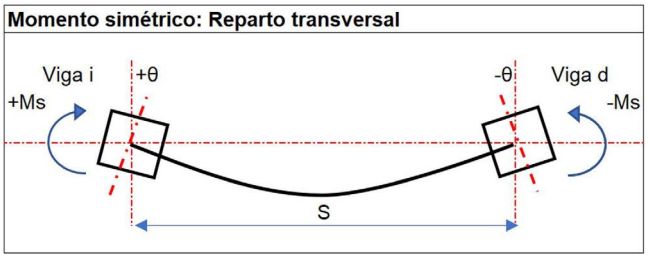

Figura 25. Nomenclatura de acciones, solicitaciones y deformaciones para momento simétrico.

Se aplica una ley de torsores Ms (x), repartiéndose entre la flexión transversal de viga y el torsor de viga:

$$ms(x) = ml(x) - mt(x)$$

Añadimos la relación entre giros de eje viga y ley de torsores, y la relación entre dichos giros y la flexión de losa

$$\frac{mt(x)}{GI,t} = \theta''(x) \qquad ml(x) = k_{\theta\theta} \cdot \theta(x)$$

Quedando la ecuación diferencial de segundo grado:

$$ms(x) = k_{\theta\theta} \cdot \theta(x) - GI,t \cdot \theta''(x)$$

Cuya solución es del tipo:

$$\theta(x) = A1 \cdot \cosh(kx) + A2 \cdot Senh(kx)$$

Siendo

$$\sqrt{\frac{k_{\theta\theta}}{GI,t}}$$

Una vez obtenida la ley de giros de torsión y su primera derivada, se obtiene directamente la ley de flexión transversal de la losa y la ley de torsores.

Las condiciones de apoyo son bastante simples:

- Caso de apoyos libres, con torsor nulo en los extremos: $\theta'(0) = \theta'(L) = 0$
- Caso de apoyos fijos a torsión: $\theta(0) = \theta(L) = 0$.

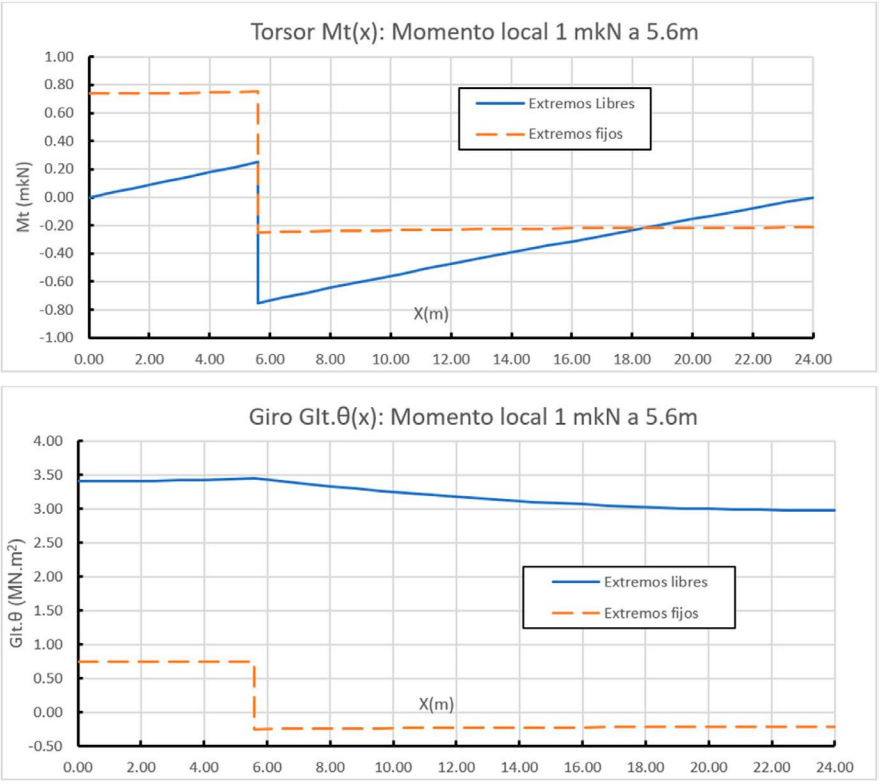

Figura 26. Diagramas de momentos y giros de torsión con momento local simétrico.

El caso general de momento puntual simétrico, existen dos funciones a cada lado de la carga con dos constantes de integración cada una. Se resuelven las cuatro constantes de integración, con las dos condiciones de extremo, y las otras dos son la continuidad de la ley de giros de torsión, y el salto de la 1ª derivada que es -Ms/GI,t.

En el caso de momento uniforme repartido en toda la viga, hay una sola constante de integración: la respuesta simétrica, para origen de coordenadas en el centro de la viga, supone que A2 sea 0. Es obvio, que en el caso de extremos libres a torsión, no hay reparto longitudinal, y toda la acción se absorbe por flexión de losa. Los resultados para el caso de momento local, también comparando la situación de extremos fijos y libres será la siguiente (Fig. 26).

Otra vez se ve la efectividad de disponer apoyos fijos, en especial en la limitación del trabajo de flexión transversal de la losa, que se liga al giro de eje viga, reduciéndose en un factor superior a 3. La contrapartida es un mayor esfuerzo de torsión en la parte de viga más próxima al apoyo fijo.

Analizando los resultados para el caso de momento simétrico repartido observamos que, si los extremos son fijos y la sección de viga posee la rigidez a torsión habitual en vigas artesa, el torsor de viga es casi igual al isostático, al cual se puede asimilar sin error apreciable, y en consecuencia la flexión de losa es muy reducida.

Lógicamente si los extremos son libres, la situación es completamente opuesta: el trabajo de flexión de losa absorbe el momento y la torsión de viga es nula. Esta apreciación posee importantes con secuencias prácticas, al requerir la losa un desempeño fundamental: el máximo giro de eje viga en el centro de vano es 15 veces mayor que en el caso anterior, con una demanda muy fuerte de rotación transversal de apoyos.

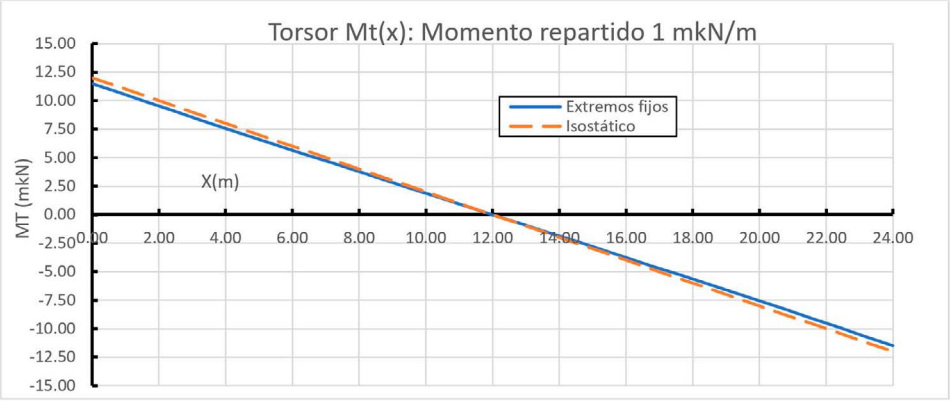

Figura 27. Diferencia de torsión para extremos fijos respecto al caso isostático con momento repartido.

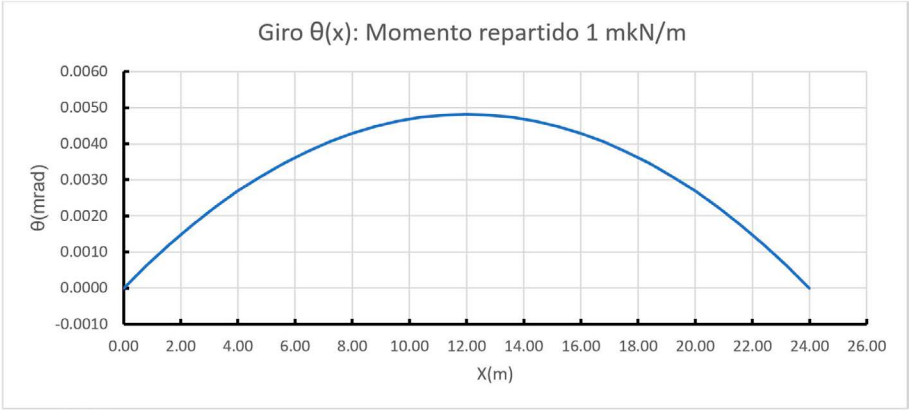

Figura 28. Giro de torsión del caso anterior.

7. DESARROLLO DE UN CASO REAL

Se presenta a continuación el cálculo de un tablero de puente ferroviario de 24 m de luz compuesto por dos vigas en artesa separadas 5.50 m de 1.70 m de canto y losa de reparto de 0.25 m de espesor. Soporta una plataforma ferroviaria de doble vía de línea convencional con un intereje de vía 4.20 m. El caso estudiado corresponde al comportamiento del tablero solicitado con sobrecarga UIC71 aplicada en una única vía. Se indican a continuación las dimensiones de la sección transversal y las cargas de tráfico afectadas por los factores dinámicos y clasificación de línea (Φ3 y α). Asimismo, se ha considerado que la acción es repartida transversalmente bajo traviesa en un ancho de 2.80 m.

El proceso de análisis, parte de establecimiento de los factores de influencia de la acción sobre el tablero; suponiendo

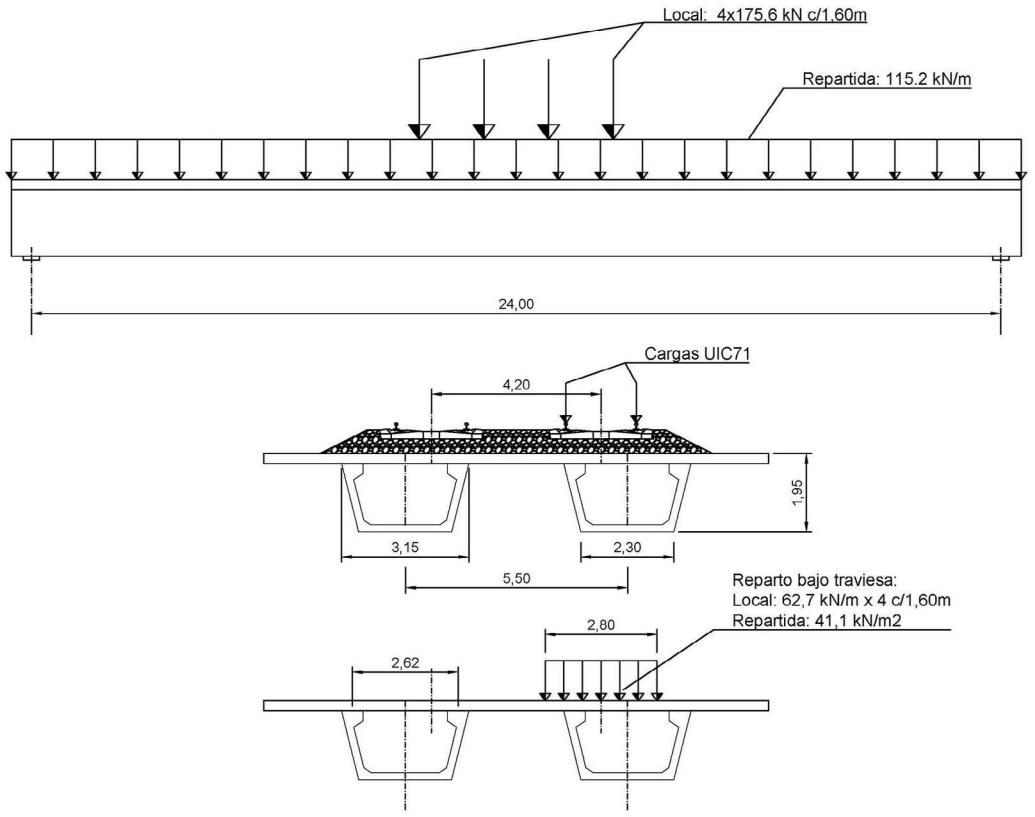

Figura 29. Esquema de cargas ferroviarias aplicadas en un única viga.

un carga de 1kN/m transversal se obtienen las reacciones en ejes de almas (R1i, R1d, R2i, R2d); se componen las resultantes en eje de vigas (P1, M1, P2, M2), y la descomposición en los cuatro de carga aplicados en ejes de vigas: Carga vertical simétrica ($q_{,sim}$), Carga vertical anti simétrica ($q_{,ant}$), Momento simétrico ($m_{,sim}$), y Momento anti simétrico (m,ant). En el siguiente esquema se presenta la descomposición, y los factores de influencia a aplicar en cada caso (los signos se consideran + en ejes globales, es decir verticales + hacia arriba y momento + en sentido de avance de eje tablero)(Fig. 30).

El resto del proceso consiste tan solo en la aplicación de los coeficientes de influencia a las cargas de tráfico reales, y la superposición de los cuatro estados. En relación a la obtención de las solicitaciones transversales de la losa, el camino más sencillo es obtener los esfuerzos de distorsión del tablero, inducidos por los giros y los movimientos verticales de cada viga obtenidos por superposición. Lógicamente a estos esfuerzos globales hay que añadir los esfuerzos locales de aplicación de la carga de tráfico sobre apoyos fijos de sección transversal.

Los parámetros considerados que determinan el comportamiento del tablero, son en este caso los siguientes:

- Rigidez a flexión (EI) por viga: 39548 MNm²
- Rigidez a torsión (GI,t) por viga: 30742 MNm²
- Factor rigidez vertical losa (Kuu) = 6.33 MN/m²
- Factor rigidez cruzada (Kuθ) = 17.39 MN/m
- Factor de rigidez al giro (Kθθ) = 55.51 MN
- Factor K1 = Kuθ x S / GI,t = 0.00311 1/m²
- Factor K2 = 2.Kuu / EI = 0.00032 1/m⁴

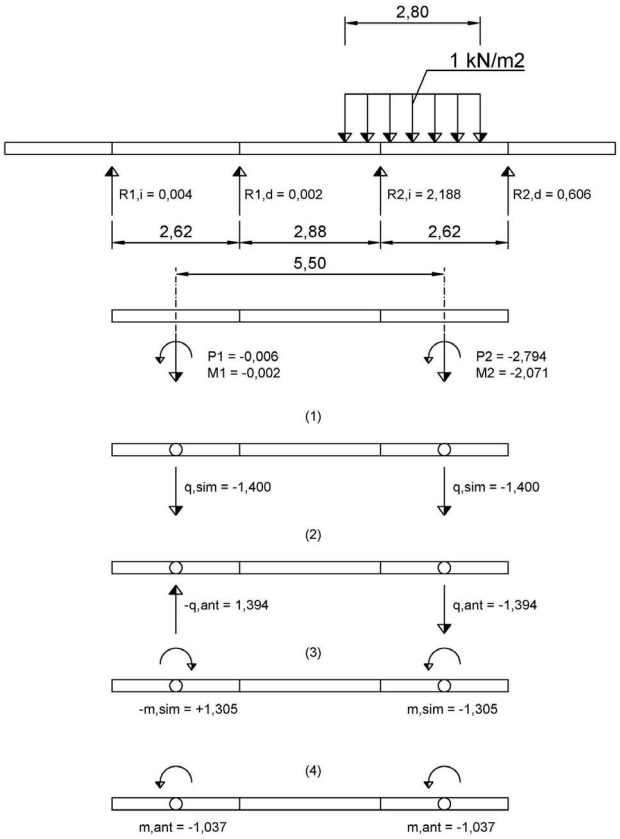

Figura 30. Esquema de coeficientes de influencia por viga y descomposición en los cuatro estados.

7.1. Resultados comparativos entre sistemas de apoyo

Se presentan los resultados de solicitaciones y deformaciones máximas en ambas vigas, con acciones repartidas y locales, para las dos configuraciones de apoyo –extremos fijos y libres a torsión–, siendo muy útil observar la contribución de las cuatro componentes de la descomposición:

TABLA 1.
Resultados en la viga derecha (la más próxima a la vía cargada) para la componente de carga repartida.

Viga Derecha: Carga Repartida. Extremos Fijos	**My (mkN)**	**Q (kN)**	**m,l (kN)**	**Mx (mkN)**	**θ (mr)**	**U (mm)**
Carga simétrica (1)	4145.8	-691.0	0.0	0.0	0.00	-6.3
Carga antisimétrica (2)	2086.2	-419.6	95.5	738.0	0.18	-3.2
Momento simétrico (3)	0.0	0.0	5.0	-470.5	-0.09	0.0
Momento antisimétrico (4)	-91.4	12.5	4.0	-477.4	-0.09	0.1
Total >>>>	**6140.6**	**-1098.1**	**104.5**	**-210.0**	**0.00**	**-9.4**
Viga Derecha: Carga Repartida. Extremos libres						
Carga simétrica (1)	4145.8	-691.0	0.0	0.0	0.00	-6.3
Carga antisimétrica (2)	3342.2	-688.0	61.6	276.1	1.25	-5.2
Momento simétrico (3)	0.0	0.0	42.6	0.0	-0.07	0.0
Momento antisimétrico (4)	-903.9	186.1	26.0	-74.7	-0.78	1.4
Total >>>>	**6584.1**	**-1192.9**	**130.1**	**201.4**	**0.40**	**-10.1**

TABLA 2.
Resultados en la viga izquierda (la más alejada de la vía cargada) para la componente de carga repartida.

Viga Izquierda: Carga Repartida. Extremos Fijos	**My (mkN)**	**Q (kN)**	**m,l (kN)**	**Mx (mkN)**	**θ (mr)**	**U (mm)**
Carga simétrica (1)	4145.8	-691.0	0.0	0.0	0.00	-6.3
Carga antisimétrica (2)	-2086.2	419.6	-95.5	738.0	0.18	3.2
Momento simétrico (3)	0.0	0.0	5.0	470.5	0.09	0.0
Momento antisimétrico (4)	91.4	-12.5	-4.0	-477.4	-0.09	-0.1
Total >>>>	**2150.9**	**-283.8**	**-94.5**	**731.1**	**0.18**	**-3.2**
Viga Izquierda: Carga Repartida. Extremos Libres						
Carga simétrica (1)	4145.8	-691.0	0.0	0.0	0.00	-6.3
Carga antisimétrica (2)	-3342.2	688.0	-61.6	276.1	1.25	5.2
Momento simétrico (3)	0.0	0.0	42.6	0.0	0.07	0.0
Momento antisimétrico (4)	903.9	-186.1	-26.0	-74.7	-0.78	-1.4
Total >>>>	**1707.5**	**-189.0**	**-45.0**	**201.4**	**0.53**	**-2.5**

TABLA 3.
Resultados en la viga derecha (la más próxima a la vía cargada) para la componente de 4 cargas locales.

Viga Derecha: Carro. Extremos Fijos	**My (mkN)**	**Q (kN)**	**m,l (kN)**	**Mx (mkN)**	**θ (mr)**	**U (mm)**
Carga simétrica (1)	1826.4	-175.6	0.0	0.0	0.00	-2.5
Carga antisimétrica (2)	1022.9	-71.7	38.3	283.7	0.07	-1.3
Momento simétrico (3)	0.0	0.0	2.2	-114.9	-0.04	0.0
Momento antisimétrico (4)	-36.6	4.4	2.1	-117.9	-0.04	0.1
Total >>>>	**2812.8**	**-242.9**	**42.5**	**50.9**	**-0.01**	**-3.7**
Viga Derecha: Carro. Extremos Libres						
Carga simétrica (1)	1826.4	-175.6	0.0	0.0	0.00	-2.5
Carga antisimétrica (2)	1505.8	-174.9	-25.2	109.3	0.48	-2.1
Momento simétrico (3)	0.0	0.0	12.0	-48.4	-0.22	0.0
Momento antisimétrico (4)	-237.3	47.3	7.5	-68.6	-0.21	0.4
Total >>>>	**3095.0**	**-303.2**	**-5.7**	**-7.7**	**0.05**	**-4.2**

TABLA 4.
Resultados en la viga izquierda (la más alejada de la vía cargada) para la componente de 4 cargas locales.

Viga Izquierda: Carro. Extremos Fijos	My (mkN)	Q (kN)	m,l (kN)	Mx (mkN)	θ (mr)	U (mm)
Carga simétrica (1)	1826.4	-175.6	0.0	0.0	0.00	-2.5
Carga antisimétrica (2)	-1022.9	71.7	-38.3	283.7	0.07	1.3
Momento simétrico (3)	0.0	0.0	2.2	114.9	0.04	0.0
Momento antisimétrico (4)	36.6	-4.4	-2.1	-117.9	-0.04	-0.1
Total >>>>	**840.1**	**-108.4**	**-38.1**	**280.7**	**0.07**	**-1.2**
Viga Izquierda: Carro. Extremos Libres						
Carga simétrica (1)	1826.4	-175.6	0.0	0.0	0.00	-2.5
Carga antisimétrica (2)	-1505.8	174.9	25.2	109.3	0.48	2.1
Momento simétrico (3)	0.0	0.0	12.0	48.4	0.22	0.0
Momento antisimétrico (4)	237.3	-47.3	-7.5	-68.6	-0.21	-0.4
Total >>>>	**557.9**	**-48.0**	**29.8**	**89.0**	**0.49**	**-0.8**

Mencionamos a continuación algunas pautas generales:

- Los flectores y las deformaciones en el centro de vano y las reacciones en apoyo, están determinados en general por las componentes simétrica y antisimétrica de carga vertical, siendo muy reducida la contribución de la distribución de momentos antisimétricos, salvo en el caso de extremos libres. Para una estimación adecuada de los torsores y de sus giros, no se puede prescindir de la consideración de los momentos antisimétricos.
- A pesar de tratarse de un tablero con una relación ancho luz relativamente pequeña, el reparto transversal es eficaz, como consecuencia de la elevada rigidez a torsión de las vigas. Lógicamente es más efectivo si se fijan los extremos: el 75% de flector y el 77% del cortante, frente a 81% y 86% respectivamente del caso de extremos libres, lo absorbe la viga más próxima a la vía cargada.
- A cambio, los torsores aumentan considerablemente en el primer caso. Este efecto es determinante en el armado de la viga, aunque para la viga artesa la demanda adicional de armado no es relevante.
- Dada la poca excentricidad de la acción de la viga cargada respecto al eje de viga, en ambos casos la torsión de la viga opuesta es muy superior a la correspondiente a la viga más próxima. Este efecto puede ser importante en el diseño de los aparatos de apoyo.
- Las deformaciones diferenciales entre vigas son mucho mayores en el caso de extremos libres (33% frente a un 22% de relación de flecha máxima entre ellas respectivamente). Este hecho puede ser determinante en la validación del estado de servicio por alabeo de vía.

A continuación se representan los gráficos, con los resultados en ambas vigas y forma de apoyo, incluyendo todas las sobrecargas

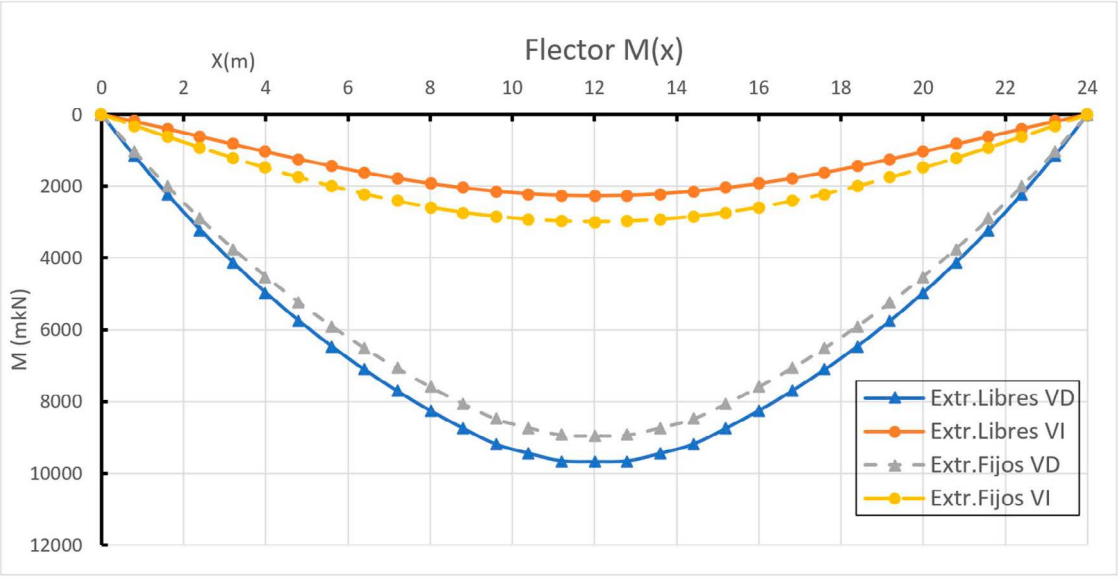

Figura 31_1. Solicitaciones en ambas vigas con apoyos libres y fijos a torsión.

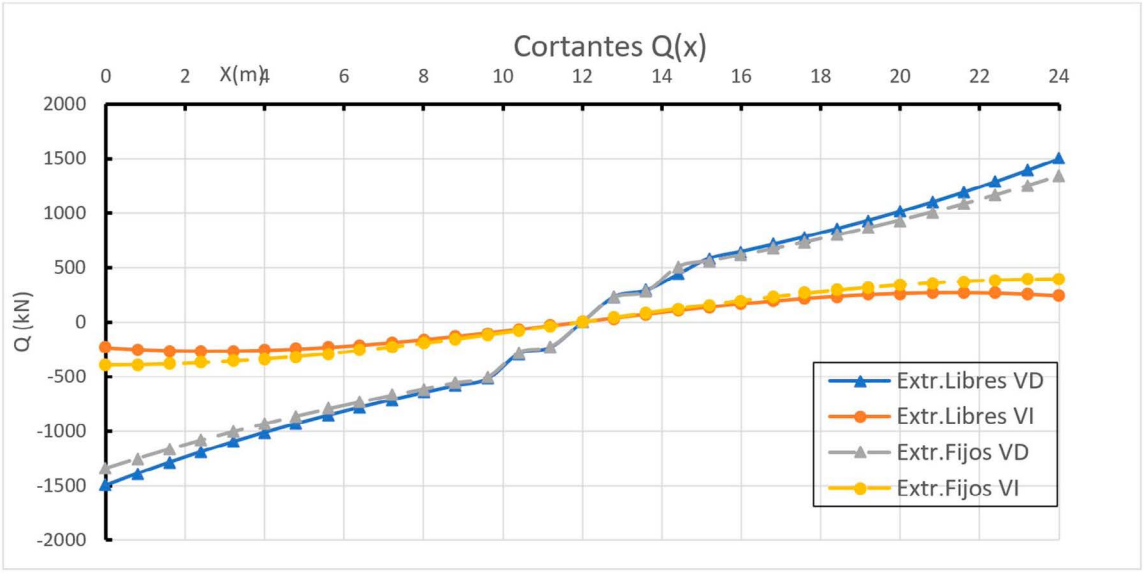

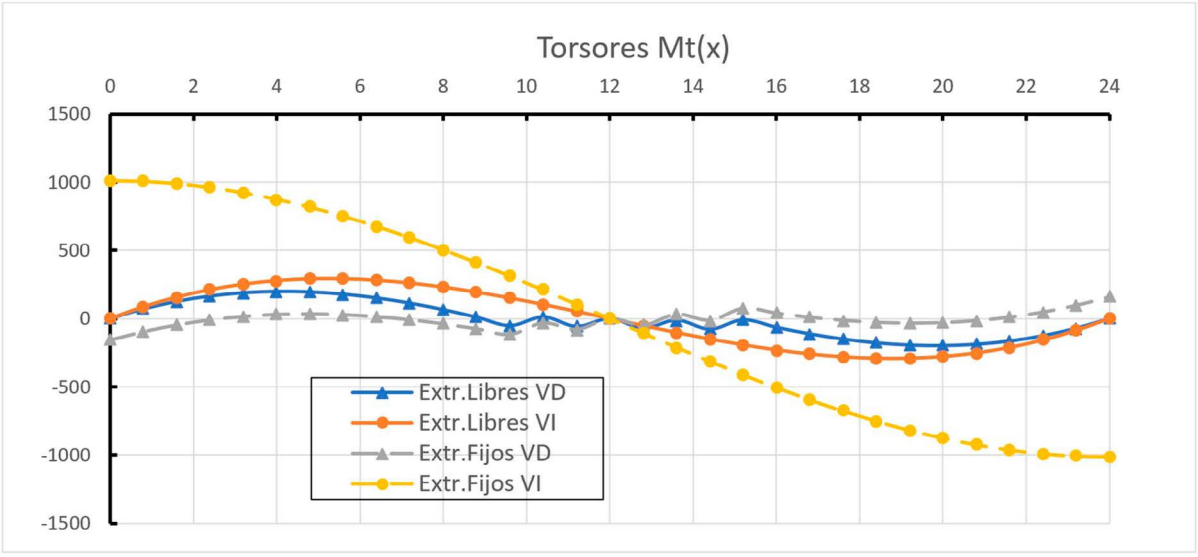

Figura 31_2. Solicitaciones en ambas vigas con apoyos libres y fijos a torsión.

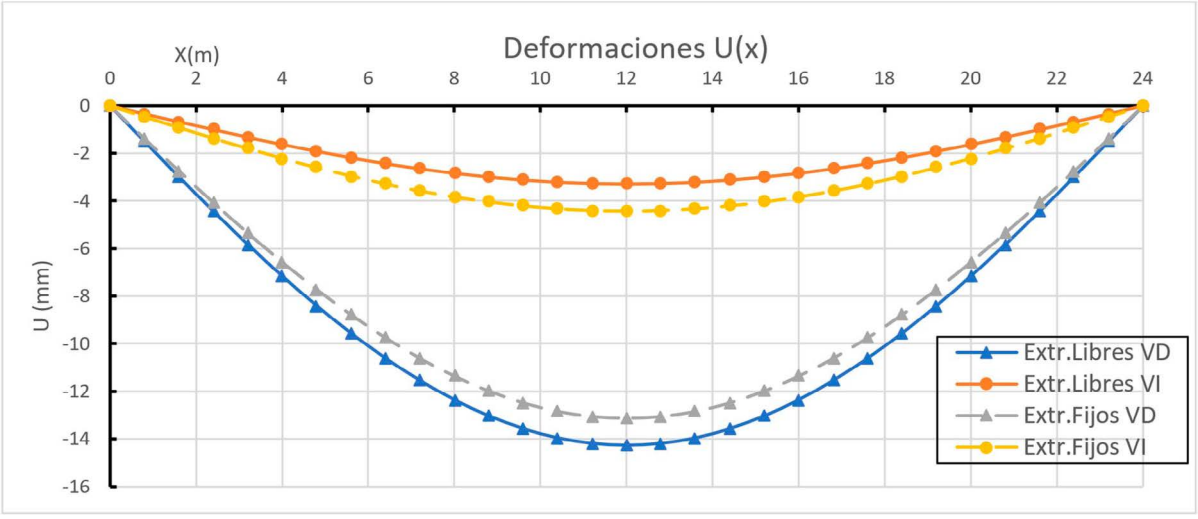

Figura 32. Deformaciones en ambas vigas con apoyos libres y fijos a torsión.

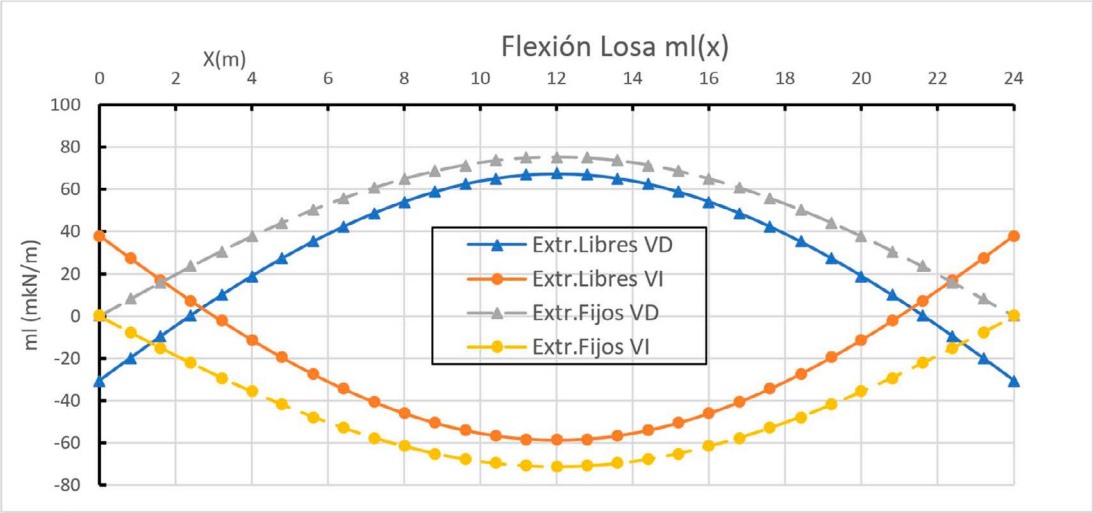

Figura 33. Flexión transversal de losa en bordes de alas de vigas en ambas condiciones de apoyo.

8. CONCLUSIONES

Se ha presentado la solución analítica de deformaciones y solicitaciones de tableros formados por dos vigas principales y losa de reparto entre ellas, que permite resolver de forma directa el cálculo de este tipo de tableros. Se basa en la descomposición en cuatro estados, con obtención de la ecuación diferencial para la solución de los dos antisimétricos. Las fórmulas pueden incorporarse a un marco de Hoja de Cálculo, para la obtención de resultados para cualquier tipo de carga, y con mucha facilidad para cargas móviles. Aquí se limita al caso habitual de vigas paralelas apoyadas y sin oblicuidad de apoyos. La extensión a tableros continuos es simple, ya que la descomposición descrita sigue vigente, y solo deben modificarse las condiciones de contorno en términos de momentos hiperestáticos de continuidad que pueden ser obtenidos por compatibilidad de giros. Una mejora consiste en la consideración de la rigidez a torsión de la losa de reparto, induciendo el acoplamiento entre ella y la flexión longitudinal, desarrollando en consecuencia un planteamiento más complejo. Esto, junto un cambio de ejes de referencia, abre la posibilidad del análisis de tableros oblicuos.

APÉNDICE 1:
Nomenclatura de símbolos utilizados

Resultantes y descomposición en estados

q,sim-q,ant: Valor en kN/m de la carga vertical en componente simétrica y antisimétrica.
m,sim-m,ant: Valor en mkN/m de la componente simétrica y antisimétrica del momento de la carga exterior
p1i, p1d = Carga vertical exterior en viga 1, en alma izquierda y derecha (kN/m)
p2i, p2d = Lo mismo en viga 2
Pv1, Mv1 = Resultantes de carga vertical y momento aplicada en viga 1 (kN/m-mkN/m)
Pv2, Mv2 = Lo mismo en viga 2

Acciones y solicitaciones en vigas

p(x): Función de descarga por reparto transversal (kN/m)
q(x): Ley de carga vertical externa aplicada (kN/m)
Q(x): Carga local o puntual en coordenada x (kN)
mt(x): Momento torsor repartido igual al flector transmitido por losa (mkN/m)
M(x): Ley de flectores en la viga (mkN)
V(x): Ley de cortantes en la viga (kN)
Mt(x): Ley de torsores en la viga (mkN/m)

Deformaciones en vigas

u(x): Deformación vertical (m)
w(x): Giro de flexión de viga alrededor eje Y (rad)
θ(x): Giro de torsión de viga (rad)

Geometría y rigideces

S: Distancia entre ejes de vigas (m)
B: Distancias entre almas de apoyo de losa (m)
EI,y: Rigidez a flexión neta del conjunto viga - ancho eficaz losa (kNm²)
GI,t: Rigidez a torsión del conjunto viga - losa (kNm²)
Kuu = Factor rigidez vertical losa. Para espesor constante: 12/EI,losa /S^3
Kuθ = Factor rigidez cruzada. Para espesor constante: 6EI/S^2
Kθθ = Factor rigidez al giro. Para espesor constante: 2EI/S

Criterios de signos

X - Y - Z: Triedro directo global con eje X el de viga e Y vertical
Deformaciones y giros +, los correspondientes a avance de ejes globales.
Solicitaciones +: En la cara frontal de sección, las correspondientes a avance en ejes globales.

APENDICE 2:

Funciones derivadas y primitivas que intervienen en la solución

Siendo la función con coeficientes de integración Ai, e incluyendo abreviaciones de las funciones trigonométricas:

f(x)=A1·Cosh(ux)·Cos(vx)+A2·Cosh(ux)·Sen(vy)+A3·Senh(ux)·Cos(vx)+A4·Senh(ux)·Sen(vx)

Las tres primeras funciones derivadas son:

f'(x)=A1· [u·Sh(ux)·C(vx)-v·Ch(ux)·S(vx)]+A2·[u·Sh(ux)·S(vy)+v·Ch(ux)·C(vx)]+A3·[u·Ch(ux)·C(vx)-v·Sh(ux)·S(vx)]+A4·[u·Ch(ux)·S(vx)+v·Sh(ux)·C(vx)]

f''(x)=A1· [r·Ch(ux)·C(vx)-2s·Sh(ux)·S(vx)]+A2·[r·Ch(ux)·S(vy)+2s·Sh(ux)·C(vx)]+A3·[r·Sh(ux)·C(vx)-2s·Ch(ux)·S(vx)]+A4·[r·Sh(ux)·S(vx)+2s·Ch(ux)·C(vx)]

f'''(x)=A1· [α·Sh(ux)·C(vx)-β·Ch(ux)·S(vx)]+A2·[α·Sh(ux)·S(vy)+β·Ch(ux)·C(vx)]+A3·[α·Ch(ux)·C(vx)-β·Sh(ux)·S(vx)]+A4·[α·Ch(ux)·S(vx)+β·Sh(ux)·C(vx)]

Y las dos primeras funciones primitivas:

F(x)={A1· [u·Sh(ux)·C(vx)+v·Ch(ux)·S(vx)]+A2·[u·Sh(ux)·S(vy)-v·Ch(ux)·C(vx)]+A3·[u·Ch(ux)·C(vx)+v·Sh(ux)·S(vx)]+A4·[u·Ch(ux)·S(vx)–v·Sh(ux)·C(vx)]} $\frac{1}{(u^2+v^2)^2}$

$F^2(x)$={A1· [r·Ch(ux)·C(vx)+2s·Sh(ux)·S(vx)]+A2·[r·Ch(ux)·S(vy)-2s·Sh(ux)·C(vx)]+A3·[r·Sh(ux)·C(vx)+2s·Ch(ux)·S(vx)]+A4·[r·Sh(ux)·S(vx)–2s·Ch(ux)·C(vx)]} $\frac{1}{(u^2+v^2)^2}$

Siendo

$r = u^2–v^2$ $s = u·v$ $\alpha = u·r – 2v·s$ $\beta = v·r + 2u·s$

Referencias

[1] Manterola, J. (1976) "La sección abierta y cerrada bajo solicitación excéntrica". Hormigón - Puentes II, A.F.C.E., Monografía n.º 15

[2] Samartín, Avelino and Martínez González, Jesús (1974). Reparto transversal de la sobrecarga en tableros de puentes. "Hormigón y Acero" (n. 113); pp. 11-37. ISSN 0439-5689.

[3] Samartín Quiroga, Avelino (1983). "Cálculo de estructuras de puentes de hormigón". Editorial Rueda. ISBN 9788472070240

[4] Salvador Monleón, Carlos Lázaro y Josep Casanova (2019). "La sección abierta y cerrada bajo solicitación excéntrica… en una viga curva. Un tributo a Javier Manterola". "Hormigón y Acero" (n. 289); pp. 7-24. ISSN 0439-5689.

[5] Salvador Monleón (2017) "Teoría unificada de elementos estructurales esbeltos". Editorial de la Universidad Politécnica de Valencia. ISBN: 978-84-9048-584-2

[6] Sadri Hassani (2012). "Mathematical Physics". Chap.20: "Green's Functions in One Dimension" Springer. ISBN 978-3-319-01194-3

ACHE

MONOGRAFÍAS

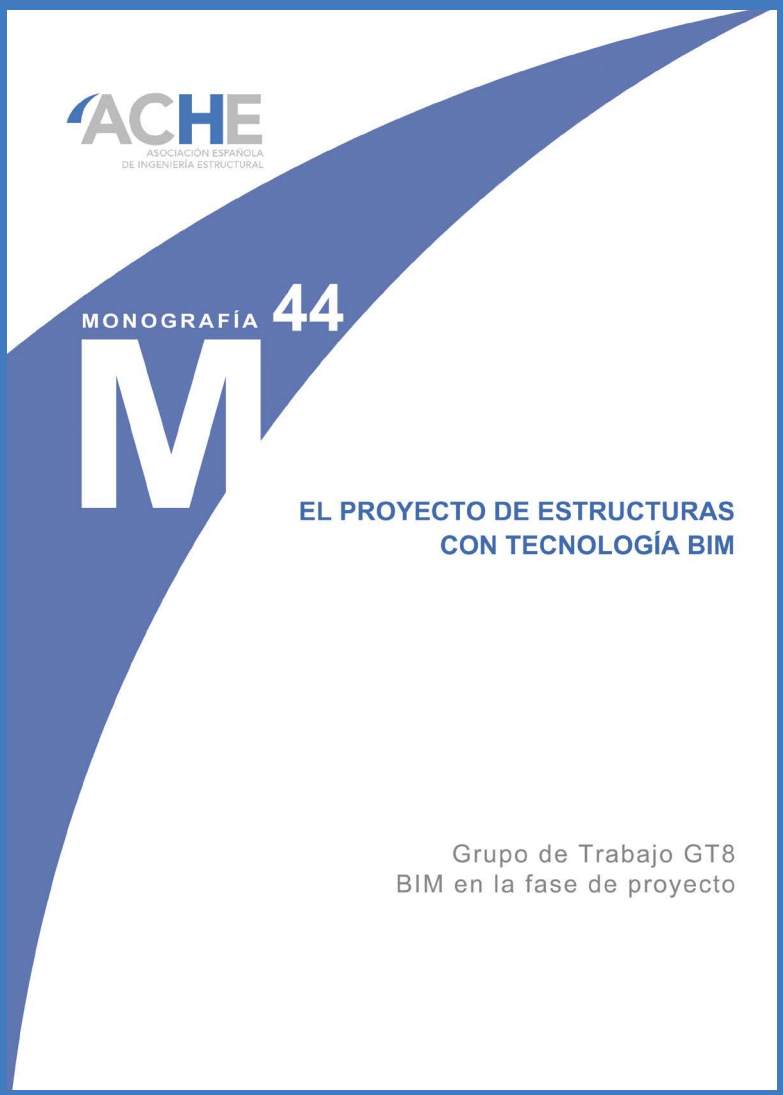

SECRETARÍA DE ACHE
Tel.: 91 336 66 98
www.e-ache.com

Disponible en **www.hormigonyacero.com**
https://doi.org/10.33586/hya.2025.3468

Pilares cortos de hormigón armado diseñados según los reglamentos *fib* Model Code 2020, Eurocode 2:2023, ABNT NBR 6118:2014 y ABNT NBR 6118:2023: *Estudio de la sostenibilidad*

Reinforced Short Columns Designed in Accordance With the Regulations fib Model Code 2020 Eurocode 2:2023 and ABNT NBR 6118:2023. Sustainability Study

Ricardo Boni [*,a], Rafael Silva[a] y Paulo Helene [a]

[a] *PhD Engenharia. Rua Visconde de Ouro Preto, 201. Consolação. 01303-060. São Paulo. SP*

Recibido el 3 de mayo de 2025; revisado el 18 de diciembre de 2024, aceptado el 25 de febrero de 2025

RESUMEN

Este trabajo tiene como objetivo presentar un estudio de la sostenibilidad, enfocado en el diseño de pilares cortos de hormigón armado respetando las premisas de cuatro reglamentos técnicos: *fib* Model Code 2020, Eurocode 2:2023, ABNT NBR 6118:2014 y ABNT NBR 6118:2023. Para el diseño del tramo de pilar, en este estudio se consideraron dos cuantías de armaduras, una mínima (≥ 0,4%) y una máxima para empalmes por solapo (< 4,0%); dos clases diferentes de resistencia del hormigón, C20 y C50; y, con f_{ck} referido a tres edades diferentes de 28, 56 y 91 días. El contexto proporcionó 16 posibilidades diferentes para detallar el tramo de pilar. También se consideró el hormigón mezclado con dos clases diferentes de cemento; CR con alto contenido de clínker (> 90%) y CS con alrededor de 30% de clínker. El análisis comparativo abordó el tema de la sostenibilidad considerando únicamente las emisiones de CO_{2eq} y la desmaterialización. En las condiciones de este estudio, se concluye que utilizando los criterios del *Eurocode 2* (EN 1992-1-1), los hormigones producidos con cementos clase CS y edades de control del f_{ck} de 56 días, siempre conducen a una mayor desmaterialización y menores emisiones de gases de efecto invernadero. Este estudio también demuestra que las decisiones de diseño, combinadas inteligentemente con la tecnología del hormigón, pueden influir significativamente en la sostenibilidad de una estructura.

PALABRAS CLAVE: diseño de pilares; desmaterialización; sostenibilidad; gases de efecto invernadero; Emisión de CO_{2eq}.

ABSTRACT

This study presents an investigation into sustainability in the design of short reinforced concrete columns, following the guidelines of four technical regulations: *fib* Model Code 2020, Eurocode 2:2023, ABNT NBR 6118:2014, and ABNT NBR 6118:2023. The design considered two reinforcement ratios, with a minimum (≥0.4%) and a maximum lap splice (<4.0%), and two strength classes, C20 and C50. The characteristic strength (f_{ck}) was referenced at three different ages: 28, 56, and 91 days, resulting in 16 possible scenarios for the column segment. The concrete mix included two types of cement: CR, with a high clinker content (>90%), and CS, with about 30% clinker. The comparative analysis focused on sustainability and dematerialization, considering only CO_{2eq} emissions. The results indicate that, according to the Eurocode 2 (EN 1992-1-1) criteria, concretes made with CS class cement and f_{ck} controlled at 56 days consistently achieve greater dematerialization and lower greenhouse gas emissions. This study demonstrates how design choices, combined with advanced concrete technology, can significantly enhance the sustainability of a structure.

KEYWORDS: column design; dematerialization; sustainability; greenhouse gases; CO_{2eq} emission.

* Persona de contacto / *Corresponding author*:
Correo-e / *e-mail*: ricardo.boni@concretophd.com.br (Ricardo Boni)

Cómo citar este artículo: Boni, R., Silva, R. Helene, P. (2025). Pilares cortos de hormigón armado diseñados según los reglamentos fib Model Code 2020, Eurocode 2:2023, ABNT NBR 6118:2014 y ABNT NBR 6118:2023: Estudio de la sostenibilidad. *Hormigón y Acero*. 76(306):103-114. https://doi.org/10.33586/hya.2025.3468

1. INTRODUCCIÓN

Este trabajo presenta un estudio de la sostenibilidad considerando las emisiones de CO_{2eq} y la desmaterialización, determinadas conforme las Declaraciones Ambientales de los Productos disponibles, enfocado en el diseño de pilares cortos de hormigón armado respetando las premisas de cuatro reglamentos técnicos: *fib* Model Code 2020 [1], Eurocode 2:2023 [2], ABNT NBR 6118:2014 [3] y ABNT NBR 6118:2023 [4]. Para el diseño del tramo de pilar, se consideraron diferentes cuantías de armaduras, tipos de cementos, clases de resistencia del hormigón, con f_{ck} referido a variadas edades.

Las premisas de proyecto adoptadas en el dimensionamiento del pilar corto de hormigón armado, macizo, de sección cuadrada, se basaron en datos de un caso real de un edificio residencial[1], con 2 pisos subterráneos, planta baja, 24 plantas estándar, sala de máquinas, tanque elevado y cubierta. Se considera solamente el tramo de pilar entre el 1er piso y el 2do piso, con una altura de techo de 2,88 m, estando la estructura sujeta a clases de agresividad ambiental que van desde CAA I para hormigón C20 a CAA II para pilares de hormigón C50, según la ABNT NBR 12655:2022 [5].

Para las acciones de viento, se diseñó el edificio considerando la velocidad básica del viento V0 = 40 m/s, factor topográfico S_1 = 1,00, categoría de rugosidad IV (S_2), clase de edificio C (S_2) y el factor estadístico S_3 = 1,00, parámetros de acuerdo con la ABNT NBR 6123:1998 [6]. Para las acciones sísmicas se cumplió con la norma ABNT 15421:2023 [7] para edificaciones ubicadas en zona sísmica 0. Para las acciones verticales, se adoptaron los valores descritos en la ABNT NBR 6120:2019 [8] para el caso de edificios residenciales. En cuanto a los requerimientos de fuego e incendio, se tomó como base lo establecido en la ABNT NBR 15200:2012 [9], considerando un TRRF de 90 minutos y sus respectivos requerimientos en cuanto al detalle de pilares. El número total de tramos de pilares de este edificio es de 1008 (mil ocho tramos) y la superficie construida estándar por piso es de 365 m².

La fuerza característica normal total (NSk) para el diseño de este tramo de pilar utilizado como ejemplo representativo fue de 4000 kN y el total de momentos característicos a los que se someterá fueron MxSk = MySk = 120 kN.m. Se consideró que las acciones accidentales corresponden al 25% del total de la fuerza característica normal.

El objetivo de este estudio es demostrar cuantitativamente que las decisiones de proyecto junto con la tecnología del hormigón influencian en las emisiones de gases de efecto invernadero y en la sostenibilidad de una estructura.

2. DISEÑO DE PILAR CORTO

El modelo para el cálculo de la resistencia a la compresión prescrito para el diseño de un nuevo proyecto, basado en un determinado valor arbitrado de la resistencia característica a la compresión del hormigón, f_{ck}, según la nueva versión del *fib Model Code for Concrete Structures 2020* (MC 2020) [1], es:

$$f_{cd} = \alpha_{cc} \cdot \eta_{cc} \cdot \frac{f_k}{\gamma_c} \qquad (2.1)$$

Dónde:

- f_{cd} → resistencia a compresión de diseño del hormigón;
- f_{ck} → resistencia a compresión característica del hormigón, a edades que pueden variar de 28 a 91 días;
- γ_c → factor de minoración de la resistencia característica del hormigón;
- α_{cc} → coeficiente que tiene en cuenta los efectos opuestos, por un lado, del aumento de la resistencia por la hidratación del cemento, y, por otro lado, la reducción de esta resistencia causada por una carga elevada[2] mantenida a largo plazo[3];
- η_{fc} → factor de reducción de la resistencia[4] que tiene en cuenta el aumento de la fragilidad con el aumento de la resistencia del hormigón, calculado mediante:

$$\eta_{cc} = \left(\frac{40}{f_{ck}}\right)^{1/3} \leq 1{,}0 \ (f_{ck} \text{ en MPa}) \qquad (2.2)$$

De acuerdo con el MC 2020 [1], en situaciones normales de diseño, se puede suponer que el aumento de la resistencia después de 28 días compensa los efectos de la carga a largo plazo, de tal manera que, para obras nuevas, cargadas a los 28 días o más, y con f_{ck} referido a 28 días, este coeficiente puede asumirse como α_{cc} = 1,0. En este estudio η_{fc} = 1,0 para f_{ck} = 20 MPa y η_{fc} = 0,93 para f_{ck} = 50 MPa.

Para estructuras cargadas a edades mayores a 91 días y en las que la fecha de referencia y control del f_{ck} sea mayor que 28 días, pero igual o menor a 56 días, según el Eurocode 2 [2], es correcto continuar considerando α_{cc} = 1,0, siempre que la clase de cemento sea CS.

Para edades f_{ck} superiores a 28 días en el caso de MC 2020 [1] y para edades superiores a 56 días en el caso del Eurocode 2 [2], hasta 91 días, el reglamento recomienda considerar α_{cc} = 0,85. El Eurocode 2 [2] también permite que el valor α_{cc} varíe de 0,8 a 1,0, dependiendo de lo prescrito en el Anexo Nacional[5] de cada país de la Comunidad Europea, y se recomienda adoptar el valor α_{cc} = 1,0 para los casos generales.

En el caso de la norma ABNT NBR 6118:2023 [4], el coeficiente es más conservador y se fija en 0,85, recordando que el coeficiente aparece en el cálculo de la tensión máxima de diseño σ_{cd} en lugar de aparecer en el cálculo de la resistencia de diseño f_{cd}.

1 Edificio del archivo de la PhD Engenharia para el cual los autores realizaron la Evaluación Técnica de Proyecto (ATP).

2 No existe una definición clara del significado de cargas altas, elevadas y duraderas. En este estudio, los autores consideran elevadas las fuerzas normales > 0,6 $*f_{cd}$ se mantienen durante más de 15 minutos, o aproximadamente 0,4 $*f_{ck}$.

3 En el Eurocode 2 [2], es decir, en la *norma EN 1992-1-1: nov2023, este coeficiente se denomina* k_{tc}, según el inciso 5.1.6 «*Hipótesis de diseño*».

4 En el Eurocode 2 [2], es decir, en la *norma EN 1992-1-1: nov2023, este coeficiente se denomina* η_{cc}, como se muestra en el inciso 5.1.6 «*Hipótesis de diseño*».

5 Cada país de la Comunidad Europea puede modificar estos coeficientes en función de su situación social y económica, ya que el Eurocode 2 es un documento de referencia para todos los países de la CE.

El texto de la norma ABNT NBR 6118:2014 [3] no consideró el coeficiente de fragilidad η_{fc}, mientras que el nuevo texto de ABNT NBR 6118:2023 [4] considera este coeficiente de fragilidad con el mismo modelo que el MC 2020 [1]. La normativa brasileña, tanto en la versión de 2014 [3] como en la actual de 2023 [4], prescribe f_{ck} referido solamente a los 28 días de edad.

Una vez definida la resistencia a la compresión de diseño del hormigón (f_{cd}), se obtiene la tensión del hormigón (σ_c) según el diagrama tensión-deformación presentado en el MC 2020 [1], ABNT NBR 6118 [4] y Eurocode 2 [2], representado en la siguiente ecuación:

$$\sigma_{cd} = f_{cd} \cdot \left[1 - \left(1 - \frac{\varepsilon_c}{\varepsilon_{c2}}\right)^n\right] \quad (2.3)$$

Para hormigones con resistencia característica de hasta 50 MPa según ABNT NBR 6118:2023 [4], y para hormigones de 12 MPa a 100 MPa, MC 2020 [1] y Eurocode 2 [2] prescriben:

- ε_{c2} = 0,20%, deformación especifica de encortamiento del hormigón al inicio de la meseta de fluencia;
- ε_{cu} = 0,35%, deformación especifica de encortamiento del hormigón en la ruptura;
- n = 2, parámetro adimensional.

Para hormigones con resistencia característica entre 55 MPa y 90 MPa, no analizados en este estudio, solo según ABNT NBR 6118:2023 [4] y su versión anterior ABNT NBR 6118:2014 [3]:

- ε_{c2} = 0,20% + 0,0085% (f_{ck} – 50)0,53;
- ε_{cu} = 0,26% + 3,5% [(90 – f_{ck}) /100]^4;
- n = 1,4 + 23,4 [(90 – f_{ck}) /100]^4

Las limitaciones en las deformaciones específicas reflejan la mayor fragilidad de los hormigones con resistencia a la compresión característica superior a 50 MPa. Del punto de vista de los autores, en la normativa brasileña, mientras se mantengan estas limitaciones en las deformaciones específicas, no hay razón técnica para introducir o mantener también el coeficiente de fragilidad η_{fc}. Por razones didácticas y conceptuales, es preferible mantener las limitaciones de deformación específica y eliminar el coeficiente de fragilidad η_{fc} de la norma brasileña ABNT NBR 6118:2023 [4].

Los factores parciales de seguridad, también conocidos como coeficientes de ponderación, tienen como objetivo introducir seguridad en el diseño de estructuras de hormigón armado, por un lado, aumentando los esfuerzos solicitantes y por otro reduciendo las resistencias características de los materiales a utilizar. Este procedimiento es conocido como método semiprobabilístico en Brasil y método de coeficientes parciales por el MC 2020 [1] y Eurocode 2 [2].

La definición de los valores de estos factores parciales de seguridad viene dada principalmente por el estudio probabilístico de las condiciones y riesgo de la estructura, sus usos, simplificaciones e incertidumbres del modelo de cálculo y las variaciones de estos parámetros. En la práctica, el método semiprobabilístico o de factores parciales es solo probabilístico en la consideración de la distribución de las resistencias de los materiales y las acciones, porque una vez introducidos los coeficientes de ponderación, el análisis es todo determinista [10].

En la tabla 2.1 se muestran los diferentes valores de los factores de seguridad parciales recomendados por los reglamentos en estudio.

En la tabla 2.2 se muestran las combinaciones consideradas en este estudio para el diseño de pilares cortos con 2 clases de resistencia característica del hormigón a compresión (C20 y C50).

Fueron seguidos los criterios clásicos de diseño y detalle de pilares, respetando las diferencias en el cálculo de defor-

TABLA 2.1.
Coeficientes de seguridad parciales según el MC 2020 [1]; EN 1992:2023-1-1 [2], EN 1990:2002 [12], ABNT NBR 6118:2023 [4] y ABNT NBR 8681:2003 [11].

ABNT NBR 6118:2023 [4] y ABNT NBR 8681:2003 [11]		MC 2020 [1]; EN 1992:2023-1-1 [2] y EN 1990:2002 [12]	
Materiales (γ_m)	**Acciones (γ_f)**	**Materiales (γ_m)** (1)	**Acciones (γ_f)** (1)
γ_c (hormigón) = 1,4 γ_s (acero) = 1,15	γ_g (acciones permanentes) = 1,4 γ_q (acciones variables) = 1,4	γ_c (hormigón) = 1,4 a 1,6 γ_s (acero) = 1,1 a 1,175	γ_g (acciones permanentes) = 1,3 a 1,4 γ_q (existencias variables) = 1,3 a 1,7

(1) En este estudio, se adoptaron los siguientes valores: γ_c=1,5; γ_s=1,15; γ_g=1,35 e γ_q=1,5, que se encaja en la clase de consecuencias CC2 del MC 2020 [1].

TABLA 2.2.
Combinaciones utilizadas en este estudio.

Reglamento	Clase de resistencia	ηfc	α_{cc}	γ_c	γ_s	γ_f Acción permanente	γ_f Acción variable	f_{cd}/f_{ck} (%)
ABNT 6118:2023 [4]	C20	1,00	0,85	1,4	1,15	1,4	1,4	61%
28 días	C50	0,93	0,85	1,4	1,15	1,40	1,40	56%
MC 2020 [1] 28d	C20	1,00	1,00	1,5	1,15	1,35	1,50	67%
EC 2 [2] 28d a 56d	C50	0,93	1,00	1,5	1,15	1,35	1,50	62%
MC 2020 [1] > 28d	C20	1,00	0,85	1,5	1,15	1,35	1,5	57%
EC 2 [2] 57d a 91d	C50	0,93	0,85	1,5	1,15	1,35	1,50	53%

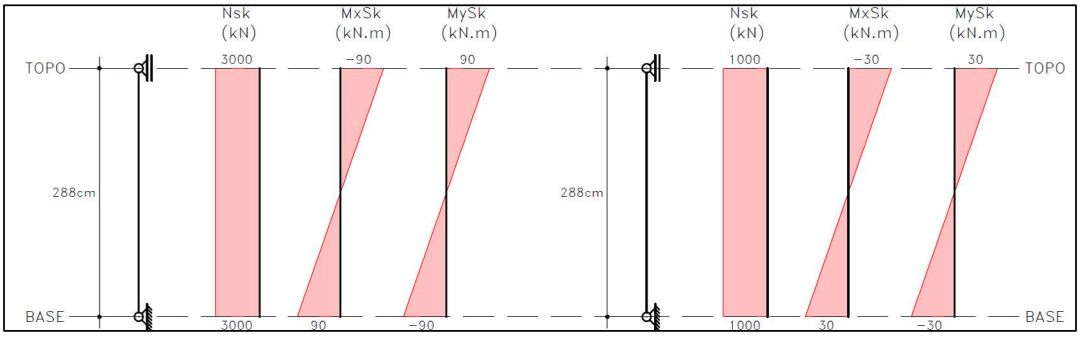

Figura 2.1. Carga nominal característica del pilar: carga permanente (lado izquierdo) y carga variable (lado derecho).

maciones específicas según cada norma. Se adoptó un recubrimiento nominal de c = 30 mm para el hormigón C20 y de c = 25 mm para el hormigón C50.

Todas las alternativas de diseño de este tramo de pilar se consideraron pilares prismáticos, de sección cuadrada y corta ($\lambda \leq 35$) con longitud l_e = 2,88 m, donde de cada clase de resistencia se extrajeron 2 (dos) detalles de pilares: una alternativa con armadura mínima cercana al límite solicitado (≥ 0,4%) y otra con detalles cercanos a la cuantía máxima de acero permitida en un tramo con un empalme por solapo (alrededor del 4% de A_s/A_c).

Para la carga nominal, la carga característica se definió como se muestra en la figura 2.1.

En la tabla 2.3 se muestran las dimensiones, las cuantías de armaduras y los índices de esbeltez, detallados para cada posible alternativa de diseño del tramo de pilar.

A medida que aumenta la clase de resistencia del hormigón, la disminución del área del pilar desde la situación de armadura mínima para la armadura máxima, no se mantiene en la misma proporción que la reducción de área de hormigón. Esto se debe a la pérdida del brazo de palanca inicial, que cambia sutilmente del dominio 5 al dominio 4 a medida que aumenta la clase de resistencia del hormigón. El diseño de la armadura mínima de los pilares requiere que el área de acero sea al menos el 15% de la relación Nd/fyd, lo que lleva a que la armadura de los pilares para la clase de resistencia C50 tenga una cuantía mínima de alrededor del 0,90% en lugar del 0,40% de C20.

Como comparación, la figura 2.3 muestra el volumen de hormigón (Vc) de cada una de las alternativas de diseño de este tramo de pilar con armadura mínima.

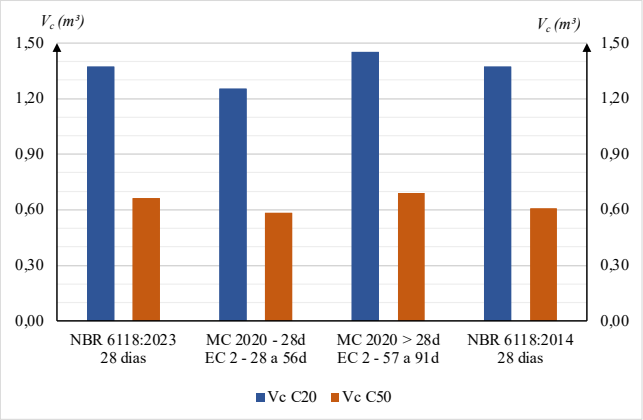

Figura 2.3. Gráfico de barras que indica el volumen de hormigón correspondiente a cada alternativa de diseño del tramo de pilar, para una cuantía mínima de armadura (≥ 0,4%).

La figura 2.4 muestra el volumen de hormigón (V_c) con el máximo de armadura (alrededor del 4%), mostrando una reducción significativa en el volumen total de hormigón de cada alternativa de diseño para el tramo de pilar.

TABLA 2.3.
Resumen de las alternativas para detallar el tramo de pilar.

Reglamento	Clase de resistencia	Dimensiones (cm)	Acero (cm²)	Cuantía de acero	Índice de esbeltez λ	Volumen de hormigón (m³)	Consumo de acero (kg)
NBR 6118:2023 [4] 28 días	C20	69 x 69	19,63	0,41%	14	1,37	82
		49 x 49	96,51	4,02%	20	0,69	235
	C50	48 x 48	19,63	0,85%	21	0,66	65
		41 x 41	64,34	3,83%	24	0,48	160
MC 2020 [1] 28 días	C20	66 x 66	19,63	0,45%	15	1,25	80
		48 x 48	91,07	3,95%	21	0,66	235
Eurocode 2 [2] 28 hasta 56 días	C50	45 x 45	19,63	0,97%	22	0,58	55
		40 x 40	57,30	3,58%	25	0,46	144
MC 2020 [1] 29 a 91 días	C20	71 x 71	19,63	0,39%	14	1,45	82
		50 x 50	96,51	3,86%	20	0,72	236
Eurocode 2 [2] 57 a 91 días	C50	49 x 49	19,63	0,82%	20	0,69	66
		42 x 42	64,34	3,65%	24	0,51	170

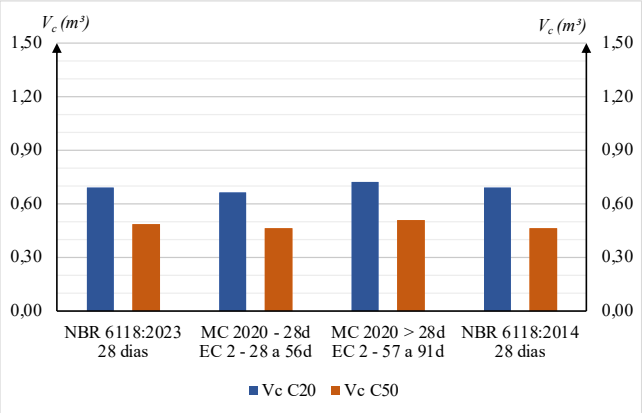

Figura 2.4. Gráfico de barras que indica el volumen de hormigón correspondiente a cada alternativa de diseño del tramo de pilar, para una cuantía máxima de armadura (alrededor del 4%).

Con el fin de mostrar la influencia de la resistencia del hormigón, C20 o C50, la figura 2.5 presenta el gráfico de barras del área acero longitudinal (A_s) para la cuantía máxima, <4%, de armadura.

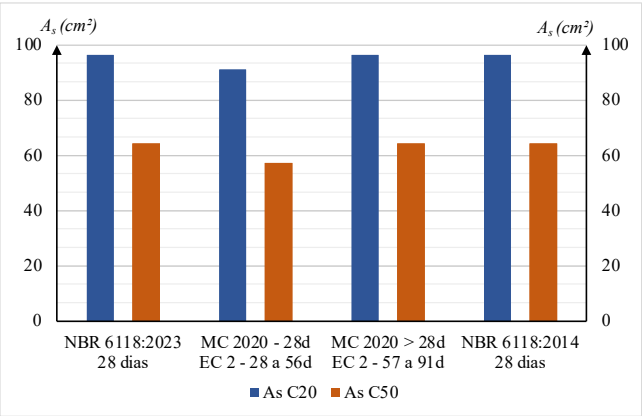

Figura 2.5. Gráfico de barras que indica el área de acero correspondiente a cada alternativa de diseño del tramo de pilar, considerando la cuantía máxima de armadura (alrededor del 4%).

Para complementar el estudio de las alternativas de diseño del tramo de pilar en base a diversos criterios normativos y clases de resistencia del hormigón, también se analizó considerar el tramo con sección cuadrada y fija de 50x50 cm para hormigón clase C20 y C50, simulando una imposición de diseño arquitectónico.

En este caso, dado que el volumen de hormigón es una constante, la figura 2.6 muestra la variación del área de acero (A_s) en función de la clase de resistencia del hormigón.

Se observa que, para el caso en estudio, el dimensionamiento según las prescripciones del MC 2020 [1] con f_{ck} a los 28 días y Eurocode 2 [2] con f_{ck} a los 28 días o 56 días, conduce a pilares más económicos independientemente de la clase de resistencia considerada. Las prescripciones de la normativa brasileña ABNT NBR 6118:2023 [4] conducen a pilares más voluminosos, es decir, es una normativa más conservadora, lo que es incoherente con un país con índices socioeconómicos inferiores a los países europeos.

Con el objetivo de la sostenibilidad, que pretende producir más con menos, es decir, es necesario desmaterializar, es evidente, en este caso de estudio, que lo ideal es utilizar hormigón de alta resistencia.

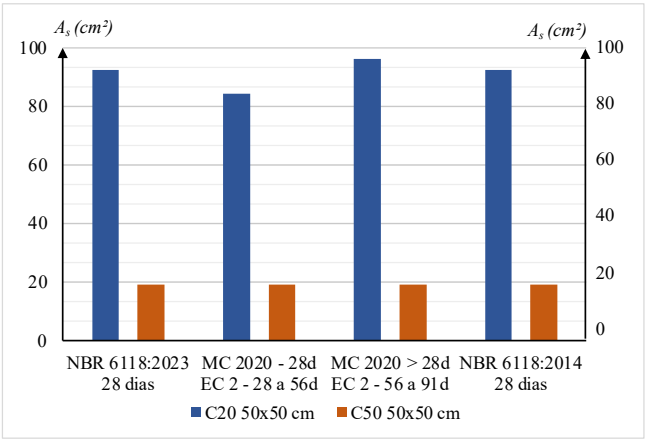

Figura 2.6. Gráfico de barras que indica la variación del área de acero (As) al fijar la dimensión del tramo de pilar y cambiar la clase de resistencia del hormigón.

Para la misma carga y optimizando la geometría, utilizando un hormigón de f_{ck} = 50 MPa en un pilar en lugar de un hormigón de f_{ck} = 20 MPa, se puede reducir el volumen de hormigón de 1,45 m³ en el caso de armadura mínima y C20, a solo 0,46 m³ con cuantía de armadura máxima y C50, contribuyendo significativamente a la desmaterialización.

Con el mismo razonamiento, la armadura de este tramo de pilar puede reducirse de 236 kg para el C20 a solo 55 kg en el caso del uso del C50, es decir, un ahorro significativo de acero, teniendo en cuenta la desmaterialización.

De la misma manera, considerando las mismas tensiones y fijando la geometría del tramo del pilar en (50 cm x 50 cm), utilizando un hormigón de f_{ck} = 50 MPa en lugar de un hormigón de f_{ck} = 20 MPa, se puede reducir la masa total de acero de 96 kg para C20 a solo 20 kg para C50, es decir, un enorme ahorro de acero, del orden de 4 veces menos material, para el mismo volumen de hormigón y área de encofrado.

Queda por considerar la influencia de la fecha de control o referencia del f_{ck}. Las dosificaciones de los mismos materiales, si se refieren a 56 días o 91 días, para el mismo valor f_{ck}, darán lugar a dosificaciones de hormigón con menor consumo de cemento por m³, lo que puede aportar aún mayores beneficios a la sostenibilidad, como se demuestra en la secuencia de este trabajo.

3. CONSUMO DE MATERIALES EN FUNCIÓN DE LA FECHA DE REFERENCIA DEL f_{ck}

El MC 2020 [1] en el inciso 14.6.1.6.1 "*Development of strength with time*", así como el Anexo B del Eurocode 2 [2] "*Time dependent behaviour of materials: strength, creep, shrinkage and elastic strain of concrete and relaxation of prestressing steel*", recomiendan el uso de una expresión en formato exponencial para representar el crecimiento de la resistencia a la compresión del hormigón en función del tiempo, a saber:

$$\frac{f_{c(t)}}{f_{c(t_{ref})}} = e^{\left\{s_c \cdot \left[1-\sqrt{\frac{t_{ref}}{t}}\right] \cdot \left(\sqrt{\frac{28}{t_{ref}}}\right)\right\}} \quad (3.1)$$

Dónde:

s_c: coeficiente adimensional que oscila entre 0,1 y 0,6, como se muestra en la tabla 3.1.

TABLA 3.1.

Valores de sc según *fib* (MC 2020) [1] y Eurocode 2 [2].

Resistencia del hormigón (MPa)	s_c Clase CR	Clase CN	Clase CS
$f_{ck} \leq 35$	0,3	0,5	0,6
$35 < f_{ck} < 60$	0,2	0,4	0,5
$f_{ck} \geq 60$	0,1	0,3	0,4

Nota: Las Clases CR, CN y CS se determinan en función del tipo y la clase de resistencia del cemento. Para determinar las Clases CR, CN y CS, consulte la tabla 14.6-8 "Strength development classes of concrete" del MC 2020 [1], así como las normas EN 197-1 [13] " Cement – Part 1: Composition, specifications and conformity criteria for common cements" y EN 206 [14] "Concrete – Specification, performance and conformity". Simplemente, se pueden asociar a la condición brasileña los siguientes: CR (hormigón con cemento CP V); CN (hormigón con cemento CP II) y CS (hormigón con cemento CP III o CP IV).

$f_{c(t)}$: resistencia a compresión a la edad t, expresada en MPa;

t: Edad del hormigón en días, calculada según la expresión:

$$t = \sum_{i=1}^{n} \Delta t_i \; e^{\left[13{,}65 - \frac{4000}{273+T_{(\Delta t_i)}}\right]} \quad (3.2)$$

Dónde:

t: es la edad del hormigón ajustada en función de la temperatura, en días;

Δ_{ti}: es el número de días en los que la temperatura T prevalece;

$T_{(\Delta ti)}$: es la temperatura media en °C durante el intervalo de tiempo Δ_{ti};

t_{ref}: edad de control y referencia f_{ck} en días, que puede variar de 28 a 91 días;

$f_{c(tref)}$: resistencia a compresión promedio a la edad t_{ref}, expresada en MPa.

Como premisa de este estudio, se consideró que el hormigón siempre estará a una temperatura de $T(\Delta t_i)$ = 20°C, durante los días hasta la edad de control, prescindiendo del uso de esta formulación.

Los autores tampoco están de acuerdo con esta formulación, ya que acelerar y mantener hormigones por encima de los 20° C conduce a resistencias finales a largo plazo más bajas que las obtenidas a partir del mismo hormigón curado a temperaturas de 20° C en las primeras edades. Los procesos de cura acelerada con un aumento de las temperaturas iniciales por encima de los 30° C conducen a mayores resistencias a edades bajas, pero a largo plazo, 28 días o más, los resultados finales terminan siendo inferiores a los hormigones mantenidos a temperaturas alrededor de 20° C a 25° C. Las altas temperaturas conducen a granos de microestructura más grandes y quebradizos en las interfaces, mientras que las temperaturas más bajas conducen a un refinamiento de los granos y, en otras palabras, por lo tanto, mayores resistencias finales.

Por simplificación en este estudio se consideran hormigones producidos con cementos CR y CS, como se muestra en la tabla 3.1. Las resistencias de $f_{c\ (28)}$, $f_{c\ (56)}$ y $f_{c\ (91)}$ también se adoptaron como referencia para la resistencia del hormigón [$f_{c(ref)}$], a efectos de análisis comparativo.

Los valores de f_{ck} adoptados en este estudio fueron 20 MPa y 50 MPa. Los valores para efectos de dosificación del hormigón, f_{cm} deben ser de 26,6 MPa y 56,6 MPa, respectivamente, considerando una desviación estándar constante igual a 4 MPa. Cabe destacar que tanto el MC 2020 [1] como el Eurocode 2 [2] prescriben una desviación estándar constante igual a 4,8 MPa, es decir, consideran una mayor variabilidad en las resistencias del hormigón que la prevista en la normativa brasileña.

De esta manera, fue posible determinar la resistencia a la compresión requerida a los 28 días de edad para las diferentes clases de resistencia estudiadas (C20 y C50), para las diferentes edades de control f_{ck} (28, 56 y 91 días) y para los dos tipos de cemento considerados CR y CS, como se detalla en la tabla 3.2.

TABLA 3.2.

Valores de resistencia promedio a compresión a los 28 días [f_{cm} (28)], calculados según la ecuación 3.1, para las clases de resistencia (C20 y C50), según la edad de control (28, 56 y 91 días), para hormigones producidos con cemento tipo CR y CS.

$t_{(t_{ref})}$ (días)	Clase de resistencia	$f_{cm(t_{ref})}$ (MPa)	Tipo de (MPa) cemento	S_c (1)	$f_{cm(28)}$ (2)
28	C20	26,6	CS	0,6	26,6
			CR	0,3	26,6
	C50	56,6	CS	0,5	56,6
			CR	0,2	56,6
56	C20	26,6	CS	0,6	22,3
			CR	0,3	24,4
	C50	56,6	CS	0,5	48,9
			CR	0,2	53,4
91	C20	26,6	CS	0,6	20,4
			CR	0,3	23,3
	C50	56,6	CS	0,5	45,3
			CR	0,2	51,8

Notas:

(1) Valor de Sc obtenido en la tabla 3.1.

(2) Resistencia media a los 28 días de edad obtenida mediante formulación del MC 2020 [1] y EUROCODE 2 [2] (ecuación 3.1), variando t(ref): 28, 56 y 91 días.

Para estimar el índice de rendimiento, expresado en kg de cemento por MPa, se adoptó la premisa de un rendimiento medio de referencia de 9/10 kg de cemento/MPa para f_{cm} de 20 a 30 MPa y de 7/7,5 kg de cemento/ MPa para f_{cm} de 40 a 60 MPa, para los cementos CR y CS, respectivamente, con base en la experiencia de los autores, la literatura sobre el tema [15] y las dosificaciones comúnmente utilizadas en las plantas de hormigón. Cabe destacar que este estudio propone discutir la sostenibilidad de forma simplificada, desconsiderando los límites normativos de consumo mínimo de cemento por m³ y relación máxima agua/cemento de las normas antes mencionadas.

Así, considerando el volumen de hormigón utilizado en cada una de las alternativas estudiadas para este tramo de pilar, dimensionado de acuerdo con los criterios de los diferentes reglamentos y el mismo índice de desempeño adoptado, se presenta un resumen del consumo de cemento obtenido en la tabla 3.3, detallando el consumo de cemento por m³ de hormigón en cada una de las alternativas para el diseño del tramo de pilar en estudio.

4. EMISIONES E INTENSIDAD DE CO_{2EQ} (IC)

El objetivo de este artículo es presentar un análisis comparativo de las emisiones de CO_{2eq} para las diferentes alternativas de diseño consideradas en este estudio. Por lo tanto, para cada una de las alternativas estudiadas, se calculó la correspondiente emisión de CO_{2eq} y los indicadores de ecoeficiencia asociados en kg CO_2/MPa, estos últimos denominados intensidad CO_{2eq}. (IC).

Para la cuantificación de las emisiones de CO_{2eq}, se utilizaron los valores de las *EPD´s* (Declaraciones Ambientales de

TABLA 3.3.
Consumo de materiales y ahorro de cemento en relación a las dosificaciones controladas a los 28 días de edad, para las diferentes alternativas de diseño.

Reglamentos edad de referencia	Clase de resistencia del hormigón	Volumen de hormigón (m³)(1)	Tipo de cemento	Consumo de cemento por m³ de hormigón (kg/m³)			Masa de cemento para la ejecución del pilar en kg		
				28 días kg/m³	Edad de referencia (28, 56 o 91) días) kg/m³	Ahorro de cemento 28 días(2 kg	28 días kg	Edad de referencia (28, 56 y 91 días) kg	Ahorro de cemento respecto 28 días (2) kg
NBR 6118:2023 [4] 28 días	C20	1,37	CS	266	266	0	364	364	0
			CR	239	239	0	328	328	0
		0,69	CS	266	266	0	184	184	0
			CR	239	239	0	165	165	0
	C50	0,66	CS	425	425	0	280	280	0
			CR	396	396	0	262	262	0
		0,48	CS	425	425	0	204	204	0
			CR	396	396	0	190	190	0
MC 2020 [1] 28 días	C20	1,25	CS	266	266	0	333	333	0
			CR	239	239	0	299	299	0
		0,66	CS	266	266	0	176	176	0
			CR	239	239	0	158	158	0
	C50	0,58	CS	425	425	0	246	246	0
			CR	396	396	0	230	230	0
		0,46	CS	425	425	0	195	195	0
			CR	396	396	0	182	182	0
Eurocode 2 [2] 56 días	C20	1,25	CS	266	223	43	333	279	54
			CR	239	220	19	299	275	24
		0,66	CS	266	223	43	176	147	29
			CR	239	220	19	158	145	13
	C50	0,58	CS	425	367	58	246	213	33
			CR	396	374	22	230	217	13
		0,46	CS	425	367	58	195	169	26
			CR	396	374	22	182	172	10
MC 2020 [1] 91 días y Eurocode 2 [2] 91 días	C20	1,45	CS	266	204	62	386	296	90
			CR	239	210	29	347	304	43
		0,72	CS	266	204	62	192	147	45
			CR	239	210	29	172	151	21
	C50	0,69	CS	425	340	85	293	234	59
			CR	396	363	33	273	250	23
		0,51	CS	425	340	85	217	173	44
			CR	396	363	33	202	185	17

(1) Valor obtenido considerando las dimensiones de los pilares indicados en la tabla 3.1 y altura de 2.88 m.
(2) Valor obtenido restando el consumo de cemento a los 28 días de edad – consumo de cemento a la edad de referencia (28, 56 o 91 días).

TABLA 4.1.
Cantidad de CO_2 liberada en kg $CO_{2eq.}$ en función del material adoptado, considerando las etapas del producto A1, A2 y A3.

Material	Sidac [1] (kg CO_2 eq.)	CECarbon [2] (kg CO_2 eq.)	Documentos EPD ArcelorMittal Piracicaba (kg CO_2 eq.) [3]	Votorantim Santa Elena (kg CO_2 eq.) [4]	Gerdau Araçariguama (kg CO_2 eq.) [4]
Acero CA-50, en t.	425,9 – 1.061,0	-	786	-	1.070
Cemento CP III (CS), en t.	235,3 – 681,7	-	-	384	-
Cemento CP V (CR), en t.	776,4 – 994,3	-	-	852	-
Madera de pino, en m² [5]	0,3 – 0,7	-	-	-	-
Madera compensada, en m² [6]	-	6,8	-	-	-
Madera cruzada laminada (CLT), en m² [7]	-	3,1	-	-	-
Madera Laminada Encolada, en m² [8]	-	3,3	-	-	-
Madera aserrada en bruto (plantada), en m³ [9]		50,6	-	-	-

(1) Fuente: www.sidac.org.br/busca
(2) Fuente: www.cecarbon.com.br
(3) Fuente: Declaración Ambiental de Producto Nº EPD-ARC-20170124-CBD1-EM (válida hasta el 22/03/2023), disponible en: www.ibu-epd.com. De acuerdo con las reglas de cálculo del ACV presentadas en este documento, las emisiones de CO_2 indicadas son válidas para las plantas de ArcelorMittal en Brasil ubicadas en: Cariacica, Itaúna, João Monlevade, Juiz de Fora y Piracicaba, aunque esta DAP está con fecha vencida.
(4) Fuente: www.environdec.com/library
(5) La cantidad de CO_2 liberada se consideró un espesor de encofrado de 18 mm. Sidac indica, para la madera de pino, una liberación de CO_2 que oscila entre 19,06 kg CO_2 eq. y 39,15 kg CO_2 eq. por m³ de madera.
(6) La cantidad de CO_2 liberada consideró un espesor de encofrado de 18 mm. Para el caso de la madera compensada, CECarbon indica una liberación de CO_2 de 378 kg CO_2 eq. por m³.
(7) La cantidad de CO_2 liberada consideró un espesor de encofrado de 18 mm. En el caso de la madera cruzada laminada, CECarbon indica una liberación de CO_2 de 171,12 kg CO_2 eq. por m³.
(8) La cantidad de CO_2 liberada consideró un espesor de encofrado de 18 mm. En el caso de la madera laminada encolada, CECarbon indica una liberación de CO_2 de 183,6 kg CO_2 eq. por m³.
(9) La cantidad de CO_2 liberada consideró listones con dimensiones de 75 mm x 75 mm y madera cruda aserrada con una masa específica de 550 kg/m³ (según la tabla 1 de la ABNT NBR 6120:2019
[8] "Ações para o cálculo de estruturas de edificações, considerando madera maciza, conífera, clase de resistencia C25"). CECarbon indica, para el caso de la madera en bruto aserrada (plantada), una liberación de CO_2 de 92 kg CO_2 eq. por tonelada.

Producto) disponibles en los "*EPD documents*" de la página web de www.environdec.com/home, los datos proporcionados por el "*Sistema de Informação do Desempenho Ambiental da Construção – Sidac*" disponibles en www.sidac.org y los datos obtenidos por la calculadora de consumo de energía y emisiones de carbono de CECarbon para edificios disponible en el sitio web de www.cecarbon.com.br.

La tabla 4.1 muestra los valores de CO_{2eq}. por tonelada de material producido en Brasil, en el caso de acero y cemento y por m² de encofrado, considerando que este último fue producido en madera compensada de 18 mm de espesor, estructurado con madera en bruto en las dimensiones de 75 mm x 75 mm (listones) [16] cada 35 cm.

Asimismo, para la ejecución del soporte para la fijación de los encofrados de los pilares (marcos inferiores), se utilizaron listones de madera de 25 mm de espesor y 100 mm de ancho. Los trabados horizontales (guías en perfiles metálicos), amarres con barras de anclaje, plomadas, escuadras, etc., no se consideraron en este estudio ya que son componentes del sistema de encofrado que pueden ser reutilizados varias veces.

Con base en los datos presentados, fue posible obtener el volumen promedio esperado de madera aserrada en bruto (en m³) por m² de tablero de madera compensada, de 0,025 m³/m². Por lo tanto, en este estudio se adoptó un índice de 8,0 $kgCO_{2eq}$/m² de encofrado, de acuerdo con los cálculos que se detallan a continuación:

A partir de los datos presentados en la tabla 4.1 y las cantidades de materiales (acero, cemento y encofrado) fue posible calcular la cantidad de CO_{2eq}. para cada una de las alternativas de diseño del tramo de pilar en estudio, así como el cálculo de la intensidad de CO_{2eq} (IC) para cada resistencia $f_{cm(tref)}$ que se presenta a continuación en la tabla 4.2.

Para una mejor visualización de las cifras presentadas en la tabla 4.2, las figuras 4.1 y 4.2 presentan gráficamente las emisiones de CO2eq. por alternativa estudiada, considerando diseños con cuantía mínima y máxima de armadura, respectivamente.

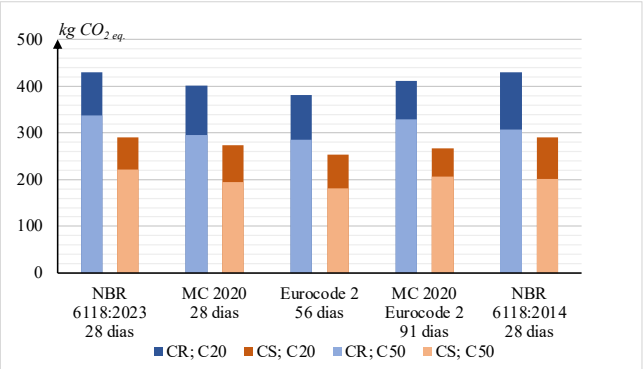

Figura 4.1. Gráfico de barras que muestra la emisión de CO_2 en kg $CO_{2eq.}$ por diseño alternativo del pilar con mínima cuantía de acero.

Emisión de $CO_{2eq.}$ *encofrados* = [6,8 *kg*$CO_{2eq.}$/m²]+[(0,025 m³/m²)·50,6 *kg*$CO_{2eq.}$ /m³]

Emisión de $CO_{2eq.}$ *encofrados* = [6,8 *kg*$CO_{2eq.}$/m²]+[1,2 *kg*$CO_{2eq.}$/m²]

Emisión de $CO_{2eq.}$ *encofrados* = 8,0 *kg*$CO_{2eq.}$/m²

TABLA 4.2.
Cantidad de $CO_{2eq.}$ liberada por alternativa estudiada en kg $CO_{2eq.}$.

Reglamentos	Clase de resistencia	Consumo de acero (kg) (1)	Área de encofrado (m^2) (2)	Masa de cemento en el pilar (kg) (3)	Emisiones de CO_2 por pilar (kg $CO_{2eq.}$)	IC por pilar (kg CO_2/MPa)
NBR 6118:2023 [4] 28 días	C20	82	7,95	364 kg CS 328 kg CR	291 431	10,9 16,2
		235	5,64	184 kg CS 165 kg CR	367 437	13,8 16,4
	C50	65	5,53	280 kg CS 262 kg CR	221 337	3,9 6,0
		160	4,72	204 kg CS 190 kg CR	287 371	5,1 6,6
MC 2020 [1] 28 días	C20	80	7,60	333 kg CS 299 kg CR	274 401	10,3 15,1
		235	5,53	176 kg CS 158 kg CR	363 430	13,6 16,2
	C50	55	5,18	246 kg CS 230 kg CR	195 296	3,4 5,2
		144	4,61	195 kg CS 182 kg CR	266 346	4,7 6,1
Eurocode 2 [2] 56 días	C20	80	7,60	279 kg CS 275 kg CR	254 381	9,5 14,3
		235	5,53	147 kg CS 145 kg CR	352 419	13,2 15,8
	C50	55	5,18	213 kg CS 217 kg CR	182 285	3,2 5,0
		144	4,61	169 kg CS 172 kg CR	256 338	4,5 6,0
MC 2020 [1] 91 días	C20	82	8,18	296 kg CS 304 kg CR	267 412	10,0 15,5
		236	5,76	147 kg CS 151 kg CR	355 427	13,3 16,1
Eurocode 2 [2] 91 días	C50	66	5,64	234 kg CS 250 kg CR	206 329	3,6 5,8
		170	4,84	173 kg CS 185 kg CR	287 378	5,1 6,7

(1) De acuerdo con el documento "*Environmental Product Declaration Reinforcing Steel Bar Gerdau GG 50*", 1.070 kg de CO_2 por tonelada de acero (kg $CO_{2\,eq.}$), valor obtenido sumando los valores de emisión en las etapas A1 (Raw material supply), A2 (Transportation) y A3 (Core process).
(2) Se consideró el valor de 8 kg de CO_2 por m² de encofrado, tal y como se justifica en el texto.
(3) Según el documento " Environmental Product Declaration for Cement CP III 40 RS", 384 kg de CO_2 por tonelada de cemento (kg $CO_{2\,eq.}$), valor obtenido sumando los valores de emisión en las etapas A1 (Raw material supply), A2 (Transportation) y A3 (Core process). Según el documento " Environmental Product Declaration for Cement CP V ARI", 852 kg de CO_2 por tonelada de cemento (kg $CO_{2\,eq.}$), valor obtenido sumando los valores de emisión en las etapas A1 (Raw material supply), A2 (Transportation) y A3 (Core process).

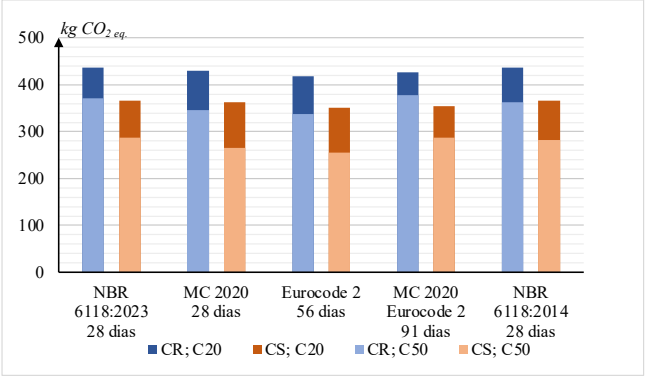

Figura 4.2. Gráfico de barras que muestra la emisión de CO_2 en kg $CO_{2eq.}$ por diseño alternativo del pilar con la máxima cuantía de acero.

Como se muestra, un tramo de pilar destinado a la misma función, para la misma carga, puede emitir desde 182 kg $CO_{2eq.}$ (IC = 3,2 kgCO2/MPa), a 437 kg $CO_{2eq.}$ (IC = 16,4 kgCO_2/MPa), de acuerdo con una decisión de diseño adoptada por el proyectista estructural en la fase de diseño combinada con tecnología de hormigón en la optimización de mezclas y diferentes cementos. En números relativos, puede ir de 1 a 2,4 veces, lo cual es muy expresivo.

La figura 4.3 presenta esquemáticamente las dos alternativas para calcular los tramos de pilares de este estudio que presentan mayor y menor emisión de CO_2 Esta figura también contiene las emisiones detalladas por insumo utilizado, así como el resto de la información que caracteriza a cada una de las alternativas para dimensionar y ejecutar el mismo pilar.

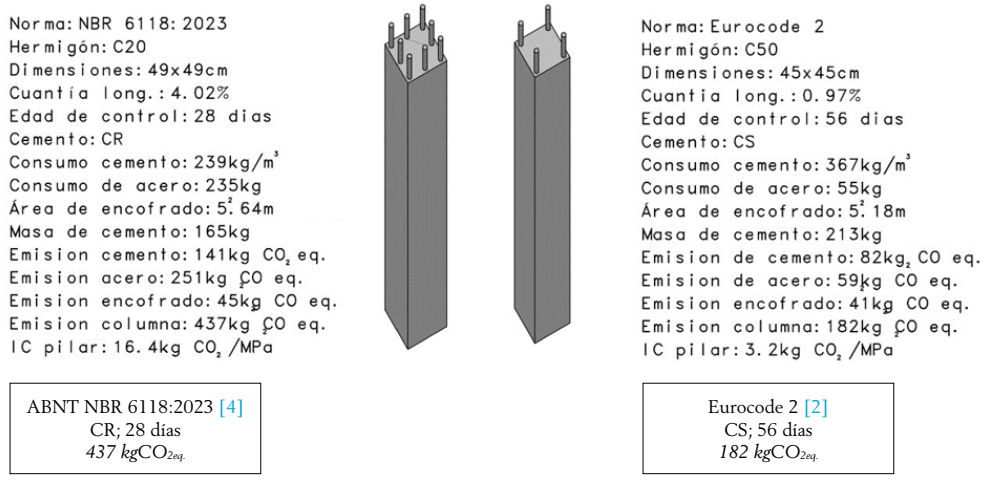

Figura 4.3. Alternativas para el cálculo de tramos de pilares en este estudio que presentan mayores y menores emisiones de $CO_{2eq.}$.

Esta enorme ventaja solo puede lograrse en condiciones ideales de libertad de diseño. En condiciones normales, con limitaciones arquitectónicas y de ejecución, los beneficios pueden ser más reducidos.

En cualquier caso, se puede decir que utilizando cemento CS en lugar de cemento CR, para cualquier situación e incluso teniendo en cuenta que se necesita de 0,5 a 1kg de cemento CS más por MPa, la estructura emitirá menos gases de efecto invernadero.

También se observó que los pilares diseñados con una cuantía mínima de armadura emiten menos gases de efecto invernadero.

La adopción de una edad de referencia del f_{ck} de 56 días en lugar de 28 días en este estudio siempre condujo a una reducción de las emisiones de gases de efecto invernadero.

También es posible realizar un análisis análogo de las emisiones de CO_2 fijando las dimensiones de este tramo de pilar y variando el área de acero (*As*), el tipo de cemento, así como la clase de resistencia del hormigón (C20 o C50).

En la tabla 4.3 se muestran las emisiones de CO2eq, fijando las dimensiones del tramo del pilar en 50 x 50 cm y una altura de techo de 2,88 m, simulando las limitaciones arquitectónicas.

Como se muestra en la tabla 4.3, un pilar destinado a la misma función, para la misma carga, con la misma geometría y sección transversal cuadrada, puede emitir desde 201 kg $CO_{2eq.}$ (IC = 3,6 kgCO_2/MPa), hasta 439 kg $CO_{2eq.}$ (IC = 16,5 kgCO_2/MPa), según una decisión de diseño, adoptada por el proyectista estructural en la fase de diseño y combinada con la tecnología del hormigón en la optimización de la mezcla y

TABLA 4.3.
Cantidad de CO_2 liberada por cada alternativa estudiada, considerando dimensiones fijas (50 x 50 x 288 cm³), en kg $CO_{2eq.}$.

Reglamento	Clase de resistencia	Consumo de acero (kg)	Área de encofrado (m²)	Masa de cemento por pilar (kg)	Emisiones de CO_2 por pilar (kg $CO_{2eq.}$)	IC (kg CO_2/MPa) por pilar
NBR 6118:2023 [4] 28 días	C20	230	5,76	192 kg CS 172 kg CR	366 439	13,8 16,5
	C50	58		306 kg CS 285 kg CR	226 351	4,0 6,2
MC 2020 [1] 28 días	C20	228	5,76	192 kg CS 172 kg CR	364 437	13,7 16,4
	C50	50		306 kg CS 285 kg CR	217 342	3,8 6,0
Eurocode 2 [2] 56 días	C20	228	5,76	161 kg CS 158 kg CR	352 425	13,2 16,0
	C50	50		264 kg CS 269 kg CR	201 329	3,6 5,8
MC 2020 [1] 91 días	C20	236	5,76	147 kg CS 151 kg CR	355 427	13,3 16,1
Eurocode 2 [2] 91 días	C50	60		245 kg CS 261 kg CR	204 333	3,6 5,9

diferentes cementos. En números relativos puede ir de 1 a 2,2 veces, lo cual es muy expresivo.

Esta enorme ventaja obtenida en un solo tramo de pilar si extrapolada simplificadamente, y multiplicada por el total de 1008 tramos de pilar de esta estructura, podría ahorrar 240 t de $CO_{2eq.}$ En otras palabras, de manera conservadora, si un análisis cuidadoso de los pilares lograra reducir, por ejemplo, apenas 30 kg de $CO_{2eq.}$ por tramo, la reducción de gases de efecto invernadero en esta estructura podría ser del orden de 30 toneladas de $CO_{2eq.}$, solo en pilares.

5. CONCLUSIONES

El texto de las normas MC 2020 [1] y Eurocode 2 [2] conducen a pilares con un menor volumen de hormigón, acero y encofrado, ya que prescriben el coeficiente α_{cc} = 1,0, para f_{ck} a los 28 días, siendo que el Eurocode 2 [2] prescribe α_{cc} = 1,0 hasta con f_{ck} a los 56 días. Por otro lado, la ABNT NBR 6118 de 2023 [4], que adoptan un valor fijo de α_{cc} = 0,85, dio lugar a un detallado con mayor consumo de material.

En este estudio, para f_{ck} = 50 MPa a los 56 días, 0,9% cuantía de armadura, Eurocode 2 [2], dio como resultado el tramo del pilar con un volumen de hormigón de 0,58 m³, 55 kg de acero y 5,2 m² de encofrado, mientras que para f_{ck} = 20 MPa a los 28 días, 0,4% de cuantía de armadura, ABNT NBR 6118 [3] [4], dio como resultado el tramo del pilar con 1,37 m³ de hormigón, 82 kg de acero y 7,95 m² de encofrado. Extrapolando groseramente al total de 1008 tramos de pilares, la elección inteligente de las opciones de dimensionamiento en este edificio podría suponer una desmaterialización, es decir, dejar de utilizar 796 m³ de hormigón, 27 t de acero y 2.772 m² de encofrado.

En general, las alternativas de diseño del tramo de pilar con una cuantía de armadura mínima, independientemente de las normas utilizadas, dieron como resultado valores de emisión de $CO_{2eq.}$ más bajos. En concreto el Eurocode 2 [2], que considera α_{cc} = 1,0, con f_{ck} a los 56 días, conduce a mejores indicadores de ecoeficiencia (IC), para cualquier detallado en comparación con las otras normas.

El diseño realizado por la actual norma brasileña ABNT NBR 6118:2023 [4] presentó los peores índices de IC, es decir, en este estudio, en particular, fue la norma que menos contribuye a la sostenibilidad de los pilares cortos.

En este estudio, para f_{ck} = 50 MPa a los 56 días, 0,9% de cuantía de armadura, Eurocode 2 [2], dio como resultado el tramo de pilar con una emisión de 182 kg $CO_{2eq.}$ (IC = 3,2 kgCO_2/MPa), mientras que para fck = 20 MPa a los 28 días, 4% de cuantía de armadura, ABNT NBR 6118 [3] [4], para la misma carga, función y seguridad, resultó en una emisión de 437 kg $CO_{2eq.}$ (IC = 16,4 kgCO_2/MPa) de gases de efecto invernadero. Extrapolando de manera grosera al total de 1008 tramos de pilares de este edificio podría suponer una reducción de las emisiones de gases de efecto invernadero de hasta 257 toneladas de $CO_{2eq.}$.

Este estudio también demostró que el uso de cemento CS, independientemente de las diferentes normas consideradas aquí, resultó en menores emisiones de $CO_{2eq.}$ en comparación con el cemento de alta resistencia inicial CR, a pesar de que fue necesario consumir más cemento CS para la misma resistencia y edad.

De hecho, en un proyecto estructural destinado a un proyecto arquitectónico definido, no hay tanta libertad como la considerada en este estudio, porque a menudo las limitaciones arquitectónicas y funcionales no permiten las dimensiones óptimas desde el punto de vista estructural. Ciertamente, en casos reales, las ganancias serán menores, pero no se pueden desconsiderar ni omitir en los estudios para verificar la seguridad y optimización del proyecto en la fase de diseño.

Este estudio buscó demostrar que las decisiones de diseño, combinadas inteligentemente con la tecnología del hormigón, pueden influir significativamente en la sostenibilidad, es decir, pueden contribuir efectivamente a la desmaterialización y reducción de las emisiones de gases de efecto invernadero de la estructura terminada.

Finalmente, tomando como referencia los resultados obtenidos en este estudio, los autores entienden que para obtener menores emisiones de gases de efecto invernadero se deben seguir las premisas de cálculo de resistencia de diseño establecidos en el Eurocode 2:2023 [2], utilizando las mayores clases de resistencia de hormigón (permitiendo así menores consumos de material) y controles a una edad de referencia de 56 días conducen a resultados más sostenibles.

A modo de sugerencia, se entiende que los estudios que incluyan, además de pilares cortos, otro tipo de elementos estructurales (vigas, losas, cimentaciones, entre otros) pueden ser objeto de estudios similares, con el fin de comprobar las conclusiones aquí mencionadas.

Referencias

[1] Fédération Internationale du Béton – *fib* (CEB-FIP). fib Model Code for Concrete Structures 2020. Lausanne, Switzerland, 2023. 1256 p.

[2] EUROPEAN COMMITEE FOR STANDARDIZATION. EN 1992-1-1: Eurocode 2: Design of concrete structures - Part 1-1: General rules and rules for buildings, bridges and civil engineering structures. Brussels, 2023. 402 p.

[3] ASSOCIAÇÃO BRASILEIRA DE NORMAS TÉCNICAS ABNT NBR 6118:2014. Projeto de Estruturas de Concreto -Procedimento. 3 ed. Rio de Janeiro, 2014. 238 p.

[4] ASSOCIAÇÃO BRASILEIRA DE NORMAS TÉCNICAS ABNT NBR 6118:2023. Projeto de Estruturas de Concreto. Rio de Janeiro, 2023. 242 p.

[5] ASSOCIAÇÃO BRASILEIRA DE NORMAS TÉCNICAS ABNT NBR 12655: 2022. Concreto de cimento Portland. Preparo, controle, recebimento e aceitação-Procedimento. Rio de Janeiro, 2022. 6 p.

[6] ASSOCIAÇÃO BRASILEIRA DE NORMAS TÉCNICAS ABNT NBR 6123:1998. Forças devidas ao vento em edificações. Rio de Janeiro, 1998. 110 p.

[7] ASSOCIAÇÃO BRASILEIRA DE NORMAS TÉCNICAS ABNT NBR 15421:2023. Projeto de estruturas resistentes a sismos. Rio de Janeiro, 2023. 27 p.

[8] ASSOCIAÇÃO BRASILEIRA DE NORMAS TÉCNICAS ABNT NBR 6120:2019. Ações para o cálculo de estruturas de edificações. Rio de Janeiro, 2019.

[9] ASSOCIAÇÃO BRASILEIRA DE NORMAS TÉCNICAS ABNT NBR 15200:2012. Projeto de estruturas de concreto em situação de incêndio. 2 ed. Rio de Janeiro, 2012. 48 p.

[10] HELENE, Paulo. Contribuição ao Estabelecimento de Parâmetros para Dosagem e Controle dos Concretos de Cimento Portland. São Paulo, Universidade de São Paulo, Escola Politécnica, Programa de Pós-graduação em

Engenharia Civil, Departamento de Engenharia de Construção Civil, 1987. 278 p. (Tese de Doutorado)

[11] ASSOCIAÇÃO BRASILEIRA DE NORMAS TÉCNICAS ABNT NBR 8681:2003. Ações e segurança nas estruturas - Procedimento. Rio de Janeiro, 2003. 18 p.

[12] EUROPEAN COMMITEE FOR STANDARDIZATION. EN 1990:2002+A1:2005: Eurocode - Basis of structural design. Brussels, 2002. 116 p.

[13] EUROPEAN COMMITEE FOR STANDARDIZATION. EN 197-1:2011: Cement – Part 1: Composition, specifications and conformity criteria for common cements. Brussels, 2011. 38 p.

[14] EUROPEAN COMMITEE FOR STANDARDIZATION. EN 206:2013+A2:2021: Concrete - Specification, performance, production and conformity. Brussels, 2013. 92 p.

[15] DAMINELI, B.L.; PILEGGI, R. G.; JUAN, V. M. Eco eficiência do uso de cimento em concreto: estado atual, possibilidades e tendências. 54º Congresso Brasileiro do Concreto 54CBC2012. Maceió. Instituto Brasileiro do Concreto IBRACON, 2012.

[16] ZORZI, Antonio C. Sistemas de Fôrmas para Edifícios: recomendações para a melhoria da qualidade e da produtividade com redução de custos. 2. ed. São Paulo: Ibracon, 2015. 195 p.

[17] DAMINELI, B.L; PILEGGI, R. G; JOHN, V. M. Eco eficiência do uso de cimento em concreto: estado atual, possibilidades e tendências. 54º Congresso Brasileiro do Concreto 54CBC2012. Maceió. Instituto Brasileiro do Concreto IBRACON, 2012.

Disponible en **www.hormigonyacero.com**
https://doi.org/10.33586/hya.2024.3189

Sensibilidad de la longitud de anclaje al fallo por hendimiento en el nuevo Eurocódigo 2

The Sensitivity of Anchorage Length to Splitting Failure in the New Eurocode 2

Luisa María Gil-Martín[a], David García-Moro[b] y Enrique Hernández-Montes[*,c]

[a] *Dra ICCP, ETSI Caminos, Canales y Puertos, Universidad de Granada*
[b] *ITOP, Director de Construcción. ERSI-Group*
[c] *Dr ICCP, ETSI Caminos, Canales y Puertos, Universidad de Granada*

Recibido el 21 de abril de 2024; revisado el 9 de julio de 2024, aceptado el 11 de noviembre de 2024

RESUMEN

En el nuevo Eurocódigo 2 [1], el cálculo de la longitud de anclaje se ha modificado notablemente con respecto a la versión anterior. La nueva formulación es significativamente más sensible al fallo por hendimiento del hormigón. En la versión anterior, la longitud de anclaje podía fluctuar hasta un máximo del 30% debido a los efectos de hendimiento, confinamiento de armadura y presión lateral. Sin embargo, en el nuevo Eurocódigo 2, debido al efecto de hendimiento del hormigón generado por la cercanía de las barras entre sí o a los bordes, la longitud de anclaje puede incrementarse hasta tres veces. Además, considerar el efecto del confinamiento de la armadura transversal puede llevar a reducciones considerables de esta longitud. Se presentan diversas representaciones gráficas y ejemplos para cuantificar la sensibilidad frente al hendimiento de la nueva formulación.

PALABRAS CLAVE: longitud de anclaje, longitud de desarrollo, fallo por hendidura, separación entre barras.

ABSTRACT

In the new Eurocode 2 [1], the calculation of anchorage length has been notably modified compared to the previous version. The new formulation is significantly more sensitive to concrete splitting failure. In the previous version, the anchorage length could fluctuate by up to 30% due to effects such as splitting, reinforcement confinement, and lateral pressure. However, in the new Eurocode 2, due to the concrete splitting effect caused by the proximity of bars to each other or to edges, the anchorage length can increase by up to three times. Additionally, considering the effect of transverse reinforcement confinement can lead to considerable reductions in this length. Various graphical representations and examples are provided to quantify the sensitivity to splitting in the new formulation.

KEYWORDS: anchorage length, development length, splitting failure, bar spacing.

* Persona de contacto / *Corresponding author*:
Correo-e / *e-mail*: emontes@ugr.es (Enrique Hernández Montes)

Cómo citar este artículo: Gil-Martín, L.M., García-Moro, D., & Hernández, E. (2025). Sensibilidad de la longitud de anclaje al fallo por hendimiento en el nuevo Eurocódigo 2. *Hormigón y Acero*. 76(306):115-118. https://doi.org/10.33586/hya.2024.3189

1. INTRODUCCIÓN. LONGITUD DE ANCLAJE EN LOS DIAGRAMAS DE CAPACIDAD

La longitud de anclaje, o de desarrollo, es un concepto fundamental en estructuras de hormigón, dado que la barra de refuerzo necesita la longitud de anclaje para poder desarrollar toda su capacidad, [2]. Además, el empalme por solape (o traslapo) está basado en el mismo concepto, [3]. La Figura 1, adaptada de la Figura 12.1 de la Eurocódigo 2, muestra la fuerza axil de tracción máxima que pueden desarrollar las barras de refuerzo de una viga. En esta figura se observa como las barras no tienen ninguna capacidad en los extremos y como esta capacidad aumenta de forma lineal a lo largo de la longitud de anclaje. Más allá de la longitud de anclaje, la barra alcanza su máxima capacidad –que se mantiene constante–.

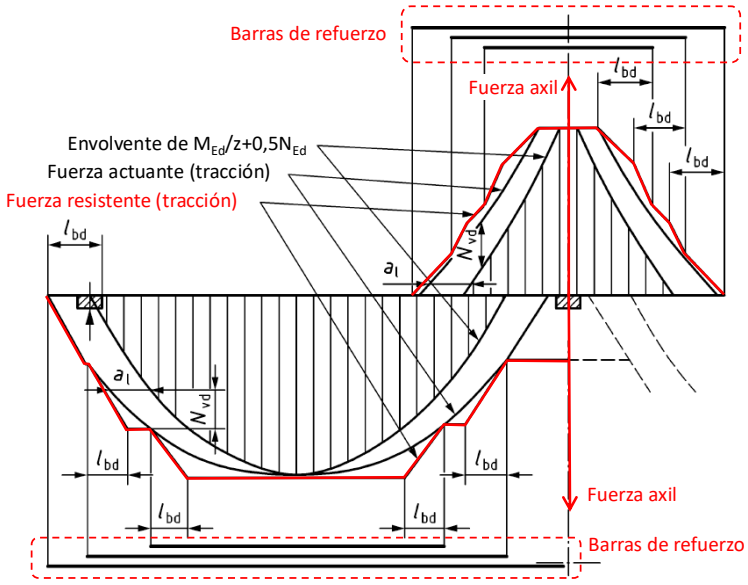

Figura 1. Capacidad a tracción de las barras de refuerzo de una viga. (Adaptado de la Figura 12.1 de la EN 1992-1-1).

El diagrama de capacidad de momentos flectores se obtiene multiplicando la fuerza resistente de las barras por su brazo mecánico. La Figura 2 muestra una viga simplemente apoyada, con un refuerzo formado por cuatro barras, junto con su correspondiente diagrama de capacidad de momentos flectores. Cualquier envolvente de momentos flectores de diseño (decalados) que actúe sobre la viga, debe de quedar dentro del diagrama de capacidad, [4]. Como se puede apreciar, la variación de la longitud de anclaje influye directamente en el diagrama de capacidad de momentos flectores.

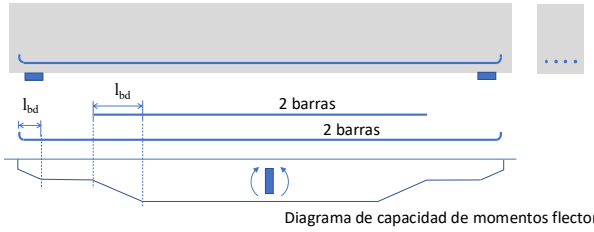

Figura 2. Diagrama de capacidad de momentos flectores y longitud de anclaje.

2. LONGITUD DE ANCLAJE EN EL EN 1992-1-1/2023

La longitud de anclaje se diseña considerando tres tipos de fallo posibles, [5]: rotura de la barra, rotura por hendimiento del hormigón (o concreto) y deslizamiento. Figura 3.

Basándose principalmente en el Boletín 72 de la FIB [6] (ver también [7]), el cálculo de la longitud de anclaje en la nueva versión del Eurocódigo 2 ha cambiado sustancialmente respecto a versiones anteriores. En el actual Eurocódigo 2, las contribuciones del recubrimiento, la armadura secundaria y la compresión transversal se han considerado con carácter de suma, a diferencia del formato multiplicativo que tenían en la versión anterior, [6] y [7]. Para el caso de anclaje por prolongación recta, la nueva formulación para obtener el valor de diseño de la longitud de anclaje es:

$$l_{bd} = k_{lb} k_{cp} \phi \left(\frac{\sigma_{sd}}{435}\right)^{1.5} \left(\frac{25}{f_{ck}}\right)^{1/2} \left(\frac{\phi}{20}\right)^{1/3} \left(\frac{1.5\phi}{c_d}\right)^{1/2} \geq 10\phi \quad (1)$$

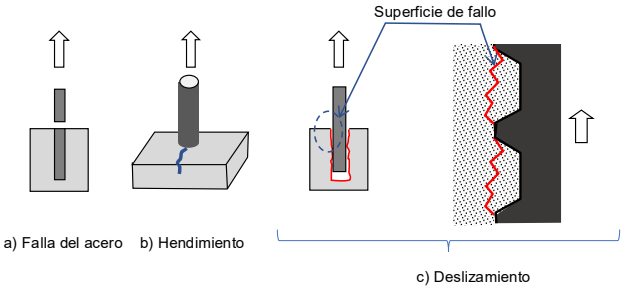

Figura 3. Tipos de fallo del anclaje de una barra.

El valor del coeficiente k_{lb} es 35 para situaciones accidentales y 50 para situaciones persistentes y transitorias. El coeficiente k_{cp}, que tiene en cuenta la influencia del hormigonado, vale 1.0 para condiciones de buena adherencia, 1.2 para condiciones de pobre adherencia y 1.4 en el caso de que se usen lodos de bentonita (p.ej. en la construcción de muros pantalla). El valor de c_d depende del recubrimiento y de la separación entre las barras (ver Figura 4). Dado que el hendimiento puede producirse para valores pequeños de la separación entre barras, este coeficiente diferencia de manera indirecta el modo de fallo. Es decir, si c_d=3.75Ø, el fallo del anclaje será por deslizamiento, mientras que para valores inferiores de c_d el fallo será por hendimiento que, según la norma, se producirá para una separación entre barras menor de 7.5Ø (téngase en cuenta que: $0.5c_s < 3.75$ Ø → $c_s < 7.5$Ø). Por tanto, la sensibilidad del valor de la longitud de anclaje con respecto a cd (i.e. al fallo por hendimiento) se considera en el último término de la Ecuación 1: $(1.5Ø/c_d)^{0.5}$).

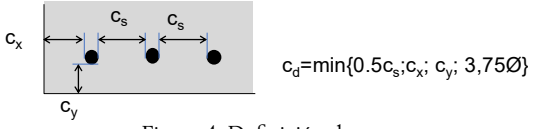

Figura 4. Definición de c_d.

En la Figura 5 se representa, en línea continua, la variación del último término de la Ecuación 1 $(1.5Ø/cd)^{0.5}$, con respecto a la separación libre entre las barras (cs), medida en unidades de diámetro de la barra, en el rango susceptible de fallo por hendimiento (es decir, $c_s < 7.5Ø$). Para forzar a que el término más limitativo en el cálculo de cd sea la separación entre barras (c_s), se ha supuesto que c_x y c_y son mayores que $0.5c_s$. Como se puede ver en la Figura 5, la longitud de anclaje para unas barras separadas 1.0Ø es 3 veces mayor que si la separación entre barras fuera 7.5Ø. En la figura se ha representado en línea negra discontinua el factor α2 del Eurocódigo 2 del 2004 [8], que tiene en cuenta el recubrimiento y la separación entre barras, para el caso de anclaje en prolongación recta en tracción. El factor α_2 tiene un efecto favorecedor (no penalizador por fallo por hendimiento, como en la versión del Eurocódigo 2 del 2023 [1]), de tal forma que la longitud de anclaje se reduce de forma lineal para separaciones libres entre barras mayores de 2Ø llegando a una reducción máxima cuando la separación libre es mayor o igual que 6Ø (i.e. α2=0.7), ver línea negra discontinua en la Figura 5.

La formulación de la ACI 318-19 [5] (Ecuación 25.4.2.4a de [5]) penaliza por fallo por hendimiento para separaciones libres menores de 4Ø. En la Figura 5 se ha representado en línea discontinua azul cómo es la función de penalización para separaciones libres entre barras menores que 7.5Ø. En Figura 5 se ha considerado que la separación libre por encima de la cual no se produce fallo por hendidura para ninguna de las dos normativas, ni ACI-318-19 [5] ni EC2 [1], es 7.5Ø.

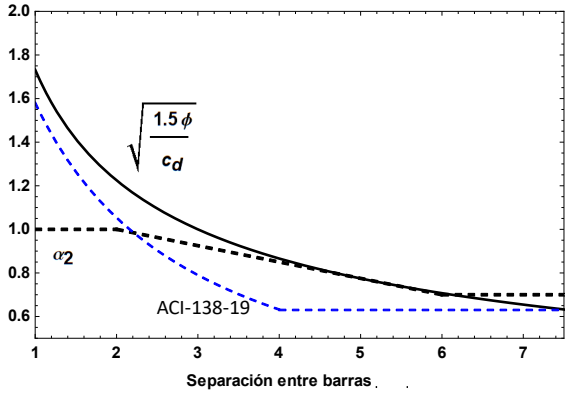

Figura 5. Influencia de la separación entre barras en las dos últimas versiones del Eurocódigo 2 y en la ACI-138-19.

La Figura 5 muestra que cuanto menor es la separación entre barras –y, por tanto, más probable el fallo por hendimiento–, mayor es la longitud de anclaje y que este efecto es muy significativo en la última versión del Eurocódigo 2 [1]. De hecho, como se aprecia en la Figura 5, el fallo por hendimiento en la nueva formulación de la longitud de anclaje conlleva un aumento de un 22% en la longitud de anclaje para separaciones entre barras de 2 veces el diámetro y de un 73% para separaciones de un diámetro de barra.

Es interesante señalar que aunque el EC2 permite separaciones mínimas de hasta un diámetro de la barra (otras normas, como la AASHTO LRFD *Bridge Design* [9], limitan esta separación a 1.5Ø), los valores pequeños de separación de barras (1.0Ø) están muy penalizados en términos de longitud de anclaje en la última versión del Eurocódigo 2.

En la Figura 6 se ha representado la longitud de anclaje de una barra Ø25 en función de la resistencia característica del hormigón para distintas separaciones libres entre barras (c_s), para la versión vigente del EC2 [8] (en líneas continuas azules y rojas) y para la última versión [1] (líneas discontinuas azules y rojas). Como antes, se ha supuesto que c_x y c_y son mayores que $0.5c_s$. Se consideran condiciones de buena adherencia, k_{lb}=50 y que la tensión de diseño de la barra es 435 MPa (σ_{sd}=435 MPa). En esta figura se puede ver cómo el efecto de la rotura por hendimiento, considerada a través de la separación entre las barras ($c_s < 7.5Ø$), en la longitud de anclaje es mucho más importante en la nueva versión del Eurocódigo 2 [1] que en la versión anterior. En línea negra se indican las longitudes de anclajes máximas y mínimas según la ACI-318-19. Las líneas rojas de la Figura 6 corresponden al caso de una separación libre entre barras de 3Ø, caso cuyos valores aparecen tabulados en el nuevo EC2 [1] (Tabla 11.1 de [1]).

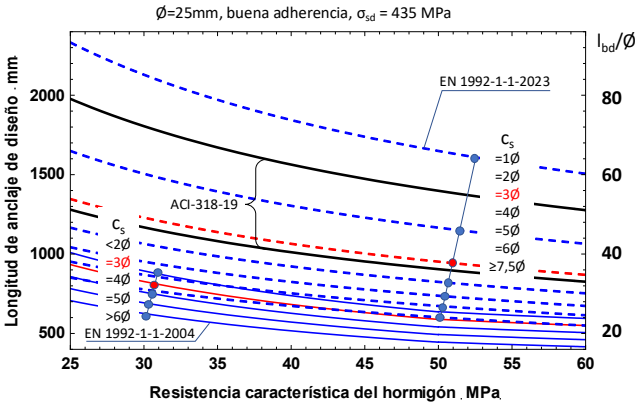

Figura 6. Longitudes de anclaje para una barra de 25 mm de diámetro tensada a 435 MPa.

2.1. Armaduras de confinamiento y transversal

La longitud de anclaje puede reducirse, respecto al valor dado por la Ecuación 1, si se cuenta con la presencia de armadura de confinamiento, armadura transversal o presión exterior, tal y como se indica en la Figura 7. En estos casos, el valor de c_d en la Ecuación 1 se sustituye por un nuevo valor, $c_{d,conf}$, definido en la Ecuación 2 (§11.4.2 del EN-1992-1-1-23 [1]), donde n_c es el número de barras del refuerzo de confinamiento que cruzan la superficie de fallo por hendimiento, nb es el número de barras ancladas o pares de barras traslapadas en la superficie potencial de fallo por hendimiento, s_c es la separación del refuerzo de confinamiento a lo largo de la barra a anclar y σ_{ccd} es el valor de diseño de la tensión de compresión media perpendicular al plano de fallo potencial por hendimiento.

$$c_{d,conf} = \min\left\{c_x; c_y + 25\frac{\phi_t^2}{s_t}; 0.5c_s; 3.75\phi\right\} + \Delta c_d \le 6\phi$$

$$\Delta c_d = \left(70\frac{n_c \pi \phi_c^2}{4 n_b \phi s_c} + 12\frac{\sigma_{ccd}}{\sqrt{f_{ck}}}\right)\phi \qquad (2)$$

La influencia de la armadura de confinamiento en la longitud de anclaje se muestra en la Figura 8 (ver caso a) de la Figura 7). En la Figura 8a se representa el último término de la Ecua-

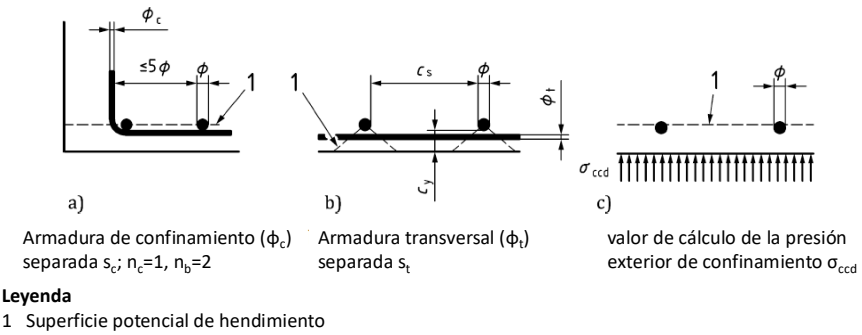

Figura 7. Definición de casos en los que la longitud de anclaje de diseño puede verse reducida por confinamiento o armadura transversal, adaptada del nuevo Eurocódigo 2.

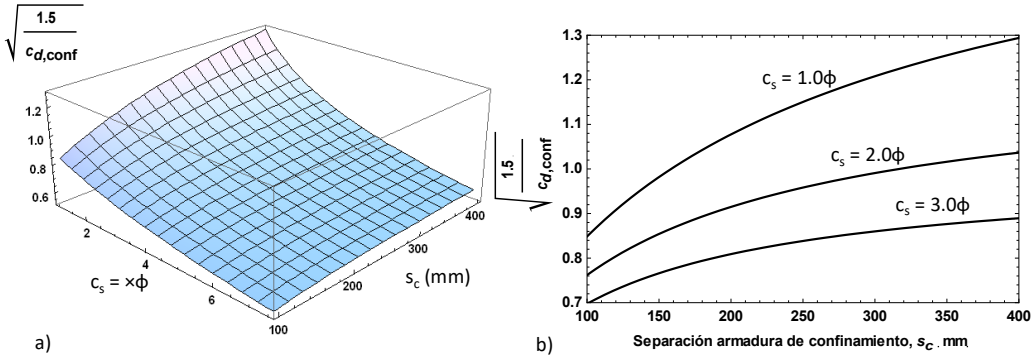

Figura 8. Ejemplo de la influencia del fallo por hendimiento para barras Ø25 considerando armadura de confinamiento.

ción 1 en función de cs y sc para el caso particular de barras Ø25 (separadas entre sí cs [×Ø]) y armadura de confinamiento Øc=12 mm (separadas s_c [mm]).

Como se aprecia en la Figura 8a, el efecto de la armadura de confinamiento, expresado en términos de separación entre barras de confinamiento (s_c), es tanto más significativo cuanto menor es la distancia libre entre las barras (c_s). La sensibilidad de la formulación de la longitud de anclaje frente al hendimiento en presencia de armadura de confinamiento se puede apreciar en la Figura 8b (extraída de la Figura 8a), en la que se representan las curvas correspondientes a separaciones entre barras: cs=1.0 Ø, 2.0 Ø y 3.0Ø. La Figura 8b muestra cómo, en el caso de una distancia libre entre barras de 1.0Ø, la longitud de anclaje se puede reducir un 45% si la armadura transversal se coloca a 100 mm en lugar de a 400 mm.

3. CONCLUSIONES

Las longitudes de anclaje en la última versión del Eurocódigo 2 han aumentado considerablemente respecto a la versión anterior. La nueva formulación es mucho más sensible al fallo por hendimiento del hormigón, especialmente para separaciones libres entre barras comprendidas entre uno y dos diámetros. La nueva norma propone expresiones para considerar la contribución de la armadura de confinamiento y transversal que habrán de ser aplicadas de manera habitual para el cálculo de las longitudes de anclaje dado que este factor puede afectar significativamene al resultado obtenido. Dado que los valores de la longitud de anclaje tabulados en la Tabla 11.1 del nuevo Eurocódigo 2 no tienen en cuenta la armadura transversal, su uso en la práctica estará muy limitado y será necesario determinar la longitud de anclaje a partir de la formulación propuesta (Ecuaciones 11.3 y 11.4 del nuevo Eurocódigo 2).

Referencias

[1] EN1992-1-1. Eurocode 2: Design of concrete structures - Part 1–1: General rules and rules for buildings, bridges and civil engineering structures EN 1992-1-1. Brussels: European Committee for Standardization; 2023.

[2] Miguel Sosa PF, Martí Vargas JR, Bonet-Senach JL, Castro-Bugallo MC, Fernández-Prada MA. Diseño de un ensayo para el estudio experimental del anclaje de armaduras pasivas en nudos C-C-T. Hormigón y Acero 2004;55:119–28.

[3] Hernández-Montes E, Pascual-Vicente RM, Sénica de la Cruz J, Gil-Martín L. Tolerancia en el empalme por solape (traslapo) de grupos (paquetes) de barras según el EC2 y la ACI-318. Hormigón y Acero 2020;71:59–62. https://doi.org/10.33586/hya.2019.2881.

[4] Hernández-Montes E, Gil-Martín LM. Concrete Structures. Design and Residual Capacity Assessment. CRC. London: 2024.

[5] ACI 318 (2019). Building code requirements for structural concrete and commentary, American Concrete Institute; Farmington Hills, MI, USA.

[6] Fib. bulletin 72 - Bond and anchorage of embedded reinforcement: background to the fib model code for concrete structures 2010. Lausanne, Switzerland: 2014.

[7] Cairns J. Design Provisions for Anchorages and Laps in the Revised EC2. Hormigón y Acero 2023;74:123–37.

[8] CEN. Eurocode 2: Design of concrete structures - Part 1–1: General rules and rules for buildings UNE-EN 1992-1-1. European Committee for Standardization. Brussels: 2004.

[9] AASHTO. AASHTO LRFD Bridge Design Specifications. 9th ed. Washington, D.C.: 2020.

Disponible en **www.hormigonyacero.com**
https://doi.org/10.33586/hya.2024.3952

Matriz de rigidez para estructuras con barras de sección o rigidez variable

Stiffness matrix for structures with bars of variable section or rigidity

Ángel Ibáñez Ceba [*,a]

[a] *Arquitecto*

RESUMEN

El cálculo matricial por el Método de la Matriz de Rigidez de estructuras compuestas por barras rectas se realiza normalmente considerando las barras de sección e inercia constantes y esta hipótesis se considera suficientemente segura en todos los casos.

Sin embargo, en la práctica, muchos sistemas estructurales están formados por barras de sección o inercia variable, como es el caso de las barras acarteladas, las barras fisuradas de hormigón armado, las barras de acero con uniones semirrígidas o las barras mixtas de hormigón y acero.

En este estudio se plantea la Matriz de Rigidez de una barra recta de sección o inercia variable cuyos coeficientes de rigidez son función de las leyes de variación del área de su sección, de su Módulo de Torsión y de los Momentos de Inercia referidos a los ejes normales a su directriz.

Este planteamiento no incrementa el número de nudos de la estructura ni el de incógnitas de la ecuación matricial y permite que, estableciendo criterios suficientemente aproximados para el cálculo de sus coeficientes de rigidez, determinar un comportamiento más real de sus elementos estructurales.

PALABRAS CLAVE: Matriz de Rigidez, sección variable, inercia variable, hormigón fisurado, conexiones semirrígidas, vigas mixtas.

ABSTRACT

The matrix calculation by the Rigidity Matrix Method of structures composed of straight bars is normally carried out considering the bars of constant section and inertia and this hypothesis is considered sufficiently safe in all cases.
However, in practice, many structural systems are made up of bars of variable section or inertia, such as haunched bars, cracked reinforced concrete bars, steel bars with semirigid joints or composite concrete and steel bars.
In this study, the Stiffness Matrix of a straight bar of variable section or inertia is proposed, whose stiffness coefficients are a function of the laws of variation of the area of its section, its Torsion Module and the Moments of Inertia referred to the axes normal to its guideline.
This approach does not increase the number of nodes in the structure or the number of unknowns in the matrix equation and allows, by establishing sufficiently approximate criteria for the calculation of its rigidity coefficients, to determine a more realistic behavior of its structural elements.

KEYWORDS: Stiffness Matrix, variable section, variable inertia, cracked concrete, semirigid connections, composite beams.

* Persona de contacto / *Corresponding author*:
Correo-e / *e-mail*: aiceba2@gmail.com (Ángel Ibáñez Ceba)

Cómo citar este artículo: Ibáñez Ceba, A. (2025) Matriz de rigidez para estructuras con barras de sección o rigidez variable , *Hormigón y Acero*, 76(306):119-134. https://doi.org/10.33586/hya.2024.3952

1. INTRODUCCIÓN

En los modelos estructurales comúnmente utilizados para proyectar estructuras de edificación o de obra civil es habitual el empleo de barras de sección no constante, por ejemplo, las barras acarteladas o aquellas otras que disponen de refuerzos en alguna zona de la barra que modifican su sección.

También es habitual el empleo de barras compuestas por varios materiales, que, aun disponiendo de una sección constante, su inercia o el área de su sección no es constante, por

ejemplo, las barras de hormigón armado en estado fisurado o las vigas mixtas de hormigón y perfiles metálicos.

Un análisis más detallado de cómo se comportan estos elementos precisa de un modelo de cálculo que tenga en cuenta la variación de las constantes mecánicas de la barra que determinan su rigidez, es decir las leyes de variación del área de su sección, de su Módulo de Torsión y de los Momentos de Inercia referidos a los ejes normales a su directriz.

Cuando se plantea el Método de la Rigidez para calcular una estructura de estas características es preciso determinar la Matriz de Rigidez de sus barras con los valores de sus constantes mecánicas que son variables a lo largo de su directriz.

En alguna de estas aplicaciones es posible que los Coeficientes de Rigidez dependan del resultado, en cuyo caso el sistema matricial deja de ser lineal y precisa de iteraciones, como es el caso de las barras de hormigón fisuradas o el de las uniones semirrígidas de perfiles de acero.

Lo que se plantea en este estudio es un método para calcular los coeficientes de la Matriz de Rigidez de la barra siempre que sean conocidas las leyes de variación de sus constantes mecánicas a lo largo de la misma, esto es: área de la sección, Módulo de Torsión y Momentos de Inercia referidos a los ejes normales a su directriz.

Por tanto, la determinación de estas leyes de variación es lo que permite un cálculo más o menos ajustado a la realidad en un modelo de cálculo.

Para calcular estas leyes de variación para un material determinado, simple o compuesto, se han venido empleado técnicas diversas entre las que pueden señalarse las siguientes:

- *Por asimilación a barras de sección constante mediante la introducción de nudos intermedios*.
- *Mediante Métodos basados en el comportamiento no lineal de los materiales*.
- *Mediante métodos de cálculo de la rigidez de una barra por integración de sus constantes mecánicas a lo largo de la misma*.

En este trabajo se utiliza un método por integración para calcular los coeficientes de la Matriz de Rigidez de una barra de sección y/o rigidez variable.

El interés principal de este estudio se centra en sus posibles aplicaciones para sistemas estructurales donde la rigidez de sus elementos puede influir en su comportamiento estructural.

2. COEFICIENTES DE RIGIDEZ PARA BARRAS RECTAS DE SECCIÓN VARIABLE

2.1. Planteamiento de la Matriz de rigidez

Para plantear la ecuación de rigidez global de una estructura se parte de la hipótesis de que los movimientos de sus nudos son inicialmente nulos, y que la sustentación inicial de las barras que la componen equivale a un empotramiento en sus extremos.

La ecuación de rigidez de la estructura sólo admite cargas que estén aplicadas en los nudos, por lo cual todas las acciones que actúan sobre las barras deben ser sustituidas en cada barra por el vector A_b de acciones equivalentes de extremo de la barra.

Coeficiente de rigidez se define como la acción que causaría una deformación unitaria en los extremos de la barra.

Cuando estos coeficientes son referidos a los extremos de la barra empotrada, el conjunto de todos ellos constituye la matriz de rigidez R_b de extremos de la barra empotrada, de tamaño 12x12, que interrelaciona el vector A_b de acciones equivalentes de extremo con el vector D_b de movimientos de extremo de la barra mediante la ecuación de rigidez de la barra:

$$R_b\, D_b = A_b \qquad (1)$$

Para determinar los diversos coeficientes de rigidez que componen R_b, que es el objeto del presente Apartado, se procederá a aplicar movimientos de valor unitario a los extremos de la barra, resultando así una serie de reacciones que son los coeficientes de rigidez.

Las ecuaciones utilizadas en este apartado para el estudio de la barra de sección variable se deducen directamente, indirectamente o por similitud de las formuladas por J. Lahuerta, [1], [2], [3],

2.2. Ejes de referencia de la barra y numeración de movimientos.

Para expresar los coeficientes de rigidez, se numeran los movimientos de traslación y rotación según los ejes de la barra de la siguiente manera:

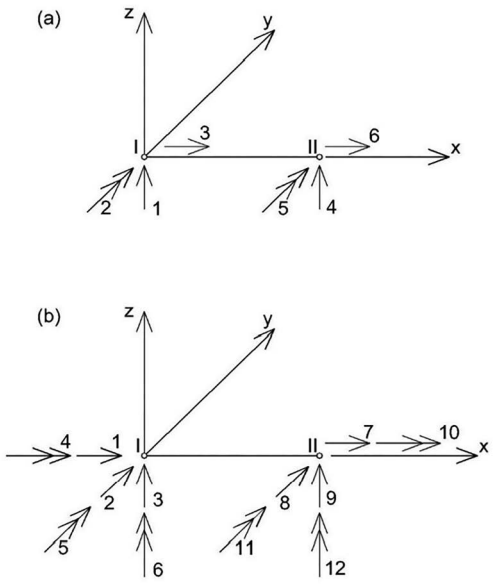

Figura 1. Ejes y movimientos de la barra: a) en el plano, b) en el espacio.

2.3. Sección e inercias variables a lo largo de la barra.

Las constantes elásticas de una barra recta de sección variable, de longitud L, se definen a partir de los valores del área de

su sección a lo largo de la barra y de los momentos de inercia y módulo de torsión, también a lo largo de la barra.

Para ello se definen la variación de estos valores:

Área de la sección variable	$A(x)=A_{0\xi1}(x)$	(2)
Módulo de Torsión variable	$I_t(x)=I_{t0\xi2}(x)$	(3)
Momento de Inercia variable en el eje y	$I_y(x)=I_{y0\xi y}3(x)$	(4)
Momento de Inercia variable en el eje z	$I_z(x)=I_{z0\xi z}3(x)$	(5)

Siendo A_0, I_{t0}, I_{y0}, I_{z0} los valores de referencia para el Área de la sección, el Módulo de Torsión y los Momentos de Inercia en los ejes *y* o *z* respectivamente, (se definen de forma similar al establecido en [1] tabla 2.05-6).

2.4. Rigidez longitudinal de una barra de sección variable.

Los coeficientes de rigidez asociados a una deformación longitudinal de una barra recta con el área de su sección variable $A(x) = A_{0\xi1}(x)$, son las acciones producidas en sus extremos por un desplazamiento longitudinal unitario aplicado en uno de ellos (deducido a partir de [2] (Fórm.22.1)).

$$D=\int_0^L \frac{N}{EA(x)}dx=\int_0^L \frac{N}{EA_0\xi_1(x)}dx=1 \qquad (6)$$

Para producir este desplazamiento se precisa aplicar en el extremo desplazado una fuerza *N*, y en el extremo opuesto, una fuerza $N'=-N$, de valor:

$$N=\frac{A_0E}{\int_0^L \frac{dx}{\xi_1(x)}}=\alpha\frac{A_0E}{L}\text{, siendo: }\quad \alpha=\frac{L}{\int_0^L \frac{dx}{\xi_1(x)}} \qquad (7)$$

Estos coeficientes de rigidez forman parte de la expresión general de la Matriz de Rigidez de la Barra en el espacio que se establece más adelante (ver Figura 1.b), y se corresponde con los movimientos unitarios números 1 y 7.

Por tanto, los coeficientes de rigidez debidos al desplazamiento 1 valen:

$$R_{1.1}=\alpha\frac{A_0E}{L} \qquad R_{7.1}=-\alpha\frac{A_0E}{L} \qquad (8)$$

Y los coeficientes de rigidez debidos al desplazamiento 7 valen:

$$R_{1.7}=-\alpha\frac{A_0E}{L} \qquad R_{7.7}=\alpha\frac{A_0E}{L} \qquad (9)$$

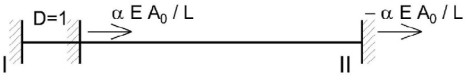

Figura 2. Coeficientes de rigidez por desplazamiento longitudinal unitario en un extremo.

2.5. Rigidez a torsión en una barra de sección variable.

Los coeficientes de rigidez asociados a una deformación angular a lo largo de una barra recta con Módulo de Torsión variable (Ec.3), son las acciones producidas en sus extremos por un desplazamiento angular unitario aplicado en uno de ellos.

$$D=\int_0^L \frac{T}{GIt(x)}dx=\int_0^L \frac{T}{GIt_0\xi_2(x)}dx=1 \qquad (10)$$

Para producir este desplazamiento angular se precisa aplicar en el extremo girado un momento torsor *T*, y en el extremo opuesto un Momento Torsor $T'=-T$, de valor:

$$T=\frac{It_0G}{\int_0^L \frac{dx}{\xi_2(x)}}=\beta\frac{It_0G}{L}\text{, siendo: }\quad \beta=\frac{L}{\int_0^L \frac{dx}{\xi_2(x)}} \qquad (11)$$

Estos coeficientes de rigidez también forman parte de la expresión general de la Matriz de Rigidez de la Barra en el espacio (Figura 1.b), y se corresponde con los giros unitarios números 4 y 10.

Los coeficientes de rigidez debidos a tales giros 4 y 10 valen respectivamente:

$$R_{4.4}=\beta\frac{It_0G}{L} \qquad R_{10.4}=-\beta\frac{It_0G}{L} \qquad (12)$$

$$R_{4.10}=-\beta\frac{It_0G}{L} \qquad R_{10.10}=\beta\frac{It_0G}{L} \qquad (13)$$

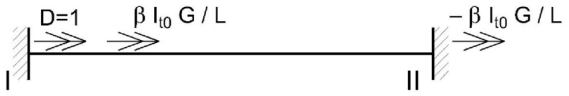

Figura 3. Coeficientes de rigidez por giro longitudinal unitario en un extremo.

2.6. Deformación de una barra de sección variable.

Para poder determinar los coeficientes de rigidez de la barra ante un giro o traslación en uno de sus extremos procedemos a estudiar, en primer lugar, la deformación de la barra.

En una barra isostática simplemente apoyada de sección variable los ángulos girados en las secciones extremas respecto del eje y, bajo el efecto de las cargas que actúan en la barra son: [1] 2.05-7

$$\theta'_y=\frac{L}{AIy}G'_y\text{, }\quad \text{siendo: }\quad G'_y=\int_0^L \frac{Mis,y(x)(L-x)dx}{L^2\,\xi3y(x)} \qquad (14)$$

$$\theta''_y=\frac{L}{AIy}G''_y\text{, }\quad \text{siendo: }\quad G''_y=\int_0^L \frac{Mis,y(x)\;x\;dx}{L^2\,\xi3y(x)} \qquad (15)$$

G'_y y G'' y son los términos de carga, que se emplearán para calcular los valores extremos de acciones en la barra de sección variable empotrada.

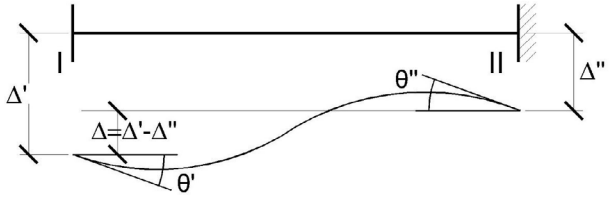

Figura 4. Barra con giros y traslaciones de extremo.

En la barra representada en la Figura 4, con giros de extremo θ', θ'' y traslaciones de extremo Δ' Δ'', el valor de los giros θ' y θ'' es: [1] 2.05-7

$$\theta' = L/EI_y\ (\lambda'_y\, M'_y + \mu_y\, M''_y + G'_y) + \Delta/L \qquad (16)$$

$$\theta'' = L/EI_y\ \ (-\mu'_y\, M'_y + \lambda''_y\, M''_y - G''_y) + \Delta/L \qquad (17)$$

Siendo λ'_y, λ''_y, μ_y, las "*formales*" o constantes de la barra respecto al eje y, de valor:

$$\lambda'_y = \int_0^L \frac{(L-x)^2\,dx}{L^3\,\xi_{3y}(x)} \quad \lambda''_y = \int_0^L \frac{x^2\,dx}{L^3\,\xi_{3y}(x)} \quad \mu_y = \int_0^L \frac{x(L-x)dx}{L^3\,\xi_{3y}(x)} \qquad (18)$$

Y para expresar la rigidez de la barra se definen: [1] 2.05-8

$$\rho'_y = \frac{\lambda''_y}{\lambda'_y\lambda''_y - \mu_y^2} \qquad \rho''_y = \frac{\lambda'_y}{\lambda'_y\lambda''_y - \mu_y^2} \qquad \eta_y = \frac{\mu_y}{\lambda'_y\lambda''_y - \mu_y^2} \qquad (19)$$

El cálculo de los coeficientes de rigidez de una barra que se produce, bien sea por un giro unitario en sus extremos, o bien sea por desplazamiento lineal en sus extremos puede obtenerse de las expresiones anteriores donde los Términos de Carga son nulos, ya que tales coeficientes son el valor de las acciones que producen un desplazamiento unitario y por tanto no existen cargas a lo largo de la barra.

Para calcular los coeficientes de rigidez analizaremos dos casos, los producidos por un giro unitario extremo normal al eje de la barra y los producidos por un desplazamiento unitario extremo normal al eje de la barra.

2.7. Rigidez por giro unitario en el extremo de la barra de sección variable.

En este caso, representado en la Figura 5, los giros unitarios se corresponden con los movimientos 5 y 11 en el plano XZ (giro en eje y) y 6 y 12 en el plano XY (giro en eje z). Ver Figura 1.b.

En el plano XZ, para los giros 5 y 11 los valores de los momentos y de las fuerzas normales en los extremos de la barra como consecuencia de un giro unitario en su extremo I, se puede obtener de (16 y 17) haciendo:

$$\theta' = 1, \quad \theta'' = 0, \quad \Delta = 0 \qquad (20)$$

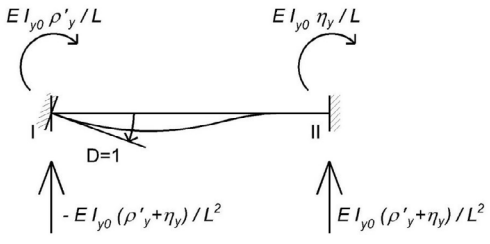

Figura 5. Coeficientes de rigidez por giro unitario en un extremo.

Los valores para el momento y fuerza en el extremo I son:

$$M_{yI} = EI_{y0}\,\rho'_y / L \qquad V_{yI} = -EI_{y0}(\eta_y + \rho'_y) / L^2 \qquad (21)$$

Los valores para el momento y fuerza en el extremo II son:

$$M_{yII} = EI_{y0}\,\eta_y / L \qquad V_{yII} = EI_{y0}(\eta_y + \rho'_y) / L^2 \qquad (22)$$

En el plano XY se puede proceder de forma análoga.

Los coeficientes de rigidez debidos al tales giros y movimientos valen:

Plano XZ (giros en eje y):

$$R_{3.5} = -R_{9.5} = -EI_{y0}(\eta_y + \rho'_y) / L^2 \qquad R_{5.5} = EI_{y0}\rho_y / L$$

$$R_{11.5} = EI_{y0}\,\eta_y / L \qquad (23)$$

$$R_{3.11} = -R_{9.11} = -EI_{y0}(\eta_y + \rho''_y) / L^2 \qquad R_{5.11} = EI_{y0}\,\eta_y / L$$

$$R_{11.11} = EI_{y0}\,\rho''_y / L \qquad (24)$$

Plano XY (giros en eje z):

$$R_{2.6} = -R_{8.6} = -EI_{z0}(\eta_z + \rho'_z) / L^2 \qquad R_{6.6} = EI_{z0}\,\eta_z / L$$

$$R_{12.6} = EI_{z0}\,\eta_z / L \qquad (25)$$

$$R_{2.12} = -R_{8.12} = -EI_{z0}(\eta_z + \rho''_z) / L^2 \qquad R_{6.12} = EI_{z0}\,\eta_z / L$$

$$R_{12.12} = EI_{z0}\,\rho''_z / L \qquad (26)$$

2.8. Rigidez por desplazamiento transversal en los extremos de una barra de sección variable.

Para determinar los coeficientes de rigidez asociados a un desplazamiento en el extremo de la barra normal a su eje, partimos del estudio de la deformación a flexión de la barra del apartado 2.6 anterior.

En este caso, representado en la Figura 6, los desplazamientos unitarios se corresponden con los movimientos 3 y 9 en el plano XZ (desplazamiento en eje z y giro en eje y) y 2 y 8 en el plano XY (desplazamientos en eje y, y giros en eje z). Ver Figura 1.b.

En el plano XZ, para los movimientos 3 y 9 los valores de los momentos y de las fuerzas normales en los extremos de la barra como consecuencia de un desplazamiento unitario en su extremo I, se puede obtener de (16 y 17) haciendo:

$$\theta' = 0, \quad \theta'' = 0, \quad \Delta = 1 \qquad (27)$$

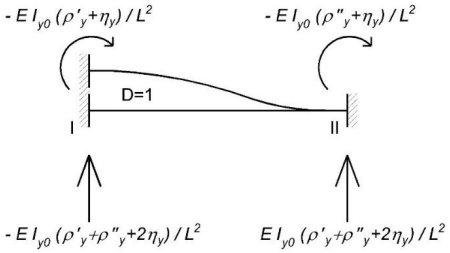

Figura 6. Coeficientes de rigidez por desplazamiento unitario en un extremo.

Los valores para el momento y fuerza en el extremo I son:

$$M_{yI} = -E\,I_{y0}(\rho'_y + \eta_y) / L^2 = R_{1.2} \qquad (28)$$

$$V_{yI} = E\,I_{y0}(\rho'_y + \rho''_y + \eta_y) / L^3 = R_{2.2} \qquad (29)$$

Los valores para el momento y fuerza en el extremo *II* son:

$$M_{yII} = -EI_{y0}(\rho''_y + \eta_y) / L^2 = R_{3,2} \quad (30)$$

$$V_{yII} = -EI_{y0}(\rho'_y + \rho''_y + 2\eta_y) / L^3 = R_{4,2} \quad (31)$$

En el plano *XY* se puede proceder de forma análoga.

Los coeficientes de rigidez debidos a tales movimientos valen:

Plano *XZ* (giros en eje *y*):

$$R_{3,3} = -R_{9,3} = EI_{y0}(\rho'_y + \rho''_y + 2\eta_y) / L^3 \qquad R_{5,3} = R_{3,5}$$
$$R_{11,3} = R_{3,11} \quad (32)$$

$$R_{3,9} = -R_{9,3} = -EI_{y0}(\rho'_y + \rho''_y + 2\eta_y) / L^3 \qquad R_{5,9} = R_{9,5}$$
$$R_{11,9} = R_{9,11} \quad (33)$$

Plano *XY* (giros en eje *z*):

$$R_{2,2} = -R_{8,2} = EI_{z0}(\rho'_z + \rho''_z + 2\eta_z) / L^3 \qquad R_{6,2} = R_{2,6}$$
$$R_{12,2} = R_{2,12} \quad (34)$$

$$R_{2,8} = -R_{8,8} = -EI_{z0}(\rho'_z + \rho''_z + 2\eta_z) / L^3 \qquad R_{6,8} = R_{8,6}$$
$$R_{12,8} = R_{8,12} \quad (35)$$

3. LA MATRIZ DE RIGIDEZ DE LA BARRA DE SECCIÓN VARIABLE

Como se ha dicho en el Apartado 2.1, la Matriz R_b de Rigidez de extremos de una barra, de tamaño 12x12, expresa la interrelación entre el vector A_b de acciones equivalentes de extremo con el vector D_b de movimientos de extremo de la barra (Ec.1)

Esta ecuación está referida a los ejes propios de la barra, existiendo para cada extremo de la barra tres posibles movimientos (dos lineales y un giro) para Sistemas Estructurales Planos (Figura 1.a), y seis posibles movimientos (tres lineales y tres giros) para Sistemas Estructurales en el Espacio (Figura 1.b).

3.1. Matriz de rigidez de una barra de sección variable en el plano.

Adoptando el convenio de signos expresado en la Figura 1.a, la matriz de rigidez R_b de una barra en el plano en función de los parámetros anteriormente definidos será la siguiente: (tabla 1).

3.2. Matriz de rigidez de una barra de sección variable en el espacio.

Adoptando el convenio de signos expresado en la Figura 1.b, la Matriz de Rigidez de una barra en el espacio será una matriz cuadrada y simétrica de tamaño 12 x 12, que corresponde a seis movimientos por cada nudo de la misma, tres lineales según los ejes y tres rotaciones alrededor de dichos ejes.

La representamos, por comodidad, mediante varias sub matrices:

Matriz de Rigidez R:

$$\mathbf{R_b} = \begin{pmatrix} \mathbf{R_{1.1}} & \mathbf{R_{1.2}} \\ \mathbf{R_{1.1}} & \mathbf{R_{1.2}} \end{pmatrix} \quad (36)$$

siendo las sub matrices (tablas 2, 3, 4 y 5):

3.3. Acciones en los extremos de la barra de sección variable.

Para determinar el vector A_b de acciones equivalentes de extremos de la barra es preciso calcular las reacciones que producen las cargas o momentos que actúan en la barra.

Entonces, el sistema equivalente de cargas aplicadas en los extremos de las barras puede calcularse a partir de los valores de las reacciones, con signo contrario.

Por tanto, el problema de la determinación del sistema de acciones de extremo de la barra se reduce al cálculo de las reacciones del sistema de cargas real en la barra supuesta empotrada.

TABLA 1.
Matriz de rigidez de una barra de sección variable en el plano.

1	2	3	4	5	6
$EI_0(\rho' + \rho'' + 2\eta) / L^3$	$-EI_0(\rho' + \eta) / L^2$		$-EI_0(\rho' + \rho'' + 2\eta) / L^3$	$-EI_{y0}(\rho'' + \eta) / L^2$	
$-EI_{y0}(\rho' + \eta) / L^2$	$EI_0\,\rho' / L$		$EI_{y0}(\rho' + \eta) / L^2$	$EI_0\,\eta / L$	
		$\alpha A_0 E / L$			$-\alpha A_0 E / L$
$-EI_0(\rho' + \rho'' + 2\eta) / L^3$	$EI_{y0}(\rho' + \eta) / L^2$		$EI_0(\rho' + \rho'' + 2\eta) / L^3$	$EI_{y0}(\rho'' + \eta) / L^2$	
$-EI_{y0}(\rho'' + \eta) / L^2$	$EI_0\,\eta / L$			$EI_0\,\rho'' / L$	
		$-\alpha A_0 E / L$			$\alpha A_0 E / L$

(Se ha suprimido el subíndice y por comodidad para I_{y0}, ρ_y', ρ_y'' y η_y) La Matriz de Rigidez R es cuadrada y simétrica y sus coeficientes se indican en tabla, siendo: A el área con A_0 valor de referencia y $\xi_1(x)$ la ley de variación, (Ec.2), I el momento de inercia con I_0 valor de referencia (Ec.4), y $\xi_3(x)$ su ley de variación, α, λ', λ'' y η, las formales (Ecs.7, 18) y ρ', ρ'' y η, rigideces (Ec.19).

TABLA 2.
Submatriz $R_{1.1}$.

1	2	3	4	5	6
$\alpha A_0 E / L$					
	$EI_{z0}(\rho'_z + \rho''_z + 2\eta_z) / L^3$				$EI_{z0}(\eta_z + \rho'_z) / L^2$
		$EI_{y0}(\rho'_y + \rho''_y + 2\eta_y) / L^3$		$-EI_{y0}(\eta_y + \rho'_y) / L^2$	
			$\beta I_{t0} G / L$		
		$-EI_{y0}(\eta_y + \rho'_y) / L^2$		$EI_{y0}\,\rho'_y / L$	
	$EI_{z0}(\eta_z + \rho'_z) / L^2$				$EI_{z0}\,\rho'_z / L$

TABLA 3.
Submatriz $R_{1.2}$.

7	8	9	10	11	12
$-\alpha A_0 E / L$					
	$-EI_{z0}(\rho'_z + \rho''_z + 2\eta_z) / L^3$				$EI_{z0}(\eta_z + \rho''_z) / L^2$
		$-EI_{y0}(\rho'_y + \rho''_y + 2\eta_y) / L^3$		$-EI_{y0}(\eta_y + \rho''_y) / L^2$	
			$-\beta I_{t0} G / L$		
		$EI_{y0}(\eta_y + \rho'_y) / L^2$		$EI_{y0}\,\eta_y / L$	
	$-EI_{z0}(\eta_z + \rho'_z) / L^2$				$EI_{z0}\,\eta_z / L$

TABLA 4.
Submatriz $R_{2.1}$.

1	2	3	4	5	6
$-\alpha A_0 E / L$					
	$-EI_{z0}(\rho'_z + \rho''_z + 2\eta_z) / L^3$				$-EI_{z0}(\eta_z + \rho'_z) / L^2$
		$-EI_{y0}(\rho'_y + \rho''_y + 2\eta_y) / L^3$		$-EI_{y0}(\eta_y + \rho'_y) / L^2$	
			$-\beta I_{t0} G / L$		
		$-EI_{y0}(\eta_y + \rho''_y) / L^2$		$EI_{y0}\,\eta_y / L$	
	$EI_{z0}(\eta_z + \rho''_z) / L^2$				$EI_{z0}\,\eta_z / L$

TABLA 5.
Submatriz $R_{2.2}$.

7	8	9	10	11	12
$\alpha A_0 E / L$					
	$EI_{z0}(\rho'_z + \rho''_z + 2\eta_z) / L^3$				$-EI_{z0}(\eta_z + \rho''_z) / L^2$
		$EI_{y0}(\rho'_y + \rho''_y + 2\eta_y) / L^3$		$EI_{y0}(\eta_y + \rho''_y) / L^2$	
			$\beta I_{t0} G / L$		
		$EI_{y0}(\eta_y + \rho''_y) / L^2$		$EI_{y0}\,\rho''_y / L$	
	$-EI_{z0}(\eta_z + \rho''_z) / L^2$				$EI_{z0}\,\rho''_z / L$

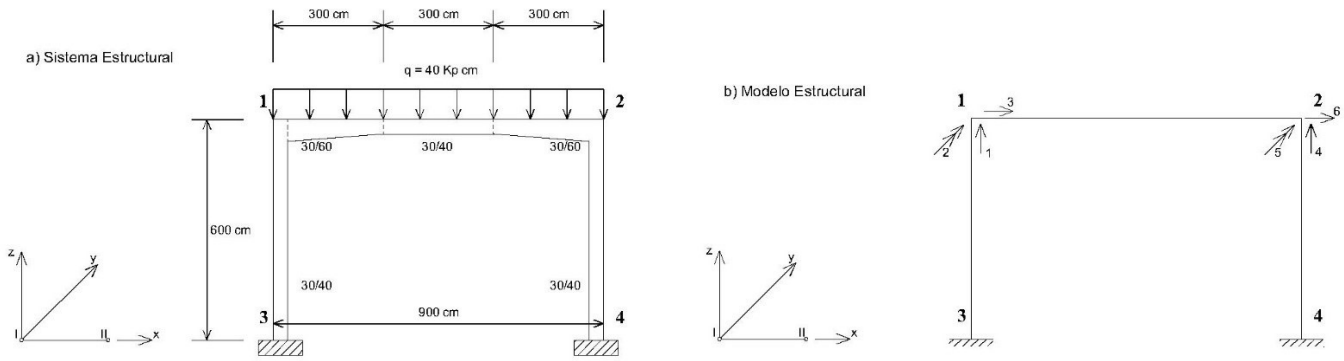

Figura 7. El caso de un pórtico simple. Sistema estructural y Modelo estructural.

Estas acciones de extremo de la barra de sección o rigidez variable son diferentes de las obtenidas para una barra de sección y rigidez constante.

Estas reacciones pueden ser determinadas a partir de las Ecuaciones (16 y 17), haciendo: $\theta'_y = \theta''_y = \Delta = 0$:

$$M'_y = -\rho'_y\, G'_y + \eta_y\, G''_y \tag{37}$$

$$M''_y = -\eta_y\, G'_y + \rho''_y\, G''_y \tag{38}$$

En esta expresión G'y, G"y son los términos de carga definidos en el Apartado 2.6 (Ec.14,15)

4. EJEMPLO DE APLICACIÓN DEL MÉTODO

Para ilustrar, paso a paso, el desarrollo del método descrito se plantea el siguiente ejemplo de cálculo

Se trata de un pórtico plano, representado en la Figura 7, compuesto por un dintel acartelado y dos soportes que se suponen empotrados en su base.

El pórtico se plantea con hormigón armado H-25 con AEH-500 y sus datos geométricos y las cargas que actúan se representan en la Figura 7. Las unidades utilizadas son Kp y cm.

4.1. Modelo estructural.

Numeración de barras y nudos.
El modelo estructural que representa esta estructura idealizada y discretizada, (Figura 7.b), está compuesto de tres elementos estructurales, en este caso las barras 1-2, 1-3 y 2-4. Las barras están conectadas entre sí en sus extremos, que son los nudos del modelo estructural, únicos puntos considerados en la relación entre acciones y movimientos o ecuación de rigidez.

Sustentación de las barras.
El sistema de sustentación de las barras está formado por las conexiones estructurales y las restricciones de movimiento de sus extremos, y es el siguiente:

Los nudos 1 y 2 son conexiones elásticas rígidas y los nudos 3 y 4 son nudos restringidos en todos sus movimientos.

Numeración de los movimientos de nudos.
Los movimientos de los nudos se numeran siguiendo el orden expresado en la Figura 7. b. Se omiten los correspondientes a los nudos 3 y 4 por ser nulos.

Todos los movimientos se refieren al sistema general de ejes de la estructura, que en este caso coinciden con los ejes de la barra 1-2.

Sección de las barras y términos de variación del área e inercia a lo largo de las barras.
Los términos de variación de la sección e inercia de las barras $A(x)$ e $I_y(x)$, definidos en el Apartado 2.3 (Ec. 2,4) son los siguientes:

Valores de referencia:
$A_0 = 30 \times 40 = 1200$ cm²
$I_{y0} = 30 \times 403 / 12 = 160.000$ cm⁴ E = 310.000 Kp/cm²

Barras 1-3 y 2-4:
Son de sección constante igual al valor de referencia:
$A = A_0 = 1200$ cm²
$I_y = I_0 = 160.000$ cm⁴

Los términos de variación son:
$\xi_1(x)=\xi_{3y}(x)=1$, con lo cual las formales (7,18 y 19) son:

$\alpha_z = 1 \quad \lambda'_y = \lambda''_y = 1/3 \quad \mu_y = 1/6 \quad \rho'_y = \rho''_y = 4 \quad \eta_y = 2$

Barra 1-2:
Es de sección variable por las cartelas y está dividida en tres tramos, de longitud 1/3 de la luz.

Los términos de variación son:
Tramo (0,300):
$\xi_1(x) = 1{,}5 - x/600 \qquad \xi_3(x) = (1/40\text{^}3) * (60 - 20x/300)^3$

Tramo (300,600):
$\xi_1(x) = 1 \qquad \xi_3(x) = 1$

Tramo (600,900):
$\xi_1(x)=1+(x-600)/600 \quad \xi_3(x)=(1/40\text{^}3)*(40+20(x-600)/300)^3$

$$\alpha = \frac{900}{\int_0^{300} \frac{dx}{1{,}5\frac{x}{600}+} \quad dx+\int_{600}^{900} \frac{dx}{1+\frac{x-600}{600}}} = 1.14422$$

$$\lambda' = (40^3/900^3)*\left(\int_0^{300} \frac{(900-x)^2\,dx}{(60-\frac{20x}{300})^3} + \int_{300}^{600} \frac{(900-x)^2\,dx}{40\text{^}3} + \right.$$

$$\left. \int_{600}^{900} \frac{(900-x)^2\,dx}{(40+\frac{20(x-600)}{300})^3} \right) = 0{,}2156$$

$$\lambda'' = (40^3/900^3)*\left(\int_0^{300} \frac{x^2\,dx}{(60-\frac{20x}{300})^3} + \int_{300}^{600} \frac{x^2\,dx}{40\text{^}3} + \right.$$

$$\left. \int_{600}^{900} \frac{x(900-x)\,dx}{(40+\frac{20(x-6)}{300})^3} \right) = 0{,}1363$$

$$\rho'_y = \frac{\lambda''}{\lambda'\ \lambda''-\mu^2} = 0{,}2156/0{,}0279 = 7{,}7249$$

$$\rho''_y = \frac{\lambda'}{\lambda'\ \lambda''-\mu^2} = 0{,}2156/0{,}0279 = 7{,}7249$$

$$\eta_y = \frac{\mu}{\lambda'\ \lambda''-\mu^2} = 0{,}1363/0{,}0279 = 4{,}8828$$

4.2. Sistema de acciones equivalente que actúa sobre los extremos de las barras.

El sistema de acciones que actúa en el sistema estructural está formado por la carga repartida q, que ha de ser sustituida por un sistema equivalente de cargas que actúe en los extremos de las barras para mantener el carácter discreto de estos elementos estructurales. El sistema equivalente está compuesto por las reacciones: M', M'', V', V'', producidas por la carga q en los nudos 1 y 2. Los valores de $M'y$, $M''y$ se determinan de la manera siguiente (Ec.36 y 37):

Para la barra *1-2*, con: $Mis_{,y}(x) = q\ x\ (L-x)/2$, los términos de carga G' y G'' son:

$$G'_y = \int_0^L \frac{Mis,y(x)(L-x)dx}{L^2\ \xi 3y(x)}\ 40 / (2*900^2)*($$

$$40^3\left(\int_0^{300} \frac{x(900-x)^2\,dx}{(60-\frac{20}{300})^3} + \int_{300}^{600} \frac{x(900-x)^2\,dx}{40\text{^}3} + \right.$$

$$\left. \int_{600}^{900} \frac{x(900-x)^2\,dx}{\left(40+\frac{20}{300}(x-600)\right)^3} \right)) = 1.103.772$$

$$G''_y = \int_0^L \frac{Mis,y(x)(L-x)dx}{L^2\ \xi 3y(x)}\ 40 / (2*900^2)*($$

$$40^3\left(\int_0^{300} \frac{x^2(900-x)\,dx}{(60-\frac{20}{300})^3} + \int_{300}^{600} \frac{x^2(900-x)\,dx}{40\text{^}3} + \right.$$

$$\left. \int_{600}^{900} \frac{x^2(900-x)\,dx}{\left(40+\frac{20}{300}(x-600)\right)^3} \right)) = 1.103.772$$

Las reacciones M', M'', V', V'', valen:

$M'_y = -\rho'_y\ G'_y + \eta_y\ G''_y = -3.137.025$ cm Kp $\quad V' = 18.000$ Kp

$M''_y = -\eta_y\ G'_y + \rho''_y\ G''_y = 3.137.025$ cm Kp $\quad V'' = 18.000$ Kp

El sistema de acciones equivalentes (reacciones cambiadas de signo) para la barra 1-2 puede representarse por el vector A, cuyas componentes concuerdan con la numeración de los movimientos:

$$\boldsymbol{A} = \begin{pmatrix} V' \\ M' \\ N' \\ V'' \\ M'' \\ N'' \end{pmatrix} = \begin{pmatrix} -18.000 \\ 3.137.025 \\ 0 \\ -18.000 \\ -3.137.025 \\ 0 \end{pmatrix} \qquad (39)$$

Las acciones equivalentes producidas por las barras 1-3 y 2-4 son nulas al no existir cargas que actúen sobre las mismas.

4.3. Cálculo de los coeficientes de la Matriz de Rigidez.

Los coeficientes de la Matriz de Rigidez del modelo estructural se determinan aplicando movimientos unitarios en sus nudos, y su valor es la suma de los coeficientes de rigidez de las barras que concurren en el nudo.

En la Figura 8 se representan los seis movimientos no coartados de la estructura, ya que los seis que corresponden a los nudos 3 y 4 son nulos por hipótesis de partida.

Los coeficientes de rigidez de las barras que concurren en cada nudo se calculan a partir de los coeficientes de rigidez de dichas barras que concurren en el nudo.

Los coeficientes de la Matriz de Rigidez se numeran con dos subíndices:

- El primer subíndice es el número del coeficiente de rigidez, para el cualseguiremos el mismo orden que para los movimientos de los nudos (ver Figura 7.b).
- El segundo subíndice es el número del movimiento que origina elcoeficiente de rigidez.

El sistema general de ejes coincide con el de la barra 1-2 y los coeficientes de rigidez debidos a las barras 1-3 y 2-4 se han referido directamente a este sistema de ejes.

Coeficientes de rigidez debidos al movimiento 1.
(Afecta a las barras *1-2* y *1-3*).

Se toma
E=310.000 Kp/cm², A_0=1.200 cm², I_0=I_{y0}= 160.000 cm⁴
(Se representan en negrita los coeficientes debidos a las barras 1-3 y 2-4)

$$R_{1.1} = \boldsymbol{A_0E/L} + \frac{EI_0(\rho'+\rho''+2\eta)}{L^3} = \frac{\boldsymbol{A_0E/L}}{\mathbf{600}} + \frac{EI_0(7{,}7249+7{,}7249+2*4{,}8828)}{900^3}$$

$$= \boldsymbol{620.000} + 1.716 = 621.716$$

$$R_{2.1} = -\frac{EI_0(\rho'+\eta)}{L^2} = -\frac{EI_0(7{,}7249+4{,}8828)}{900^2} = -772.025$$

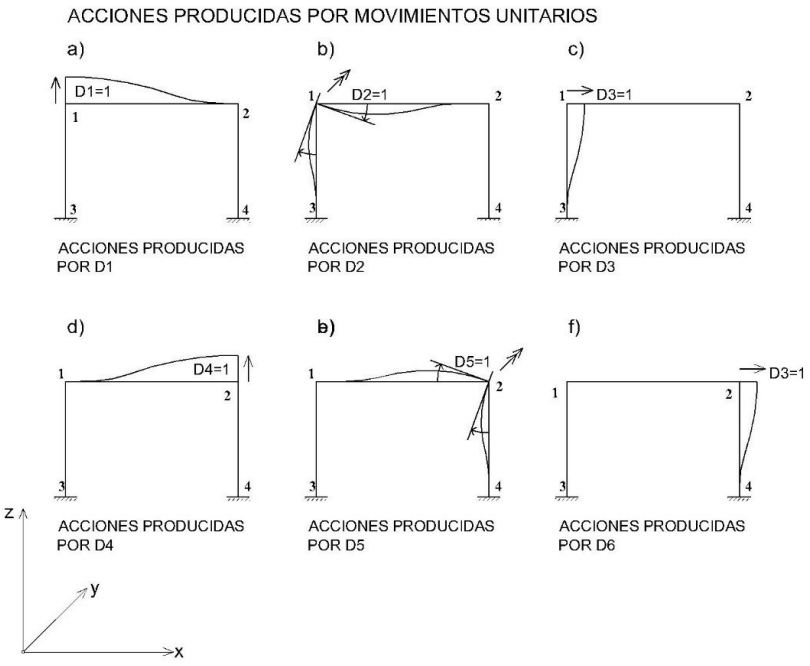

Figura 8. Movimientos unitarios para el cálculo de los coeficientes de rigidez.

$R_{3.1} = 0$

$$R_{4.1} = -\frac{EI_0(\rho'+\rho''+2\eta)}{L^3} = -\frac{EI_0(7{,}7249+7{,}7249+2*4{,}8828)}{900^3} = -1.716$$

$$R_{5.1} = -\frac{EI_0(\rho''+\eta)}{L^2} = -\frac{EI_0(7{,}7249+4{,}8828)}{900^2} = -772.025$$

$R_{6.1} = 0$

Coeficientes de rigidez debidos al movimiento 2.
(Afecta a las barras *1-2* y *1-3*).

Se toma
E=310.000 Kp/cm², A_0=1.200 cm², I_0=I_{y0}= 160.000 cm⁴
(Se representan en negrita los coeficientes debidos a las barras 1-3 y 2-4)

$R_{1.2} = R_{2.1}$

$$R_{2.2} = \frac{\mathbf{4EI}}{\boldsymbol{L}} + \frac{EI_0\rho'}{L} = \frac{\mathbf{4EI_0}}{\mathbf{600}} + \frac{EI_0*7{,}7249}{900} = \mathbf{330.666} + 425.727 = 756.393$$

$$R_{3.2} = -\frac{\mathbf{6EI_0}}{\boldsymbol{L^2}} + \frac{\mathbf{6EI_0}}{\mathbf{600^2}} = \mathbf{-826.667}$$

$$R_{4.1} = -\frac{EI_0(\rho'+\eta)}{L^2} = -\frac{EI_0(7{,}7249+4{,}8828)}{900^2} = -772.025$$

$$R_{5.2} = \frac{EI_0\eta}{L} = \frac{EI_0*4{,}8828}{900} = 269.096$$

$R_{6.2} = 0$

Coeficientes de rigidez debidos al movimiento 3.
(Afecta a las barras *1-2* y *1-3*)

Se toma
E=310.000 Kp/cm², A_0=1.200 cm², I_0=I_{y0}= 160.000 cm⁴
(Se representan en negrita los coeficientes debidos a las barras 1-3 y 2-4)

$R_{1.3} = R_{3.1}$

$R_{2.3} = R_{3.2}$

$$R_{3.3} = \frac{\mathbf{12EI}}{\boldsymbol{L3}} + \alpha A_0 E\,\frac{\mathbf{12EI_0}}{\mathbf{600^3}} = 1.14422*A_0E = \mathbf{2.756} + 472.946 = 475.702$$

$R_{4.3} = 0$

$R_{5.3} = 0$

$R_{6.3} = \alpha A_0 E = -472.946$

Coeficientes de rigidez debidos al movimiento 4.
(Afecta a las barras *1-2* y *2-4*)

Se toma
E=310.000 Kp/cm², A_0=1.200 cm², I_0=I_{y0}= 160.000 cm⁴
(Se representan en negrita los coeficientes debidos a las barras 1-3 y 2-4)

$R_{1.4} = R_{4.1}$

$R_{2.4} = R_{4.2}$

$R_{3.4} = R_{4.3}$

$$R_{4.4} = \boldsymbol{\alpha A_0 E} + \frac{EI_0(\rho'+\rho''+2\eta)}{L^3} == \frac{\boldsymbol{A_0 E}}{600} +$$

$$\frac{EI_0(7{,}7249+7{,}7249+2*4{,}8828)}{900^3} = \boldsymbol{620.000} + 1.716 = 621.716$$

$$R_{5.2} = \frac{EI_0(\rho''+\eta)}{L^2} = \frac{EI_0(7{,}7249+4{,}8828)}{900^2} = 772.025$$

$$R_{6.4} = 0$$

Coeficientes de rigidez debidos al movimiento 5.
(Afecta a las barras *1-2* y *2-4*)

Se toma
E=310.000 Kp/cm², A_0=1.200 cm², I_0=I_{y0}= 160.000 cm⁴
(Se representan en negrita los coeficientes debidos a las barras 1-3 y 2-4)

$$R_{1.5} = R_{5.1}$$

$$R_{2.5} = R_{5.2}$$

$$R_{3.5} = R_{5.3}$$

$$R_{4.5} = R_{5.4}$$

$$R_{5.5} = \frac{\boldsymbol{4EI}}{\boldsymbol{L}} + \frac{EI_0\rho'}{L} = \frac{\boldsymbol{4EI_0}}{\boldsymbol{600}} + \frac{EI_0 * 7{,}7249}{900} = \boldsymbol{330.666} + 425.727 = 756.393$$

$$R_{3.2} = -\frac{\boldsymbol{6EI_0}}{\boldsymbol{L^2}} + \frac{\boldsymbol{6EI_0}}{\boldsymbol{600^2}} = \boldsymbol{-826.667}$$

Coeficientes de rigidez debidos al movimiento 6.
(Afecta a las barras *1-2* y *2-4*)

Se toma
E=310.000 Kp/cm², A_0=1.200 cm², I_0=I_{y0}= 160.000 cm⁴
(Se representan en negrita los coeficientes debidos a las barras 1-3 y 2-4)

$$R_{1.6} = R_{6.1}$$

$$R_{2.6} = R_{6.2}$$

$$R_{3.6} = R_{6.3}$$

$$R_{4.6} = R_{6.4}$$

$$R_{5.6} = R_{6.5}$$

$$R_{6.6} = \frac{\boldsymbol{12EI}}{\boldsymbol{L^3}} + \alpha A_0 E = \frac{\boldsymbol{12EI_0}}{\boldsymbol{600}} 1.14422 * A_0 E = \boldsymbol{2.756} + 472.946 = 475.702$$

4.4. Matriz de Rigidez y ecuación de rigidez.

Los coeficientes que componen la Matriz de Rigidez total R han sido calculados en el Apartado anterior. Los movimientos de los nudos están expresados por el vector D y las acciones asociadas a los mismos se expresan por el vector A, calculado en el Apartado 4.2.

La ecuación de rigidez del modelo es:

$$\boldsymbol{RD = A}$$

que es una matriz simétrica, con valores:

$\boldsymbol{R}$ =

621.716	**-772.025**	**0**	**-1.716**	**-772.025**	**0**
-772.025	**756.393.320**	**-826.667**	**772.025**	**269.095.631**	**0**
0	-826.667	**475.702**	**0**	**0**	**-472.946**
-1.716	772.025	0	**621.716**	**772.025**	**0**
-772.025	269.095.631	0	772.025	**756.393.320**	**-826.667**
0	0	-472.946	0	-826.667	**475.702**

$$\boldsymbol{A} = \begin{pmatrix} -18.000 \\ 3.137.025 \\ 0 \\ -18.000 \\ -3.137.025 \\ 0 \end{pmatrix}$$

Al resolver la ecuación $\boldsymbol{RD = A}$ se obtienen los valores de los movimientos $\boldsymbol{D}$, cuyo valor es:

$$\boldsymbol{D} = \begin{pmatrix} -0{,}0290323 \\ 0{,}00644712 \\ 0{,}00561812 \\ -0{,}0290323 \\ -0{,}0064471 \\ -0{,}0056181 \end{pmatrix}$$

4.5. Cálculo de acciones en los extremos de las barras.

Las acciones en los extremos de cada barra se calculan a partir de la Matriz de Rigidez de la barra, de las acciones iniciales en sus extremos y de los movimientos resultantes en dichos extremos.

Para la barra 1-2, su Matriz de Rigidez (considerando solo los valores que corresponde a esta barra) es la siguiente:

$\boldsymbol{R_{1\text{-}2}}$ =

1.716	**-772.025**	**0**	**-1.716**	**-772.025**	**0**
-772.025	**425.726.653**	0	**772.025**	**269.095.631**	**0**
0	0	**472.946**	**0**	**0**	**-472.946**
-1.716	772.025	0	**1.716**	**772.025**	0
-772.025	269.095.631	0	772.025	**425.726.653**	0
0	0	-472.946	0	0	**475.702**

Las acciones totales de la barra $A_{1\text{-}2}$ serán la suma de las acciones inicialmente supuestas para sus extremos con movimientos nulos en sus extremos $A_{1\text{-}2,r}$ más las acciones $A_{1\text{-}2,d}$ producidas por los movimientos de extremo que resultan de la ecuación de rigidez que se obtiene multiplicando la matriz anterior $R_{1\text{-}2}$ de la barra 1-2 por el vector D.

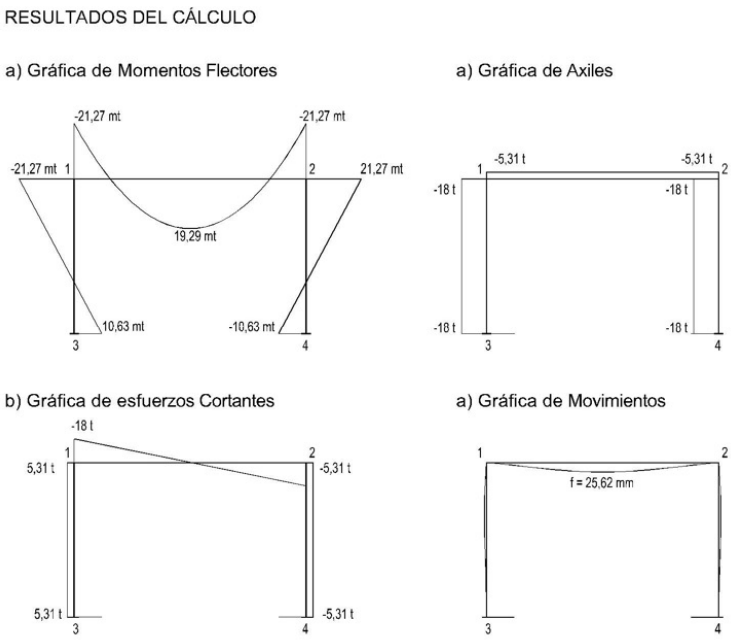

Figura 9. Resultados del Cálculo.

$$A_{1\text{-}2} = - A_{1\text{-}2r} + R_{1\text{-}2}\, D$$

$$A_{1\text{-}2r} = \begin{pmatrix} -18.000 \\ 3.137.025 \\ 0 \\ -18.000 \\ -3.137.025 \\ 0 \end{pmatrix}$$

$$R_{1\text{-}2}D = \begin{pmatrix} 0 \\ 1.009820 \\ 5.314 \\ 0 \\ -1.009820 \\ 5.314 \end{pmatrix}$$

$$A_{1\text{-}2} = \begin{pmatrix} 18.000 \\ -2.127.205 \\ 5.314 \\ 18.000 \\ 2.127.205 \\ 5.314 \end{pmatrix} \begin{pmatrix} V' \\ M' \\ N' \\ V'' \\ M'' \\ N'' \end{pmatrix}$$

Estos valores representan el esfuerzo cortante, el momento y el esfuerzo normal en el extremo izquierdo y en el derecho respectivamente de la barra *1-2* expresados en Kp y en cm Kp.

Las acciones en los extremos de las barras 1-3 y 2-4 se determinan a partir de los valores de acciones extremas en la barra 1-2 ya que los valores de los momentos de empotramiento en la base son iguales a la mitad y con signo contrario a los de su extremo superior.

4.6. Resultados del Cálculo.

Las solicitaciones que resultan del cálculo se exponen a continuación de forma gráfica cambiando las unidades a *m* y *t* (metros y toneladas).

Una vez dimensionadas las barras con hormigón H-25 y AE-500, las secciones de acero necesarias para la flexión según la norma EHE-08 y comprobadas con tricalc-11, son las siguientes:

Figura 10. Secciones de armaduras necesarias.

5. APLICACIÓN DEL MÉTODO PARA EL CÁLCULO ANELÁSTICO DEL HORMIGÓN ARMADO

Una aplicación del método puede ser el cálculo de pórticos compuestos por barras de hormigón armado teniendo en cuenta su fisuración, la cual se produce en buena parte de la longitud de algunas de sus barras donde se reduce considerablemente la rigidez en las zonas fisuradas.

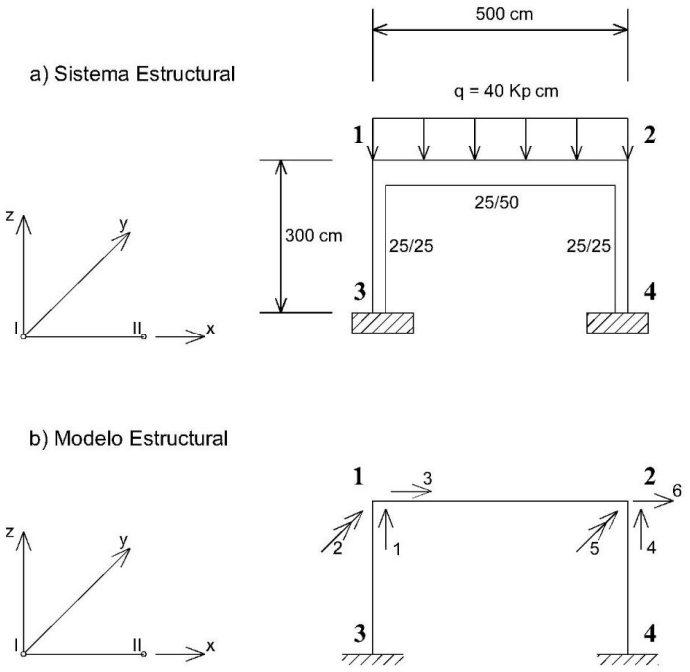

Figura 11. Pórtico y Modelo Estructural.

Sin embargo, la rigidez en estas zonas fisuradas depende de las características del hormigón y también de la sección y características de las armaduras que se disponen, por lo cual es necesario realizar un cálculo previo que determine la sección de tales armaduras y, con estos datos, calcular las leyes de variación de la sección equivalente, y de la rigidez equivalente a lo largo de las barras para, nuevamente recalcular el pórtico con estos valores.

Si tras resultado que se obtiene es preciso modificar las armaduras, el pórtico se deberá recalcular una vez más, hasta conseguir una aproximación suficiente.

5.1. La rigidez en una barra de hormigón armado en estado no fisurado y fisurado.

En cada barra las leyes de variación a lo largo de su eje de: *a)* el área de su sección, *b)* el módulo de torsión y *c)* los momentos de inercia en los ejes normales a su directriz, se han definido en 2.3 a partir de unos valores de referencia A_0, I_{t0}, I_{y0}, I_{z0}, que, para un pórtico plano sin torsión son solo estos dos:

Área de la sección variable $A(x)=A_0\xi_1(x)$
Momento de Inercia variable en el eje y $I_y(x)=I_{y0}\xi_{y3}(x)$

Leyes de variación en Estado no Fisurado
En estado no fisurado estas leyes de variación son $\xi_1(x) = \xi_{y3}(x) = 1$ con lo cual las formales y rigideces (*7, 18* y *19*) son:

$\alpha_z = 1 \quad \lambda'_y = \lambda''_y = 1/3 \quad \mu_y = 1/6 \quad \rho'_y = \rho''_y = 4 \quad \eta_y = 2$

Leyes de variación en Estado Fisurado
En estado fisurado, para determinar las leyes de variación $\xi_1(x)$ y $\xi_{y3}(x)$ se plantea lo siguiente:

a) Para la variación de la sección, tanto en vigas como en soportes,considerar la sección constante con $\xi_1(x) = 1$.
La razón para ello es que los soportes, salvo los extremos, no suelen estar fisurados en la mayor parte de su longitud, y las vigas resultan con esfuerzos normales de escaso valor, con lo que la rigidez normal es poco relevante.
b) Para la variación de la inercia $\xi_{y3}(x)$, considerar una inercia equivalente igual a la establecida para calcular la flecha instantánea en EHE-08 50.2.2 y su Anejo 8º 2.2, [4], esto es:

$$I_e = \left(\frac{Mf}{M(x)}\right)^3 \cdot Ib + \left[1-\left(\frac{Mf}{M(x)}\right)^3\right] \cdot If \le Ib, \text{ con:} \qquad (40)$$

$M_f = f_{ctm,fl}\, W_b$ *Momento de fisuración*
$M_{(x)}$ *Momento en la sección (x)*
$f_{ctm,fl} = max\ [(1{,}6 - h/1000) fctm;\ fctm]$
Resistencia a flexotracción
W_b *Módulo resiste sección bruta*
I_b *Mom. de Inercia sección bruta*
I_f *Mom. de la sección fisurada*

El valor de la inercia fisurada I_f (Anejo 8º 2.2 EHE-08) es el siguiente:

$$I_f = n\, A_{s1}\, (d-X)\, (d-X/3) + n\, A_{s2}\, (X-d')\, (X/3-d') \qquad (41)$$

Siendo X la profundidad de la fibra neutra, de valor:

$$X = d \cdot n \cdot \rho 1 \cdot (1+\rho 2/\rho 1)\left[-1+\sqrt{1+\frac{2\cdot\left(1+\frac{\rho 2\cdot d'}{\rho 1\cdot d}\right)^2}{n\cdot\rho 1\left(1+\frac{\rho 2}{\rho 1}\right)^2}}\right], \text{con:} \qquad (42)$$

$$n = Es/Ec; \qquad \rho_1 = A_{s1}/bd; \qquad \rho_2 = As_2/bd \qquad (43)$$

A partir de estos valores de Mf, Ib, If y del valor I(x) en cada sección a lo largo de la barra, se pueden determinar las formales y las rigideces de la barra: α_z; λ'_y; λ''; μ_y; ρ'_y; ρ''_y; η_y.

5.2. Ejemplo de aplicación y comparación de resultados.

La mejor forma de ilustrar el resultado de aplicar los criterios anteriores es mediante un ejemplo.

Para ello se propone estudiar un pórtico plano similar al analizado en el apartado 4 y con estas características:

Pórtico plano compuesto por un dintel y dos soportes de sección constante empotrados en su base.

El pórtico se plantea con hormigón armado H-25 con AEH-500 y sus datos geométricos y las cargas que actúan se representan en la Figura 11. Las unidades utilizadas son Kp y cm.

5.2.1 Cálculo elástico.

En primer lugar, se realiza un cálculo elástico del pórtico (utilizando Tricalc-11) obteniendo los valores siguientes para las armaduras:

Los axiles, cortantes y momentos en los extremos del dintel son:

N = -1,22 t; V = -10 t y M = - 2,45 mt, que equivale a un qL^2 / 40,86.

En los pilares N = -10 2 t; V = -1,22 t y M = - 2,45 mt en cabeza y 1,23 mt en la base.

Las armaduras necesarias son las indicadas en la Figura 12.

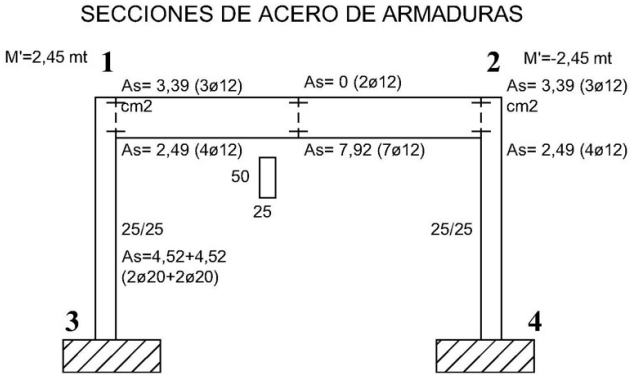

Figura 12. Secciones de armaduras necesarias.

Nota: se consideran las secciones reales de las armaduras, no las necesarias.

5.2.2. Cálculo anelástico.

A partir de los valores anteriores se calculan en primer lugar las leyes de variación de la Inercia equivalente para lo cual hay que partir de los valores de la inercia bruta Ib, momento de fisuración Mf, inercia fisurada If, momentos de empotramiento M' y M", tanto para el dintel como para los soportes. En el dintel, Mf e If son diferentes en la zona de momentos negativos y en zona de momentos positivos, ya que dependen de la sección de las armaduras en estas zonas.

Al realizar el cálculo hay que suponer unos ciertos valores de empotramiento M' y M" que a su vez dependen de las formales y términos de carga. Esto obliga, en el caso del dintel, a realizar un tanteo con unos valores M' y M" supuestos inicialmente, y modificarlos según resulte el valor calculado de estos momentos de empotramiento hasta un valor con aproximación suficiente.

Una vez ajustados, de manera que los valores supuestos para *M'* y *M"* coincidan con el calculado a través de las formales y términos de carga, se determina la ley de variación de la inercia equivalente $\xi_3(x)$, así como de la $\xi_1(x)$ que hemos supuesto de valor 1.

Los valores obtenidos una vez ajustados los valores de *M'* y *M"* son:

a) *Dintel 1-2 en las zonas de momentos negativos y positivos:*

DATOS SECCIÓN	ZONA NEG	ZONA POS	PARA CÁLCULO	ZONA NEG	ZONA POS
b=	25,00	25,00	PROF. FIBRA NEUTRA		
d=	47,00	47,00	A	3,62686681	4,29258449
d´=	3,00	3,00	X=	7,76885026	11,8335565
h=	50,00	50,00	INERCIA BRUTA		
As1=	3,39	7,92	**Ib=**	**260.416,67**	260.416,67
As2=	4,52	2,26	MODULO RES. SECCION BRUTA		
ρ1=	0,00288511	0,00674043	Wb=	10.416,67	10.416,67
ρ2=	0,00384681	0,00192340	MOMENTO DE FISURACIÓN		
n=	6,77	6,77	Mf=	297.917	297.917
fctm,fl=	28,6	28,6	INERCIA FISURADA (NEG-POS):		
fct,m=	26,00	26,00	**If=**	**39.925,74**	**81.311,71**
A=	1.250,00	1.250,00	MÓD. DE ELASTICIDAD		
DATOS DE LA BARRA		**cm y kp**	**E=**	**310.000,00**	310.000,00
L=	500	500			
q=	40	40			
M´=	749.027,5	cmkp		**= q L²/**	**13,35**
M´´=	-749.027,5	cmkp		**= q L²/**	**13,35**
N=	0	kp			

Con estos datos se obtienen los valores de formales: λ'_y; λ_y"; μ_y; términos de carga ***G'***; ***G"***, rigideces ρ'_y; ρ''_y; η_y, y momentos ***M'*** y ***M"***

$$\lambda'_y = \lambda_y'' = 0{,}605216743$$
$$\mu_y = 0{,}258898341$$
$$G' = G'' = 647.245{,}85$$
$$\alpha = 1$$
$$\rho'_y = \rho''_y = 2{,}02238474$$
$$\eta_y = 0{,}865131477$$
$$M' = -M'' = 749.027{,}38$$

En el ***dintel 1-2***, los valores que se obtienen de $\xi_3(x)$ se aprecian en el siguiente gráfico:

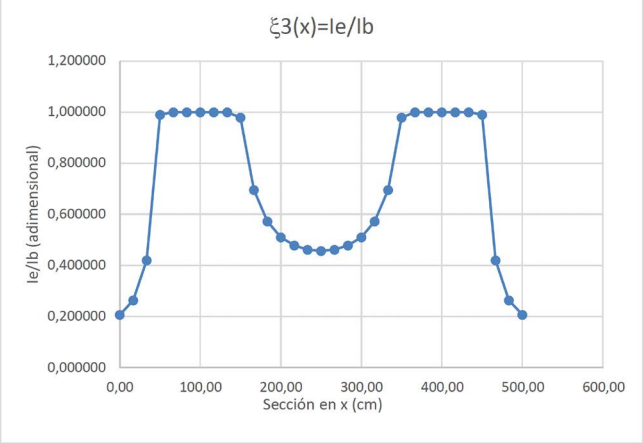

Figura 13. Gráfica de rigideces relativas.

a) Soportes 1-3 y 2-4:

DATOS DE LA SECCIÓN			DATOS PARA EL CÁLCULO		
b=	25,00	cm	PROFUNDIDAD FIBRA NEUTRA		
d=	22,00	cm	A	1,889678737	
d´=	3,00	cm	x=	6,427266026	
h=	25,00	cm	INERCIA BRUTA		
As1=	6,28	cm2	**Ib=**	**32.552,08**	**cm4**
As2=	6,28	cm2	MODULO RES. SECCION BRUTA		
ρ1=	0,01141818		Wb=	2.604,17	
			MOMENTO DE FISURACIÓN		
ρ2=	0,01141818				
n=	6,77		**M_f=**	133.073	cmkp
fctm,fl=	51,1	kp/cm2	INERCIA FISURADA:		
fct,m=	26,00	kp/cm2	**If=**	**13.022,43**	
A=	625,00	cm2	MÓD. DE ELASTICIDAD DEL HORMIGÓN		
DATOS DE LA BARRA		**cm y kp**	**E=**	**310.000,00**	**kp/cm2**
L=	300	cm			
q=	0	kp/cm	**0**	t/ml	
M´=	749.027,50	cmkp	**7,490275**	mt	
M´´=	-374513,75	cmkp	**-3,7451375**	mt	
N=	-10000	kp	**-10**	t	

Nota: Para establecer el valor del momento de fisuración M_f se ha tenido en cuenta la carga axil, incrementando el valor de *fctm,fl*.

Con los datos anteriores, para el dintel, se obtienen los valores de formales: λ'_y; λ_y"; μ_y; términos de carga ***G'***; ***G"***, rigideces ρ'_y; ρ''_y; η_y, y momentos ***M'*** y ***M"***

λ'_y = 0,605216743
λ_y" = 0,605216743
μ_y = 0,258898341
G' = ***G"*** = 647245,85
α = 1
ρ'_y = 2,02238474
ρ''_y = 2,02238474
η_y = 0,865131477
M' = - ***M"*** = -749.027,38

En los ***soportes 1-3 y 2-4***, los valores que se obtienen de $\xi_3(x)$ se aprecian en el siguiente gráfico:

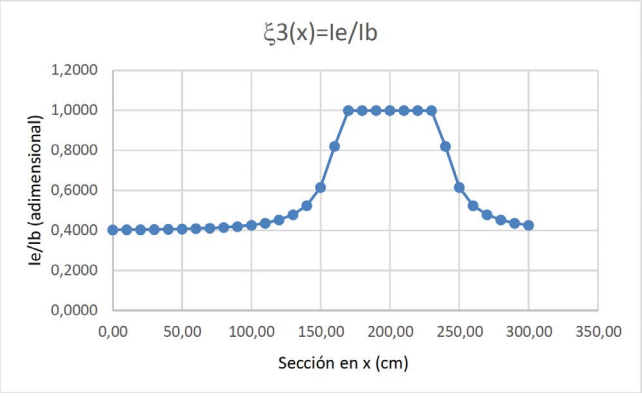

Figura 14. Gráfica de rigideces relativas en soportes 1-3 y 2-4.

Realizado esto, se calculan los coeficientes de la Matriz de Rigidez de cada barra y del total del modelo y se realiza el cálculo.

Las acciones de extremo de barra para el cálculo matricial son estas:

ACCIONES DE EXTREMO

V´= -10.000,00 kp
M´= 749.027,50 cm*kp
N´= 0,00 kp
V´´= -10.000,00 kp
M´´= -749.027,50 cm*kp
N´´= 0,00 kp

La Matriz de Rigidez es:

649.563	-932.427	0	-3.730	-932.427	0
-932.427	383.502.416	-289.553	932.427	139.682.686	0
0	-289.553	777.145	0	0	-775.000
-3.730	932.427	0	649.563	932.427	0
-932.427	139.682.686	0	932.427	383.502.416	-289.553
0	0	-775.000	0	-289.553	777.145

Las acciones de extremo resultantes del cálculo son:

D=	Rm*D=	Amr=	Am=	Am en m y t
-0,015483871	0,00	-10.000,00	-10.000,00	**-10,00**
0,003072735	574.135,00	749.027,50	174.892,50	**1,75**
0,00057322	888,49	0,00	-888,49	**-0,89**
-0,015483871	0,00	-10.000,00	-10.000,00	**-10,00**
-0,003072735	-574.135,00	-749.027,50	-174.892,50	**-1,75**
-0,00057322	-888,49	0,00	888,49	**0,89**

En la última columna los valores son en metros y toneladas y en la anterior en cm y Kp.

Se observa que los momentos equivalen a: q L² / 57,18, que es un 40% menor que el resultado del cálculo elástico.

5.2.3. Recálculo de la sección de armaduras necesarias.

Con los valores anteriores se procede a calcular la sección de armaduras necesaria en dintel (negativos y positivos) y soportes, resultando:

Dintel:

En apoyos (negativo):

$A_{s,sup}$ = 3,39 cm² (3ϕ12); $A_{s,inf}$ = 4,52 cm² (4ϕ12)

Centro vano (positivo):

$A_{s,sup}$ = 2,26 cm² (2ϕ12); $A_{s,inf}$ = 7,92 cm² (7ϕ12)

Soportes (armadura continua):

$A_{s,sup} = A_{s,inf}$ = 4,02 cm² (2ϕ16)

Al modificar los parámetros y recalcular resulta:

D=	Rm*D=	Amr=	Am=	Am en m y t
-0,015483871	0,00	-10.000,00	-10.000,00	-10,00
0,003295069	615.677,60	749.027,50	133.349,90	1,33
0,000441778	684,76	0,00	-684,76	-0,68
-0,015483871	0,00	-10.000,00	-10.000,00	-10,00
-0,003295069	-615.677,60	-749.027,50	-133.349,90	-1,33
-0,000441778	-684,76	0,00	684,76	0,68

Al comparar los resultados se aprecia que el momento flector es 1,33 mt, es decir un 54% de lo que resulta en cálculo elástico. Y esto se debe solo a la disminución de la armadura de los soportes que pasa de 4ϕ20 a 4ϕ16 mientras que en el dintel resulta con la misma armadura anterior.

5.2.4. Análisis del resultado.

Se observa una pérdida de rigidez respecto del cálculo elástico bastante elevada, debido solo a la escasa rigidez de los soportes, con poca carga axil en este ejemplo, y fisurados en buena parte de su longitud, y esto es un caso extremo.

En la mayor parte de los pórticos la rigidez de los soportes es bastante más elevada, por lo que resulta interesante observar cómo cambia el resultado aumentando la rigidez de los soportes; y para ello se ha modificado la sección de los soportes a 50/25 en lugar de 25/25, obteniéndose lo siguiente:

Con sección de los soportes de 25/50.

En cálculo elástico, el momento de los extremos del dintel es de 6,38 mt y las secciones de acero necesarias son:

Dintel:

En apoyos (negativo):

$A_{s,sup}$ = 4,52 cm² (4ϕ12); $A_{s,inf}$ = 4,52 cm² (4ϕ12)

Centro vano (positivo):

$A_{s,sup}$ = 2,26 cm² (2ϕ12); $A_{s,inf}$ = 4,52 cm² (4ϕ12)

Soportes (armadura continua):

$A_{s,sup} = A_{s,inf}$ = 6,78 cm² (6ϕ16)

En cálculo anelástico el momento de los extremos del dintel resultante es 5,84 mt, es decir, un 91,5% Del valor elástico.

En resumen, es la rigidez de los soportes la que más influye en la diferencia entre los resultados que se obtienen en los cálculos elástico y anelástico en barras de hormigón fisuradas. De manera que, en soportes centrales con carga elevada que no sufren fisuración, la rigidez de los dinteles y los momentos extremos que se obtienen es inferior a la obtenida en cálculo elástico mientras que en conexiones con soportes poco rígidos y/o parcialmente fisurados la rigidez de los dinteles cambia sensiblemente.

En cuanto a los dinteles en estado fisurado tanto en zonas de momentos positivos como negativos, se observa que sus valores de empotramiento elástico son similares a los del cálculo elástico, con escasa redistribución plástica.

En todo caso las deformaciones obtenidas en cálculo anelástico se aproximan mucho más a las reales que las deformaciones elásticas.

6. CONCLUSIÓN

Mediante este planteamiento de la Matriz de Rigidez de la barra de sección variable, se puede calcular por el Método de la Matriz de Rigidez cualquier estructura compuesta de barras rectas con sección variable.

Las ecuaciones matriciales que resultan son de igual tamaño que las empleadas para barras de sección constante, si bien, los coeficientes de la matriz son diferentes y hay que obtenerlos por integración a lo largo de la barra.

Lo mismo sucede con las acciones equivalentes de extremo de barra, que también hay que calcularlos por integración.

Debido a que la obtención de los Coeficientes de la Matriz de Rigidez por integración a lo largo de la barra puede ser laborioso cuando la variación de sus constantes mecánicas o la distribución de momentos se complica, resulta ventajosa la integración numérica.

A tal efecto, la regla de Simpson, obtiene una precisión suficiente, con no demasiados intervalos.

En ***materiales isotrópicos***, la aplicación directa del método para barras de sección variable se puede realizar directamente a partir de su geometría sin necesidad de hacer hipótesis del comportamiento del material como cuando este no es isotrópico.

Esto sucede en el ejemplo del apartado 4 y también es el caso de perfiles de acero que tienen refuerzos en alguna zona. Por ejemplo, cartelas o refuerzos en barras que aumentan su rigidez en las zonas reforzadas, como puede suceder en los pilares metálicos cuando se utiliza cierto tipo de uniones semirrígidas que los regruesa y que tiene bastante influencia en el cálculo sísmico.

En el caso de ***materiales no isotrópicos***, como el caso del hormigón armado o las vigas mixtas, es necesario establecer hipótesis que definan las leyes de variación de las constantes mecánicas de las barras como se ha hecho, a título de ejemplo, en el apartado 5 estimando el efecto de la fisuración en la rigidez de las barras de hormigón armado.

Existen numerosos sistemas estructurales donde la rigidez variable de las barras puede ser significativa, por lo que aplicar el método puede resultar útil y ser objeto de nuevos estudios.

Notaciones.

Mayúsculas:

A	Área
Ab	Acciones equivalentes de extremo de barra
D	Desplazamiento longitudinal
Db	Movimientos de extremo de barra
E	Módulo de deformación
F	Acción
G′, G″	Términos de carga.
I	Momento de inercia
It	Módulo de torsión
K	Coeficiente
L	Longitud
M	Momento flector
N	Fuerza normal
Rb	Matriz de Rigidez
T	Momento torsor
U	Capacidad mecánica
V	esfuerzo cortante W Módulo resistente

Minúsculas:

a	Distancia. Flecha
b	Anchura
d	Canto útil
e	Excentricidad f Resistencia
g	Carga permanente repartida
h	Canto total
i	Radio de giro
k	Coeficiente
l	Longitud, luz
m	Momento flector por unidad de longitud
w	Flecha

Minúsculas griegas:

α	(Alfa)	Angulo, coeficiente
β	(Beta)	Angulo, coeficiente
γ	(Gamma)	Coeficiente de ponderación
ε	(Epsilon)	Deformación relativa
η	(Eta)	Coeficiente rigidez
θ	(Theta)	Angulo
λ	(Lambda)	Formal de la barra
μ	(Mu)	Formal de la barra
ν	(Nu)	Esfuerzo normal relativo
ξ	(Xi)	Coeficiente de variación
ρ	(Rho)	Cuantía geométrica
ρ', ρ''		Coeficientes rigidez
σ	(Sigma)	Tensión. Tensión tangencial
φ	(Phi)	Coeficiente
ψ	(Psi)	Coeficiente
ω	(Omega)	Cuantía mecánica

Referencias

[1] Lahuerta, J. A. Formulario para el Proyecto de Estructuras Dossat Madrid, 1.955

[2] Lahuerta, J. A. Apuntes de Estructuras I, ETSAUN

[3] Lahuerta, J. A. Estructuras de edificación, ETSAUN 1.985

[4] EHE-08. Ministerio de Fomento

[5] Xu, Leiping & Hou, Pengfei & Han, Bing. (2016). Stiffness Matrix of Timoshenko Beam Element with Arbitrary Variable Section. 2991/mmebc-16.2016.405

[6] Mancuso, Caitlin & Bartlett, F.. (2017). ACI 318-14 Criteria for Computing Instantaneous Deflections. ACI Structural Journal. 114. 10.14359/5168972654 55 56

ÚLTIMOS NÚMEROS PUBLICADOS

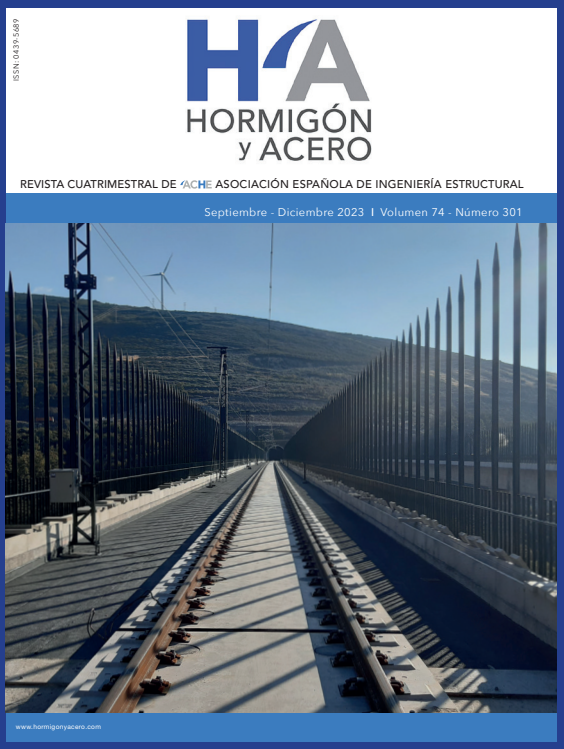

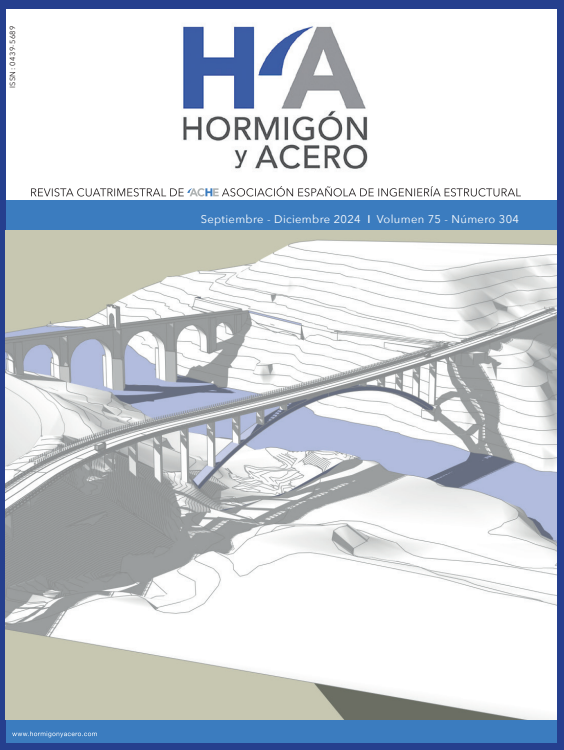

ACHE

Base de datos de artículos publicados en números:
www.hormigonyacero.com


HA
HORMIGÓN
y ACERO